# SOME STUDIES RELATING TO THE DESIGN OF SHALLOW, FLUIDIZED BED, BOILERS

by

KRISHNA KUMAR PILLAI

*A thesis submitted in fulfilment of the requirements for the degree of Doctor of Philosophy*



DEPARTMENT OF MECHANICAL ENGINEERING
THE FACULTY OF ENGINEERING
THE UNIVERSITY OF ASTON IN BIRMINGHAM

*September 1975*

# SUMMARY

The concept of shallow fluidized bed boilers is defined and a preliminary working design for a gas-fired package boiler has been produced. Those areas of the design requiring further study have been specified. Experimental investigations concerning these areas have been carried out.

A two-dimensional, conducting paper analog has been developed for the specific purpose of evaluating sheet fins. The analog has been generalised and is presented as a simple means of simulating the general, two-dimensional Helmholtz equation.

By recording the transient response of spherical, calorimetric probes when plunged into heated air-fluidized beds, heat transfer coefficients have been measured at bed temperatures up to 1 100°C. A correlation fitting all the data to within ±10% has been obtained. A model of heat transfer to surfaces immersed in high temperature beds has been proposed. The model solutions are, however, only in qualitative agreement with the experimental data.

A simple experimental investigation has revealed that the effective, radial, thermal conductivities of shallow fluidized beds are an order of magnitude lower than the axial conductivities. These must, consequently, be taken into account when considering heat transfer to surfaces immersed within fluidized beds.

Preliminary work on pre-mixed gas combustion and some further qualitative experiments have been used as the basis for discussing the feasibility of combusting heavy fuel oils within shallow beds. The use of binary beds, within which the fuel could be both gasified

and subsequently burnt, is proposed.

Finally, the consequences of the experimental studies on the initial design are considered, and suggestions for further work are made.

## ACKNOWLEDGEMENTS

Acknowledgement, with gratitude, is due to the following:

Professor D E Elliott, under whose supervision this work was carried out and for his enthusiasm and advice throughout the project;

Stone-Platt (Crawley) Ltd, for financing this work;

Mr P R Smith of Stone-Platt Ltd for his help and encouragement;

Dr J R Howard, Dr J Broughton and others in the Department of Mechanical Engineering for their advice and assistance in carrying out this work;

Messrs C Geens, A Evitts, N Moss, J Hirons, G Rickers and other technical staff, without whose ingenuity the experimental work would not have been possible;

Messrs D A Lewin, E H Ohuonu and other colleagues for the many constructive discussions which have been invaluable.

## DECLARATION

Some of the material included in Chapters 2 and 3 has been published as two papers, full references for which are given below:

[1] "Some Design Considerations for Shallow Fluid-bed Boilers" with D E Elliott. Proceedings IChemE/IMechE Symposium on Multi-Phase Flow, Paper B4, Glasgow, April 1974

[2] "A Two-dimensional Analog Simulating the Helmholtz Equation for Heat Flow". Int.J.Heat & Mass Transfer, 18, 341-344, 1975.

All the work reported in this thesis has been carried out during the period October 1972 - May 1975, and apart from the material mentioned above, has not been published before.

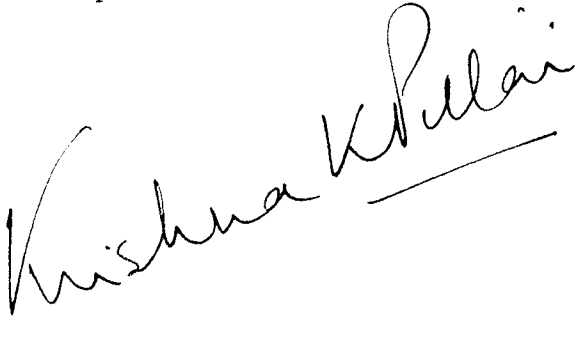

Krishna K Pillai

September 1975

# C O N T E N T S

# LIST OF ILLUSTRATIONS

# NOMENCLATURE

| | | |
|---|---|---|
| A | Area | |
| Ar | Archimedes number | $gD_p^3\rho_f\rho_s/\mu_f^2$ |
| Bi | Biot number | $hR/k$ |
| c | Concentration | |
| | A constant | |
| $c_p$ | Specific heat | |
| $C_d$ | Drag coefficient | |
| $C_g$ | Diffusional velocity coefficient | |
| d | Diameter | |
| D | Diameter | |
| $D_e$ | Equivalent bubble diameter | |
| $D_g$ | Diffusion coefficient | |
| e | Emissivity | |
| $\underline{E}$ | Electrostatic field strength vector | |
| $f_o$ | Volume fraction | |
| $f_u$ | Unburnt fuel fraction | |
| F | Shape factor | |
| Fo | Fourier number | $\alpha t/R^2$ |
| g | Gravitational acceleration | |
| h | Heat transfer coefficient | |
| H | Bed height | |
| H{a} | Heaviside unit step function | |
| i | Current | |
| | Current density | |
| | Spatial node | |

| | | |
|---|---|---|
| I | Modified Bessel function of the first kind | |
| j | Temporal node | |
| J | Modified Bessel function of the second kind | |
| k | Thermal conductivity | |
| $k_r$ | Thermal conductivity ratio | |
| $\ell$ | Length | |
| m | Mass | |
| n | Order of modified Bessel function | |
| | Index in regression analysis | |
| N | Fluidization index | $Re_f/Re_{mf}$ |
| Nu | Nusselt number | $hD_p/k_f$ |
| p | Pressure | |
| | A temperature excess ratio | |
| | Index in regression analysis | |
| | Non-dimensional position | |
| P | Constant potential | |
| Pr | Prandtl number | $\mu_f c_{pf}/k_f$ |
| q | Gas flow | |
| Q | Gas flow | |
| | Heat flow | |
| r | Radius | |
| R | Radius | |
| | Finning ratio | |
| Re | Reynolds number | $\rho_f D_p U/\mu_f$ |
| Ro | A temperature excess ratio | |
| $\underline{S}$ | Non-dimensional radiation parameter | |
| s | Current density vector | |

| | |
|---|---|
| $t$ | Time |
| | Temperature |
| | Fin thickness |
| | Paper thickness |
| $T$ | Temperature |
| $u$ | Argument of modified Bessel functions |
| $U$ | Velocity |
| $U_{br}$ | Relative bubble rise velocity |
| $V$ | Volume |
| | Voltage |
| $w$ | Bed weight |
| $x,y,z$ | Cartesian coordinate axes |
| $X$ | Non-dimensional radiating temperature |
| $Z$ | Non-dimensional distance |

## GREEK LETTERS

| | |
|---|---|
| $\alpha$ | Thermal diffusivity |
| $\beta$ | Non-dimensional material concentrations |
| | A constant |
| $\gamma$ | Electrical conductivity |
| | Material concentration |
| $\delta$ | Thickness |
| $\Delta$ | Difference (as a prefix) |
| $\epsilon$ | Area voidage |
| $\phi$ | Fin effectiveness |
| $\phi_s$ | Sphericity |
| $\lambda$ | Bed temperature coefficient |

| | |
|---|---|
| | A constant |
| $\mu$ | Viscosity |
| | Non-dimensional wall temperature |
| | A constant |
| $\theta$ | Potential |
| | Temperature excess |
| | Non-dimensional temperature |
| $\rho$ | Density |
| $\sigma$ | Stefan-Boltzmann constant |
| $\tau$ | Non-dimensional time |
| $\xi$ | Non-dimensional height |
| $\nabla^2$ | Laplacian operator |

## SUFFIXES

| | |
|---|---|
| b | Bubble; bulk; bed |
| c | Conductive; corrected |
| d | Diffusional |
| e | Effective; equivalent; emulsion |
| f | Fluid; fin; fluidization |
| i | Internal; instantaneous; at node i |
| j | At node j |
| l | Laminate |
| LM | Log mean |
| m | Metal; mean; time-mean; maximum |
| max | Maximum |
| mf | At minimum fluidization |
| o | external; root; at time zero |

| | |
|---|---|
| opt | Optimum |
| p | Particle; packet |
| r | Residence; radiative; radial |
| s | Solid; surroundings; surface |
| t | Tip; terminal; tube; at time t |
| x | In the x-direction |
| y | In the y-direction |
| z | In the z-direction |
| xy | On the xy-plane |

# CHAPTER 1

# INTRODUCTION

## 1.1 PRELUDE

Fluidization is the process by which a bed of solid particles is made to assume liquid like characteristics. The process is achieved by forcing a fluid (liquid or gas) through a bed of particles at a rate greater than that at which the frictional drag exerted on the particles by the fluid exactly counter-balances the weight of the particles. In this work only gas-fluidized beds are considered. A bed in which the particle's weight is only just balanced is said to be just fluidized and the conditions at such a point are referred to as minimum fluidization conditions[1,2]. At fluid flow rates greater than that for minimum fluidization, the two-phase theory of fluidization provides a simplistic model for treating the formation, growth and motion of fluid bubbles[1,3].

The motion of gas bubbles through a fluidized bed results in the rapid agitation and mixing of the solid particles. This mixing in turn brings about high heat and mass transfer rates between the gas and the fluidized particles, and high heat transfer rates between the bed and surfaces immersed within it[2,4]. It has further been shown that if a fuel is introduced into an air-fluidized bed which is at a temperature sufficiently high to initiate combustion, then, under certain conditions, stable and efficient combustion may be maintained within the bed. If energy is being extracted from such a bed, relatively low temperature combustion may be achieved. The efficiency of the combustion process is largely determined by the ability of the fuel to contact sufficient air within the bed[5].

While the two-phase theory of fluidization goes a long way towards explaining bubble behaviour, the mechanisms controlling rate processes within a fluidized bed are, as yet, imperfectly understood. Though a large body of data has been accumulated and though several mechanisms have been postulated, an element of empiricism has always been required to reconcile theory with experiment. References [1] and [2] provide an up-to-date survey of the existing literature.

## 1.2 THE TWO-PHASE THEORY: A SIMPLE EXPOSITION

### 1.2.1 Fluidization Regimes

Consider a bed of particles through which a fluid is forced to flow upwards. At low flow rates the fluid seeps through the interstices between stationary particles, forming a *packed bed*. As the flow rate is increased, the interstitial volume expands as the particles separate to counter the effects of increasing drag. At a specific flow rate, however, the particles still remain stationary in space though they may vibrate about a fixed point. This is an *expanded bed*. As the flow rate is increased still further, the frictional drag exerted on each particle increases until it is equal to the weight of each particle. In this state the bed is referred to as a bed at *minimum fluidization* conditions, or as an *incipiently fluidized bed*. With gas-fluidized beds, any further increase in flow rate results in very little further bed expansion. The gas flow which is in excess of that required for incipient fluidization passes through the bed as bubbles. If the gas flow rate eventually exceeds the terminal velocity of the

particles, the particles are progressively entrained by the gas flow above the bed until all the particles are elutriated. As gas bubbles rise through a fluidized bed, the bubble volume increases as small bubbles coalesce to form larger ones, and in a deep bed bubbles may grow to be as large as the containing vessel itself. In such a situation the portion of the bed above the bubble travels upwards as a slug of material which gradually disintegrates and falls back upon itself, forming a further slug upon meeting another bubble. This phenomenon, known as *slugging*, is an unstable, oscillatory condition, generally to be avoided. While other regimes of fluidization do exist, they are not applicable to the species of gas-fluidized beds being considered here.

Numerous experimental correlations and theoretical expressions are now available for the prediction of minimum fluidizing velocities[1,2,3,4]. The expressions consistently used in this work are given below. These equations derive from the Ergun equation[7] for the pressure drop through fixed beds. This pressure drop comprises a viscous loss term and a kinetic loss term, and hence

$$Ar_p = 150 \frac{(1 - \varepsilon_{mf})}{\phi_s^2 \varepsilon_{mf}^3} Re_{mf} + \frac{1.75}{\varepsilon_{mf}^3 \phi_s} Re_{mf}^2 \qquad (1.1)$$

However, at low particle Reynolds Numbers, kinetic energy losses may be neglected, giving

$$Re_{mf} = \frac{\phi_s^2 \varepsilon_{mf}^3}{150(1 - \varepsilon_{mf})} Ar_p \qquad \text{for } Re_{mf} < 20 \qquad (1.2)$$

At high Reynolds Numbers, the kinetic term predominates:

$$Re_{mf}^2 = \frac{\phi_s \, \varepsilon_{mf}^3}{1.75} Ar_p \qquad \text{for } Re_{mf} > 1\,000 \qquad (1.3)$$

1.2.2 The Simple Two-Phase Theory

The basic premise on which the two-phase theory is built is that a bubbling gas-fluidized bed can be considered a two-phase system comprising

(a) the emulsion or dense phase, containing solid particles and the attendant gas flow necessary to keep the particles in the incipiently fluidized state, and

(b) the gas bubbles or lean phase, which is made up of gas pockets within the emulsion phase[7].

This model, as anunciated by Davidson[3], was used to account for the motion of single bubbles through an incipiently fluidized bed. The model assumes that

i. gas bubbles are spherical and free of solids

ii. the emulsion phase behaves as an inviscid, incompressible fluid, of density equal to $\rho_s(1 - \varepsilon_{mf})$

iii. the pressure within the gas bubble is uniform

iv. the pressure distribution remains undisturbed far from the bubble.

Davidson showed that the gas flow pattern around the bubble was dependent only upon the ratio of the bubble rise velocity to the velocity of the gas in the emulsion phase. Bubble rise velocities have been extensively studied[1,3,4] and are generally presented in a form analogous to that for the velocity of a gas bubble in a liquid[2].

$$U_{br} = 0.711\ (g\ D_b)^{\frac{1}{2}} \tag{1.4}$$

The velocity of the gas through the emulsion phase is given by

$$U'_f = \frac{U_{mf}}{\varepsilon_{mf}} \tag{1.5}$$

The model identifies two regimes of flow patterns; one corresponding to a 'slow' bubble where $U_{br} < U'_f$, and another for a 'fast' bubble with $U_{br} > U'_f$. In the case of a slow bubble, gas from the emulsion phase uses the bubble as a short circuit and flows upwards through the bubble. There is little or no circulation of gas round the bubble. In the case of fast bubbles, a circulation region is set up around the bubble. Gas flows upwards through the bubble but now, on leaving, is swept around to re-enter the bubble at the bottom. The region occupied by the circulating gas is termed the *cloud*, and its size is determined by the ratio $U_{br}/U'_f$. This simple model is useful in that it explains the observed stability of bubbles and the observation that the gas within a bubble can pass through a bed without contacting the rest of the bed.

Apart from the fact that bubbles do not occur singly in gas-fluidized beds, the major deviation observed in real beds has been that the lower part of a bubble is not, in fact, spherical[2,8]. This portion of the bubble is concave due to a partial collapse, for reasons still unclear, of the spherical form. This collapse brings about a stream of turbulence behind the bubble and is probably the main mechanism responsible for solids mixing[9]. Various extensions of the simple two-phase model have been proposed, but none invalidate the essential correctness of the Davidson model.

To apply the simple model to real situations, the following assumptions are made[2]. Within the immediate vicinity of a bubble, gas flow is considered to be well approximated by the model. It is assumed that most of the bubble growth due to coalescence occurs close to the distributor. Thus, apart from a small entry region, the bubble size is taken to be constant through the rest of the bed. The rise velocity of bubble swarms is taken[1] as

$$U_b = 1.2[(U_f - U_{mf}) + U_{br}] \qquad (1.6)$$

where $U_{br}$ is the relative velocity of rise of the bubble. The emulsion phase is all considered to be at incipient conditions. In spite of the experimental evidence that there is usually a small quantity of solids within bubbles, for simplicity, the bubble phase is considered to be completely solids free. The volume fraction of the bubble phase can be expressed in terms of the voidage, or heights, of incipiently and well fluidized beds[11,12,13].

$$f_o = (\varepsilon_f - \varepsilon_{mf})/(1 - \varepsilon_{mf}) = (H_f - H_{mf})/(1 - H_{mf}) \qquad (1.7)$$

## 1.3 THE OBJECT STATEMENT

*It is the purpose of this work*

- *to carry out a study of the feasibility of fluidized bed package boilers*
- *consequently to identify ill-defined or unspecified areas of the required knowledge*
- *to investigate as many of such areas as is possible*
- *to refine the initial set of design criteria.*

Thus Chapter 2 consists of the initial design study where the proposed areas for investigation are specified. The remainder of the thesis is an account of these investigations. The concluding chapter is concerned with the consequences of these investigations on the initial set of design criteria.

# CHAPTER 2

# PRELIMINARY DESIGN CONSIDERATIONS

## 2.1 THE CONCEPT OF A FLUIDIZED BED BOILER

### 2.1.1 The Definition of a Package Boiler

For the purpose of this work, a package boiler is considered to be a fully automated, self-contained unit, producing either steam or hot water. The unit, using either a gaseous or a liquid fuel, will have a maximum thermal output of 5 MW, with the working fluid outlet conditions not exceeding a temperature of 1 000 K or a pressure of 7 atmospheres.

### 2.1.2 The Concept of a Fluidized Bed Boiler

The basic criterion that a design for a fluidized bed boiler must satisfy is that it must appear to have significant advantages over conventional package boilers in performance, in size or in cost.

The design concept envisages the use of two or more inert, fluidized bed stages arranged in series, and each containing heat transfer surfaces. Gaseous or liquid fuel combustion will take place solely in the first bed where the combustion air will serve as the fluidizing medium. The temperature of this bed will be maintained at a value high enough to permit stable combustion, yet low enough to allow the extraction of the required thermal energy. The exhaust gases will then serve to fluidize one or more further inert beds where additional heat transfer to boiler tubes will take place. These further stages will be analogous to the economiser in a conventional unit and will enable the final exhaust temperature to be lowered to any desired value. The air-side pressure drop, and hence

the required fan power, will be kept to a minimum by utilising the minimum number of stages with each stage being kept as shallow as possible. (The critical factor determining the minimum height of each stage is the requirement that for efficieint heat transfer all surfaces be immersed within the dense phase of each bed). Consequently it is envisaged that a fluidized bed boiler will consist only of shallow bed stages where a shallow bed is qualitatively defined as one within which the bubble coalescence process is far from complete at the bed surface. A schematic layout of such a unit is shown in Figure 2.1.

## 2.2 THE DESIGN PARAMETERS

### 2.2.1 Fluidization Velocities

The required boiler duty specifies the mass flow of air required to support the necessary combustion. At a particular temperature, any desired superficial fluidizing velocity can then be achieved by controlling the bed area used. The importance of the value of the superficial fluidizing velocity, $U_f$, in describing the prevailing fluidization conditions, suggests that this should be the first parameter chosen; the other design parameters then being tailored to suit this value.

It is therefore necessary that a design range of fluidization velocities be specified within the limits set by the minimum fluidization velocity, $U_{mf}$, and the terminal velocity, $U_t$, of the particles being considered. Equations (1.1) to (1.3) provide for the calculation of minimum fluidization velocities. The terminal velocity of a sphere within a stationary fluid can be shown to be

$$U_t = \left[\frac{4\ g\ D_p(\rho_s - \rho_f)}{3\ \rho_f\ C_d}\right]^{0.5} \qquad (2.1)$$

where $C_d$ is an experimental drag coefficient[10]. However, $C_d$ is a complicated function of the gas and solid physical properties. A system of equations corresponding to different ranges of Archimedes Number must therefore be used to calculate terminal velocities[1]. Thus

$$Ar_p = 18\ Re_t \qquad \text{for } Ar_p < 3.6 \qquad (2.2)$$

$$Ar_p = 18\ Re_t + 2.7\ Re_t^{1.687} \qquad \text{for } 3.6 < Ar_p < 10^5 \qquad (2.3)$$

$$Ar_p = \tfrac{1}{3}\ Re_t^2 \qquad \text{for } Ar_p > 10^5 \qquad (2.4)$$

where $Re_t = \rho_f D_p U_t / \mu_f$.

The above expressions for the calculation of $Re_{mf}$ and $Re_t$ are strictly applicable only to spherical particles, but providing the value of particle diameter, $D_p$, used is that of a sphere having the same surface area as the particles under consideration, the expressions may still be used[2].

For satisfactory operation it is essential that the fluidizing velocity through the combustion bed be such that both the combustion and heat transfer processes operate at sufficiently high efficiencies. In the additional stages only heat transfer criteria need be met. Previous work, reported in [1,2,4], has shown that heat transfer coefficients to surfaces immersed in fluidized beds increase with increasing fluidizing velocity, until a maximum is reached at $U_f \simeq 1.2\ U_{mf}$. It then remains virtually constant until $U_f$ approaches

$U_t$, at which point it decreases sharply. Consequently, a useful regime of fluidization velocities, measured at prevailing bed temperatures, can arbitrarily be defined by

$$2\ U_{mf} < U_f < 0.5\ U_t \qquad (2.5)$$

Generally modulation requirements for package boilers specify that a turndown ratio of about 5:1 be available on the combustion air flow. The ratio $U_t/U_{mf}$ usually lies between 10 and 100, and hence an additional requirement in the combustion bed is

$$U_t/U_{mf} > 20 \qquad (2.6)$$

Smaller values of this ratio could only be used if a facility for altering the fuel/air mixture strength were available.

A further requirement is that velocities should not be such that slugging may be initiated. However, since only shallow beds are being considered, this condition should be readily satisfied.

### 2.2.2 Combustion Considerations

#### 2.2.2.1 Combustion regimes

Only the combustion of liquid and gaseous fuels is being considered here. There are two basic methods by which fuel may be introduced into an air-fluidized bed which is at an elevated temperature and then induced to burn. The fuel can either be injected directly into the bed or it can be pre-mixed with the combustion air, upstream of the bed.

(a) If the fuel is injected directly into the bed, bubbles of gaseous fuel will eventually be formed. For a liquid fuel,

a liquid or a liquid/vapour bubble will initially be formed which will eventually become a vapour bubble. With a gaseous fuel, a gas bubble will be formed immediately on injection. Whether combustion will take place, or whether the now gaseous fuel will pass unburnt through the bed, will depend upon the mechanisms by which the fuel within the bubble mixes with the combustion air in the dense phase, and by which heat is transferred to the resultant combustible mixture. (This combustible mixture could be present within either the bubble phase or the dense phase). The mixing and heat transfer process will in turn be controlled by the prevailing fluidization conditions and the height of bed through which the bubbles have to travel.

(b) The second method requires that the fuel be intimately mixed with the combustion air prior to entering the bed. This implies the use of a gaseous fuel, or of a liquid fuel which can easily be vaporised before injection. It is now the combustible fuel-air mixture, rather than the combustion air alone, which serves to fluidize the solid particles. Thus, the interstitial gas mixture in the dense phase will combust directly upon attaining the ignition temperature. The remainder of the gas mixture will initially form bubbles, and only that proportion of the bubble phase which is transferred to the dense phase will react within the dense phase. The rest of the bubble phase will pass unburnt through the bed, unless the temperature within the bubble exceeds the ignition temperature, whereupon the bubble will explode.

2.2.2.2 The combustion of pre-mixed gases

The fluidized combustion of heavy oils or of any other fuels which are difficult to vaporise, has never yet been successfully carried out within a shallow fluidized bed. Even with relatively deep beds, direct combustion has not been achieved, though some success has been attained with the gasification of such fuels[14]. Unless otherwise stated, therefore, fluidized combustion in the context of this work refers to the combustion of a gas or a vapour.

Consideration of the methods of fuel injection makes it intuitively obvious that the mixing of the fuel with air prior to entering a particles bed will provide a more efficient combustion process than the direct injection of the fuel into an air-fluidized bed.

In spite of the oversimplifications and assumptions inherent in the simple two-phase theory, it is instructive to consider the efficiency of the pre-mixed combustion process on this basis. The following further assumptions are made:

(i) The combustion reaction of a combustible mixture at ignition temperature is instantaneous

(ii) Within the dense phase, the heat transfer rate from solids to gas, though much slower than combustion rates, is fast enough to neglect the time required for the gas to attain ignition temperature

(iii) All the gas flow in excess of that required for minimum fluidization forms bubbles at the surface of the distributor plate

(iv) Through a small interval of bed height, the bubble diameter

may be considered constant and equal to some equivalent bubble diameter, $D_e$.

Assumptions (i) and (ii) together imply that at any point in the bed, unburnt gas can only exist within the bubble phase. The combustion efficiency consequently depends upon the rate at which gas is exchanged between the bubble and the surrounding dense phase. This exchange must consist of a bulk flow term and a diffusional term[1,2]. However, most gas combustors will operate within velocity regimes at which a cloud may be expected to exist around the bubble phase. The gas exchange must occur, therefore, via the cloud. If we postulate that assumptions (i) and (ii) above are still valid within the cloud even though the voidage here will be considerably higher than in the dense phase[15], then only the gas exchange between the bubble and the surrounding cloud need be considered.

The bulk flow of gas circulating through the bubble and into the cloud has been estimated, in [3, p69] as,

$$q_b = 0.75 \pi D_e^2 U_{mf} \tag{2.7}$$

Davidson and Harrison[3] also estimate a diffusional contribution taking place parallel to the bulk flow:

$$q_d = C_g \pi D_e^2 \tag{2.8}$$

where $C_g$ = diffusional velocity coefficient

$$= 0.975 D_g^{0.5} g^{0.25} D_e^{0.25} \Delta c \tag{2.9}$$

If these represent the only mechanism by which gas may be exchanged between the bubble and the cloud, it can be shown (Appendix A1) that the fraction of gas passing unburnt through the bed is given by

$$f_u = \frac{U_f - U_{mf}}{U_f} \quad \frac{b\, c_o}{e^{bt_b}(b + ac_o) - ac_o} \tag{2.10}$$

If the diffusional contribution is neglected this reduces to

$$f_u = \frac{U_f - U_{mf}}{U_f}\, c_o\, e^{-bt_b} \tag{2.11}$$

Broughton[5] in an experimental study of premixed fluidized combustion has presented a correlation for gas by-pass:

$$f_u = \frac{U_f - U_{mf}}{U_f}\, e^{-0.11\, U_{mf}\, H_{mf}} \tag{2.12}$$

where $U_{mf}$ and $H_{mf}$ are in cgs units.

Figure 2.3 compares Broughton's experimental correlation with equations (2.10) and (2.11). It is immediately apparent that the diffusional contribution is small. This is to be expected with premixed combustion, since the nitrogen concentration in both the unburnt gas mixture and in the products of combustion is high, and consequently the effective composition difference across the bubble boundary is low. However, it is also apparent that gas exchange considerations alone are not sufficient to explain the experimental evidence. Some additional combustion mechanisms must come into play, especially in the region some distance from the distributor. One may expect that combustion will be enhanced by the following mechanisms:

(a) Bubble formation commences only at a distance of some ten particle diameters from the distributor[17,18]. Thus any

reaction in the dense phase prior to bubble formation would be significant and the concentration of unburnt gas within the bubble at the point of bubble formation, $c_o$, may be considerably lower than that assumed.

(b) Some combustion will probably take place within the bubble phase itself. This is supported by the observation that a fluidized combustor has a characteristic 'popping' sound associated with it. The suggestion is that this is caused by the detonation of gas bubbles as they attain ignition temperature. The detonation mechanism will be complex, but the process may be considered to involve the establishment of a flame front around the perimeter of the bubble. This flame front must propagate radially inwards and must be extinguished at some point within the bubble. However, it has been observed in this work that these explosive sounds are virtually non-existent at bed temperatures of above 840°C. The cessation of sounds is extremely abrupt, and the level at which it occurs is completely reproducible. However, no consequent changes in fuel by-pass levels have been observed. No satisfactory explanation for this effect can be advanced.

In an effort to verify the predictions of equations (2.10), (2.11) and (2.12), the pre-mixed combustion of propane in fluidized sand beds has been investigated. Experiments were carried out in a quartz bed, 100 mm diameter, and fitted with a ceramic distributor plate. Various sizes of zircon and silica sand were tested. The air flow rate was varied, the propane flow rate always being adjusted

to provide a stoichiometric mixture.

$CO/CO_2$ levels were continuously monitored, and fuel by-pass fractions were estimated from these levels. The data was obtained using a "MEXA 300", $CO/CO_2$ infra-red gas analyser, the sampling probe being positioned immediately above the bubble bed surface. The derived fuel by-pass levels are presented as functions of the bed height in Figures 2.4 to 2.9, where they are compared with the predictions of equation (2.12).

It is apparent from these data that some or all of the proposed mechanisms by which combustion is enhanced must be coming into play. The data while of limited accuracy, does indicate that, if anything, equation (2.12) provides an over-estimate of maximum fuel by-pass and hence may safely be used as a design equation. The experimental evidence also shows that excess air is not generally required for efficient combustion. Thus, most fluidized gas combustors within feasible velocity and size regimes may be expected, generally, to have sufficient depth available for complete combustion.

### 2.2.3 Heat Transfer Considerations

#### 2.2.3.1 Heat transfer coefficients

Although within fluidized beds the bed-side heat transfer coefficients to immersed tubes are extremely high, they are still low enough, relative to the water, or steam, side coefficients to warrant the use of extended surface tubing[19,20]. However, no generalised correlation for the prediction of these bed-side coefficients is yet available. Reviews of the various experimental

correlations, each valid only within the experimenters specific conditions, are available in references [1] and [2]. Bartel *et al*[21,23] and Petrie *et al*[22] have investigated finned tubes within relatively deep beds but their data, while confirming the order of magnitude of the coefficients to be expected, does not lend itself to design correlations. The data available for heat transfer to finned tubes in shallow beds[24,31,32] indicates coefficient values somewhat higher than those reported for bare tubes in deep beds [2,4,25-30].

Although it is difficult to predict precisely these heat transfer coefficients in any given system, the following relationships have now been well established[1,2,4]:

(a) The heat transfer coefficient increases with increasing fluidizing velocity, reaching a maximum at about 1.2 $U_{mf}$ and then remaining virtually constant over a large velocity range.

(b) With bed temperatures up to 700 K, the available data indicates that the maximum coefficient is proportional to the 0.6 power of gas conductivity.

(c) The maximum coefficient has also been found to be inversely proportional to the 0.36 power of the particle diameter.

These conclusions appear to be valid even in shallow beds[24,31,32] as illustrated in Figure 2.10. Thus

$$h_{b_{max}} = k_g^{0.6}/D_p^{0.36} \qquad (2.13)$$

For design purposes an initial value of $h_b$ must be assumed, and it is proposed that some mean value which is an under-estimate be used.

2.2.3.2 The use of extended surface

The information available[31,32] indicates that when using extended surface tubing in fluidized beds, with fin spacings of more than about ten particle diameters, no adverse effect on particle mobility, and hence on heat transfer, is encountered. It has also been found that providing the above condition is satisfied, completely packing a bed with heat exchange surface has no apparent effect on the heat transfer performance.

Once values of heat transfer coefficients in each proposed stage have been established, the surface areas required in each stage may then be estimated. However, when using extended surfaces it is necessary that the reduced effectiveness of the increased surface area, brought about by the temperature gradients within the surfaces, be taken into account. This is best done by using the concept of fin effectiveness as proposed by Carrier and Anderson[33] and Gardner[34]. The effectiveness, $\Phi$, is defined as

$$\Phi = \frac{\text{heat transferred by the extended surface}}{\text{heat that would be transferred if the entire surface were at the fin root temperature}}$$

The use of this parameter enables a finned tube to be treated as a bare tube having an unchanged inside diameter, $D_{ti}$, but now having an effective external surface area given by

$$A_e = A_{to} + \Phi A_f \qquad (2.14)$$

The entire surface area may thus be considered to be at a metal temperature, $t_m$, which is a function only of the tube length, l, and of the heat transfer rate to the tube. It must be noted that the

concept of fin effectiveness assumes a uniform heat transfer coefficient over the entire surface area. This condition is unlikely to be satisfied within a fluidized bed, but since only area-averaged coefficients can generally be measured experimentally, this should not be a major source of error.

Within any fluidized bed stage the heat transfer to the working fluid will be given by:

$$Q = \frac{A_{ti}}{l} \int_0^1 h_f (t_m - t_f) dx \qquad (2.15)$$

where $t_m$ = local metal temperature

$t_f$ = local fluid temperature.

If the fluid temperature is being raised linearly from a temperature $T_{f1}$ to $T_{f2}$, and if the fluid is subject to a constant fluid-side heat transfer coefficient, $h_f$, then

$$t_m = \frac{h_f [T_{f1} + (T_{f2} - T_{f1})\ x/l] + R\ h_b\ T_b}{h_f + R\ h_b} \qquad (2.16)$$

where R is the finning ratio defined as

$$R = A_e/A_{ti} = \frac{A_{to} + \Phi\ A_f}{A_{ti}} \qquad (2.17)$$

The bed is considered isothermal at a temperature $T_b$ and hence no account is taken of any temperature gradients that may exist in the vicinity of the extended surface. Integration of equation (2.15) yields

$$Q = \frac{R\ h_f\ A_b\ A_{ti}}{h_f + Rh_b} \{T_b - 1.5\ T_{f1} - 0.5\ T_{f2}\} \qquad (2.18)$$

The assumption that $h_f$ is constant is reasonable within the evaporation or the superheating stage, but may be subject to an absolute error of about 30% when considering heat transfer to just the liquid phase. In such a situation, providing the temperature of the fluid is not increasing by more than about 200 K within the stage, a linear relationship between $h_f$ and $t_f$ may be used with an accuracy of better than 10% in the resultant value of $h_f$. The Dittus Boelter correlation for turbulent flow, subject to the Sieder Tate correction, may then be used[35] for the prediction of the coefficient $h_f$. The use of such a linear relationship in equation (2.15) makes the integral somewhat cumbersome, but this can be shown to be

$$Q = \frac{\pi R h_b D_{ti} \ell}{h_{f2}-h_{f1}} \times P \qquad (2.19)$$

where P represents the product of effective heat transfer coefficient and temperature difference averaged over the entire tube length (Appendix A2).

$$P = \left\{\Delta T_f(h_{f1}+Rh_b)\left[\frac{h_{f1}}{\Delta h_f}\ln\frac{h_{f2}+Rh_b}{h_{f1}+Rh_b} + \ln(h_{f2}+Rh_b) + \frac{2(T_b-T_{f1})}{\Delta T_f} + \frac{3Rh_b-h_{f1}}{2\Delta h_f}\right] + h_{f1}(T_b-T_{f1}) + h_{f1}T_{f1}\frac{Rh_b-h_{f2}}{\Delta h_f} - Rh_b(T_b-T_{f1})\ln\frac{h_{f2}+Rh_b}{h_{f1}+Rh_b}\right\} \qquad (2.20)$$

where $h_{f1}$ = $h_f$ at $T_{f1}$

$h_{f2}$ = $h_f$ at $T_{f2}$

$$\Delta T_f = T_{f2} - T_{f1}$$

$$\Delta h_f = h_{f2} - h_{f1}$$

However, it is proposed that equation (2.18) be used in preference to equation (2.19) when there is any doubt as to the precise value of $h_b$ since with $R < 10$, the resultant error in Q is less than ±10%. The use of the above set of equations enables tube lengths for each stage to be estimated under specified temperature conditions, for any required thermal duty.

### 2.2.3.3 The distribution of thermal duty in a multi-stage fluidized unit

The energy extracted from each stage may be regulated by altering the surface area available for heat transfer in each bed of a multi-stage unit. It is patent, therefore, that there will be some particular combination of extraction rates from each stage which will maximise the total amount of energy which can be extracted under any specified temperature configuration.

Figure 2.11 illustrates a typical temperature profile that might exist in a two-stage unit. The inlet gas temperature, $T_{g1}$, is considered to be the adiabatic temperature achieved by the given mass flow of air and gas under stoichiometric combustion conditions. The combustion bed temperature and the inlet fluid temperature are considered fixed. The required output conditions determine the fluid temperature and the gas temperature at exit. The problem is therefore to determine the optimal proportions of the total output to be derived from each bed. The total duty is given by

$$Q = h_1 A_1 \Delta T_{LM1} + h_2 A_2 \Delta T_{LM2} \qquad (2.21)$$

where

$$\Delta T_{LM1} = \frac{\theta_3 - \theta_2}{\ln \frac{\theta_3}{\theta_2}}$$

and

$$\Delta T_{LM2} = \frac{\theta_1 - \theta_2}{\ln \frac{\theta_1}{\theta_2}}$$

and with the other parameters as defined in Figure 2.11. The heat transfer coefficients here refer to the overall energy transfer between the gas and the working fluid. Thus, if the heat transfer coefficients and the surface areas available in each bed are known, the maximum energy, Q, that can be extracted from the system is dependant only upon, the temperature differences $\theta_1$, $\theta_2$ and $\theta_3$. Hence

$$Q_{max} = f(\theta_1, \theta_2, \theta_3)$$
$$= f(R_o, p)$$

where $p = \frac{\theta_1}{\theta_2}$

and $R_o = \frac{\theta_3}{\theta_1}$

Assuming further that $R_o$ is fixed by the prevailing input and output conditions, it is possible to maximise on p for Q. This procedure determines the value of the intermediate temperature difference, $\theta_2$, which corresponds to $Q_{max}$ for the particular conditions defined by the ratio $R_o$.

Thus,

$$h_1A_1\{(\ell n\ p)^2\ R_o p - (\ell n\ p)^2\ [1 + \ell n\ p + \ell n\ R_o]\}$$

$$+ h_2A_2\{(\ell n\ pR_o)^2\ [p - 1 - \ell n\ p]\} = 0 \qquad (2.22)$$

For known values of the ratio $h_1A_1/h_2A_2$, equation (2.22) may be solved iteratively for p. Hence, the proportion of the energy to be extracted from each bed (equation (2.21)), may then be calculated. Figure 2.12 illustrates the dependance of the optimum heat extraction rates on the ratio $R_o$ for different values of $h_1A_1/h_2A_2$.

A similar analysis can be carried out for units with more than two stages which may be further complicated by the working fluid undergoing a phase change. However, recourse must then be made to tedious, iterative or trial and error methods. These solutions, though simple, are cumbersome and since they only apply to specific thermal conditions, are not included here.

### 2.2.4 Control Considerations

#### 2.2.4.1 Start-up procedures

With premixed combustion, ignition will take place above the surface of the bed. A gas flame is initially established in the freeboard above the bed surface. Heat is transferred to the surface layer of particles by the motion of these particles, which come into contact with the gas flame, are heated up, and then return to the body of the bed. Some heat is apparently transferred by back-radiation as well. The bulk of the bed then heats up as energy is propagated back into the bed by the motion of particles, by the conduction of heat through the particles and the gas and by radiation mainly between particles. Whether or not the bed will

heat up sufficiently for the reaction zone to be established within the body of the bed will depend upon the rate of energy transfer through the bed and upon the losses from the bed itself. If, for example, cooling tubes are allowed to extract heat during this critical start-up period, the process may be halted at a low temperature and the reaction will be prevented from establishing itself within the dense phase. If, however, the cooling tubes are prevented from performing their function during the start-up period, there could be some difficulty in keeping the tubes within their metallurgical temperature limits. There are two feasible solutions:

(a) Selective fluidization (Figure 2.13a).

Here the cooling tubes are positioned around the periphery of the combustion bed and only the remaining central portion of the bed is fluidized during the start-up sequence. A defluidized region of low effective thermal conductivity is set up around the tubes. This zone is only activated when the main combustion bed has reached a suitably high temperature and stable, self-sustaining combustion has been established within it. This start-up temperature will be higher than the operating temperature of the bed, and its value will depend upon the thermal capacity of the self-insulating zone. This method assumes that the radial conductivity of the fluidized bed will be sufficiently high to prevent the setting up of any significant temperature gradients within the bed in that part of the bed near the cooling tubes.

(b) Bed expansion (Figure 2.13b).

This system requires that the cooling tubes be positioned above the static height of the combustion bed. The positioning must be such that only when the bed approaches its operating temperature does the dense phase of the bed come into contact with the tubes. However, at the operating temperature the tubes must, for efficient heat transfer, be completely immersed within the bed. There are consequently, some dangers associated with this system. The bed heights are extremely critical, and if the quality of fluidization is not entirely consistent, the tubes run the risk of being over-heated. Additionally, the period during which a gas flame exists above the bed must be kept very short to prevent any possibility of over-heating.

2.2.4.2 Controls

The envisaged control system will be similar to that employed in conventional units, but will have the advantage of being somewhat simplified. Since a 'flame' as such does not exist within the dense phase, flame failure devices may be replaced by simple temperature sensing devices. The existence of a satisfactory level within the bed will be sufficient proof that the reaction is proceeding normally within the dense phase. Spark ignition can be arranged simply above the surface of the bed.

Modulation will be based on the control of the air flow rate, the fuel flow rate being governed by the air flow to provide a fixed mixture strength.

The high thermal capacity of the bed means that response will

be relatively slow, and hence temperature control will be easily exercised. Sudden changes of load will be catered for by utilising the principle of selective fluidization. By using banks of tubes within beds composed of a number of sections, it will be possible to bring sections into or take them out of the heat transfer system, simply by fluidizing or de-fluidizing different regions of the bed. Consequently, rapid changes in output requirements will be met with no danger of combustion being quenched, or of the system being over-heated.

## 2.3 A TYPICAL DESIGN PROCEDURE

### 2.3.1 A Specification

For simplicity, consider the specification for a hot water heater, having a maximum duty of 3 MW, and using propane gas as fuel. The outlet water temperature is to be 200°C and the inlet feed water temperature is assumed to be 20°C. Modulation of 5:1 on the duty is to be provided, and stack corrosion conditions are assumed to restrict the exhaust temperature to 300°C. Water flow is to be fully turbulent (Re > 20 000) and extended surface is to be used wherever possible. It is required that the relevant design parameters for a fluidized unit be calculated.

### 2.3.2 Illustrative Procedure

It is arbitrarily decided that the combustion bed will operate at 900°C. The economiser bed will operate at 300°C to satisfy the stack requirements. The energy liberated in the combustion bed can then be obtained from design curves as illustrated in Figure 2.14.

These curves represent a fuel having a calorific value of 44 500 kJ/kg, and requiring a 20:1 air/fuel ratio for stoichiometric combustion. The curves have been calculated on the basis of complete combustion with the exhaust leaving at 900°C.

The design range of fluidization velocities must now be fixed. It is therefore necessary that the bed material be chosen. The material must be capable of withstanding a temperature of 1 000°C indefinitely, must be as dense as possible to minimise the bed area required, as small as possible (for heat transfer considerations), yet sufficiently large to enable complete combustion to be carried out in as shallow a bed as possible. This leads to the choice of zircon sand (specific gravity = 4.615) as a suitable refractory, high density material. Figure 2.15 shows the variation of minimum fluidization velocity and terminal velocity for different sizes of zircon at 900°C. These curves have been calculated from equations (1.1 - 1.3) and (2.2 - 2.4). It is evident that with particles of about 400 microns in diameter, the required turndown ratio of 5 is well within the capabilities of the velocity design range.

The use of equation (2.12) confirms that at a fluidizing velocity of 1 m/s, and using zircon of 400 microns diameter, complete combustion can be obtained within 30 mm of bed depth. Since it is unlikely that the heat transfer surface can be accommodated completely within 30 mm, it is the depth of bed required to immerse the heat transfer tubes that limits the minimum height of bed that can be used.

It is only necessary now to check that the envisaged design velocity of 1 m/s at 900°C does not fall outside the design range

for the economiser bed operating at the lower temperature of 300°C. The reduction in velocity due to the lower temperature means that smaller or lighter particles can be utilised here. However, for simplicity only one material will be considered. It can easily be verified from equations (1.1) to (1.3) and (2.2) to (2.4) that with 150 micron particles the velocity requirements are all fulfilled. It would, in fact, be theoretically possible to use even smaller particles but it has been observed that with particles of less than 100 microns in size the quality of fluidization is somewhat impaired, probably due to the existence of electrostatic, inter-particle forces.

For design purposes some conservative value of the heat transfer coefficients must be assumed. Extrapolating available data to 900°C suggests that in the combustion bed these may be as high as 0.6 - 0.8 $kW/m^2K$, while in the economiser bed they would be 0.5 - 0.7 $kW/m^2K$. It is therefore initially assumed that a value of 0.5 $kW/m^2K$ can safely be used for both beds. Equation (2.18) or (2.19) can now be used to produce families of curves as in Figure 2.16, which enable specified bed duties to be estimated for different values of the finning ratio, R, and the heat exchanger length, $\ell$. The adiabatic gas temperature at inlet, $T_{g1}$, is of the order of 2 000 K on the basis of which $R_o$ is about 4.5. With the use of the curves in Figure 2.12, the optimal proportions of energy to be extracted from each bed can then be determined.

By using Figure 2.12 in conjunction with Figure 2.16, suitable combinations of the finning ratio and tube length may be specified. Having obtained values for the optimum heat extraction rates from each bed, the area of each bed required can be determined from curves

similar to those in Figure 2.14.

This design procedure is iterative in that the entire procedure must be repeated with the value of bed area just calculated. The heat exchange parameters must all be recalculated to ensure that all the design criteria are satisfied.

Finally, the fan power required to run the unit can be estimated once the bed heights to be used are known; the air pressure drop being equal to the weight of bed to be supported[1,2].

### 2.3.3 The Design Parameters Specified

Having carried out the above procedure, a fluidized bed unit to satisfy the initial specification can be described as follows:

(1) The two-stage unit will consist of a combustion bed, operating at 900°C, and an economiser bed operating at 300°C.

(2) The combustion bed will contain zircon sand sized between 400 and 450 microns, and the economiser bed will consist of the same material, but sized between 150 and 200 microns.

(3) A fluidizing velocity of 1 m/s through the combustion bed will provide the required output of 3 MW.

(4) For optimum heat transfer, 65% of the required output will be obtained from the combustion bed. Hence the water temperature will rise to 95°C in the economiser bed, and then on to 200°C in the combustion bed.

(5) Extended surface tubing of 25 mm bore will be used in both beds (to provide turbulent flow).

(6) With a finning ratio of 5, a tube length of 2.8 m will be required in the combustion bed, and with a finning ratio of

10, a tube length of 1.5 m will suffice in the economiser bed.

(7) Each bed will have an area of 3.8 $m^2$.

(8) Each bed will be 50 mm in height (to ensure that all tubes are immersed).

(9) The distributor in each bed will provide a pressure drop of about 50 mm of water, this being sufficient to ensure uniform fluidization.

## 2.4 THE AREAS FOR INVESTIGATION

Some assumptions of doubtful validity have been required to carry out the design procedure for the simple case outlined above. The following areas of incomplete knowledge have consequently been identified and their investigation is essential to the satisfactory design of a prototype boiler.

(1) In order that the pressure drop across each bed be kept within acceptable limits, it may be necessary to use beds too shallow to immerse conventional finned tubes completely. In these circumstances it will be essential to use fins encompassing more than one tube. A simple technique to evaluate the heat transfer performance of multi-tube configurations is required.

(2) A design correlation for the prediction of heat transfer coefficients, to surfaces immersed within fluidized beds, and valid at combustion temperatures, is urgently needed.

(3) Further information covering the effective thermal conductivity of fluidized beds is required so that the temperature gradients within the bed, set up by the heat extraction process, may be

predicted.

(4) The assumption that the hydrodynamic behaviour of shallow beds is identical to that of relatively deep beds requires investigation.

(5) The mechanism by which liquid fuels will burn within a fluidized bed must be studied so that the feasibility of oil combustion can be predicted.

# CHAPTER 3

# ON THE HEAT TRANSFER PERFORMANCE OF EXTENDED SURFACES

## 3.1 INTRODUCTION

When heat is to be transferred through the walls of a tube, the thermal resistance consists of three components:

(1) the resistance to convective transfer at the inner surface

(2) the resistance to conduction through the tube wall

(3) the resistance to convective transfer at the outer surface.

The largest component resistance limits the overall heat transfer, and the most efficient performance will be obtained when the three component resistances each take up the smallest possible value (i.e. no single component dominates so as to limit the rate of heat transfer).

In general, the conductive resistance is an order of magnitude lower than the convective components. However, there is often a significant imbalance between the two convective components (i.e. there is wide variation in the heat transfer coefficients). The overall rate of heat transfer governed by the lowest heat transfer coefficient can be improved by extending the tube surface area on the side subject to the lowest heat transfer coefficient.

The existence of such extended surface, generally fins, alters the conduction through the tube. The temperature profile through the fin and tube material will be dependent only upon the fin geometry and the thermophysical properties of the fin material.

Fins fall into two categories:

(a) Longitudinal fins, having their axes parallel to the tube axis

(b) Transverse fins, having their axes perpendicular to the tube axis.

When using tubes immersed within a fluidized bed, the heat transfer coefficient on the outside surface will be significantly lower than that on the inside surface. This requires, therefore, that externally finned tube be used. Further, the orientation of the fins must be such as to minimise the resistance to the fluidizing gas flow. This, in turn, requires the use of transverse fins, and only cases of external, transverse fins will be considered further.

## 3.2 HEAT FLOW THROUGH A TRANSVERSE FIN

Consider an elemental area of a fin, surrounding a round tube, as shown in Figure 3.1. The following assumptions are made:

*(1) Heat flow through the fin is steady.*

*(2) The fin material is homogenous and its thermal conductivity, k, is constant.*

*(3) The heat transfer coefficient, h, is constant over the fin surface.*

*(4) The temperature of the surrounding medium is constant at* $T_s$

*(5) The fin thickness, t, is small compared to the other fin dimensions, such that* $\partial T/\partial t = 0$.

*(6) There is no additional resistance introduced by the bond between the fin and the tube.*

*(7) There are no heat sources within the fin.*

Consideration of the continuity of heat flow through the elemental area leads to the equation

$$\frac{\partial^2 T}{\partial x^2} + \frac{\partial^2 T}{\partial y^2} = \frac{2\,h}{k\,t}(T - T_s) \qquad (3.1)$$

Using the transformation $\theta = T - T_s$ and putting $\lambda^2 = 2\ h/k\ t$,

$$\frac{\partial^2\theta}{\partial x^2} + \frac{\partial^2\theta}{\partial y^2} - \lambda^2\theta = 0 \qquad (3.2)$$

which is the Helmholtz equation subject to the boundary conditions,

(1) the temperature at the tube boundary is considered constant, i.e. along the circle $x^2 + y^2 = r_o^2$,

$T - T_s = \theta_o$

(2) there is assumed to be no heat flow through the fin edge, i.e. $\partial\theta/\partial n = 0$ along the perimeter of the fin, where n signifies the direction normal to the edge.

3.2.2 The Effectiveness of Annular Fins

The effectiveness of round fins, of outside radius $r_t$, surrounding a round tube of radius $r_o$, has been treated comprehensively by Gardner[34]. When transformed to polar co-ordinates, 3.2 is a form of the Modified Bessel Equation when considering round fins having certain specific cross-sections. Gardner considers those cases where the fin thickness is a function of the radius and is given by

$$t = t_o\left[\frac{r}{r_o}\right]^{-2n/(1-n)} \qquad (3.3)$$

where $t_o$ is the base thickness of the fin. Thus for $n = 0$, $t = t_o$ = constant; for $n = 1/3$, $r\ t$ = constant (i.e. the cross-sectional area of the fin, normal to the direction of heat flow remains constant); for $n = 1/2$, $r^2 t$ = constant.

Gardner presents solutions in terms of Modified Bessel

Functions for various cases dependant upon n, and on whether n is an integer or a fraction. The temperature excess, $\theta$, along the fin is given by:

For n = 0 or an integer

$$\theta = \theta_o \left[\frac{u}{u_o}\right]^n \quad \frac{I_n(u) + \beta K_n(u)}{I_n(u_o) + \beta K_n(u_o)} \tag{3.4}$$

where

$$\beta = \frac{I_{n-1}(u_t)}{K_{n-1}(u_t)}$$

and $I_n(u)$ = Modified Bessel Function of the first kind, of order n and argument u

$K_n(u)$ = Modified Bessel Function of the second kind, of order n and argument u

For n = a fraction

$$\theta = \theta_o \left[\frac{u}{u_o}\right]^n \quad \frac{I_n(u) + \beta K_n(u)}{I_n(u_o) + \beta K_n(u_o)} \tag{3.5}$$

where

$$\beta = \frac{- I_{n-1}(u_t)}{K_{n-1}(u_t)}$$

For both 3.4 and 3.5

$$u = (1-n)\left[\frac{r}{r_o}\right]^{1/(1-n)} \sqrt{\frac{2\,h\,r_o}{k\,t_o}} \tag{3.6}$$

Once the temperature distribution is known, the effectiveness of the fin, $\Phi$, as defined in Chapter 2, can be calculated from the expression

$$\Phi = \frac{\int \theta \, dA}{\theta_o A_f} \tag{3.7}$$

Some of Gardner's solutions for constant thickness, annular fins are illustrated in Figure 3.2.

It is not always necessary to resort to a solution involving Bessel functions. Constant thickness annular fins can equally well be treated as having an infinite Fourier series solution[33]. However, such a series may not converge very rapidly, and these solutions offer no significant computational advantages over Gardner's solutions.

The disadvantage of these solutions lies in that some of the assumptions are incorrect. Assumption 3 is only justified in situations where mean values of the heat transfer coefficient can be ascertained. The only case of a variable heat transfer coefficient which can be treated analytically is that of the coefficient varying linearly with radius. Here an infinite series solution can readily be obtained but is of questionable utility.

The assumption that there is no bond resistance at the base of the tube will, in all cases of commercially manufactured finned tube, be incorrect. The diversity of bonds that are encountered, however, makes it unlikely that a simple way of dispensing with this assumption can be found.

The boundary conditions used are also open to some question.

It seems reasonable, though, that an average root temperature, based on the inside film coefficient, will provide sufficiently accurate information for the design of heat exchangers. The condition of no heat flux through the fin edge, however, is certainly in error, but the Harper-Brown modification[36] permits this particular condition to be used with little loss of accuracy. By considering the height of the fin to be increased by some length, $\delta_c$, such that the additional fin area accounts for the heat transfer through the fin edge, Harper and Brown showed that the zero flux condition would still exist at the extremity of the corrected fin. They showed that the length correction is given by

$$\delta_c = t_t/2 \qquad (3.8)$$

where $t_t$ is the thickness of the fin at the edge being corrected.

Consequently, whenever the zero flux condition is used in this work, it is implied that the Harper-Brown modification is also being utilised.

### 3.2.3 The Effectiveness of Square and Rectangular Fins of Constant Thickness

Although the two-dimensional Helmholtz equation, (3.2), applies to the case of square or rectangular fins surrounding a round tube, the spatial boundary conditions do not, now, permit analytical solutions. Numerical or approximate methods have to be used.

Relaxation methods[16] are simple to apply, but can be extremely tedious. Except for the most simple cases, the time

required for digital computer solutions can be prohibitive.

Schmidt[37] has considered such fins on the basis of annular fins of equivalent area. He presents correction factors for fin height, the use of which enables the effectiveness to be calculated from solutions of annular fins. These correction factors are of limited accuracy, and can only be used over small ranges of fin height.

Rich[38] assumes the flow of heat to be radial, and by considering square and rectangular fins to be made up of annular segments of varying radii, he has obtained effectiveness values by summing the contributions made by each segment. The effectiveness of each component segment was calculated using Gardner's solutions. Zabronsky[39] has presented values of effectiveness for square fins, calculated numerically.

While such solutions are useful, they cannot be readily extended to consider sheet fins containing more than a single tube, especially when such tubes are running at different temperatures.

## 3.3 A TWO-DIMENSIONAL ANALOG SIMULATING THE HELMHOLTZ EQUATION

### 3.3.1 The Helmholtz Equation

Consider the two-dimensional xOy plane. A Laplacian potential field (e.g. thermal, electrical, hydraulic etc.) in this plane is represented by

$$\nabla^2\theta(x,y) = 0 \tag{3.9}$$

If this field of $\theta(x,y)$ is constrained to permit a flow, $q(x,y)$, normal to the xOy plane, such that it is directly proportional to the local potential

$$q(x,y) \propto \theta(x,y) \tag{3.10}$$

then, by flow continuity, the Laplacian field will be distorted into one represented by the Helmholtz equation.

$$\nabla^2\theta(x,y) - \lambda^2\theta(x,y) = 0 \tag{3.11}$$

where $\lambda$ is a constant.

Equation (3.11) is, in the case of a two-dimensional thermal field, exactly the same as equation (3.2). Assumption 5, $\partial\theta/\partial z = 0$, is implied in (3.11) whereas it is a basic assumption used in deriving (3.2). Electrical conducting paper analogies are widely used[40] in the simulation of Laplacian fields. A technique to distort such a field into a Helmholtzian field has been developed and is described below.

### 3.3.2 Two-Dimensional, Electrical, Conducting Fields

Within any conductor, which is subject to a steady current flow, the electrical potential, V, will be independent of time. For continuity of current flow it can be shown, Appendix B.1, that the potential must satisfy the equation

$$\frac{\partial}{\partial x}\left(\gamma_x \frac{\partial V}{\partial x}\right) + \frac{\partial}{\partial y}\left(\gamma_y \frac{\partial V}{\partial y}\right) + \frac{\partial}{\partial z}\left(\gamma_z \frac{\partial V}{\partial z}\right) = 0 \tag{3.12}$$

If the conductor is an electrically conducting sheet of paper where the plane of the paper is the xOy plane, then the field may essentially be considered a two-dimensional one. Hence

$$\partial V/\partial z = 0 \tag{3.13}$$

and (3.12) becomes

$$\frac{\partial}{\partial x}\left(\gamma_x \frac{\partial V}{\partial x}\right) + \frac{\partial}{\partial y}\left(\gamma_y \frac{\partial V}{\partial y}\right) = 0 \tag{3.14}$$

If the electrical conductivities, $\gamma_x$ and $\gamma_y$ are constant

$$\gamma_x \frac{\partial^2 V}{\partial x^2} + \gamma_y \frac{\partial^2 V}{\partial y^2} = 0 \tag{3.15}$$

In isotropic media, $\gamma_x = \gamma_y$, and hence the field is Laplacian

$$\nabla^2 V = 0 \tag{3.16}$$

[When using conducting papers which are often anisotropic, with $\gamma_x \neq \gamma_y$, the spatial co-ordinates can be transformed so as to keep the field Laplacian[41]. By putting $x = x_1$

$$\left[\frac{\gamma_x}{\gamma_y}\right]^{\frac{1}{2}} y = y_1$$

we get

$$\nabla^2_1 V = 0 \tag{3.17}]$$

If now a local current density, $i_z(x,y)$, which at any point $(x,y)$

is proportional to the local potential V(x,y), is externally induced normal to the xOy plane, the flow continuity equations now give (Appendix B.1)

$$\nabla^2 V - \mu^2 V = 0 \tag{3.18}$$

which is the two-dimensional Helmholtz equation.

### 3.3.3 The Analog

If a lamination is made up from sheets of conducting paper pasted together, and if in addition to potentials applied to boundaries on the top surface, a portion of the bottom surface is held at a potential P, a normal current flow will be induced over this region. The local current density will be given by

$$i_z(x,y) = \frac{\gamma_z(x,y)}{\delta_\ell(x,y)} [V(x,y) - P] \tag{3.19}$$

where $\gamma_z$ is the effective conductivity of the laminate in the z-direction and $\delta_\ell$ is the local laminate thickness. If $\gamma_z$, $\delta_\ell$ and P are all constant, the potential on the top surface of the lamination must satisfy

$$\nabla^2 (V-P) - \frac{\gamma_z}{\gamma_{xy} \delta_\ell^2} (V-P) = 0 \tag{3.20}$$

which is a Helmholtz field of (V-P). Hence equation (3.20) is analogous to equation (3.2) with

$$(V-P) \equiv \theta$$

$$i_z(x,y) \equiv q(x,y)$$

$$\frac{\gamma_z}{\gamma_{xy}\delta\ell^2} = \mu^2 \equiv \lambda^2$$

### 3.3.4 The Modelling Technique

Laminations were constructed by pasting sheets of graphitised (Teledeltos) paper together. Single sheets of paper were found to have a resistance of 1 500 ±3% ohms per square, along both the x and y axes. The single sheets were therefore considered to be isotropic with

$$\gamma_{xy} = \gamma_x = \gamma_y = \text{a constant.}$$

However, the absolute values of $\gamma_{xy}$ and $\gamma_z$ were found to vary from one sample of laminate to another. Qualitatively this variation was found to be consistent with the observed variations in the thicknesses of adhesive layers used. It was found that the laminate thickness was extremely difficult to measure by mechanical means and even simple optical methods were not satisfactory. The value of the parameter, $\mu$, could not therefore be directly measured. It is evident though that if this parameter remains constant over the laminate, the Helmholtz equation will still apply. It was consequently necessary to derive the simulated value of $\lambda^2$ instead.

A number of models representing constant thickness, annular fins, were cut out from a single sample of laminate. Problems of geometrical similarity were eliminated by only using full-scale

models. To facilitate the use of the zero flux boundary condition the Harper-Brown modification was employed. Thus, fin heights being simulated on the model were all extended by a distance equal to half the thickness of the simulated fin. The required conditions were then simulated as follows:

(a) Constant base temperature - by applying a constant potential (assumed 100%) over that area of the top surface of the model representing the tube area.

(b) Constant surroundings temperature - by applying a constant potential, P, over the fin area projected onto the bottom surface of the model.

(c) Zero heat flux along the perimeter - by the absence of any applied potentials and the existence of an air gap along the simulated boundary.

Potentials were applied to the laminate via a silver paint which ensured that the applied potential remained constant (within 0.5%) over any specified region.

Using a standard field plotter (ALPHA-PR), the circuit for which is illustrated in Figure 3.3, iso-potentials were mapped out over the model surface. Models for fins of varying geometries were all cut from the same sample of laminate. The effectiveness of the simulated fins were then calculated from a numerical form of equation (3.7) so that

$$\Phi = \sum_{o}^{A_f} \theta_m A_m / \theta_o A_f \qquad (3.21)$$

where $A_m$ = area of model surface between iso-potentials

$\theta_m$ = mean potential applicable to $A_m$.

All areas were measured using a planimeter.

These values of effectiveness were then fitted to curves representing Gardner's solutions (Figure 3.2). A least squares fit was used and hence the mean value of $\lambda^2$ being simulated by that particular sample of laminate was derived. For any given sample the simulated value of $\lambda^2$ varied by no more than ±5%, confirming that the parameter, $\mu$, could effectively be considered a constant.

Having, in effect, calibrated each laminate sample, models of fins of other geometries could then be investigated. Values of $\lambda^2$ derived for various samples of laminate are tabulated in Appendix B.2.

### 3.3.5 Verification of the Technique

The above technique was verified by the simulation of square and rectangular fins having known approximate or numerical solutions. Various samples of laminate were constructed and from each sample three models of constant thickness annular fins were used to calibrate for $\lambda^2$. These values were then used in the simulation of square and rectangular fins. A comparison of these results with the solutions of [37, 38, 39] is shown in Figures 3.4 and 3.5.

That the technique is accurate is illustrated in Figure 3.6 where it is evident that all the analog data falls within ±7% of known solutions.

## 3.4 ANALOG APPLICATIONS

### 3.4.1 Sheet Fin Performance

When using sheet fins, the effectiveness will depend upon the geometry of the fin and upon the temperature levels within the various tubes. The use of the above technique enables complex configurations to be readily evaluated.

The particular case of a rectangular sheet fin containing two tubes at differing temperatures has been investigated. The analog results are presented in Figure 3.7 where they are compared with numerical solutions obtained using relaxation methods. Here the effectiveness is calculated as before, but $\theta_o$ is now considered to be the maximum root temperature existing within the fin.

### 3.4.2 Other Applications

The analog is capable of use in any situation where the Helmholtz equation arises. The major limitations are those set by the values of $\lambda^2$ which can be simulated. With care errors in the derived values of $\lambda$ can be kept within ±10%. The electrical conductivity of the laminate is very sensitive to changes in atmospheric humidity and temperature. This can, however, be minimised by subjecting the laminate to an initial drying period, during which steady state conditions are attained.

# CHAPTER 4

# HEAT TRANSFER TO SURFACES IMMERSED IN FLUIDIZED BEDS

## 4.1 INTRODUCTION

The agitation of solid particles brought about by bubble motion is responsible for the high, effective, thermal conductivities of fluidized beds, and consequently for their remarkable temperature uniformity. To maintain a bed at a particular temperature, heat may have to be extracted from the bed. This is most conveniently achieved by immersing a heat exchanger within the bed itself. It is, therefore, necessary that some means of predicting the rate of heat transfer to immersed surfaces be available.

The qualitative behaviour of the heat transfer process has now been well established. The heat transfer coefficient to immersed surfaces increases with increasing fluidizing velocity, as the solids circulation is enhanced. A maximum is reached when the increasing bed voidage just offsets the effects of increased particle mobility. A gradual reduction of the heat transfer coefficient is then observed until the fluidizing velocity approaches the terminal velocity of the particles, whereupon it decreases sharply (Figure 4.1).

Quantitatively, however, there is wide discrepancy in the experimental data available, and all the proposed correlations are only applicable within narrow limits

## 4.2 A REVIEW OF THE AVAILABLE EXPERIMENTAL DATA

### 4.2.1 Introduction

The most comprehensive review of previous experimental work

is to be found in Zabrodsky[4]. More recent data has been included in the texts by Kunii and Levenspiel[2] and by Davidson and Harrison[1]. The experimental data can broadly be classified into three categories.

(a) Heat transfer to the walls of the containing vessel

(b) Heat transfer to tubes immersed within the bed

(c) Heat transfer to calorimeters immersed within the bed.

The parameters generally used in describing the heat transfer processes are:

| | | |
|---|---|---|
| Nusselt number | Nu | $= h D_p/k_f$ |
| Archimedes number | Ar | $= g D_p^3 \rho_f (\rho_s - \rho_f)/\mu_f^2$ |
| Reynolds number | Re | $= \rho_f D_p U/\mu_f$ |
| Fluidization index | N | $= Re_f/Re_{mf}$ |

Gelperin and Einstein (in 1) have shown that the maximum heat transfer coefficient occurs at a flow given by

$$Re_{opt} = C\ Ar^{0.5} \qquad (4.1)$$

where $0.08 < C < 0.25$.

The 'optimum' Reynolds number, $Re_{opt}$, corresponds to the point of maximum heat transfer coefficient, implied in $Nu_{max}$. It is the prediction of $Nu_{max}$ that is required for design purposes. Since it has been specified in Chapter 2 that the envisaged boiler will operate within a velocity regime in excess of $Re_{opt}$, the various correlations available for the prediction of the heat transfer coefficient within the rising zone are not reported here.

4.2.2 Previous Experimental Findings

Though the various correlations available for the prediction of $Nu_{max}$ do not display very good agreement, they generally express a functional relationship of the form

$$Nu_{max} = f\{(Ar)^n\} \qquad (4.2)$$

where $0.17 < n < 0.25$.

Some of the more comprehensive correlations are now considered below.

Baerg et al[43] investigated heat transfer between fluidized beds and a heated vertical wall. Over a wide range of experimental conditions they obtained the empirical relationship

$$Nu_{max} = 239.5 \frac{D_p}{k_f} \log \frac{0.00705\ \rho_s (1 - \varepsilon_{mf})}{D_p} \qquad (4.3)$$

This equation is dimensional and all properties are in S.I. units.

Vreedenberg[26,27,28] studied heat transfer from heated beds to water cooled tubes. Though his investigations were conducted mainly within the rising zone of the h-U curve, he did notice that the tube position appeared to have no significant effect on the heat transfer.

van Heerden et al[25,44] used various gases in their investigations of heat transfer from heated beds to cooled walls. They too only considered the rising portion of the h-U curve. They did, however, confirm the conclusions of other workers concerning the effect of the gas conductivity on the heat transfer coefficient.

Kharchenko and Makhorin[45] used a large spherical, calorimeter to investigate heat transfer in beds at temperatures up to 1 050°C. They proposed an expression for $Nu_{max}$ which fits their data with an accuracy of ±12%

$$Nu_{max} = 0.138\left[\frac{c_{ps}\,\rho_s}{c_{pf}\,\rho_f}\right]^{0.25}(1-\varepsilon_{mf})^{0.33}\,Ar^{0.17} \qquad (4.4)$$

Baskakov and Maskaev[46] used large particles in their investigations and they presented a correlation

$$Nu_{max} = 0.21\,Ar^{0.32} \qquad (4.5)$$

in the range $10^5 < Ar < 10^8$.

Varygin and Martyushin (in 4), used a spherical silver calorimeter and obtained

$$Nu_{max} = 0.86\;Ar^{0.2}\,(k_f/k_{air})^{0.6} \qquad (4.6)$$

within the range $30 < Ar < 1.4 \times 10^6$.

Gelperin et al[47] show that for heat transfer to immersed tubes

$$Nu_{max} = 0.7\,Ar^{0.22} \qquad (4.7)$$

over roughly the same range as for equation (4.6) and with an experimental accuracy of ±10%.

Zabrodsky[4] in non-radiative beds has obtained the empirical

dimensional expression

$$Nu_{max} = 0.431 \left[\frac{\mu_f^2}{g\rho_f k_f^2}\right]^{0.2} Ar^{0.2} \qquad (4.8)$$

where all the parameters are in S.I. units.

Kim et al[48] investigated much the same range and they present a correlation

$$Nu_{max} = 1.034\ Pr_f^{0.33}\ Ar^{0.2} \qquad (4.9)$$

These correlations are illustrated in Figure 4.2 and although there is some considerable variation, it is evident that the functional relationship of the form $Nu_{max} = aAr^n$ is substantially true. Zabrodsky[4] and Gelperin and Einstein (in 1) suggest that the variations can mainly be attributed to the variations in system geometry and that the underlying mechanisms of heat transfer must be the same for all systems. Thus, in any design process, these mechanisms must be considered.

Relatively little information is available on high temperature systems where radiation may be expected to contribute significantly to heat transfer and it is unlikely that the correlations reported above can be extended into such regions. Jolley[49] in 1949 estimated that in a bed at 1 000°C, radiation contributed some 50% of the total flux. However, Kharchenko and Makhorin in 1964 concluded that at 1 000°C, radiative transfer was insignificant. This conclusion, although accepted at the time, must now be in some doubt. Kharchenko and Makhorin used the transient heating of

a copper sphere in their determination of heat transfer coefficients. Their spheres, however, were about 60 mm in diameter, giving Biot numbers (Bi = hR/k) in the range 0.4 - 4.0. With such large Biot numbers the precise value of the surface temperature of the sphere is in some doubt, with consequent errors in their values of heat transfer coefficients. Moreover, their assumption that the radiative heat transfer is merely additive and takes place parallel to all other mechanisms is questionable.

This argument is reinforced by the subsequent findings of Ilchenko and Mahkorin[51] who reported that when using spherical calorimeters of relatively large Biot numbers, the apparent heat transfer coefficient increased with decreasing sphere diameter. Botterill and Sealey[52] summarise even more recent Russian work by Ilchenko et al[53] where a quartz tube was used to separate the radiant flux from the total flux and the results indicated that the radiative contribution rose from about 10% of the total at 500°C to about 60% at 1 400°C. Here they concluded that the radiative and convective components are not independent of each other.

Baskakov and Goldobin[54] showed that the radiative contribution increased with increasing particle size and gas velocity. Baskakov[55] has further shown that the heat transfer coefficient apparently increases linearly with the square root of the gas conductivity, but it is unlikely that this holds good within the radiative region.

Yoshida et al[56] presented experimental evidence to support their model of radiative heat transfer, and conclude that at temperatures up to 1 000°C radiation is insignificant. In contrast,

Zabrodsky (in 4) has argued that radiation must be important at temperatures above 900°C.

It is clear, therefore, that there is, as yet, little agreement on the quantitative contribution of the radiative mechanism. Even the qualitative behaviour of this contribution is in some doubt.

## 4.3 MODELS FOR HEAT TRANSFER IN FLUIDIZED BEDS

### 4.3.1 Introduction

Numerous mathematical models[57-68] have now been postulated for the prediction of heat transfer rates to surfaces immersed in fluidized beds. None of these is definitive, yet the most successful of these are those which consider the periodic, unsteady state heat transfer between the bed and the surface. In general, these consider transient conduction alone and consequently only apply to non-radiative situations.

All the proposed models consider the fluidized bed as a two-phase system and can broadly be divided into those which consider a continuous gas phase with a discrete solid phase made up of single particles, and those which consider a continuous emulsion phase containing a discrete gas phase. The emulsion phase is taken to be the solid particles together with the attendant gas flow required for minimum fluidization, while the discrete gas phase is made up of gas bubbles. The models are all 'surface renewal models' in that they consider transient conduction between the surface and either single particles or the emulsion phase to take place only during the period when a particle or an emulsion

packet is resident at the surface. The renewal mechanism itself, is usually attributed to the bubble motion.

### 4.3.2 Single Particle Models

Botterill and Williams[57] considered single spherical particles coming into contact with the immersed surface; transient conduction then taking place through the gas film at the point of contact until the particle was replaced by another.

Using relaxation techniques, the transient heat conduction equations were solved numerically. The model solutions were found to overpredict when tested against experimental data gathered under controlled residence time conditions. However, good correspondence was subsequently obtained when a further assumption, that a gas film having a thickness equal to 10% of the particle diameter surrounds the particle, was made. The major drawback of this model lies in that the assumed gas film thickness is purely arbitrary, and is not based on direct experimental evidence. Additionally, this model cannot be expected to be accurate in situations where the temperature penetration depth may exceed the diameter of a single particle. From Carslaw and Jaeger[50], the thermal penetration depth in one-dimensional conduction is

$$x/D_p \propto Fo^{0.5} \tag{4.10}$$

where $x$ = temperature penetration depth at some residence time, $t_r$

$Fo$ = Fourier Number = $\alpha_e t_r / D_p^2$

and $\alpha_e$ = effective thermal diffusivity of particle/gas film system.

Thus, the single particle model is limited to use in situations where the residence time is low enough for $x/D_p << 1$, a condition not generally achieved in conventional fluidized beds.

Gabor[58] used the Botterill model, and attempted to take the surrounding particles into consideration. He proposed an 'alternate slab model' in which the bed was assumed to consist of alternating layers of gas and solid. The problem is again one of one-dimensional conduction, and though Gabor's solutions show good agreement with experimental data, they are critically dependant upon the width of the gas slab used in the solution. This width is a variable and the particular values used by Gabor have little physical significance. Gabor did demonstrate, however, that his solutions were not critically dependant upon the nature of particle packing assumed.

Botterill and Butt[59] extended the single particle model to consider a double layer of particles. The added complexity of the solution now ensured that for low values of residence time they were more accurate than the single particle model, but the assumption for gas film thickness was still required. The model was still unsatisfactory for long residence times[60,61].

Ziegler et al[62] used a similar approach, where they considered transient conduction between a gas film and the solid particles. The gas film was assumed to be at the surface temperature, and the particles never actually came into contact with the surface. They assumed that the particle residence time distribution

was a gamma function, and that the particles were packed in a rectangular array. Their solution gives

$$Nu = 7.2 \Big/ \left[ 1 + \frac{6\, k_f\, t_m}{\rho_s\, c_{ps}\, D_p^2} \right]^2 \qquad (4.11)$$

where $t_m$ is some mean residence time defined by the assumed gamma function. Equation (4.11) thus predicts a maximum instantaneous Nusselt number of 7.2, and this is in reasonable agreement with the data of Botterill and Williams[57]. However, this model, too, is inaccurate at long residence times.

### 4.3.3 Emulsion Packet Models

All emulsion phase models are based on the Mickley and Fairbanks model[64], as originally proposed in Fairbank's thesis[63]. Here, transient conduction is considered to take place between the surface and a 'packet' of the emulsion phase, which comes into contact with the surface for a short period and then returns to the body of the bed. The packet is defined as a semi-permanent grouping of particles having uniform and constant thermo-physical properties which are equal to those of the incipiently fluidized bed. The packet is assumed to be rigid, with no relative motion between the particles making up the packet. The packet is further assumed to be stationary during its residence time at the surface. Using a constant wall temperature boundary condition, they arrive at an instantaneous Nusselt number given by

$$Nu_i = 1 \,/\, (\pi\, F_O)^{0.5} \qquad (4.12)$$

where $Nu_i = h D_p / k_f$

$F_o = \alpha_e t / D_p^2$

The suffix e signifies emulsion properties. The time-mean Nusselt number at any time will depend upon the form of residence time distribution assumed.

The major drawback of this model is the assumption that the thermo-physical properties of the packet are constant. The effect of any voidage variations in the vicinity of the surface are not considered. Thus, the model effectively assumes that the temperature penetration depth into the packet is much larger than the depth of any variations at the packet/wall interface. Consequently, the model may be expected to be accurate for long residence times (large $F_o$), but will fail for low values of $F_o$.

Baskakov[65] utilised the Mickley-Fairbanks model and attempted to extend it to low Fourier numbers. He introduced a gas film between the packet and the surface such that the added resistance of the film accounted for any property variations within the packet at the packet/wall interface. He obtained experimental data which agreed with his model extremely well. However, the existence of the gas film is not based on physical evidence, and its introduction must be considered an expedient to enable the Mickley-Fairbanks model to be fitted to low Fourier number data. Here Baskakov has used the frequency of bubble passage at a given point to obtain mean values of residence time.

### 4.3.4 Residence Time Distribution

The 'uniform surface renewal' form of residence time

distribution is the one most widely used in the literature. Here if $t_r$ is the time taken for the replacement of a packet at the surface

$$Nu_m = \frac{1}{t_r} \int_0^{t_r} Nu_i \, dt \qquad (4.13)$$

When (4.13) is applied to the Mickley-Fairbanks solution, equation (4.12)

$$Nu_m = 2 / (\pi F_o)^{0.5} \qquad (4.14)$$

More complex forms of time distribution can be used, but it has been shown by many workers that the precise form used is not critical to such transient solutions[1,2].

### 4.3.5 The Kubie-Broughton Model

This is a variation of the Mickley-Fairbanks solution, where now the variable packet properties at the wall/packet interface are taken into account. Kubie[67] has approximated the voidage variation at a surface by a simple geometrical function. He assumes that the voidage within the packet is a function only of x, the normal distance from the constraining surface. Thus he gives

$$\varepsilon(z) = 1 - 3(1 - \varepsilon_b)(z - 2z^2/3) \qquad \text{for } z < 1 \qquad (4.15)$$

and

$$\varepsilon(z) = \varepsilon_b \qquad \text{for } z > 1 \qquad (4.16)$$

where

$z = x / D_p$

$\varepsilon_b$ = voidage in the bulk of the bed.

Kubie and Broughton[68] then assume that all the packet thermo-physical properties can be represented as simple functions of the voidage. The one-dimensional transient conduction equations were solved numerically using a constant flux boundary condition, and the results have shown very good agreement with existing data. This model assumes that the surface effect penetrates only up to one particle diameter. Apart from the assumption of the expression for voidage variation, no physically unjustified concepts are used, and within the conductive regime, is the most successful model proposed so far.

## 4.4 EXPERIMENTAL WORK

### 4.4.1 The Experimental Equipment

The experimental layout was as illustrated in Figure 4.3. The object was to measure heat transfer coefficients from heated beds to a calorimetric probe by monitoring the transient temperature response of the probe when it was immersed within the bed.

The apparatus was arranged so that a mixture of propane and air could be burnt within the bed. Two containing vessels of similar dimensions and identical design were used. A mild steel container, 100 mm in diameter, was used at temperatures up to 700°C, and a stainless steel container, 140 mm in diameter, permitted temperatures of over 1 000°C to be attained. The combustor design is illustrated in Figure 4.4. All the beds utilised porous ceramic distributors, 25 mm thick. The outside walls of the

container were insulated by means of an asbestos jacket, 20 mm thick.

The heat transfer probes consisted of small metal spheres, having a thermocouple positioned at their centres. Four probes were manufactured; one of brass, one of mild steel, and two of copper. Dimensional details are given in Figure 4.5. The thermocouples were protected by a sheath of stainless steel, having an outside diameter of 1 mm. A hole, of diameter 0.95 mm, was accurately drilled, radially, half-way through each sphere. An interference fit was consequently obtained, when the thermocouples were inserted into the spheres. The spheres were heated up to 500°C for ease of insertion. The entrances to the holes were crimped after insertion to complete a sound mechanical joint.

An 8 mm diameter, sheathed, thermocouple was used to measure the bed temperature. All the thermocouples used were of the chromel alumel type and temperatures were recorded on a multi-channel pen recorder of certified accuracy ±1% f.s.d.

Gas and air flow measurements were made by means of banks of rotameters as shown in Figure 4.3.

### 4.4.2 The Experimental Procedure

Gas combustion was initiated by ignition above the bed surface, and after an initial heating up period during which the reaction was established within the bed, the air/fuel ratio was adjusted to give the required temperature (700° - 1 050°C). The air/fuel ratio was always kept well above stoichiometric.

The uniformity of the bed temperature was checked by moving

the bed thermocouple to all parts of the bed. Temperature variations of the order of 100°C were found to exist in the 5 mm of bed immediately above the distributor. The temperature in the remainder of the bed, however, was found to vary by no more than 10°C, and a mean value of the temperature in the bulk of the bed was recorded.

With the mean bed temperature constant, the probe was plunged into the bed along the bed axis until submerged to a pre-selected depth. The temperature of the probe was recorded continuously. All thermocouple junctions were located at a common terminal box at ambient temperature. The ambient temperature was recorded separately by a mercury in glass thermometer.

By means of an analytical procedure described later, the temperature history of the probe was used to calculate heat transfer coefficients within the bed.

At each value of mean bed temperature the above procedure was repeated at different air flow rates, temperature control being exercised solely by varying the fuel flow rate. The range of air flow investigated was such as to give superficial fluidizing velocities from just below $U_{mf}$ to about 10 $U_{mf}$ (approximately 1.5 m/s).

Tests were carried out both in the presence of combustion and in its absence. However, these were only possible at temperatures above 700°C. Below this value, since combustion could not then be maintained, tests were only performed with the gas supply shut off, while the bed itself was cooling down.

Three different bed materials were used; silica sand, zircon

sand, and silicon carbide. Various sizes of these materials were used, and their thermo-physical properties are detailed in Appendix C.1. The methods used in their determination are also included.

### 4.4.3 The Experimental Programme

#### 4.4.3.1 Tests on probes

The different probes were first investigated to determine the effects of probe material and size on the measured values of heat transfer coefficient. No significant variation could be observed. Results obtained with a particular probe were found to be reproducible to within ±7% when using any of the other probes, and within this range of variation no trends could be observed. This was taken to be confirmation of the argument that the validity of the previous work carried out using spheres was in question only due to the large values of the Biot numbers of those spheres. All the probes used here had Biot numbers below 0.05, and the consistency of data obtained using them was therefore to be expected. To minimise errors, all subsequent tests were conducted using the smallest copper sphere (No.4).

#### 4.4.3.2 The influence of combustion on heat transfer

The next series of tests were performed at temperatures above 700°C, to investigate the influence of the combustion process itself on heat transfer. There appeared to be no difference in the heat transfer coefficients obtained when combustion was taking place in the bed, and those obtained when the combustion was temporarily stopped. However, it was observed in a transparent bed

that whenever combustion was taking place, it always appeared to be established within a very narrow zone, 10 - 20 mm above the distributor. Consequently, no firm conclusions can be drawn about the effect the combustion process may have on the heat transfer. For consistency, all further tests were performed with the combustion process stopped for the duration of the probe response.

4.4.3.3 The influence of probe position

The influence of the probe position within the bed was then studied. Measured heat transfer coefficients were found to be smaller in the regions within 10 mm of either the container walls or the distributor plate. Elsewhere in the bed, heat transfer coefficients were independant of position. The regions of reduced coefficients largely correspond to the regions of lower temperatures, but no attempt to quantify these effects were made.

All subsequent trials were carried out with the probe positioned along the bed axis at a distance of half the static bed height above the distributor plate.

The effects of varying the static bed height were then investigated. Tests were conducted with different depths of bed ranging from 20 mm to 80 mm in the unfluidized state. Within this range the heat transfer coefficient appeared to reduce slightly with increasing bed depth. However, the variation was always within 10%, and all the data fell within the bounds of reproducibility. It was assumed therefore that within this range the bed depth was not a very significant parameter and would not be investigated any further. In all further experiments, the bed depth was kept constant at 50 mm, and the probe centre was positioned

25 mm above the distributor plate.

Subsequently each size of each test material was subjected to a range of constant temperature tests; each temperature test covering a range of fluidization velocities.

### 4.4.4 Processing of raw experimental data

A typical experimental trace is illustrated in Figure 4.6. Since no combustion was taking place, the bed temperature was always reducing during the period of a test. However, the probe response period never exceeded one minute, and it was found that the temperature-time relationship for the bed was very nearly linear during this short period.

In all cases the measured centre temperature was assumed to be the surface temperature of the sphere. The justification for this assumption lies in that the Biot numbers of the spheres were always low enough for them to be considered isothermal (Appendix C.2). The quantities measured directly from the trace were:-

(a) the mean bed temperature level during the test period

(b) the coefficient of linear decrease of the bed temperature with time, $\lambda$

(c) the temperature excess at the start of the test, $\theta_o$

(d) the temperature excess, $\theta$, at some time, t

(e) the value of the time, t.

From these data, a value of heat transfer coefficient was obtained by an iterative method which is detailed in Appendix C.3. Each value of heat transfer coefficient was thus a time mean value, averaged over the elapsed time, t. Three values of heat transfer

coefficient were calculated from each response curve, and the arithmetic mean of these was taken to be a representative value. The maximum deviation in values of the coefficient derived from a single trace was ±3%.

The values of heat transfer coefficient obtained were plotted against a non-dimensional air velocity, $(U_f - U_{mf})/U_{mf}$. Some typical results are illustrated in Figures 4.7, 4.8 and 4.9. A least squares straight line, weighted to pass through the origin was then fitted to all data points in the region $U_f < 2\ U_{mf}$. A second straight line, also obtained from a least squares regression, was then fitted to all points in the region $U_f > 3\ U_{mf}$. The point of intersection of the two lines was taken to be the 'optimum point' for heat transfer. The value of heat transfer coefficient here was taken to be $h_{max}$, and the corresponding value of $U_f/U_{mf}$ was assumed to give $N_{opt}$. All these derived data are presented in Tables 4.1 to 4.20. Each tabulation corresponds to a particular size of a specific material. Values of the particle Archimedes number and the maximum Nusselt number, calculated on the basis of the gas conductivity, are also included.

### 4.4.5 The Experimental Results and their Analysis

The heat transfer coefficients, tabulated in 4.1 to 4.20, exhibit a strong temperature dependence which is illustrated by means of some typical results in Figures 4.10, 4.11 and 4.12.

As a comparison with previous published correlations, the data has been plotted in the form $Nu_{max}$-Ar as shown in Figures 4.13, 4.14 and 4.15. Here, surprisingly, the expected relationship

$Nu_{max} = f(Ar^{0.2})$ was not immediately apparent. The data is presented as a family of curves, each curve corresponding to a particular material size and apparently exhibiting a relationship of the form

$$Nu_{max} = f(Ar^{-n}) \tag{4.17}$$

where $0.1 < n < 0.2$.

However, when, after interpolation, constant temperature straight lines are superimposed on to these plots, the expected relationship does materialise. Thus, with temperature constant

$$Nu_{max} = k\, Ar^{n} \tag{4.18}$$

where k and n are temperature dependent.

To elicit this temperature dependence, the transforms of the above plots have been created and these are shown in Figures 4.16, 4.17 and 4.18. Here $Nu_{max}$ has been plotted against a non-dimensional temperature, arbitrarily defined as $\theta = T_b/273$, where $T_b$ is the absolute bed temperature. Again, a family of curves is generated. Data points having the same Archimedes number lie on straight lines.

A relationship of the form

$$Nu_{max} = C\, \theta^{p} \tag{4.19}$$

is apparent where C is a function of Archimedes number.

For clarity not all the data points are shown on the plots.

Putting equations (4.18) and (4.19) together suggests that a correlation of the form

$$Nu_{max} = C_1 \, Ar^n \, \theta^p \qquad (4.20)$$

should satisfactorily fit all the data.

It is clear that while k in (4.18) is a strong function of temperature, n is not. Equally, p is only a weak function of Archimedes number. Values of n and p from Figures 4.13 - 4.18 have been found to lie in the ranges

$$0.17 < n < 0.27$$

$$0.73 < p < 0.87$$

A least squares regression for $Nu_{max}$ on $Ar^n \, \theta^p$ has been carried out by varying p and n in turn within the limits set out above. The best fit has been obtained with p = 0.82 and n = 0.22. The lines of best fit obtained for each material are shown in Figures 4.19, 4.20 and 4.21. The best correlation obtained for all the data points is

$$Nu_{max} = 0.365 \; \theta^{0.82} \; Ar^{0.22} \qquad (4.21)$$

Equation (4.21) fits some 300 data points with a maximum deviation of ±4%. However, all these data points have been obtained using the smallest probe. After including some 100 data points obtained

using the other probes the maximum deviation of the correlation is increased to ±10%.

## 4.5 A MODEL FOR RADIATIVE TRANSFER TO IMMERSED SURFACES

### 4.5.1 The Proposed Model

This model is based on the Mickley-Fairbanks conception of transient heat transfer to packets of particles which periodically come into contact with the immersed surface. Here, too, the packet is defined as a semi-permanent grouping of particles which during its contact time with the surface is rigid and stationary (Figure 4.22). The approach so far is similar to that used by Vedamurthy and Sastri[72]. However, based on the Kubie-Broughton concept of variable packet properties at the constraining surface[68], the interior of the packet is considered to be a simple gas/solid system. The area voidage, $\varepsilon$, within the packet is considered to be constant along any plane parallel to the surface and hence is a function only of the normal distance, x, from the surface. Thus, the proportion of solid area at any point is given by

$$\gamma(x) = 1 - \varepsilon(x) \tag{4.22}$$

and the packet interior takes up the form illustrated in Figure 4.22. The cross-sectional area of the solid phase along a plane parallel to the constraining surface is consequently given by

$$A(x) = A_p \gamma(x) \tag{4.23}$$

where $A_p$ = cross-sectional area of the packet.

It is further assumed that the temperature within the packet varies only with time and the distance, x. Along any vertical plane, therefore, the temperature within the solid phase is assumed equal to that in the gas phase. Thus, only one-dimensional, unsteady state heat transfer need be considered.

Whether radiative transfer will take place from the packet to the surface, or from the bulk of the bed to the packet, or across the voids within the solid phase of the packet itself, will depend upon the form the voidage function takes and consequently, upon the position within the packet. With the gas phase assumed to be completely transparent to radiation, the packet can be divided into regions corresponding to the different directions of nett radiative transfer.

| Region | Nett Radiation from | to |
|---|---|---|
| from x = 0 to dA/dx = 0 (max) | packet | immersed surface |
| at dA/dx = 0 | 0 | 0 |
| from dA/dx = 0(max) to dA/dx = 0 (min) | packet or bulk of the bed | packet |
| for A = constant | 0 | 0 |

The model thus assumes that:

(a) for conductive transfer the packet can be treated as a porous slab, and

(b) for radiative transfer the packet can be treated as a solid

having a shape defined by the voidage function.

Assuming further that the heat capacity of the gas phase is negligible in comparison with that of the solid phase of the packet, an energy balance on an elemental slab of thickness $\delta x$ gives

$$\frac{\partial^2 T}{\partial x^2}\left[A(x) + \frac{k_f}{k_s}(1 - A(x))\right] + \left[1 - \frac{k_f}{k_s}\right]\frac{dA(x)}{dx}\frac{\partial T}{\partial x} + \frac{Qr}{k_s \delta x} - \frac{A(x)}{\alpha_s}\frac{\partial T}{\partial t} = 0 \qquad (4.24)$$

where $k_f$ = gas conductivity

$k_s$ = solids conductivity

Qr = nett radiative flux leaving the element

$= \sigma\, e\, F \frac{d}{dx} A(x).\delta x(T^4 - T_X^4)$

$\sigma$ = Stefan-Boltzmann constant

e = emissivity

F = shape factor

$\alpha_s$ = thermal diffusivity of solids

Tx = temperature of radiating surface

Replacing A(x) by $A_p\gamma(x)$, and using the following transformations:

$$\theta = T/T_b; \quad z = x/D_p; \quad \tau = \alpha_s t/D_p^2; \quad \beta(z) = \gamma(x); \quad k_r = k_f/k_s;$$

$$s = \sigma\, e\, F\, D_p\, T_b^3/k_s; \quad X = T_x/T_b$$

the general equation (4.24) can now be non-dimensionalised to

$$\frac{\partial\theta}{\partial\tau} = 1 + K_r \frac{(1-\beta(z))}{\beta(z)} \frac{\partial^2\theta}{\partial z^2} + \frac{1-k_r}{\beta(z)} \frac{d\beta(z)}{dz} \frac{\partial\theta}{\partial z}$$

$$+ \frac{s}{\beta(z)} \frac{d\beta(z)}{dz} (\theta^4 - \chi^4) \qquad (4.25)$$

Equation (4.25) is subject to the initial condition

$$\text{at } \tau = 0, \quad \theta = 1 \quad \text{for all } z \qquad (4.26)$$

and to the boundary conditions

(a) at some specified value of z, $\theta = 1$ for all $\tau$ (4.27)

(b) an energy balance at the surface of the packet.

An experimental investigation of the voidage variation adjacent to surfaces immersed in packed beds indicates that Kubie's geometrically derived expression[67] should be sufficiently accurate for use with most heat transfer models. The details of this investigation are given in Appendix C.4. Thus, using Kubie's expression

$$\beta(z) = 3(1-\varepsilon_b)(z - 2z^2/3) \quad \text{for } z \leq 1 \qquad (4.28)$$

for $z > 1$

$$\beta(z) = 1 - \varepsilon_b \qquad (4.29)$$

where $\epsilon_b$ is the voidage in the bulk of the bed. Hence

$$\frac{d\beta(z)}{dz} = 3(1 - \varepsilon_b)(1 - 4z/3) \quad \text{for } z \leq 1 \tag{4.30}$$

$$= 0 \qquad \text{for } z > 1 \tag{4.31}$$

The variation of $\beta(z)$ with z and the consequent directions of nett radiative transfer are shown in Figure 4.23. The general equation (4.25) now takes up different forms in each of the different regions of radiative transfer within the packet. For $0 < z < 0.75$

$$\text{equation (4.25) holds with } X = \mu = T_{wall}/T_b \tag{4.32}$$

for $0.75 \leq z \leq 1$,

$$\text{equation (4.25) holds with } X = 1 \text{ and } S = -S \tag{4.33}$$

and for $z > 1$

$$\frac{\partial\theta}{\partial\tau} = \left[1 + \frac{k_r(1 - \beta_b)}{\beta_b}\right] \frac{\partial^2\theta}{\partial z^2} \tag{4.34}$$

The system of equations (4.32) to (4.34) is subject to

$$\text{(a) } \theta = 1 \text{ for all } z \text{ at } \tau = 0 \text{ (initial condition)} \tag{4.35}$$

$$\text{(b) } \theta = 1 \text{ for all } \tau \text{ at } z = 10 \text{ (assumes that the thermal penetration depth is always less than } 10D_p) \tag{4.36}$$

(c) at $z = 0$

$$\frac{\partial\theta}{\partial\tau} = \left[\frac{1}{\delta z\beta(\delta z/2)}\beta(\delta z) + k_r(1 - \beta(\delta z))\right]\frac{\partial\theta}{\partial z}$$

$$- \frac{2}{\delta z^2}(\theta - \mu)\left[1 + k_r\left[\frac{1}{\beta(\delta z/2)} - 1\right]\right]$$

$$- S\,\beta(\delta z/2)(\theta^4 - \mu^4) \qquad (4.37)$$

Equation (4.37) is obtained from considering the energy balance on a surface element of the packet of thickness $\delta z$. The first term gives the heat conduction into the surface element from the rest of the packet, the second term gives the heat conducted from the element to the wall and the last term gives the radiation from the element to the wall. Here again, the specific heat of the gas in the packet is assumed negligible.

The above system of equations has been solved for $\theta$ numerically, using finite difference techniques. The method of solution is outlined in Appendix C.5.

Once the instantaneous temperature profiles within the packet are known, the conductive and radiative fluxes from the packet to the wall can be calculated. If the mean temperature of the surface slab is $\theta_s$,

$$Nu_{ic} = \frac{(1 - f_o)2}{\delta z}\left[\frac{\beta(\delta z/2)}{k_r} + (1 - \beta(\delta z/2))\right]\frac{(\theta_s - \mu)}{(1 - \mu)} \qquad (4.38)$$

$$Nu_{ir} = \frac{f_o S(1 - \mu^4)}{k_r(1 - \mu)} + \sum_{z=0}^{z=0.75}\frac{(1 - f_o)S}{(1 - \mu)k_r}(\theta_s^4 - \mu^4)\frac{d\beta(z)}{dz}\delta z \qquad (4.39)$$

where $Nu_{ic}$ = instantaneous, conductive Nusselt number

= $h_c D_p/k_f$

$Nu_{ir}$ = instantaneous, radiative Nusselt number, including radiative transfer through the transparent bubble phase.

= $h_r D_p/k_f$

$f_o$ = fraction of bed occupied by bubbles from equation (1.7).

The time mean values can then be obtained from a numerical integration of

$$Nu_m = \frac{1}{\tau} \int_0^{\tau} Nu_i \, d\tau \qquad (4.40)$$

The conductive or convective transfer from the bubble phase is thus neglected. Radiative transfer is assumed to be between black bodies, and the shape factor, F, is taken to be unity.

## 4.5.2 Predictions of the Model

The solutions for the system of equations (4.32) to (4.34) have separated the conductive and radiative components of the total flux to the wall. These solutions are presented in the form of Nu-Fo plots, where the non-dimensional variables are:

$N_u$ = Nusselt Number = $h D_p/k_f$

$F_o$ = Fourier Number = $\alpha_s t/D_p^2$

$S$ = Radiation parameter = $\sigma \varepsilon F D_p T_B^3/k_s$

$k_r$ = conductivity ratio = $k_f/k_s$

$\mu$ = wall temperature = $T_w/T_b$

Typical solutions are illustrated in Figure 4.24. The effect of wall temperature on the radiative flux and that of the conductivity ratio on the conductive component is shown in Figures 4.25 and 4.26.

Since these solutions are merely 'marching' solutions, comparison with experimental data requires the choice of some particular value of residence time. Additionally the experimental data in this work has not been obtained at constant wall temperatures. By interpolating between numerical solutions obtained at different values of wall temperature, a comparison has been attempted. This has required that assumptions be made for values of the residence times. These have been obtained by using the expressions given by Gelperin and Einstein [in 1].

$$t_r = \left[\frac{H_{mf}'}{0.711\ H_f}\right]\left[\frac{U_f - U_{mf}}{1.5g}\right]\left[\frac{H_{mf}}{H_f - H_{mf}}\right]^2 \qquad (4.41)$$

where

$$H_f = H_{mf}\,\frac{(1 - \varepsilon_{mf})}{(1 - \varepsilon_f)} \qquad (4.42)$$

and

$$\frac{1 - \varepsilon_f}{\varepsilon_f{}^3} = \frac{U_{mf}}{U_f}\left[\frac{1 - \varepsilon_f}{\varepsilon_{mf}{}^3}\right] \qquad (4.43)$$

Although there is considerable doubt as to the accuracy of these expressions[1,2,67,72] they only provide a means of illustrating the predictions of the model.

By using values of residence time calculated for specific experimental conditions, a theoretical value for $Nu_m$ can be obtained

from the $N_u$-$F_o$ plots. This was done with solutions obtained at various wall temperatures corresponding to the range of variation of the probe temperature, and thus a mean theoretical value of $Nu_m$ was obtained for each value of residence time considered. This could then be compared with the experimental value of $Nu_m$ obtained under the same conditions as those used for the residence time calculation.

This comparison was carried out for the experimental conditions pertaining to two different sizes of zircon sand, and these are illustrated in Figures 4.27 and 4.28. (The properties of zircon are tabulated in Appendix C.1).

## 4.6 DISCUSSION

The heat transfer model described above is an extension of the Kubie-Broughton model[67], in that radiation is now included. The method of solution is similar to that of Vedamurthy and Sastri[72] but voidage variation within the packet is now taken into account. The concept of treating the packet as a simple gas-solid system for conduction derives from the methods often used to treat porous materials[80,83]. In addition, the definition of the area voidage within the packet is effectively assumed to be the shape function controlling the nett radiation emanating from within the packet. The model thus consideres a variable voidage packet, the conduction within which can be separated into a solid and a gaseous component and from which radiation takes place only through the gaseous area.

The comparison of the model solutions with experimental data is not satisfactory in that the values of $Nu_m$ predicted are

considerably lower than those measured experimentally. The comparison process itself is unsatisfactory since the values of residence time, calculated using equation (4.41), are questionable. Furthermore, the process of interpolation between solutions for different wall temperatures is necessarily approximate. The model can only be satisfactorily tested when experimental data at high bed temperatures, obtained under controlled residence time conditions, is available.

In spite of these reservations, however, some tentative conclusions can be drawn:

(a) The packet residence time does not appear to be significant to the Nusselt number describing radiative transfer ($h_r D_p/k_f$) (Figure 4.24)

(b) The importance of this radiative Nusselt number increases with increasing packet residence time (or Fourier number) as the conductive component decreases (Figure 4.24)

(c) Increasing the wall temperature brings about a large increase in the radiative component (Figure 4.25)

(d) The radiative Nusselt number increases with increasing particle size and is largely unaffected by variations in the conductivity ratio ($k_f/k_s$) (Figure 4.26)

(e) The conductive component is not very sensitive to the radiation parameter, S, and hence to the bed temperature (Figure 4.24)

(f) The conductive Nusselt number decreases sharply with increasing residence time (Figures 4.24 and 4.26)

(g) The conductive component is sensitive to the conductivity

ratio ($k_f/k_s$) (Figure 4.26).

These conclusions are in general qualitative agreement with the experimental data. Quantitatively, however, the method of comparison is unsatisfactory. The uncertainty about the residence times used (at least ±50%) suggests that this is the major source of the disagreement between the predicted and the measured values of Nusselt number.

The qualitative agreement does indicate, however, that the concept of treating the packet interior as a simple gas-solid system is justified. The assumption that the fluidized bed behaves as a black body is now open to some question since recent evidence[73] suggests that the packet emissivity may be as low as 0.8. The model could thus be overestimating the radiative contribution, but since this contribution is only significant at long residence times, the error may not be large.

Further evidence that the packet may be treated as a simple gas solid system for conduction is presented in Figure 4.29. Here the model solution for the instantaneous conductive Nusselt number is compared with the solutions presented by Mickley-Fairbanks and Kubie-Broughton. Both these models have used an emulsion conductivity in their solutions but, except for very small Fourier numbers, the disagreement is not large. This suggests that the added complications of calculating emulsion properties may not be necessary.

The model solutions (Figure 4.24) also show that the radiative and conductive components of heat transfer can be considered independant of each other.

# CHAPTER 5

# THE EFFECTIVE THERMAL CONDUCTIVITY OF FLUIDIZED BEDS

## 5.1 INTRODUCTION

By analogy with the thermal characteristics of solids, and specifically with those of porous solids, a fluidized bed has an 'effective' thermal conductivity, the quantitative value of which will specify temperature gradients within the bed.

Relatively little information on the conductivity of fluidized beds is available in the literature. However, it has long been noticed that when temperature gradients arise within fluidized beds, they are significantly steeper in the radial rather than in the axial direction. All the available data[2,4] suggest that the thermal conductivity of fluidized beds is not isotropic and that the axial conductivities are extremely high, making temperature gradients difficult to measure with any accuracy. However, Lewis et al[79] and Shrikhande[78] have obtained axial temperature distributions using very long cylindrical beds. They investigated various gas/solid systems and concluded that the fluidization velocity was the parameter of major significance. Their results indicate that the axial conductivity, $k_a$, is linearly dependant upon the fluidization velocity, and they estimate values in the range 100-2 500 W/mK compared with 387 W/mK for copper. Axial temperature gradients may therefore be neglected in the shallow fluidized beds being considered here. Consequently, only the 'effective' radial conductivity, $k_r$, will be considered further.

## 5.2 THE 'EFFECTIVE' RADIAL CONDUCTIVITY OF FLUIDIZED BEDS

### 5.2.1 Introduction

The transport of thermal energy within a fluidized system can only be brought about by the following mechanisms:

(a) Conduction between particles in contact

(b) The motion of particles

(c) Convection within the gas phase

(d) Radiation between particles.

It has been shown by many workers that the convection term is small and may generally be neglected[2,4,67,79,80]. The radiation term will only become significant at temperatures above 600°C, and even at 1 000°C will be no larger than the conductive term[4]. The axial conductivity data[2,4,78,79], indicates that only the motion of particles is significant. However, the motion of solids is less pronounced in the radial direction, making it difficult to assess the relative importance of the conductive contribution. By considering the fluidized bed to consist of a porous emulsion phase which is in constant motion, the 'effective' radial conductivity will consist of the stationary emulsion phase conductivity and a mass transfer term. Simple measurements of the radial temperature gradients can provide an estimate of the heat flows and hence of the total 'effective' conductivity. The conductivity of the constant voidage emulsion phase can be estimated from one of the many expressions available for the prediction of the thermal conductivity of porous systems[80-83]. Consequently, the term due to particle motion can be estimated by subtraction and the relative importance of particle motion and particle conduction can then be assessed.

### 5.2.2 The Thermal Conductivity of Porous Systems

Porous systems (e.g. porous solids, fibrous materials, fixed particulate beds, etc) have now been intensively studied. A large number of correlations are now available for the prediction of the thermal conductivity of such systems. Generally, expressions for the conductivity, $k_e$, are presented as functions of $k_s$, $k_f$ and $\varepsilon$, where

$k_s$ = solids conductivity

$k_f$ = void conductivity

$\varepsilon$ = area voidage or porosity.

These correlations, however, are usually only valid over small ranges of voidage, and even within the same range display considerable variations. Many theoretical studies[80-84] postulating the governing mechanisms of heat transfer have also been made, but the diversity of systems involved has precluded any definitive treatment. The range of the available correlations is illustrated in Figures 5.1 and 5.2.

While it is clear that accurate predictions are not possible, the order of magnitude to be expected can be confidently estimated.

### 5.2.3 The Experimental Method

The experimental method consisted of measuring the horizontal temperature profiles in a shallow, two-dimensional fluidized bed within which a heater was immersed. A schematic layout is shown in Figure 5.3. A perspex bed, 0.5 m long and 20 mm wide, having a porous plastic ("Porvair") distributor plate was used. The heater consisted of a simple resistance coil, and the supply voltage was

continuously variable from 0 to 250 V. Voltage and current values were continuously monitored, and the heater output could be varied from 0 to 750 W. A static bed height of 50 mm was always employed. The test length, situated between planes (1) and (2) was 160 mm. So as to discount any entrance region effects, the first 10 mm of bed depth was excluded from the test section. Fixed Chrome/Alumel thermocouples, positioned at the centre of the test height, were used to measure the temperature along the reference planes. A movable thermocouple was used to measure intermediate temperatures. The ambient temperature, $T_o$, was also recorded.

### 5.2.4 Data Analysis

Within the test section only steady-state one-dimensional conduction is considered. The temperature at any point, T, is thus a function only of the distance, x, and must satisfy

$$\frac{d^2T}{dx^2} - \frac{\rho_f c_{pf} U_f}{H k_r} (T - T_o) = 0 \qquad (5.1)$$

where the second term is due to the heat carried away by the fluidizing air. Using the transformations

$$\theta = (T - T_o)/(T_1 - T_o); \qquad z = x/L$$

equation (5.1) takes the non-dimensional form

$$\frac{d^2\theta}{dz^2} - \lambda^2\theta = 0 \qquad (5.2)$$

where $\rho_f$ = air density

$c_{pf}$ = specific heat of air

$U_f$ = fluidizing velocity

H = height of test section

L = length of test section

$k_r$ = effective radial conductivity

$T_o$ = air temperature at entry to bed

and

$$\lambda^2 = \frac{\rho_f c_{pf} U_f L^2}{H k_r} \tag{5.3}$$

Suffixes 1 and 2 refer to planes 1 and 2 respectively. Equation (5.2) is subject to the boundary conditions

$$\text{at } z = 0, \quad \theta = 1 \tag{5.4}$$

$$\text{at } z = 1, \quad \theta = \theta_2 \tag{5.5}$$

The solution of (5.2) is, therefore,

$$\theta = \frac{e^{\lambda z}(e^{-\lambda} - \theta_2) + e^{-\lambda z}(\theta_2 - e^{\lambda})}{e^{-\lambda} - e^{\lambda}} \tag{5.6}$$

By converting all the experimental data to the non-dimensional form, $\theta$-z, and by comparison with the solutions of equation (5.6), values for the 'effective' radial conductivity, $k_r$, can be estimated. The method of conversion is described below.

### 5.2.5 The Experimental Data

Two sizes of silicon carbide and three of silica sand were investigated. The fluidizing velocity was varied in each case through the range $U_{mf}$ - 6 $U_{mf}$. The raw data was put into the form of a non-dimensional θ-z plot, onto which were superimposed the analytical solutions given by equation 5.6. These solutions were for values of $\lambda^2$, such that all the experimental points were enclosed within them. Thus, the range of $\lambda^2$, and hence of applicable conductivity, could be derived. The results from one such test are illustrated in Figure 5.4. Here the solutions for various $\lambda^2$ have also been included. It is apparent that the experimental points from this test are all encompassed by the solutions corresponding to $\lambda^2 = 2$ and $\lambda^2 = 4$. Since for this case $U_f = 0.3$ m/s, $k_r$ can be estimated from equation (5.3) to have a value within the range 52 W/mK (for $\lambda^2 = 4$) to 105 W/mK (for $\lambda^2 = 2$).

The above procedure has been carried out for all tests and the values obtained for the 'effective' radial conductivity are shown in Figures 5.5 and 5.6.

## 5.3 DISCUSSION

The thermal conductivity of a porous air/solid system can never exceed the solids conductivity. Since the conductivity of refractory materials is very low, the high values obtained for $k_r$ makes it clear that, for the systems considered, conduction between particles in contact contributes little to the 'effective' radial conductivity. The only significant mechanism of thermal transport is, therefore, the motion of the solids themselves. This conclusion

cannot, however, be extrapolated to include systems where the conductivity of the solids is high. For fluidized systems of pure metal powders, for example, conduction through the emulsion phase may be as significant as the solids motion.

The data obtained does suggest that particle size is not a significant parameter, and neither is particle density. The fluidization index is clearly the predominant factor and some form of linear relationship is apparent. The values derived for $k_r$ lie in the range 30 - 300 W/mK, and thus, the radial conductivity appears to be an order of magnitude lower than the values for axial conductivity quoted in the literature[78,79]. However, if the motion of particles is the only significant parameter governing the 'effective' conductivity of fluidized beds, this is only to be expected.

Peters et al[88] calculated a theoretical radial conductivity and for air/sand systems give values for $k_r$ in the range 1 000 - 2 500 W/mK. It is clear that their values are much too high, confirmation being provided by Zabrodsky[4] who also has obtained experimental data generally giving values of the order of 100 W/mK.

It is evident that the usual assumption of temperature uniformity within a fluidized bed may be subject to serious error in the *radial* direction. In situations where localised cooling is taking place within a fluidized bed, it is necessary therefore to take account of the temperature gradients that will be established.

# CHAPTER 6

# PRESSURE DROP PHENOMENA IN SHALLOW FLUIDIZED BEDS

## 6.1 INTRODUCTION

It has generally been accepted[1-4] that in a well fluidized particles' bed the air-side pressure drop is equal to the weight of the bed per unit area. This assumes that the only hydro-dynamic consideration is that imposed by the frictional drag between the particles and the fluid. This relationship is generally expressed in the form

$$\frac{\Delta p}{H} = \rho_s(1 - \varepsilon_{mf}) \qquad (6.1)$$

In the course of experimentation, however, it was observed that the pressure drop across a shallow bed was never quite sufficient to balance the entire bed weight. Consequently, pressure drop measurements have been made with various shallow fluidized beds, and these are reported in this chapter.

## 6.2 EXPERIMENTAL DATA

### 6.2.1 Pressure Measurement

The pressure, at any point within the bed, was measured by means of a tube of diameter 0.75 mm. This probe could be positioned at any point within the bed and the probe opening was always kept perpendicular to the direction of air flow. All pressures were measured at an inclined manometer, having an accuracy of 0.1 mm of water. Pressure readings were checked by means of a differential probe which measured pressure differences across a fixed vertical

height of 10 mm. The probe was manufactured from 0.75 mm diameter steel tubes and was connected to a water displacement manometer which was accurate to better than ±0.005 mm of water.

A pressure tapping, within the plenum chamber, immediately below the distributor plate provided upstream pressure values.

### 6.2.2 The Experimental Programme

Pressure measurements were obtained for a wide variety of particles and particle sizes using a 140 mm diameter bed having a porous ceramic distributor plate. The pressures were measured for each particular material size and for each particular bed height at velocities ranging from 0 to 5 $U_{mf}$. This process was repeated with each particular material size for bed heights ranging from 10 mm to 170 mm. A typical set of experimental data is illustrated in Figure 6.1. Values for the maximum pressure drop attained in any given bed were thus obtained, and these are shown in Figure 6.2.

To elicit any distributor effects, the above procedure was repeated using the following distributor plates, all within the same bed:

(a) a porous plastic distributor ('Porvair')

(b) a sintered bronze plate

(c) a stainless steel pierced plate ('Conidur').

To obtain the effects of varying bed diameter, measurements were also carried out in a 100 mm diameter and a 170 mm diameter bed. Both beds were fitted with porous ceramic distributors.

### 6.2.3 The Experimental Data

The data obtained is shown in Figures 6.3, 6.4 and 6.5. In all cases the bed height has been measured directly and has been verified by measuring the bed weights used. The pressure drop and the bed height are presented in non-dimensional form:

$P = \Delta p_m A_b / w$, and

$\zeta = H/D_b$ = non-dimensional height

where

$\Delta p_m$ = maximum pressure drop

$A_b$ = bed area

$w$ = bed weight

$H$ = bed height

$D_b$ = bed diameter.

## 6.3 DISCUSSION

It is evident from Figures 6.2 - 6.5 that at no time is the manometric pressure loss equal to the total bed weight, and that this effect is exhibited with all the distributor plates.

It is also clear that this effect is more pronounced with the spherical metal particles than with angular refractory materials. However, the effect is apparently dissipated within a height equal to the bed diameter, though the small range of bed diameters used does not allow any firm conclusions to be drawn. The bed diameter, however, is used as a convenient means of obtaining a non-dimensional bed height. The non-dimensional pressure drop always reached an asymptotic value which lay within -5% of the total bed weight.

In order to test the possible existence of a recovery of the

pressure loss through the distributor plate, the pressure drop across the distributor was measured at various air flow rates, both with and without a bed above it. It became clear that some pressure recovery was taking place since the pressure drop across the distributor decreased when a bed was present. However, this recovery was never found to exceed 5% of the bed pressure drop, and hence does not provide a complete explanation.

The fact that the type of distributor used makes little difference suggests that the observations cannot be entirely due to particles resting upon the distributor itself. The plates used had open areas as follows:-

| | |
|---|---|
| sintered bronze | 8 - 12% |
| pierced plate | 10 - 15% |
| plastic sheet | 10 - 15% |
| ceramic tile | 15 - 23%. |

Consequently, if the observed effects were due only to the existence of de-fluidized regions being supported on the surface of the distributor, the ceramic plate could be expected to support less of the bed weight than any of the other distributors. That this is not so shows that the support directly provided by the distributor may be a contributory factor, but cannot be the sole cause of the low pressure drops measured.

The possibility that friction between moving particles and the container walls is also a contributory factor can largely be discounted. Any frictional support should be directly proportional to the "wetted area" and hence to the bed height, and the evidence does not support such an explanation.

It is also possible that the particles themselves act as a repository of potential and kinetic energy. This would require that upon fluidization, there would be a pressure-loss surge, this additional energy then being stored within the particles. While pressure fluctuations have often been noticed, no surge, large enought to account for the data has been observed. There is some evidence[17,18] that the first few diameters of a fluidized bed vibrate at frequencies much lower than those attributable to bubble passage or collapse. This may be due to the lower region of the bed acting as a combined mass, and thus having some natural frequency of vibration. The fact that the observed effect reduces with increasing bed height could thus be attributed to the existence of a vibrating, energy storage region, independant of bed depth.

The effect of material shape and size is not clear, but it is significant that the metallic particles used all had sphericities considerably higher than the refractory particles.

It is also possible that a shallow fluid bed is merely a transition region between two extremes - a "jetting" region containing particles in transport on the one hand, and a fully fluidized region on the other. Thus, within the jetting region momentum transfer would be taking place from the fluid to the particles being transported, thus reducing the measured static pressure. Such a mechanism could explain the observed effect of particle sphericity. An increase in sphericity would reduce the drag forces acting on the particle, thus enhancing the momentum transfer process. The presence of such a jetting region would

consequently explain the low pressure drops observed - but whether this can be a complete explanation still remains to be proved.

As yet there appears, therefore, to be no single mechanism which can satisfactorily explain the observed data. It is possible that one or more of the mechanisms suggested operate in concert. The final explanation must lie in a study of the hydrodynamic instabilities of shallow fluidized beds.

# CHAPTER 7

# THE FEASIBILITY OF OIL COMBUSTION IN SHALLOW FLUIDIZED BEDS

## 7.1 INTRODUCTION

A series of ad hoc experiments, designed to establish the most promising means of combusting heavy fuel oils in shallow air-fluidized beds, has been performed. With little information available as to the mechanisms by which liquids evaporate within fluidized beds, these experiments have, necessarily, been qualitative. No precise, quantitative measurements have been made, and only subjective conclusions are drawn.

The major problem envisaged in combusting non-vaporisable oils, lay in ensuring that sufficient air/fuel contacting could take place within a shallow fluidized bed. Essentially, therefore, the problem was considered to be one of finding a satisfactory method of fuel injection.

Various methods of oil injection have been tested experimentally and their relative merits are discussed.

## 7.2 EXPERIMENTAL APPARATUS

A stainless steel bed, designed as a gas combustor, was used to carry out the oil injection trials. The experimental layout was as for gas combustion (Chapter 4). Silica sand, of 455 micron mean particle size, was used as the bed material. Two oils were used in all tests:

(a) Diesel oil of viscosity 45 seconds Redwood, at 20°C

(b) A heavy fuel oil of viscosity 950 seconds Redwood at 20°C

Fuel flow rates were achieved by means of a peristaltic pump.

The pump was initially calibrated with the two oils for flow at different temperatures.

All bed temperatures were monitored by means of Chromel/Alumel thermocouples connected to a digital voltmeter. Reference junctions were all at a common terminal, the temperature of which was measured by a thermometer.

## 7.3 THE EXPERIMENTAL PROGRAMME

### 7.3.1 General Method

The insulated, fluidized combustor being used was first calibrated for heat loss rates. The bed was heated up to 900°C by means of gas combustion and the cooling rate of the bed was then recorded with the fuel flow shut off. The gradient of the cooling curve provided an estimate of the heat loss from the bed. Gradients were calculated over 50°C intervals, and thus heat loss rates at different bed temperatures (400°C - 900°C), and different air flow rates were obtained.

When testing oil combustion, the gas flow was always stopped at a bed temperature of 900°C and oil injection was always commenced when the bed had cooled to 850°C. A comparison of the subsequent temperature history of the bed with the calibrated cooling rates permitted an estimate of the combustion efficiency to be made.

The oil flow rates were always adjusted to give lean mixtures, with excess air varying within the range 20% to 150%.

### 7.3.2 Direct Injection Trials

#### 7.3.2.1 Injection onto the bed surface

The fuel oil was allowed to drip from a height of 0.25 m onto the bed surface. This method proved abortive for both oils. Combustion, which was luminous and sooty, took place only in the freeboard well above the bed surface. Some cracking was evident when using the heavy oil; agglomoration of the bed was observed and, subsequently, a mass of residual carbon was recovered from the bed. Variations of the air flow rate, the bed height, the bed temperature at ignition, and the mixture strength provided no improvement.

By means of an air cooled, stainless steel injection tube positioned immediately above the bubbling bed surface, the oils were then injected directly onto the bed surface. The light oil vaporised immediately on injection and burnt at the mouth of the injection tube and within the freeboard. No evidence of combustion within the bed could be later discerned. The heavy oil cracked at the injection point, blocking the tube within a few minutes. Again, varying the fluidization and the injection conditions provided no improvement.

#### 7.3.2.2 Injection within the bed

The oils were then injected through the side of the container at the container wall, immediately below the bed surface. Once again the light oil burnt in the freeboard and no evidence of any combustion within the bed could be detected.

However, some initial success was achieved when using the heavy oil. For eight minutes after injection, the bed cooling

rate indicated that some 10% of the fuel input was releasing its energy within the bed. However, agglomeration set in after this time and fluidization ceased. Cracking was clearly taking place, and a mass of residual carbon, some 30 mm in diameter, was later recovered from the bottom of the bed. By increasing the excess air from 20% to 150%, the operating time was increased to about fifteen minutes, but no improvement of the combustion efficiency could be observed. In all cases, a luminous flame was present within the freeboard. Though the fluidization parameters were all varied and the bed height was increased to a maximum of 150 mm, no more than 10% of the fuel input burnt within the bed. When supporting gas combustion was utilised, the operating time could be extended to about 20 minutes but no improvement in the efficiency of oil combustion could ever be observed.

Various other injection points were used but the best results were obtained by the above method where injection was at the wall immediately below the bed surface. Air cooled injection tubes, however, proved satisfactory in preventing cracking at the mouth of the tube and the tube blockage was eliminated. The successful injector design is illustrated in Figure 7.1.

### 7.3.3 Indirect Injection

In an effort to ensure that the fuel remained within the bed for sufficient time for combustion to be established, a porous, particulate material was impermeated with the heavy fuel oil and then introduced into the heated silica sand bed. The particles were a refractory material ('MOP', manufactured by Caltex Ltd) of

density 2 950 kg/m$^3$ and having a mean size of 770 microns. Weighing provided an estimate of the average amount of oil absorbed by the particles. The soaked material was poured onto the bed surface through a 20 mm diameter tube.

The temperature history of the bed indicated that between 5% and 15% of the oil input was burning within the bed. Visually it was apparent that the dense coated particles were initially sinking to the bottom of the bed as required. Subsequent examination of the particles showed that cracking of the oil was still taking place and that residual carbon deposits were still being formed. These deposits were, now, all less than 5 mm in diameter indicating that they were forming on the surface of the charged particles and that their coalescence was relatively slow. The use of supporting gas combustion delayed the onset of agglomeration for up to one hour. Again, luminous combustion could always be observed in the freeboard and variations of bed height or mixture strength produced no significant changes.

It was also observed that the apparent combustion efficiency increased from 5-15% at a bed temperature of 650°C, to 8-20% at 850°C. At bed temperatures below 650°C no combustion was evident and thick vapour clouds could be observed above the bed surface. At temperatures below 325°C even these vapour clouds were absent. These observations were taken as an indication that gasification of the fuel oil was somehow improved at bed temperatures between 325°C and 650°C.

When using the light oil with this same method, up to 40% of the input burnt within the bed with 100% excess air. Auto-thermal

operation could never be achieved, but the use of support gas combustion enabled the combustor to be run continuously for six hours. Luminous combustion above the bed surface was always evident.

## 7.4 TWO-STAGE COMBUSTION

### 7.4.1 The Concept

The trials described above suggested that attempts to burn heavy fuel oil directly within a shallow fluidized bed promised little hope of early success. The results, however, indicated that gasification of a heavy oil might well be feasible within a shallow fluidized bed. If the gasification process were such that the coalescence of the residual carbon was prevented, a two-stage process could be envisaged where gasification was followed by the fluidized combustion of both the solid residuals and the inflammable vapour.

The problem is thus transformed from one attempting to achieve good fuel/air contacting, to one of trying to create two separate regions within a single fluidized bed; one conducive to gasification and one to the combustion of both the gas and the solid residue.

### 7.4.2 The Creation of Temperature Gradients Within a Fluidized Bed

The major attribute of fluidized beds is generally considered to be their temperature uniformity. However, the gasification and combustion of a fuel oil can be considered to be two temperature dependant processes, each requiring a closely controlled operating

range. Furthermore, while gasification requires temperatures well below 650°C, combustion considerations require bed temperatures of at least 750°C. Some method had, therefore, to be devised such that different regions of a single fluidized system would run at different temperatures. The use of binary beds was therefore considered.

Rowe and co-workers[89-93] have studied the behaviour of fluidized beds containing binary mixtures of particles. They have found that segregation of the component particles is very pronounced when the mass of one component particle is greater than about three times the mass of the other component particle. The segregation reduces as the fluidizing velocity increases and the particle mixing is improved. Broughton[94] in a study of incipient fluidization conditions has observed that segregation is somewhat enhanced at high temperatures. It is patent that in such systems, each component will be subject to a different fluidization index ($U_f/U_{mf}$) and hence to a different degree of mixing. These differences will be most marked in strongly segregating systems and will, in consequence, bring about regions of different effective thermal conductivity. It can, therefore, be expected that when combustion is carried out within the lean phase of a strongly segregating system, the dense phase, closest to the distributor plate, will run at a temperature considerably lower than the combustion temperature. The prediction of the temperature profiles within such systems is dependant upon a knowledge of the effective thermal conductivities applicable within the two regions.

Axial temperature gradients have been measured for some binary

mixtures with gas combustion present within the bed. These profiles are illustrated in Figures 7.2, 7.3 and 7.4. It is evident that by a judicious choice of mixtures, the lower portion of the bed can be constrained to run at temperatures significantly lower than the combustion temperature. Thus, depending upon its vapourisation characteristics, the fuel oil could be injected into the region best suited to gasification. If a very low temperature region (<200°C) were required, a packed bed could be used in place of the lower region. The required temperatures could easily be achieved by varying the depth of the packed bed.

### 7.4.3 The Two-Stage Combustion of a Heavy Oil

A binary mixture of 50% silica sand (425 microns) and 50% silicon carbide (710 microns) was introduced into a quartz gas combustor of 100 mm diameter. A static bed height of 100 mm was used. With a fluidization velocity of 50 cm/s, gas combustion was initiated within the bed. The gas flow was stopped when the bed temperature at the surface had reached 900°C. At this stage segregation was clearly visible. The surface of the ceramic distributor was at a temperature of about 180°C and the first 25 mm of bed depth was running at below 350°C. No gradients were discernible within the top 50 mm of bed depth.

The heavy oil was injected by means of the air-cooled injector onto the distributor surface at the centre of the bed. A comparison of the temperature history of the bed with previously calibrated cooling rates indicated that with 100% excess air, 30-40% of the oil was releasing its energy within the system. With

the excess air reduced to 50%, less than 20% of the fuel input burnt within the bed. The process was never self-sustaining, a combustion efficiency of 55% being the required level for auto-thermal operation. Luminous combustion was always present above the bed surface. Subsequent examination of the bed material showed little evidence of cracking. Roasting of the bed material later showed that about 3-5% by weight of the fuel input was present as carbon residue. The process could, however, be carried on indefinitely with the use of supporting gas combustion.

## 7.5 CONCLUSIONS

The simple experiments reported here suggest the following:

(a) The direct injection of heavy fuel oils into a single component fluidized bed is not promising as a means of combustion.

(b) Gasification of the fuel oil prior to fluidized combustion is essential.

(c) The use of binary beds shows promise as a means of carrying out gasification and combustion within the same bed.

It is clear that oil combustion will require beds somewhat deeper than those for gas combustion, but the extra fan power necessitated may not be prohibitive. It is evident that a considerable amount of further work is required. It is imperative that the mechanisms by which liquids evaporate within packed or fluidized beds be studied. It is further required that the thermophysical properties of binary and multi-component fluidized mixtures be characterised, so that such systems may be tailored to

provide the conditions necessary for two-stage oil combustion.

# CHAPTER 8

# CONCLUSIONS

The objectives specified in Chapter 1 have largely been fulfilled. A preliminary design for a gas-fired, shallow, fluidized bed hot water heater has been produced. The difficulties arising in the design study have served to identify those areas of the knowledge which have required further investigation.

An analog technique, designed to permit the analysis of sheet fins has been devised. The analog which simulates the two-dimensional Helmholtz equation has been generalised so that it may be applied to other situations where the Helmholtz equation arises. The technique has been successfully utilised in the evaluation of rectangular fins carrying two tubes running at different temperatures.

To facilitate the design procedure, heat transfer to surfaces immersed within high temperature beds has been investigated. Data has been obtained from the transient response of a calorimetric probe, plunged into heated fluidized beds. The reproducibility of the data is good, and all the data has been correlated to within ±10% by the expression:

$$Nu_{max} = 0.365 \quad \theta^{0.82} \quad Ar^{0.22}$$

The data indicates that the probe position, discounting any wall effects, is not significant to heat transfer and neither is the bed height within the range investigated. The heat transfer coefficient always reached its maximum value at fluidizing velocities between $U_{mf}$ and $2\ U_{mf}$, but no trends could be observed in this region.

A model accounting for the radiative transfer in high temperature beds has been proposed. The model, based on the packet model, considers one-dimensional, unsteady state, conduction and radiation. A function for the voidage variation within the packet at a constraining surface has been used to define the shape of the packet interior. The defined shape has been used to specify the directions of nett radiative transfer. The model is in qualitative agreement with the experimental data, but the quantitative agreement is unsatisfactory. However, the comparison process in itself is not accurate and only controlled residence time data will provide a sufficient test of the model's validity.

Thus, though the mechanisms of radiative transfer have yet to be satisfactorily explained, the proposed correlation should provide preliminary design values for the heat transfer coefficients to be expected.

Previous work predicting the efficiency of pre-mixed gas combustion in shallow fluidized beds has been experimentally verified. It has been demonstrated that Broughton's correlation[5] can safely be used as a design equation to predict the depth of bed required for complete combustion. The fact that excess air is not generally required for efficient combustion has also been demonstrated.

An experimental study has suggested that the effective radial conductivity of fluidized beds is an order of magnitude lower than the effective axial conductivity. The radial conductivity has been found to be largely dependant upon the fluidizing velocity and the experimental values were found to range from 30 to 350 W/mK. It appears that solids motion is the only significant mechanism of

energy transport, both in the radial and in the axial directions.

It is clear, therefore, that the assumption that a bed is isothermal can be subject to significant errors, especially when localised cooling is taking place. Thus, when considering heat transfer to cooling tubes immersed within a fluidized bed, the effective radial conductivity must be taken into account. By using values within the range given above, it is apparent that the lengths of cooling tubes required, as calculated in Chapter 2, must be increased by some 5-15%.

A qualitative investigation has indicated that the use of binary beds may well be a means of both gasifying and combusting heavy fuel oils within shallow fluidized beds. Direct injection of the fuel oil into a fluidized bed appears to be impracticable. The concept of combined gasification and combustion though has yet to be proved in that self-sustaining combustion has yet to be achieved.

The design procedure can, thus, be carried out more accurately. It can also be easily extended to consider steam raising units, having three or even more stages. However, the final arbiter must be the manufacturing and operating costs applicable to such a unit.

## SUGGESTIONS FOR FURTHER WORK

The major investigative effort now needed must consider the mechanisms of liquid fuel evaporation within a fluidized bed. Part of this effort may involve the further characterization of the properties of binary beds.

Additional work is also required to establish the mechanisms

controlling radiative transfer within fluidized beds. Controlled residence time data is essential if transient heat transfer models are to be considered.

The collection of additional data is necessary before design correlations, predicting the effective conductivities of fluidized beds, can be derived.

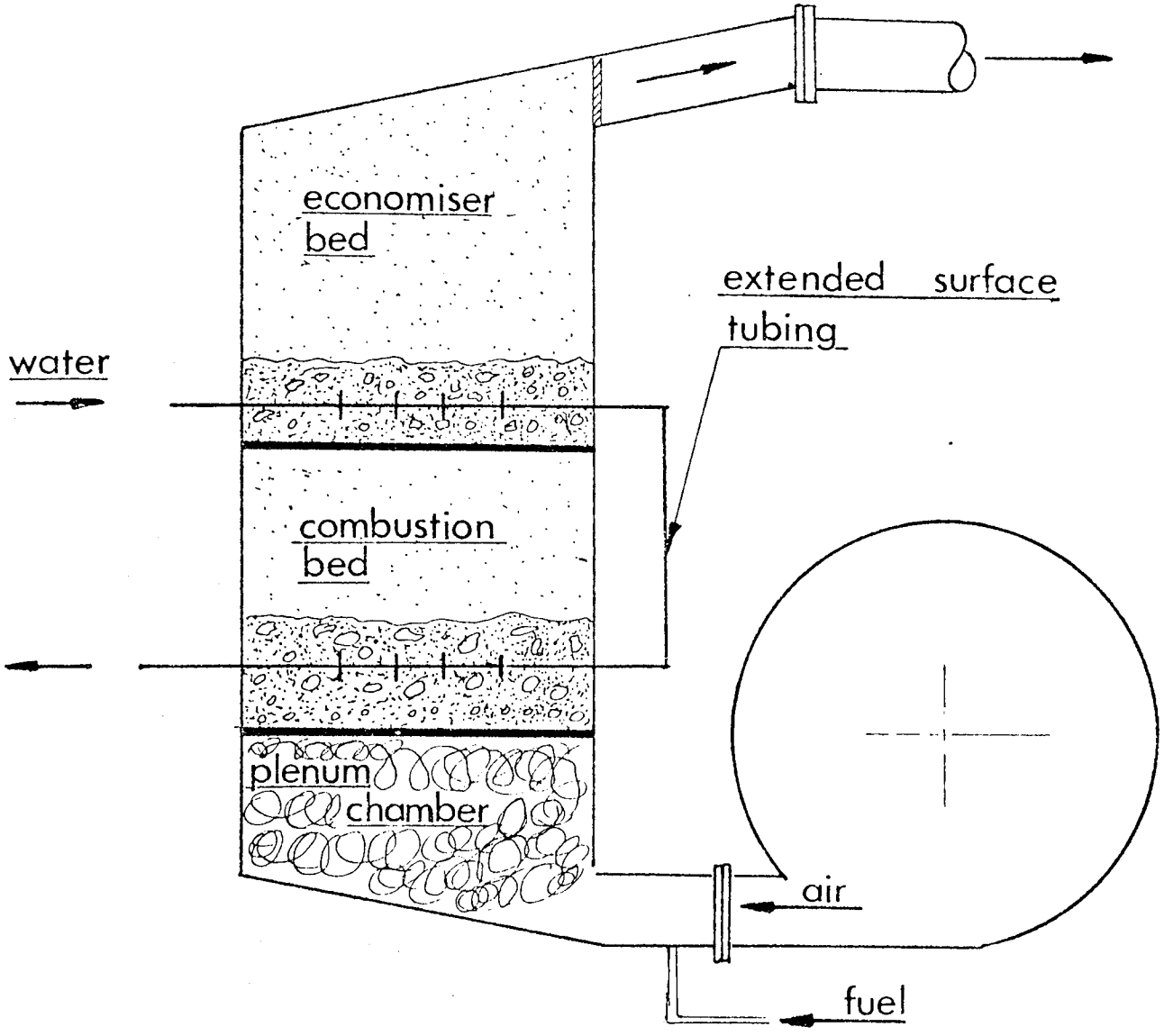


Fig. 2.1 Schematic layout of a two-stage fluidized bed boiler

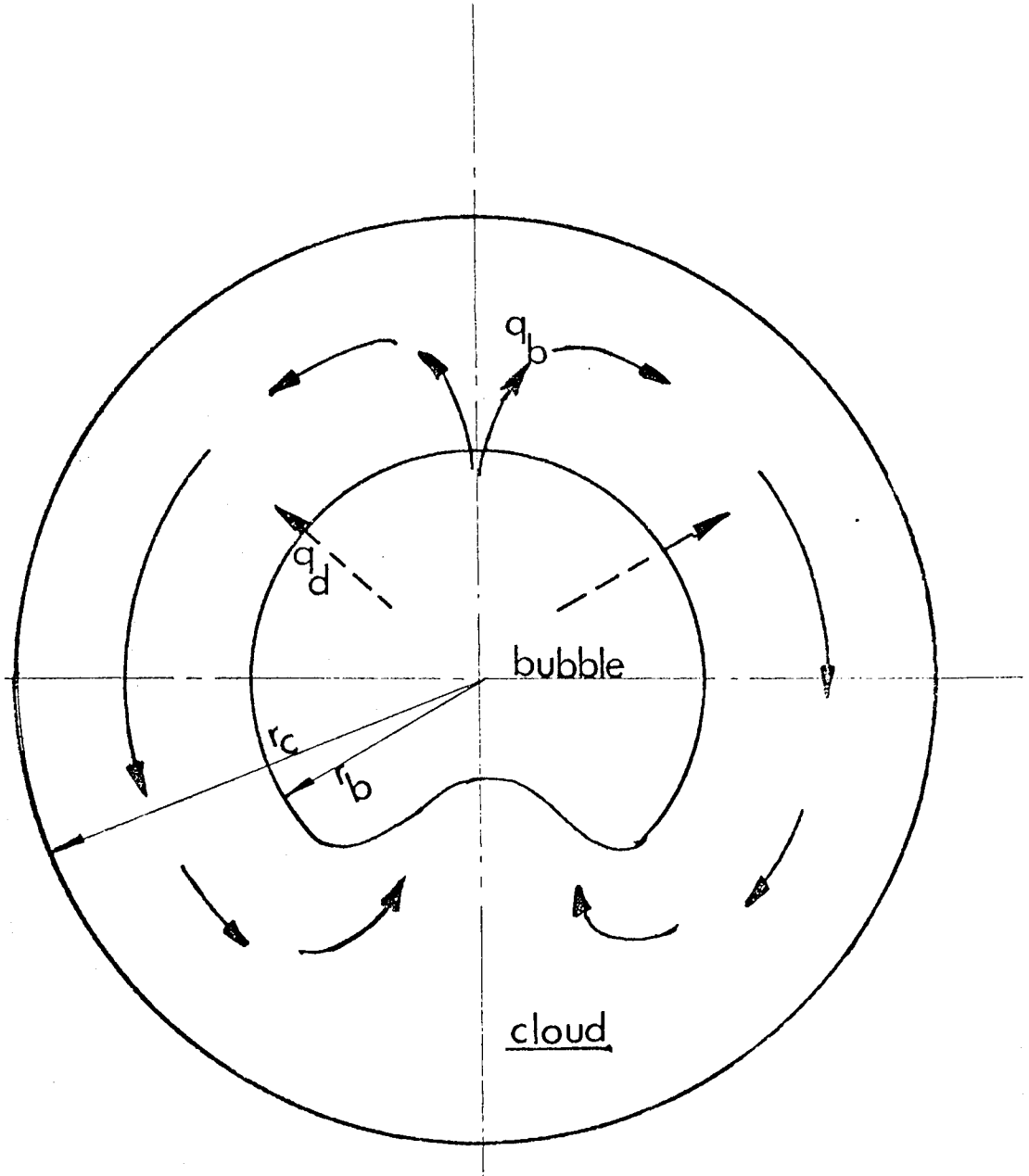


$$r_c = r_b \sqrt[3]{\frac{U_{br} + 2U_f'}{U_{br} - U_f'}}$$

Fig. 2.2 Gas exchange from bubble to cloud

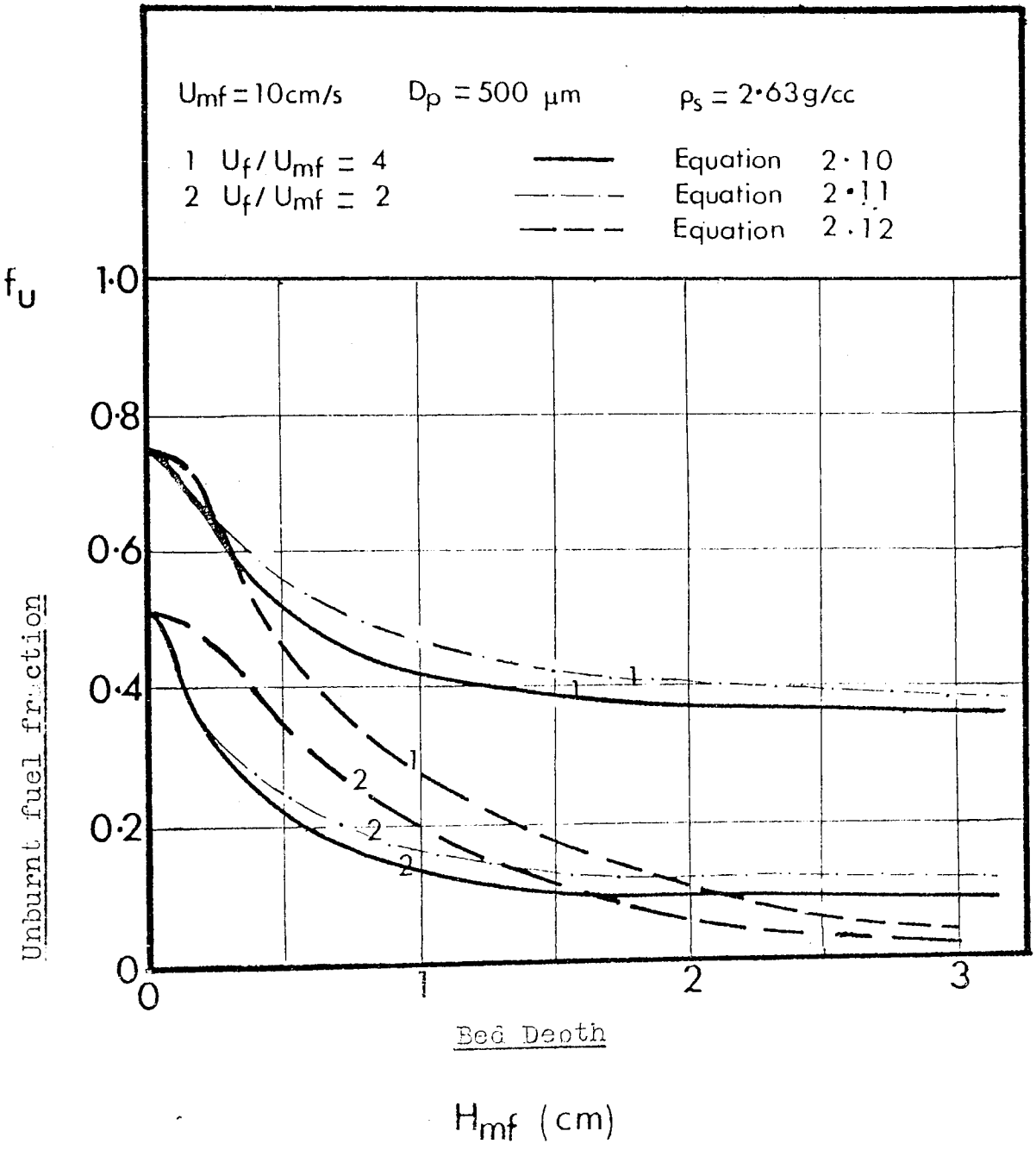


Fig. 2.3 Fuel bypass for gas combustion

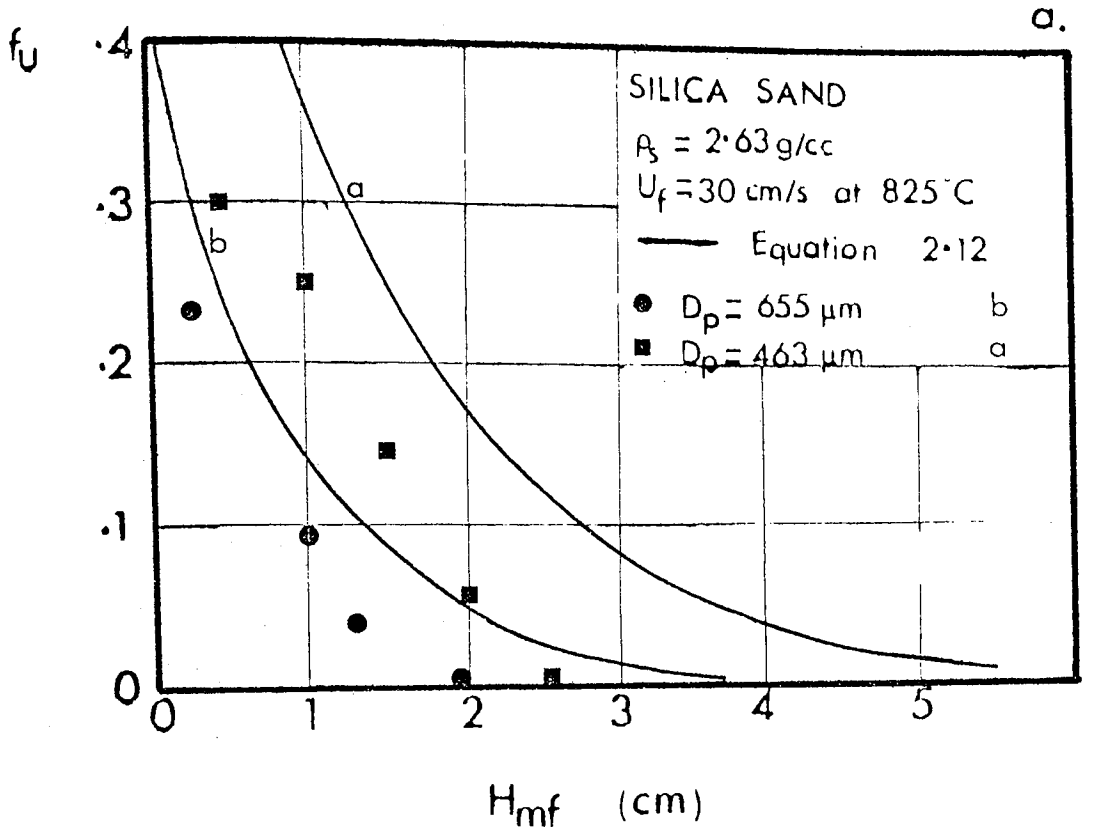


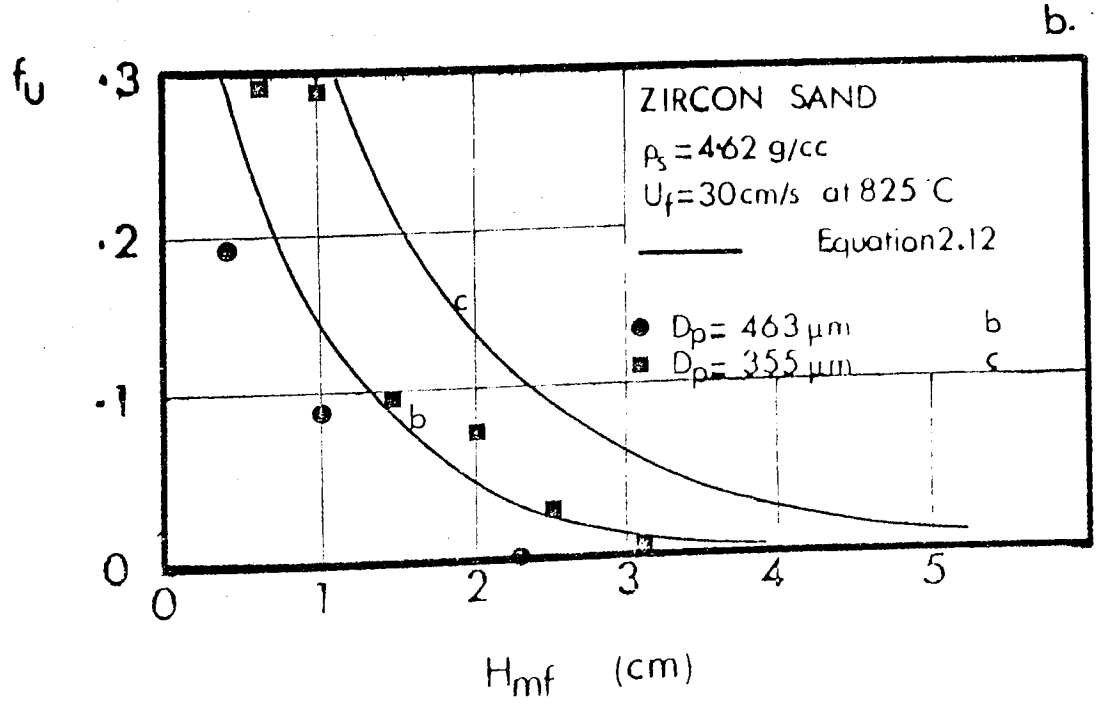


Fig. 2.4 Fuel bypass for stoichiometric pre-mixed gas combustion

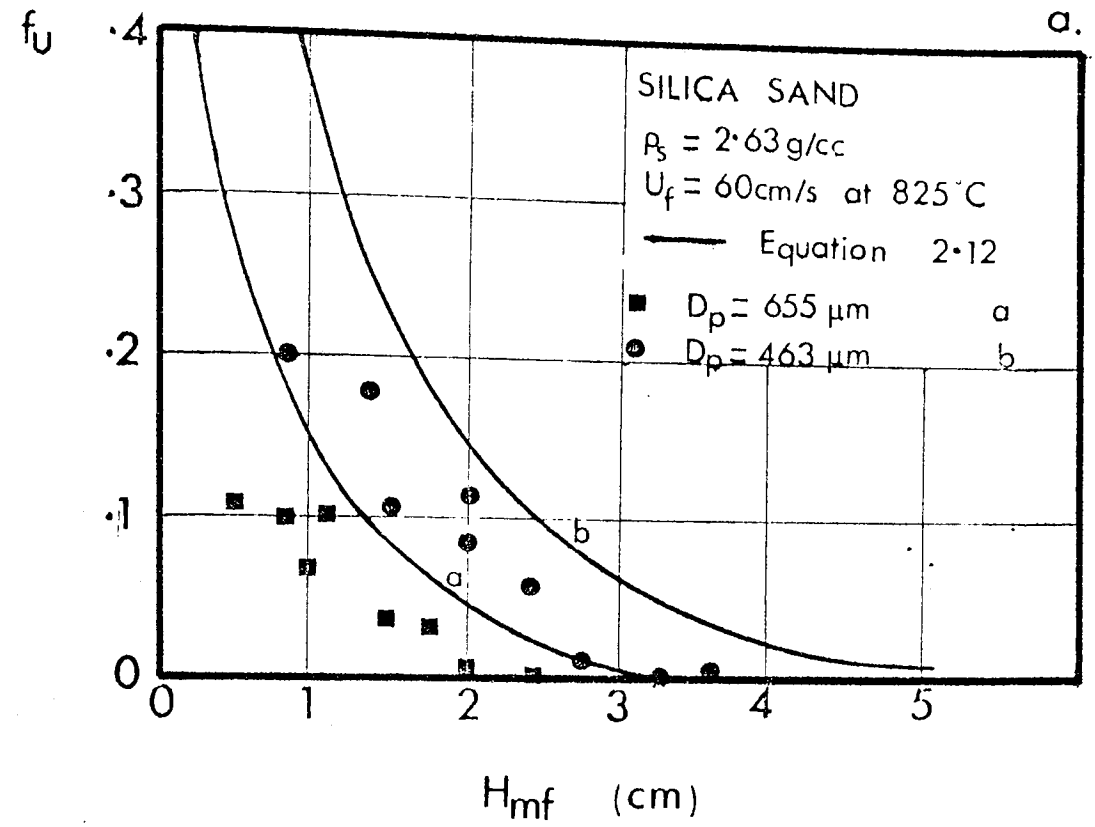


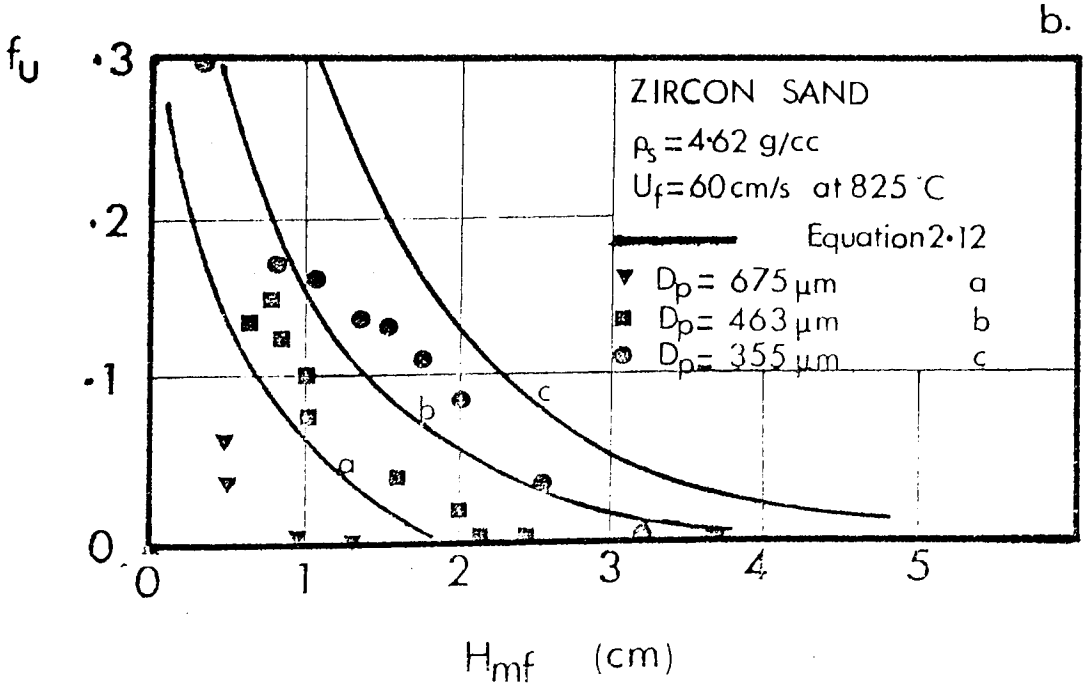


Fig. 2.5 Fuel bypass for stoichiometric pre-mixed gas combustion

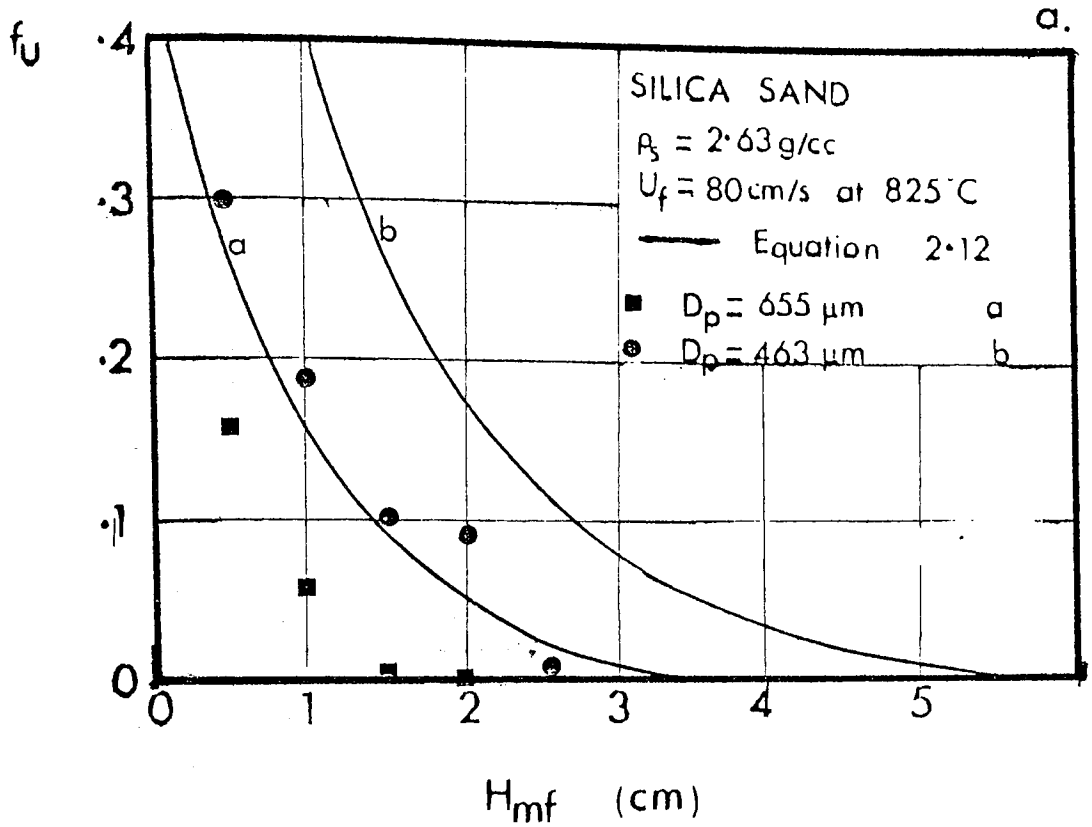


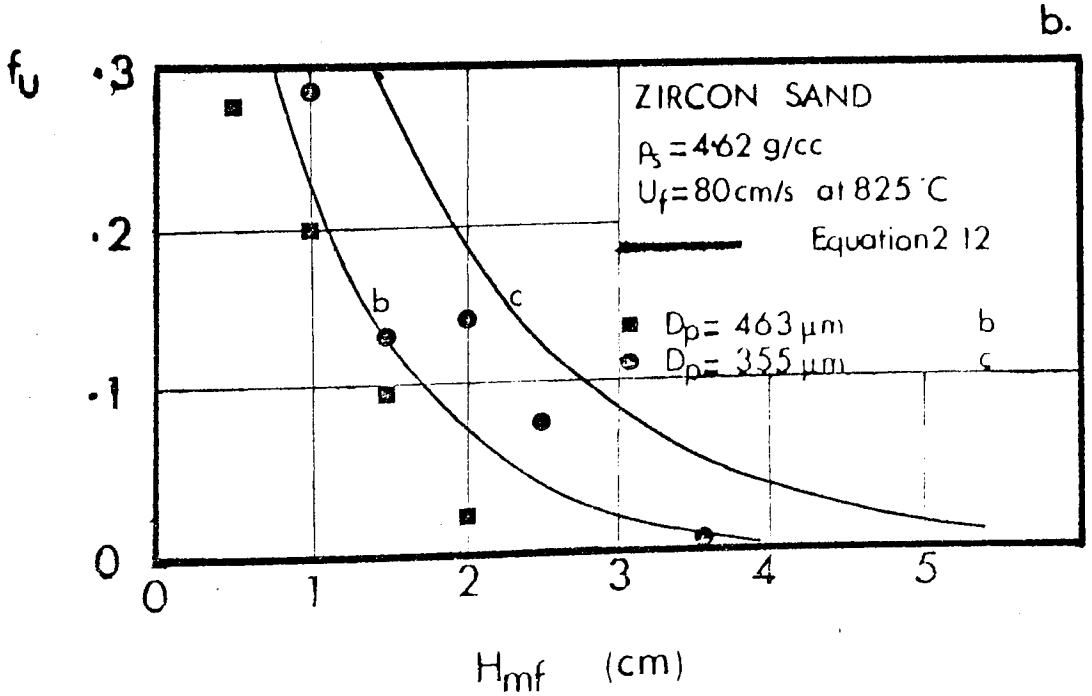


Fig. 2.6 Fuel bypass for stoichiometric pre-mixed gas combustion

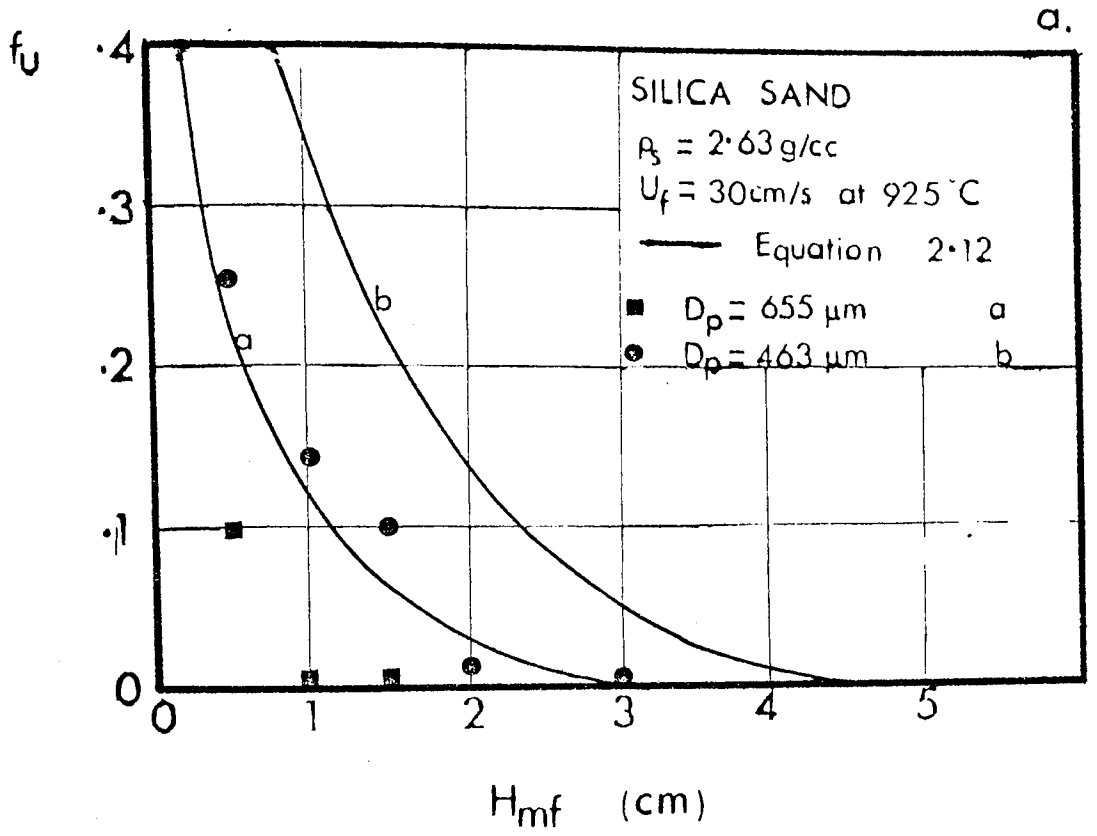


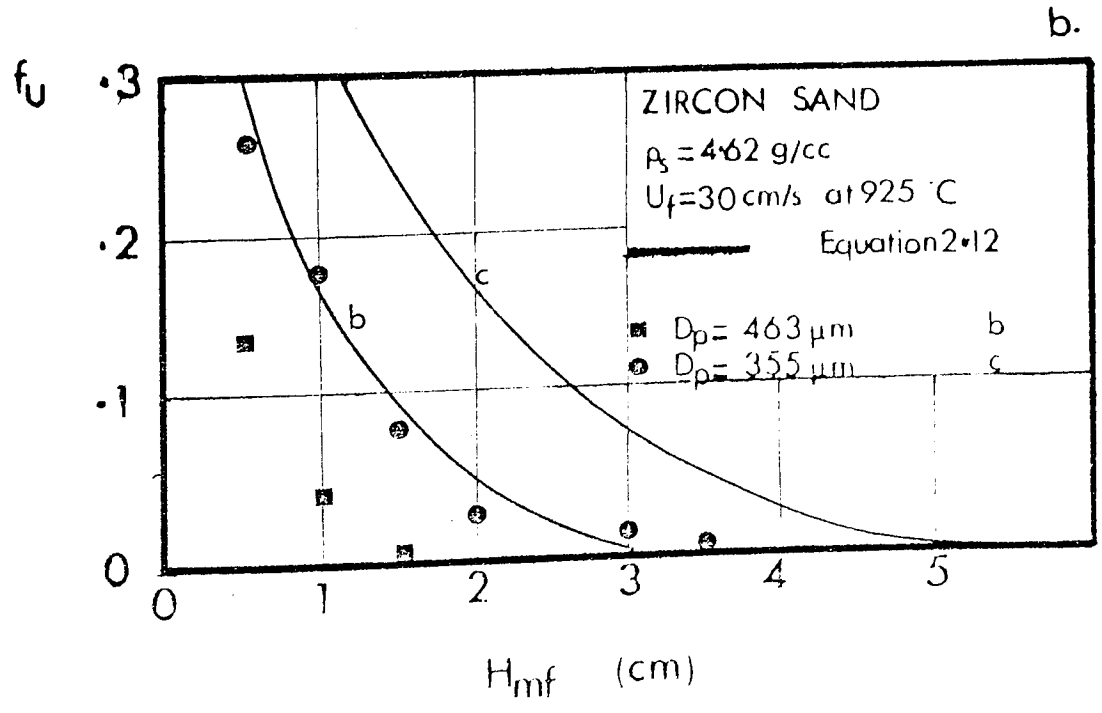


Fig. 2.7 Fuel bypass for stoichiometric pre-mixed gas combustion

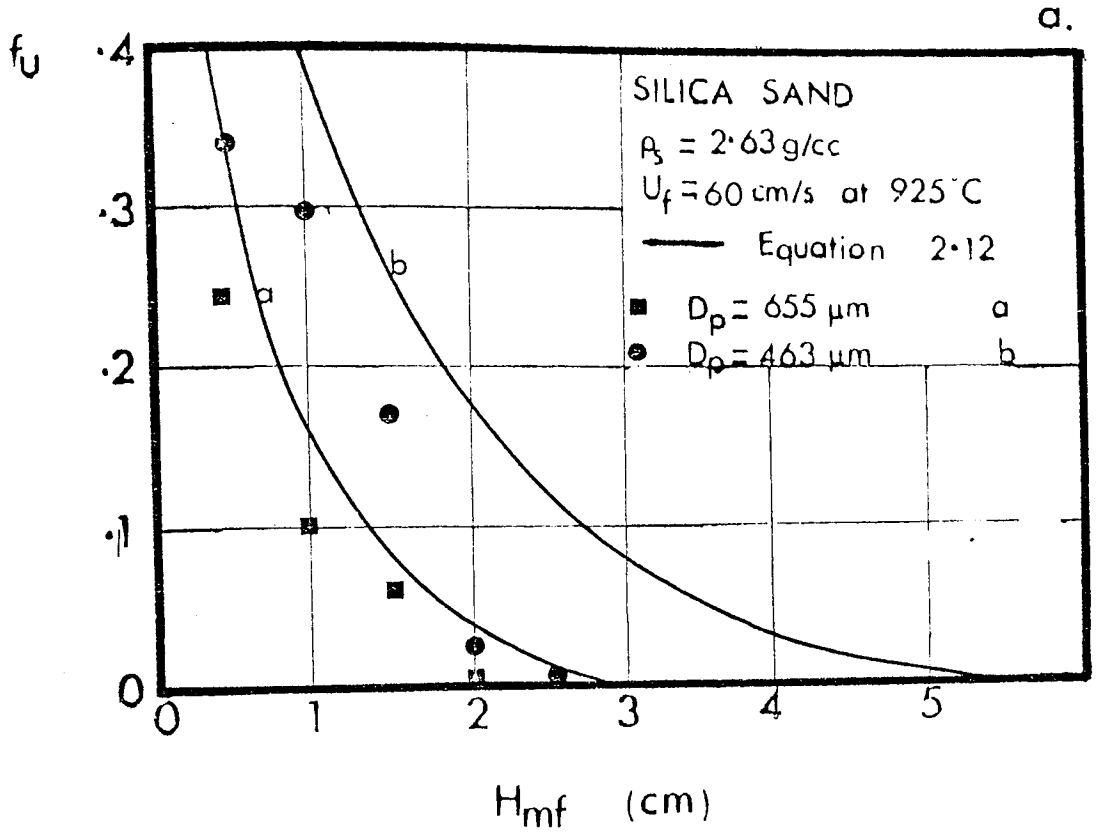


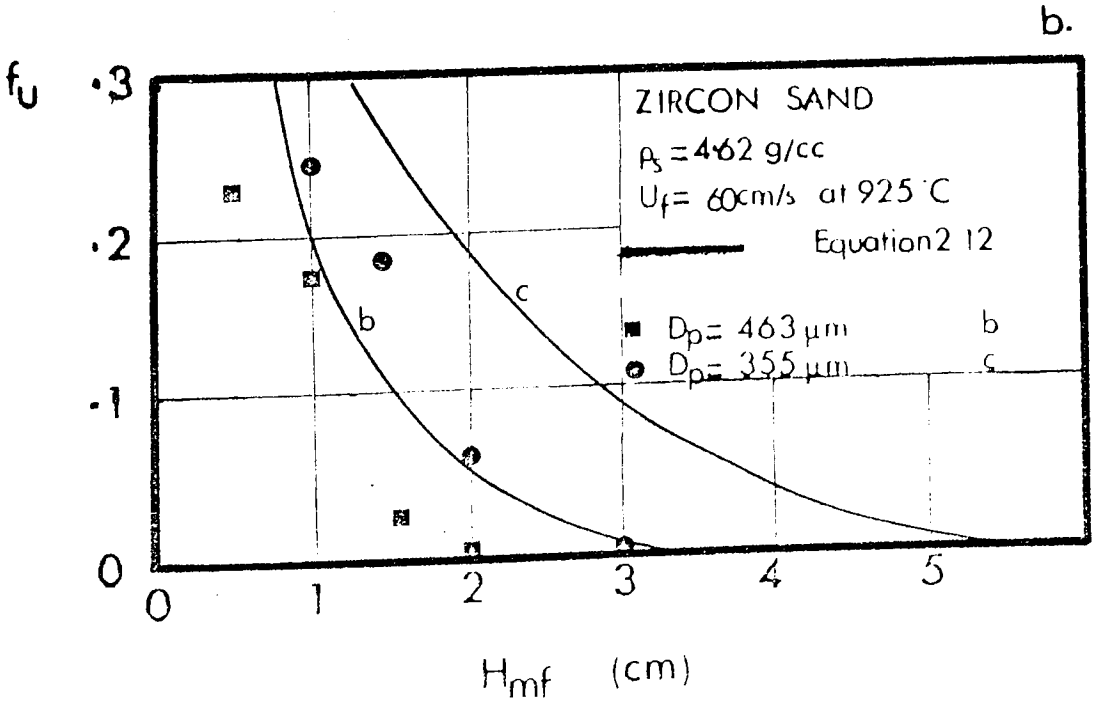


Fig. 2.8 Fuel bypass for stoichiometric pre-mixed gas combustion

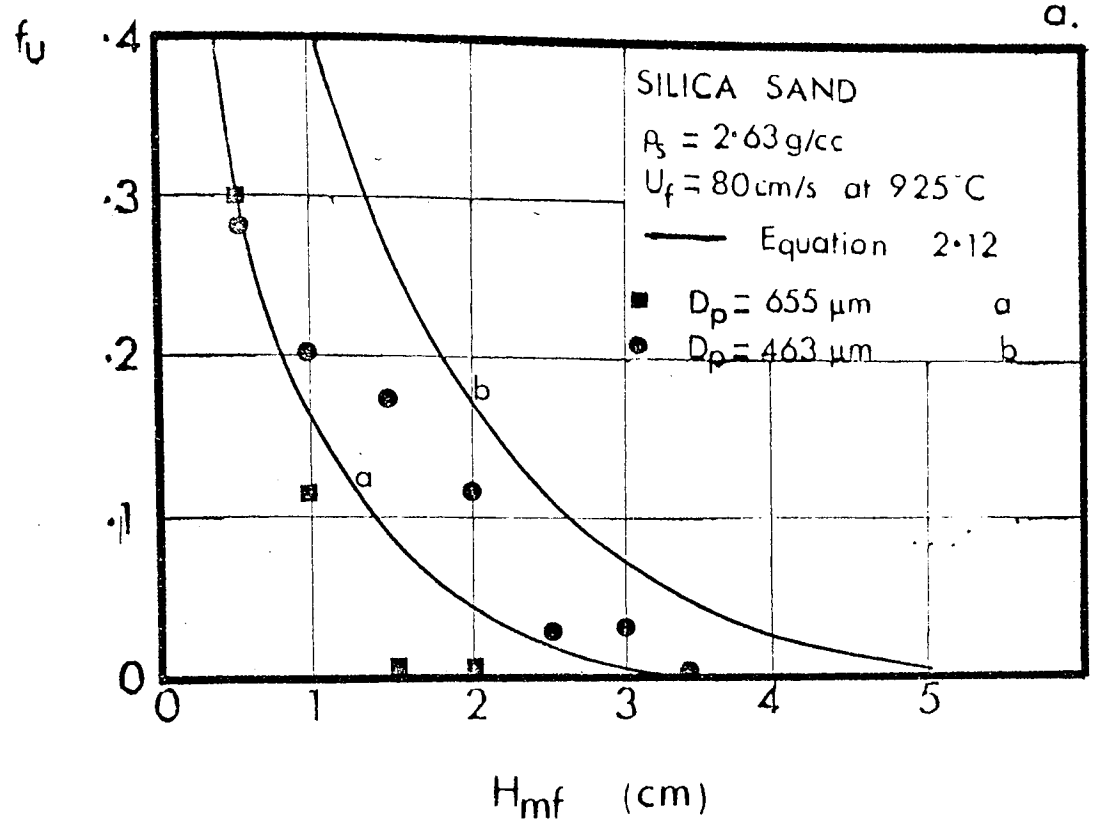


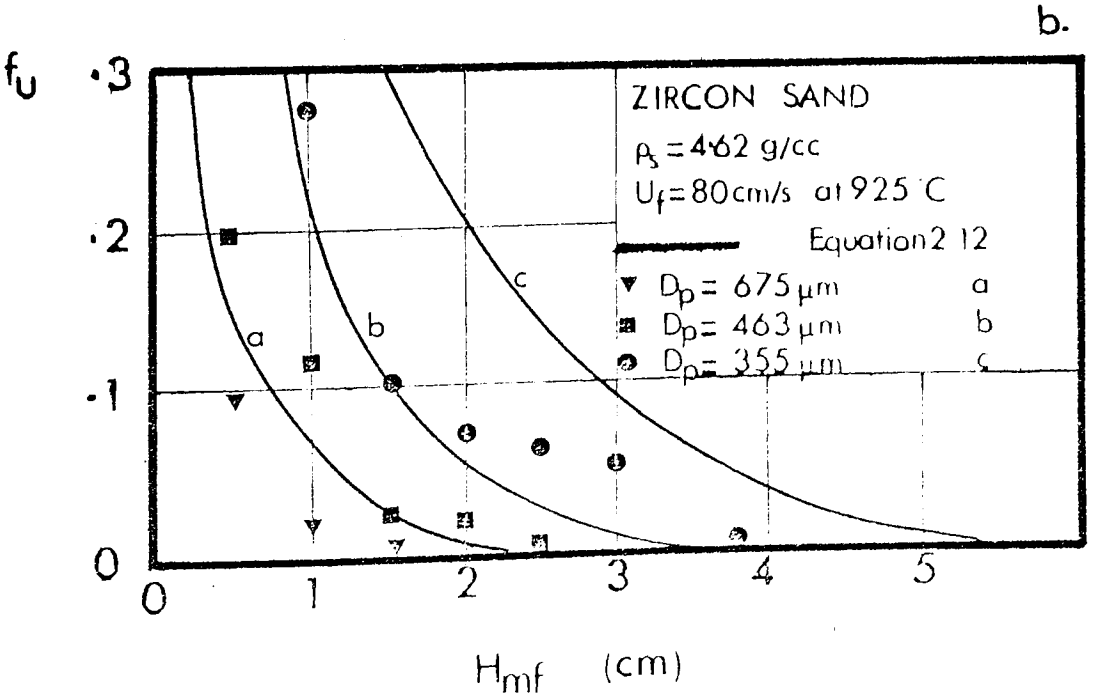


Fig. 2.9 Fuel bypass for stoichiometric pre-mixed gas combustion

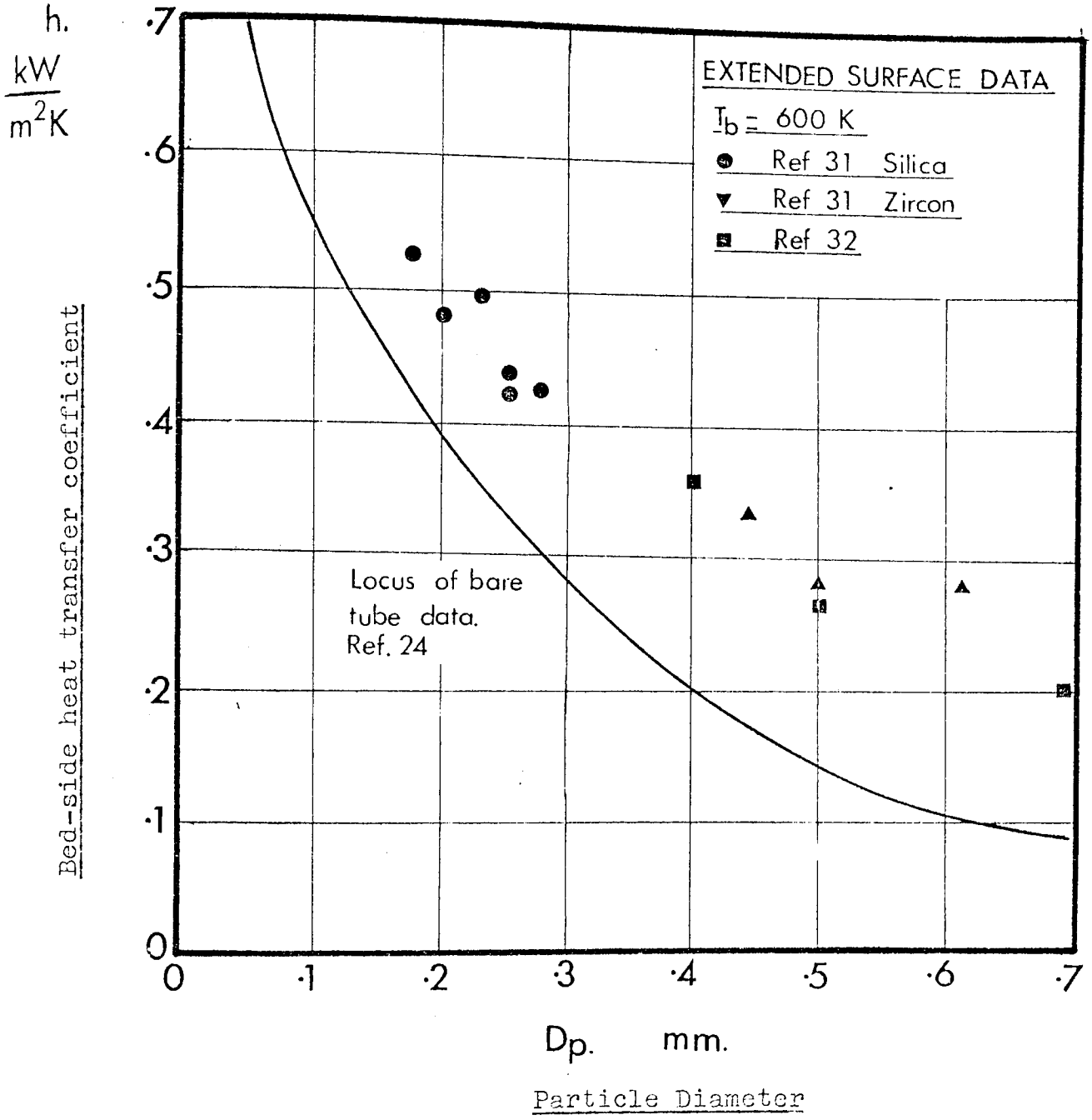


Fig 2.10 Heat transfer coefficients in fluidized beds

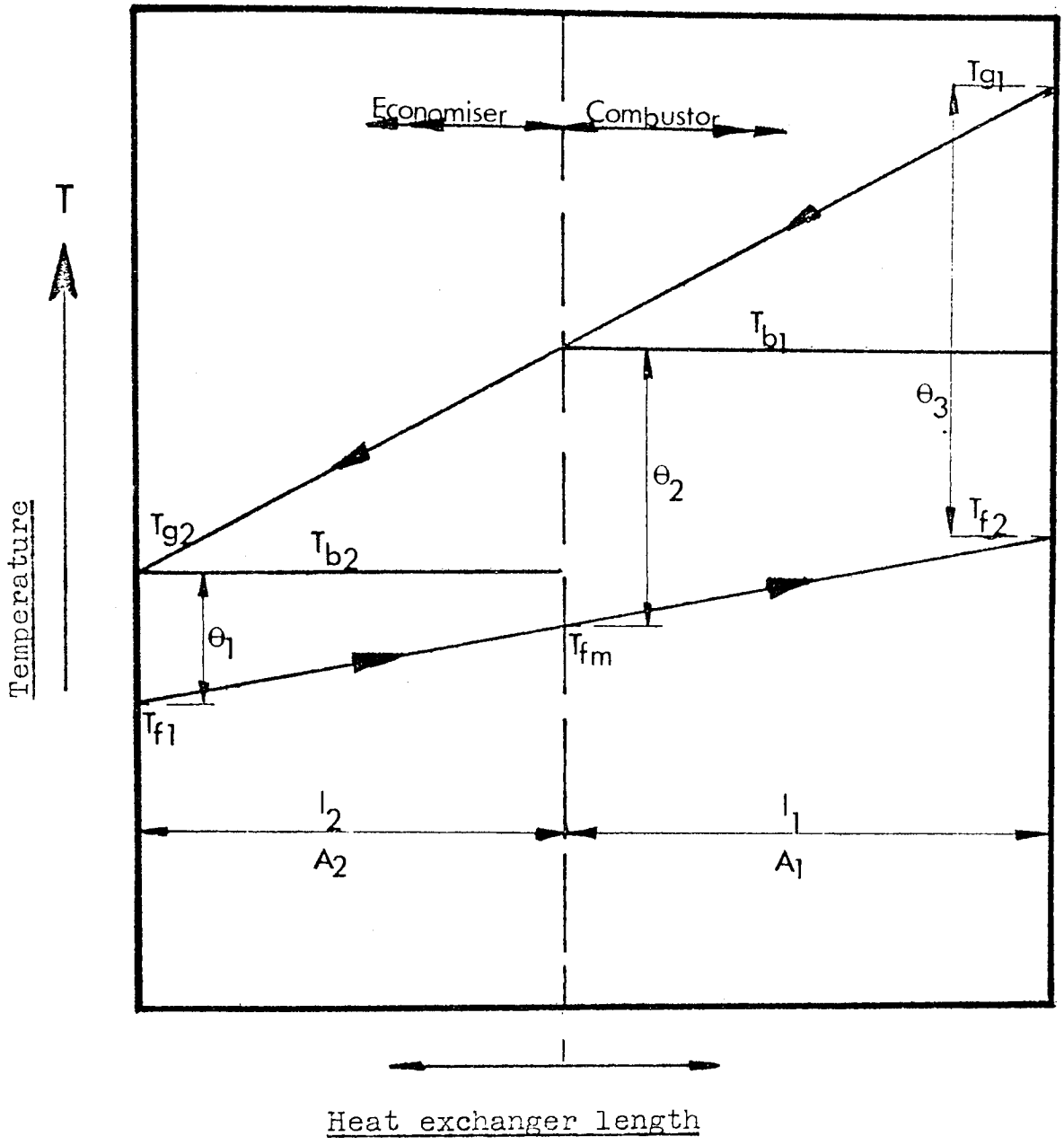


Fig. 2.11 Temperature profiles in a two-stage unit

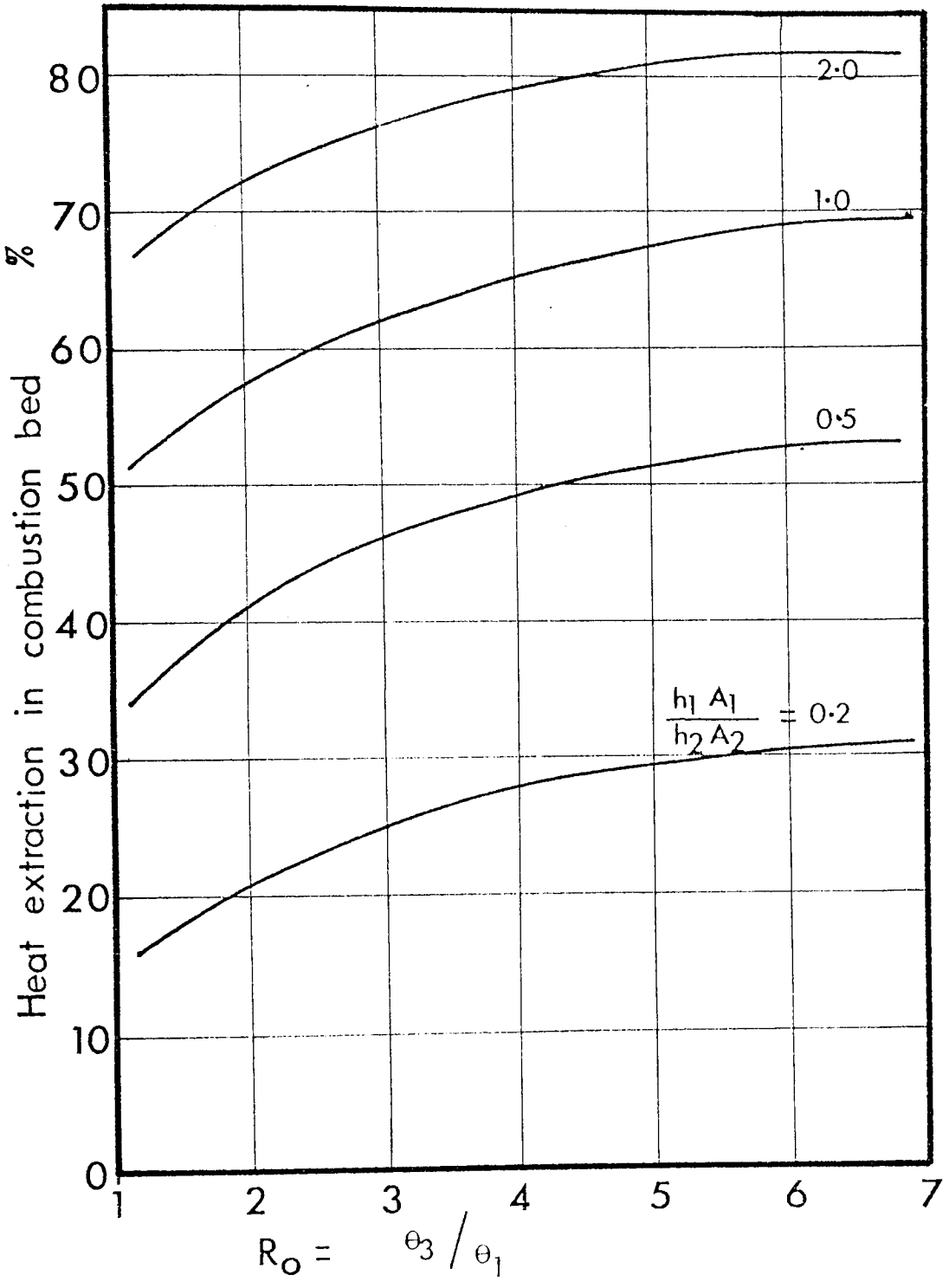


Fig. 2.12 Optimal heat extraction rates

a

Selective

Fluidization

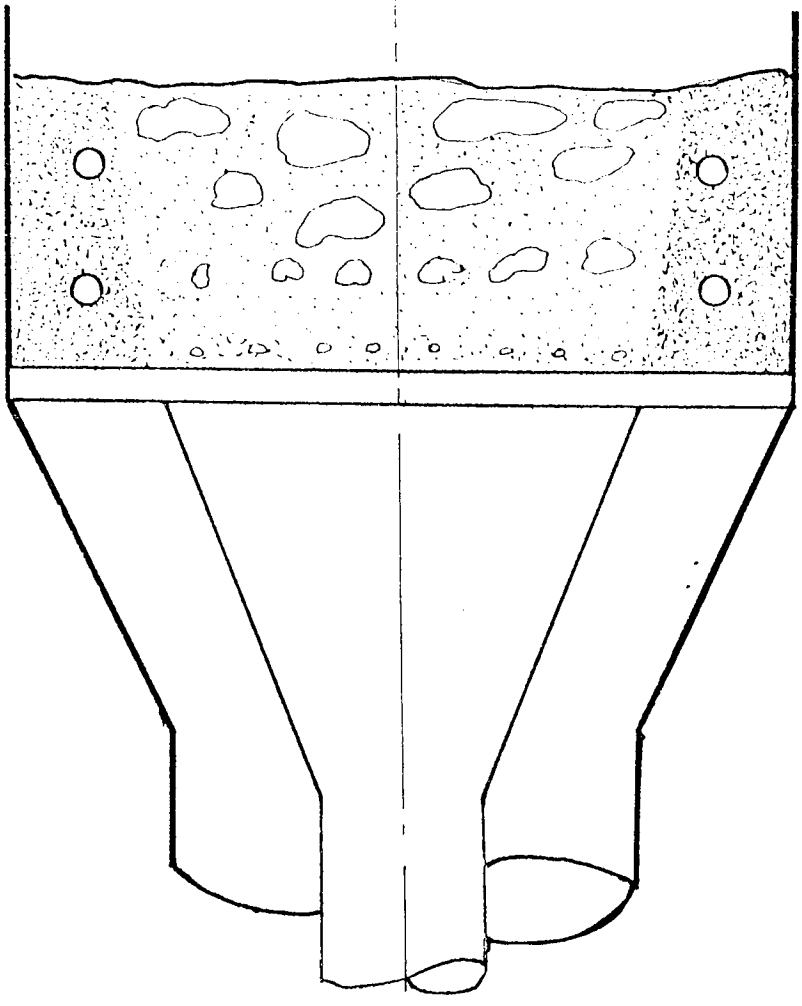

b

Bed

Expansion

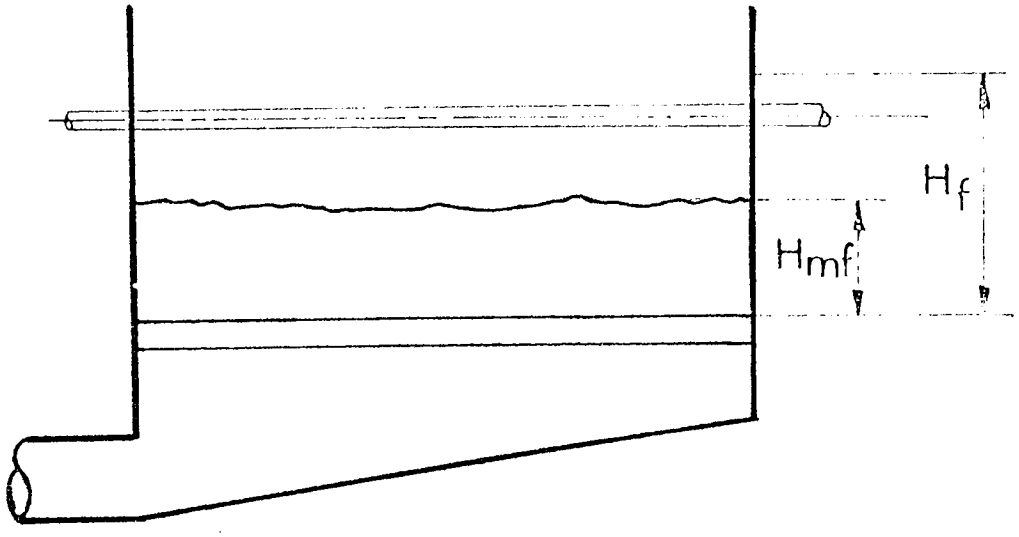


Fig. 2.13 Start-up systems

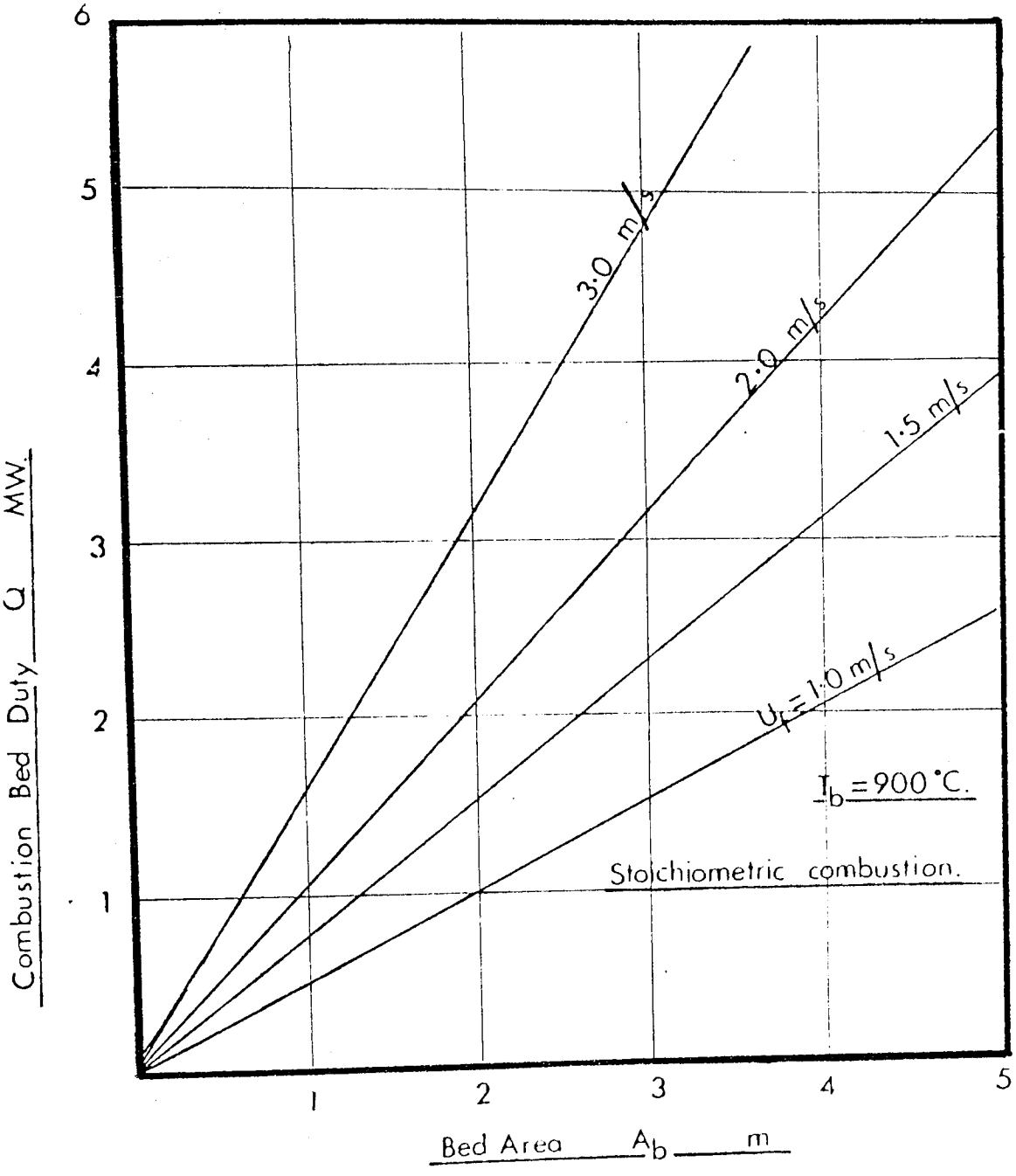


Fig. 2.14 Heat release rates

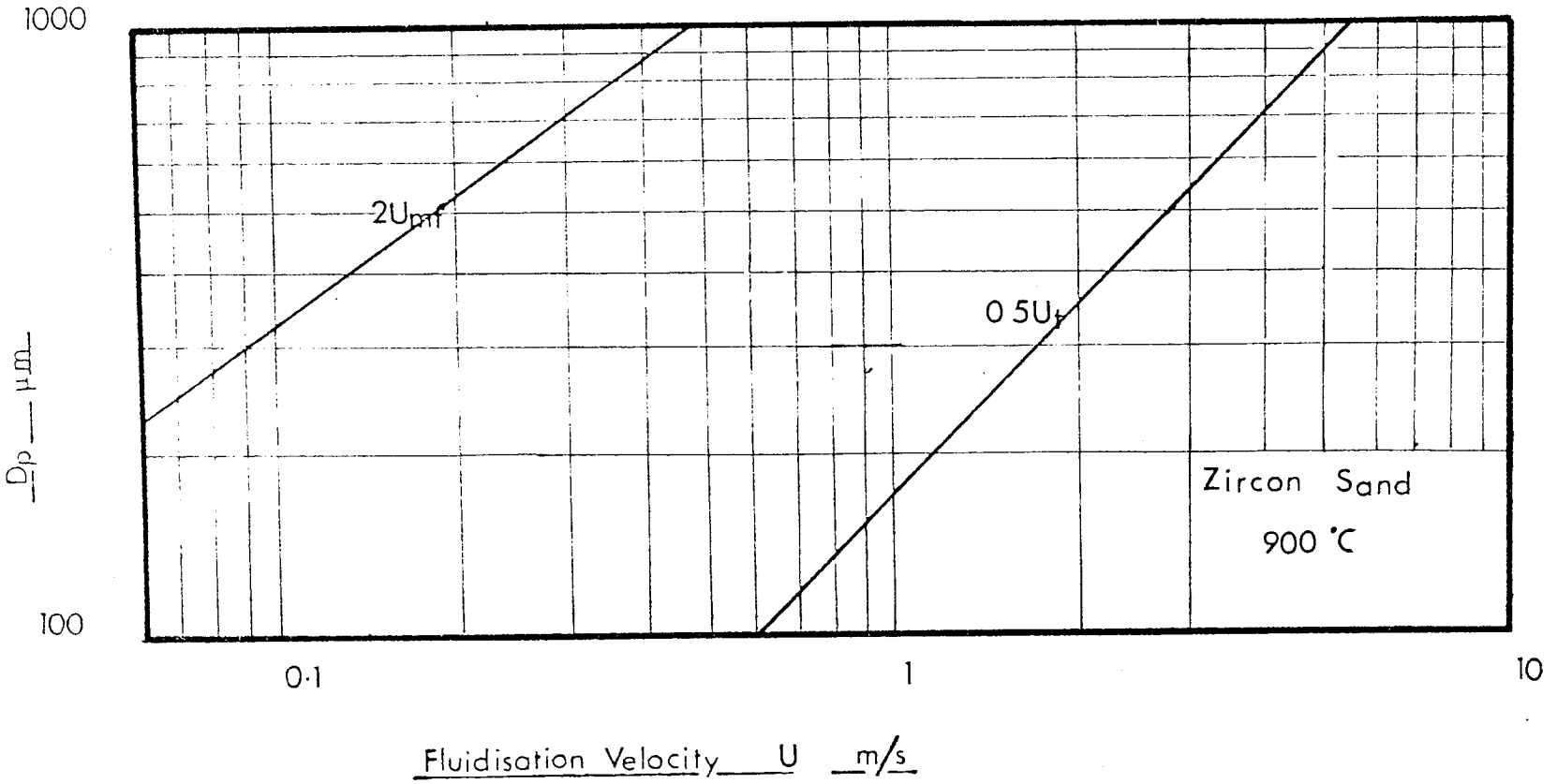


Fig. 2.15 Velocity design range

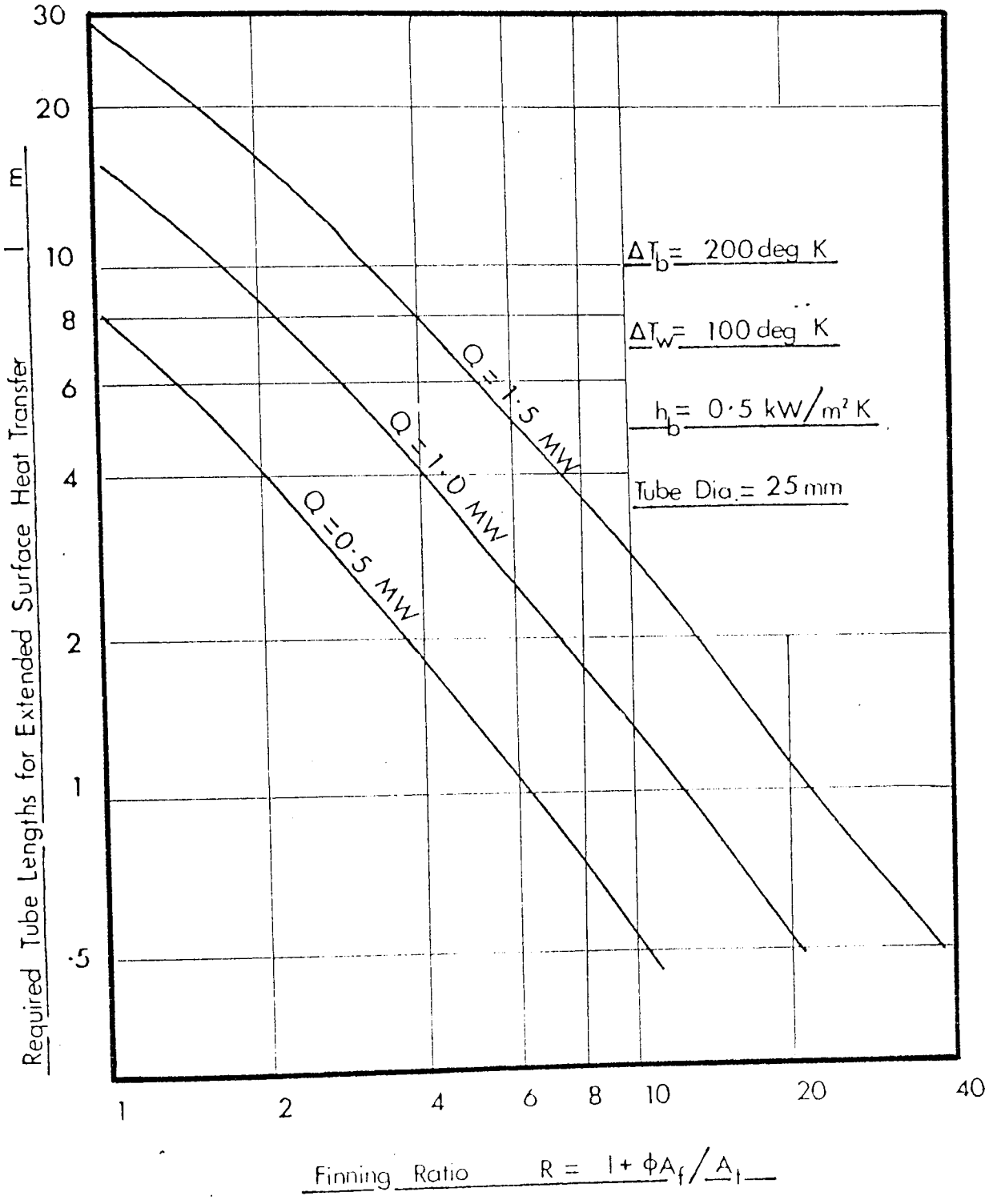


Fig. 2.16 Extended surface performance

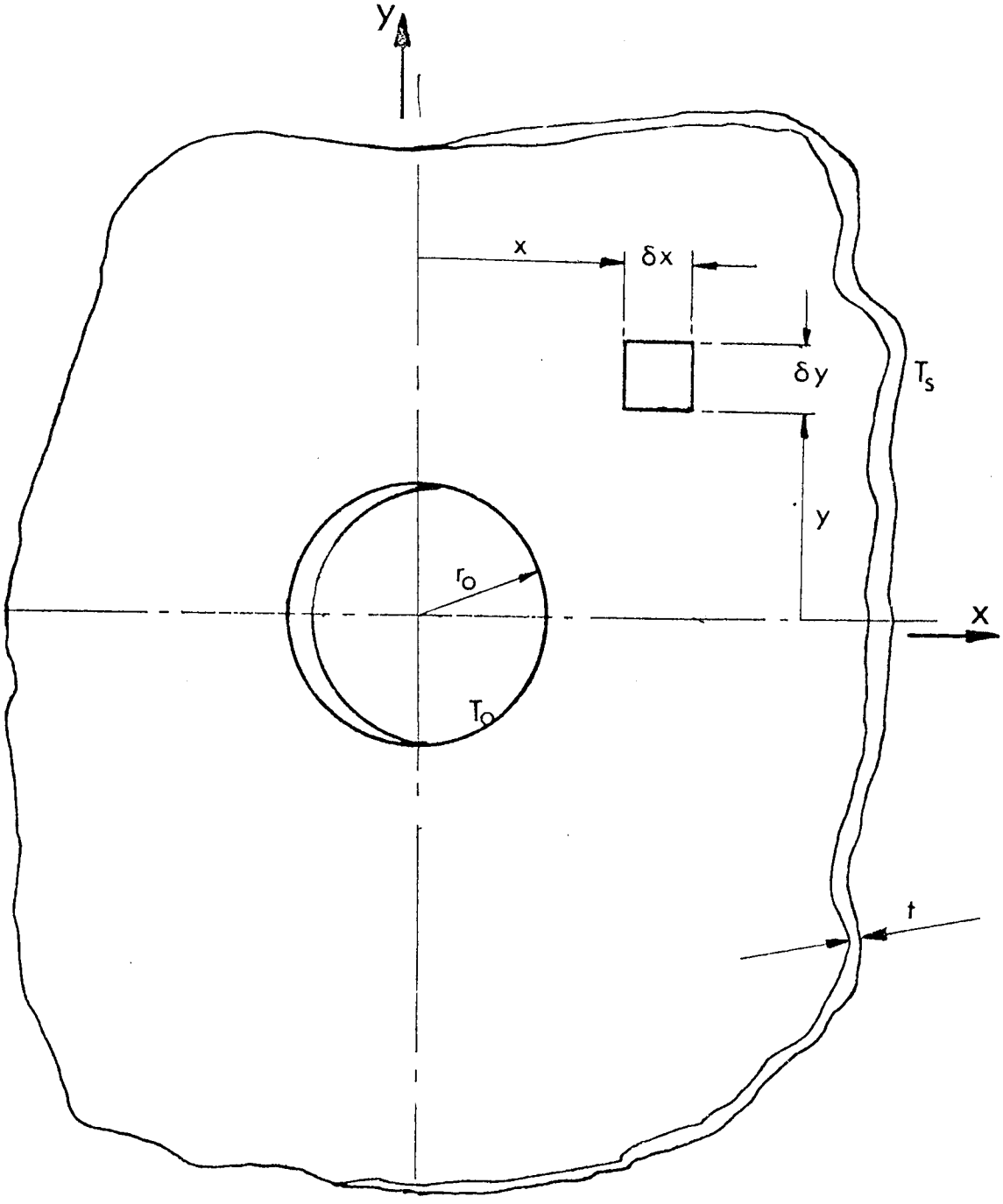


Fig. 3.1 Heat flow through a transverse fin

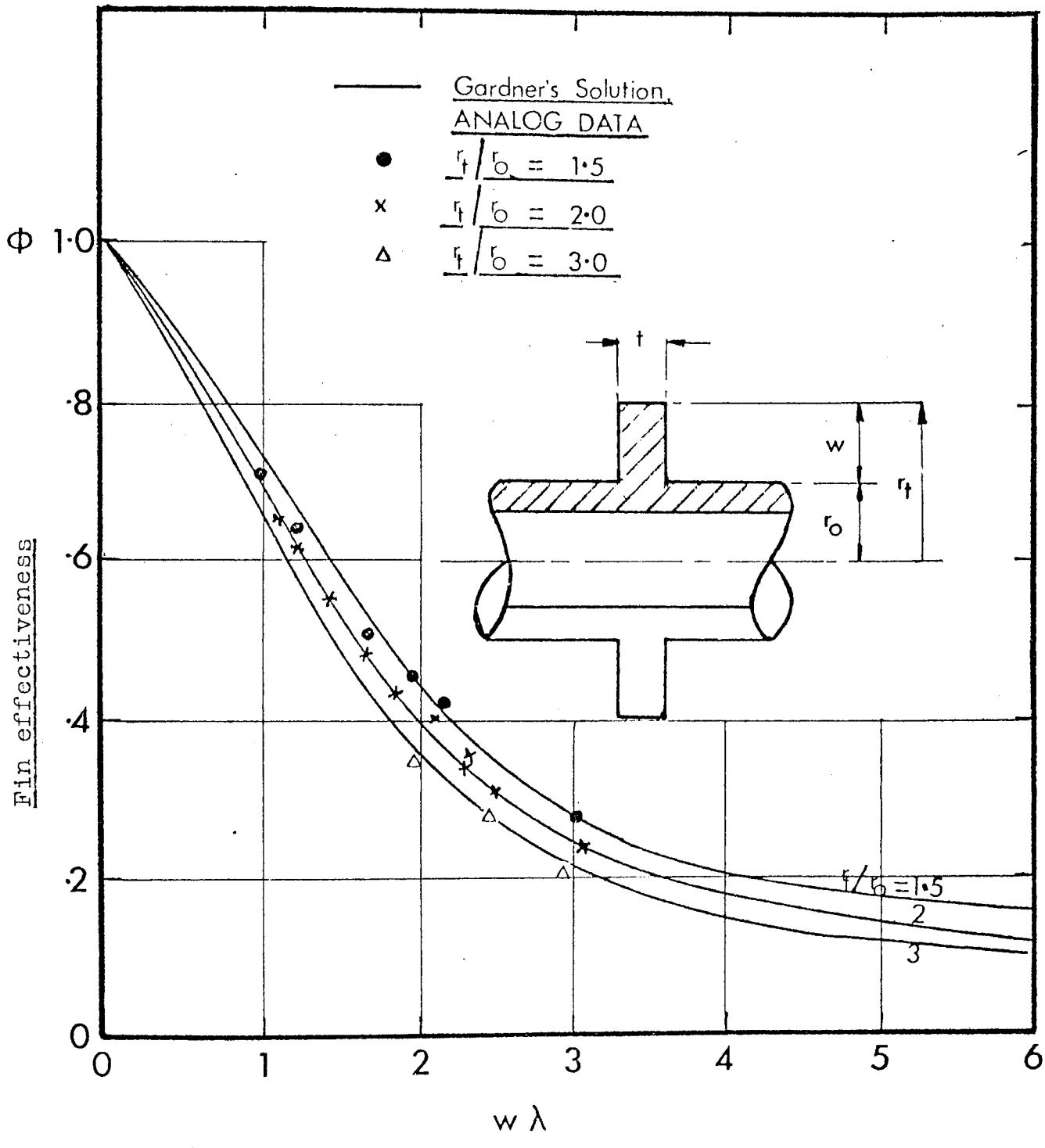


Fig. 3.2 Effectiveness of annular fins

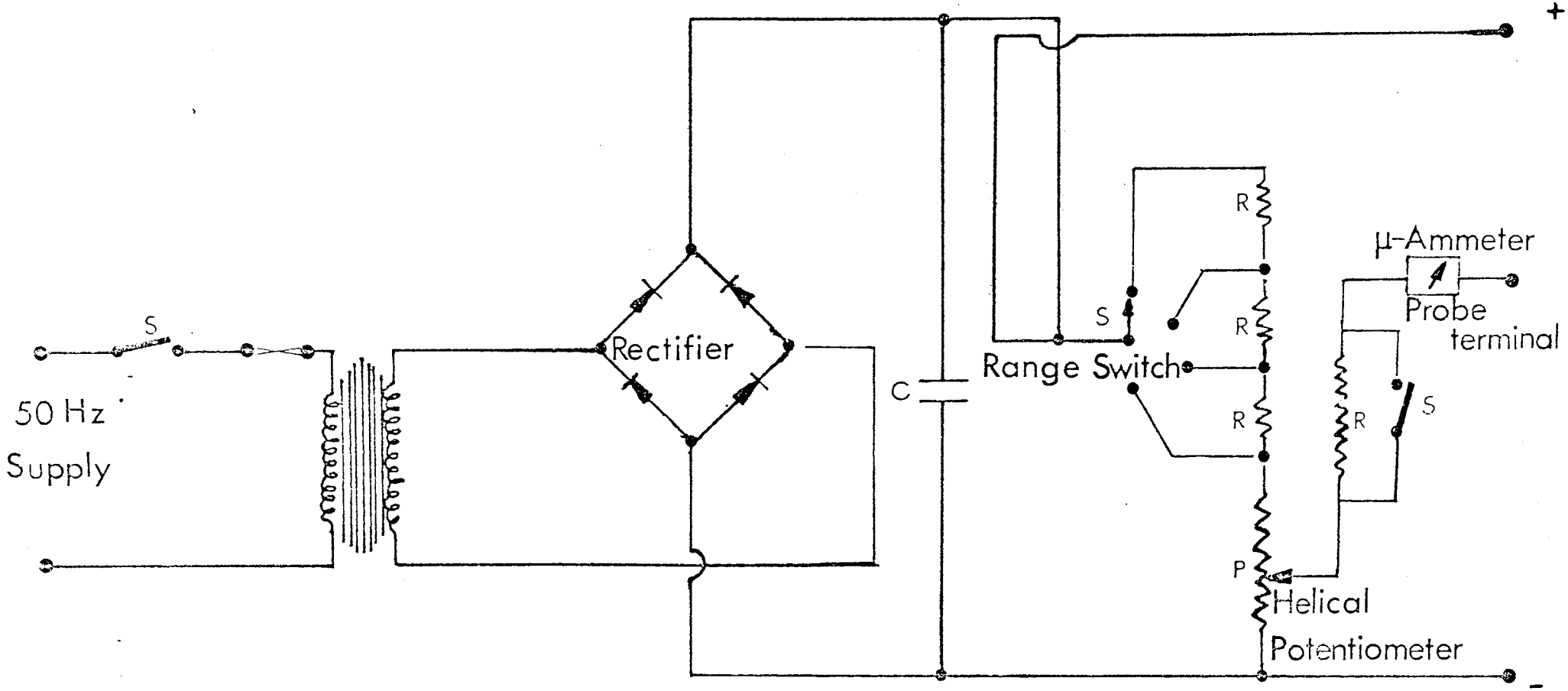


Fig. 3.3 A typical field-plotter circuit

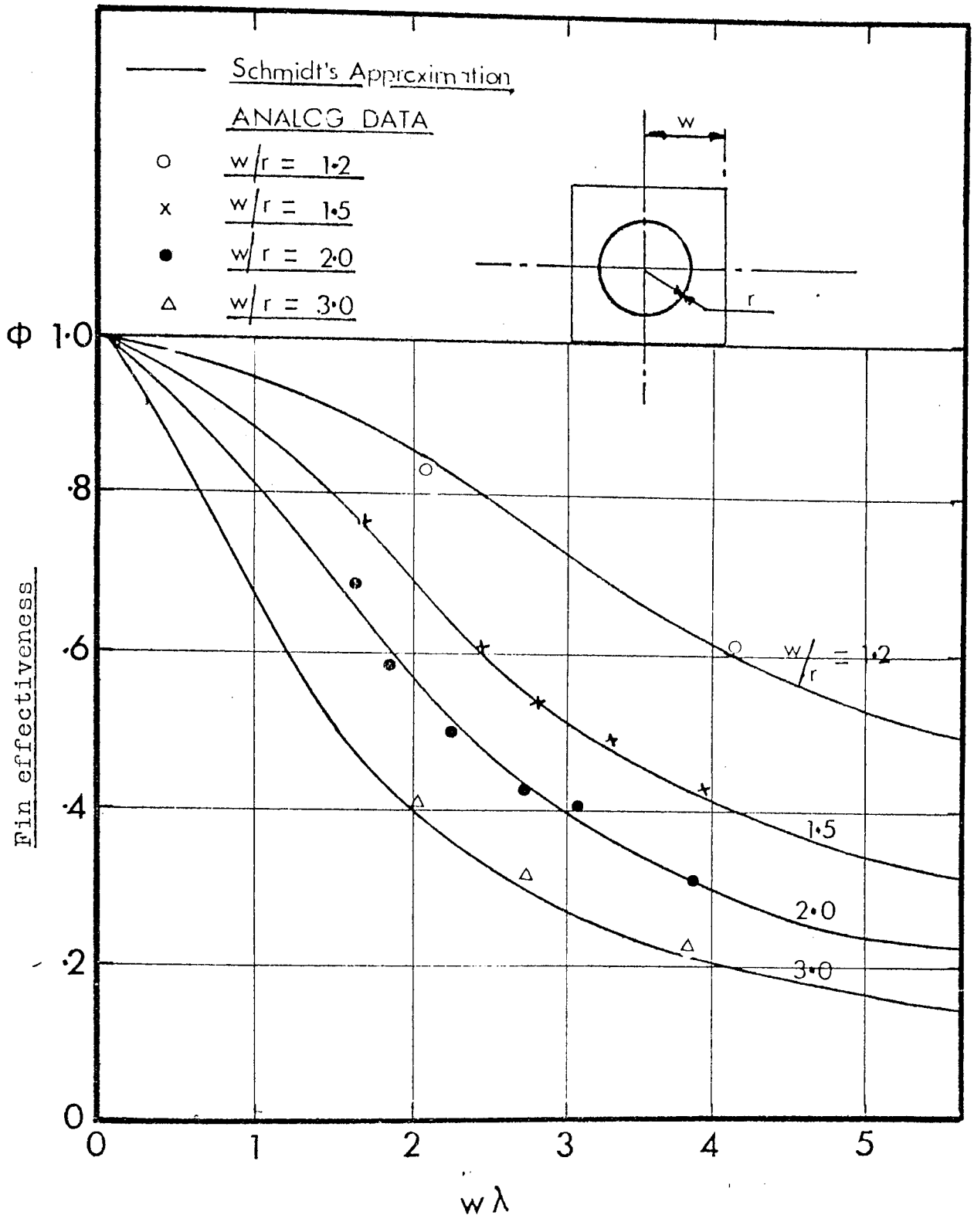


Fig. 3.4 Effectiveness of square fins

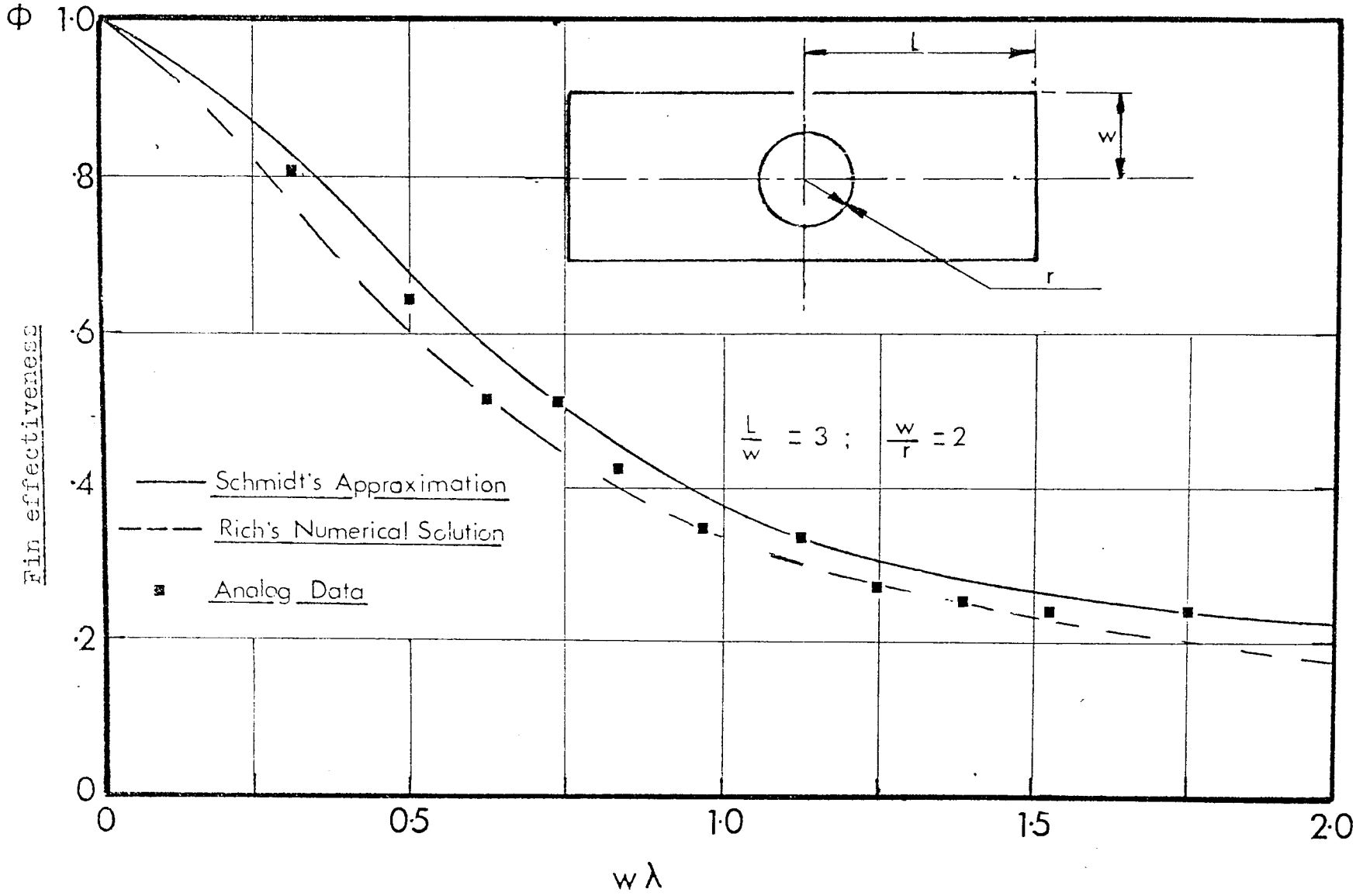


Fig. 3.5 Effectiveness of rectangular fins

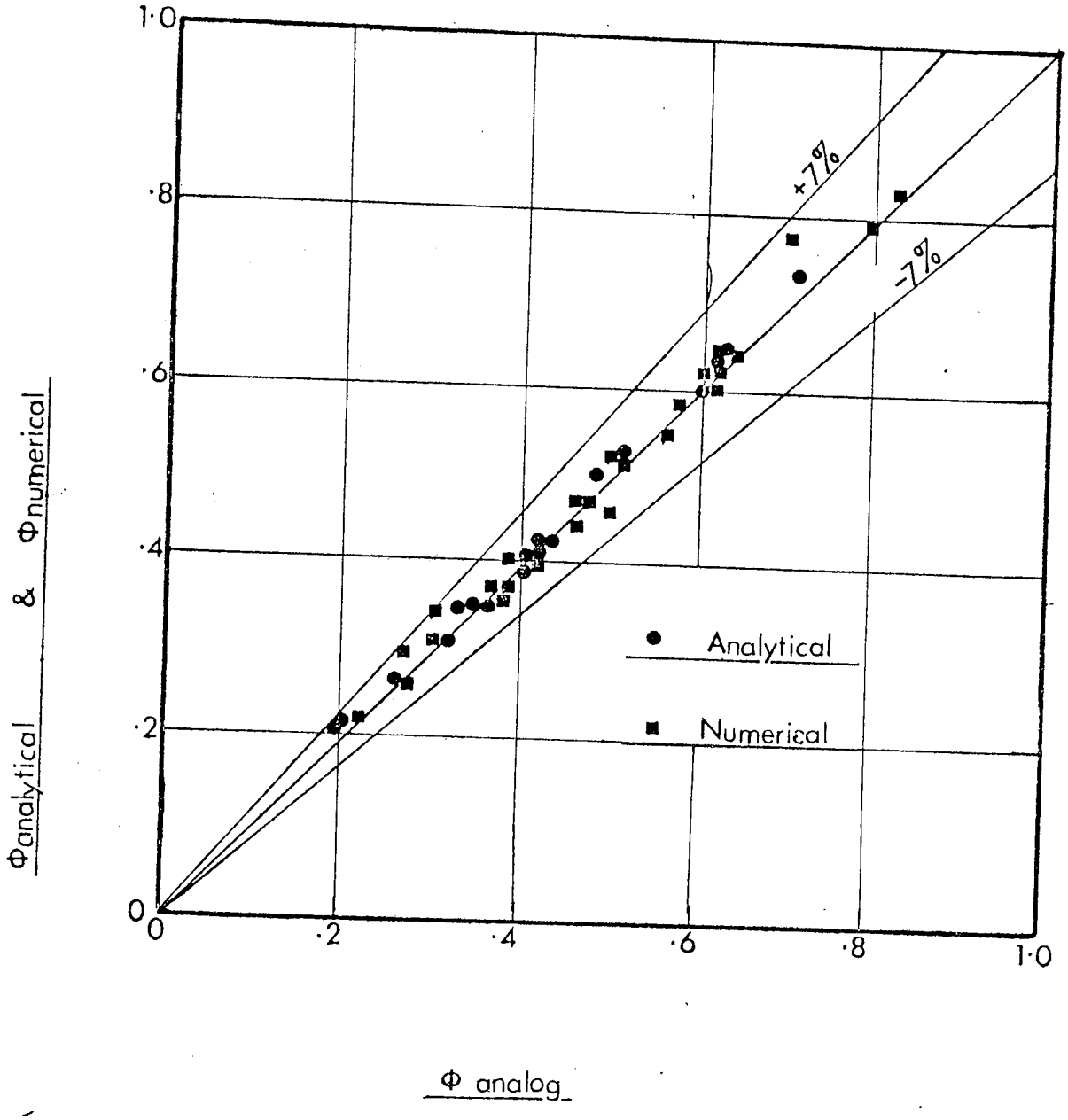


Fig. 3.6 Analog accuracy

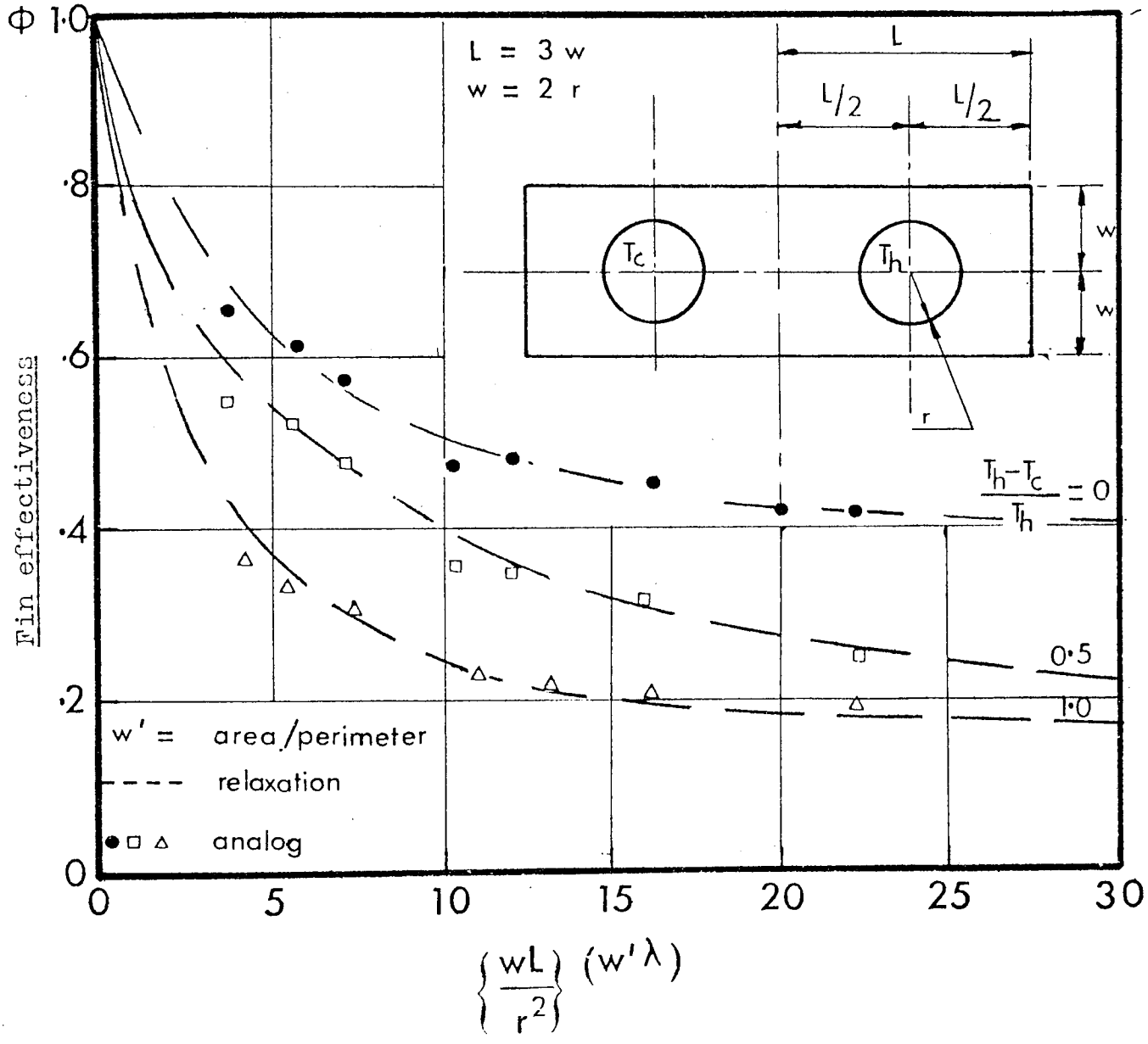


Fig. 3.7 Sheet fin performance

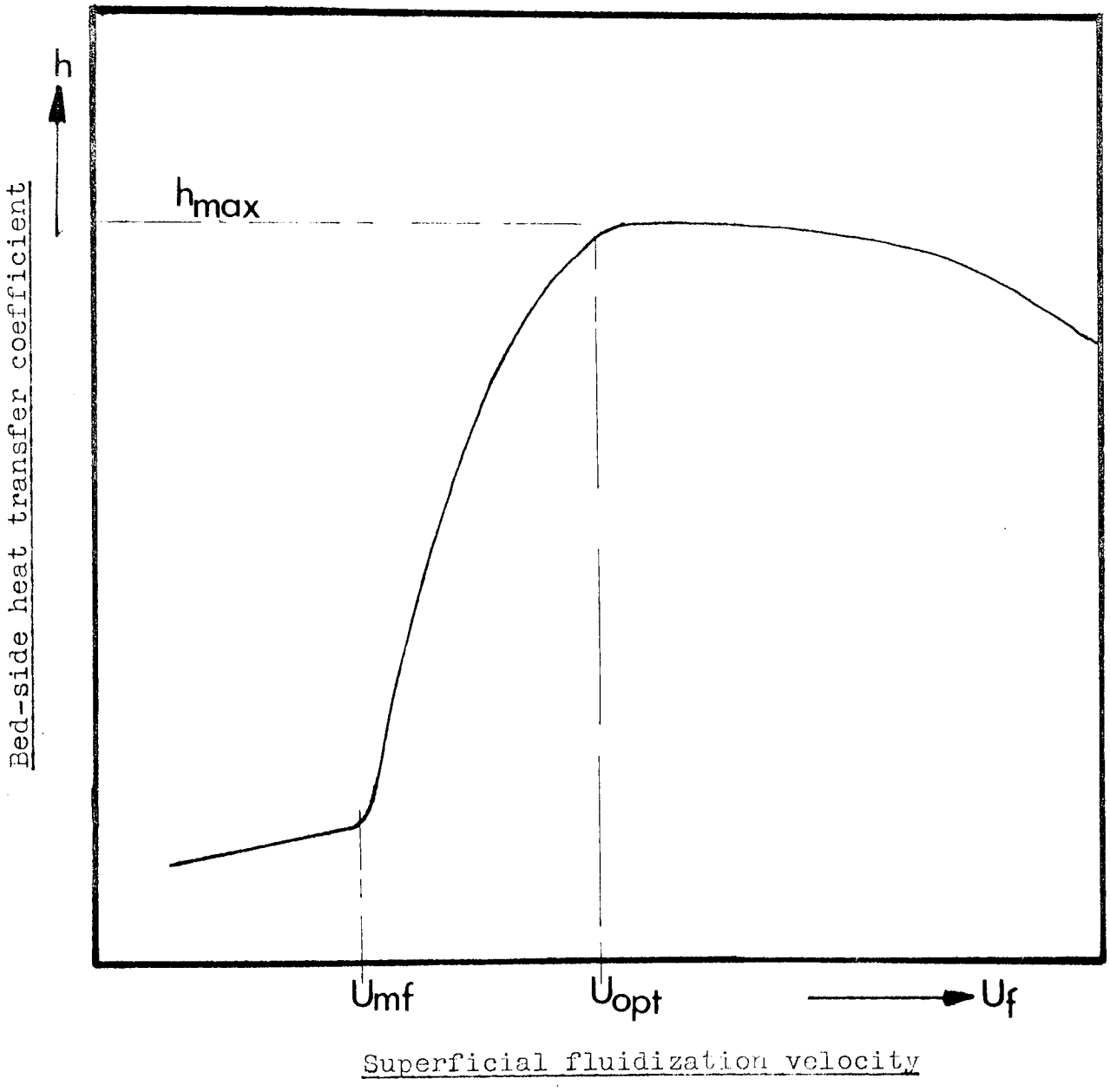


Fig. 4.1 Typical heat transfer curve

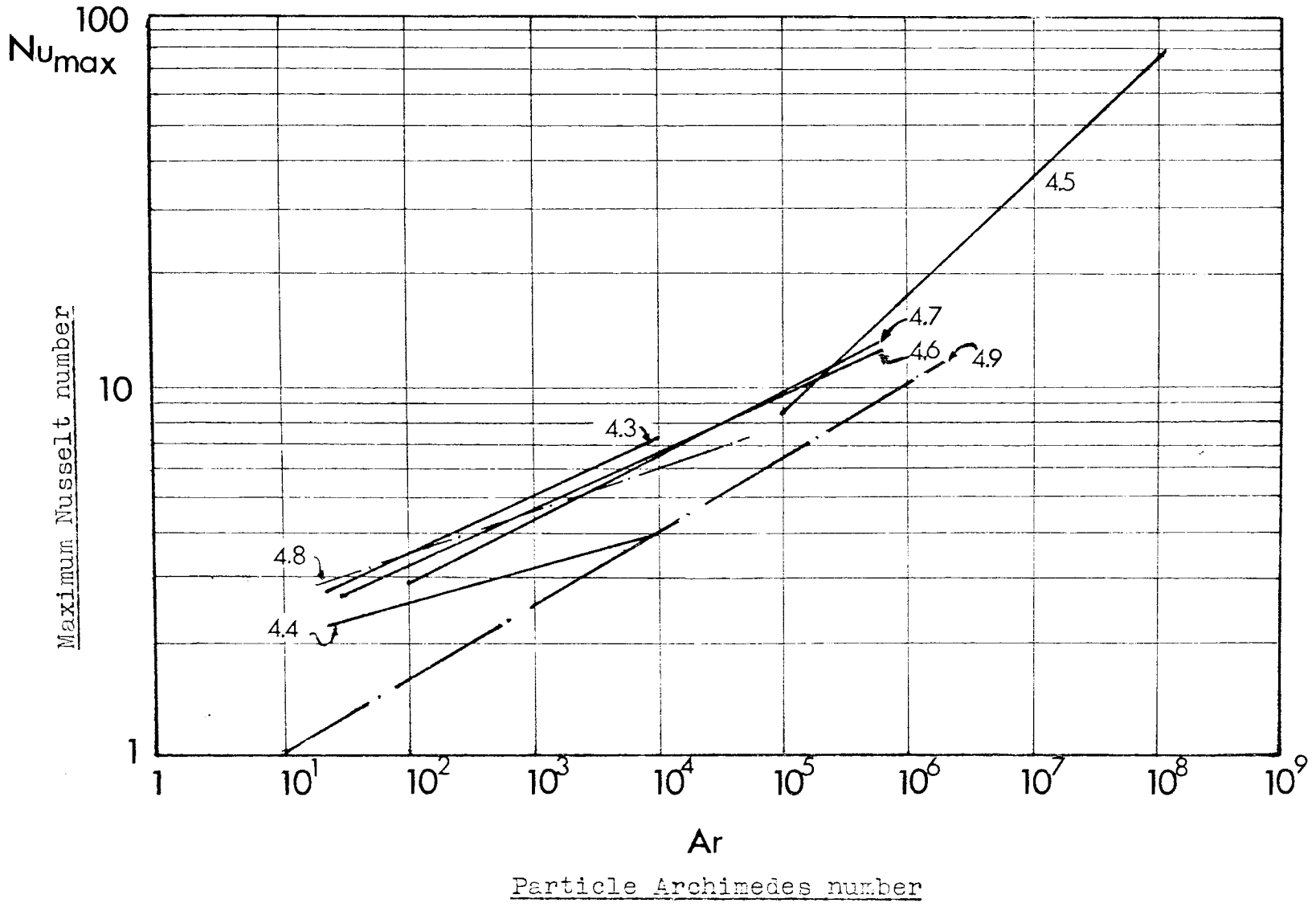


Fig. 4.2 Heat transfer correlations

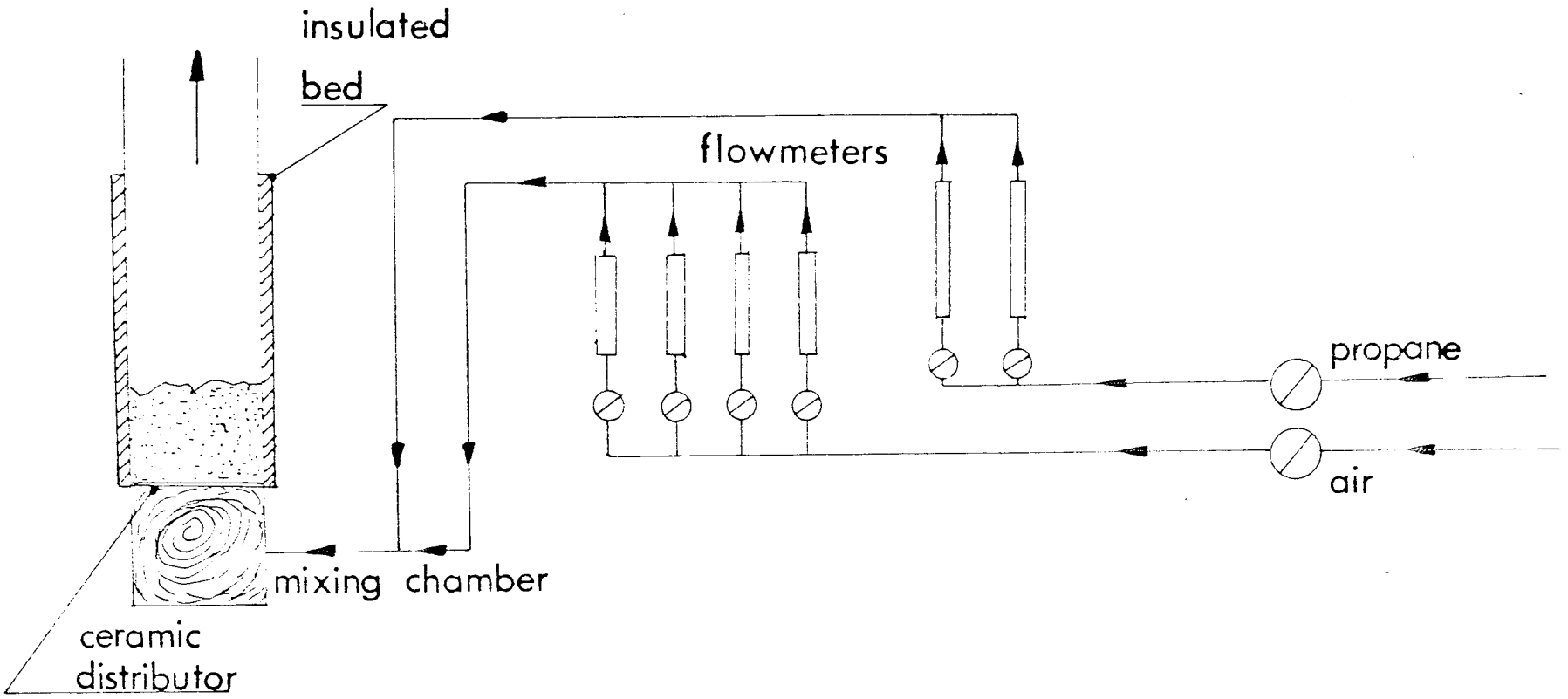


Fig. 4.3 Schematic layout of the experimental apparatus

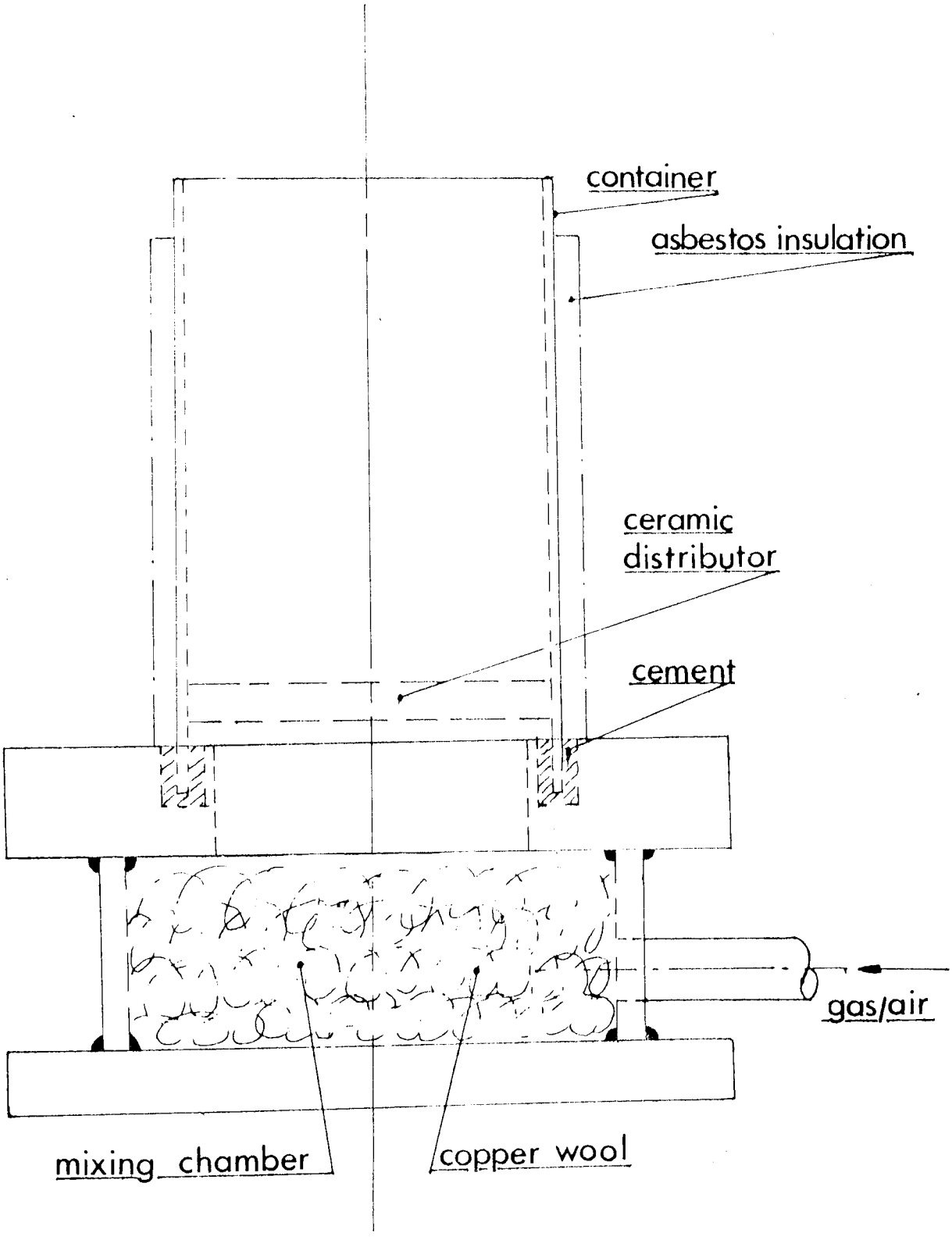


Fig. 4.4 Combustor design

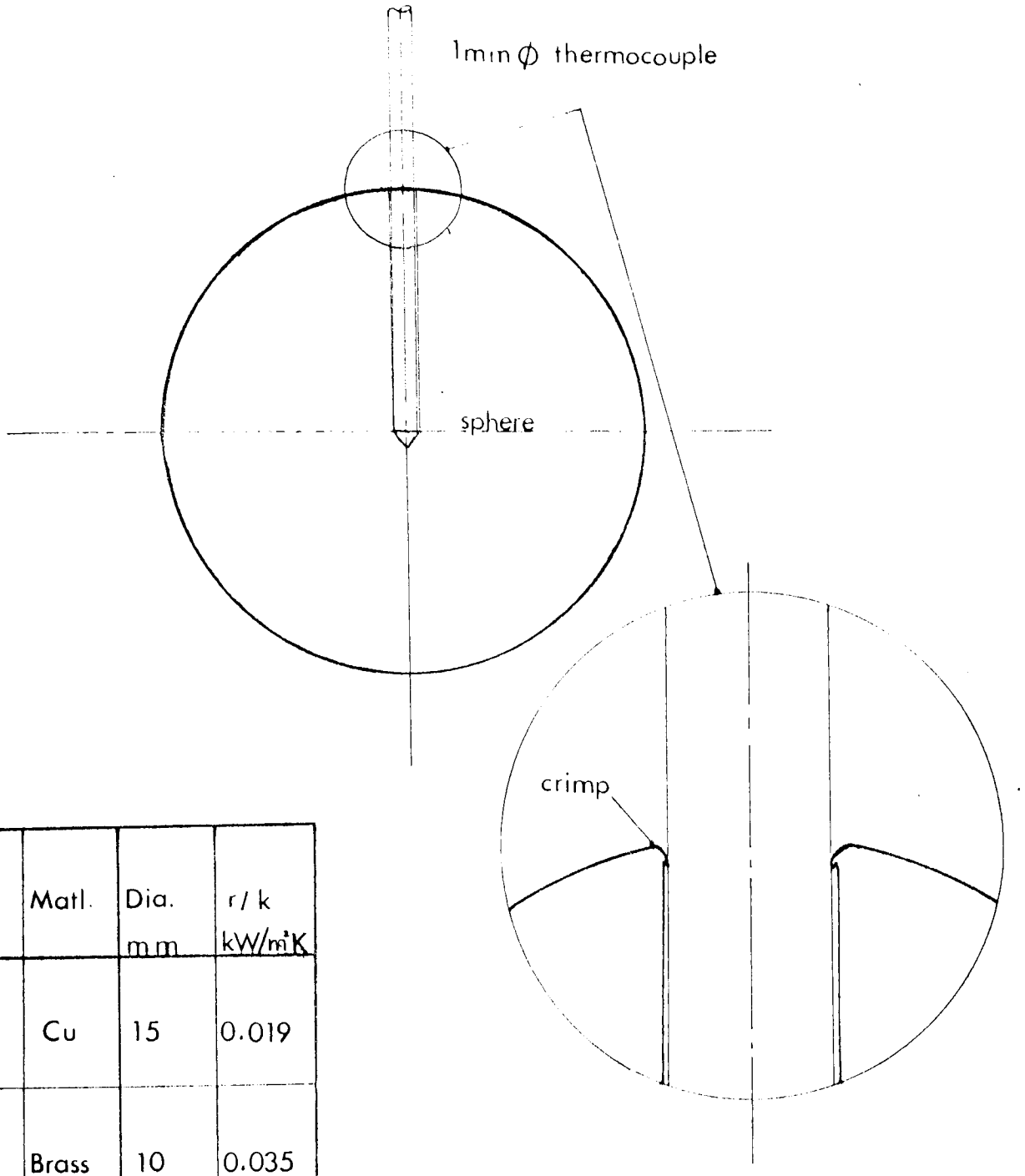


| No. | Matl. | Dia. mm | r / k kW/m²K |
|---|---|---|---|
| 1 | Cu | 15 | 0.019 |
| 2 | Brass | 10 | 0.035 |
| 3 | Steel | 5 | 0.036 |
| 4 | Cu | 6 | 0.008 |

Fig. 4.5 Probe details

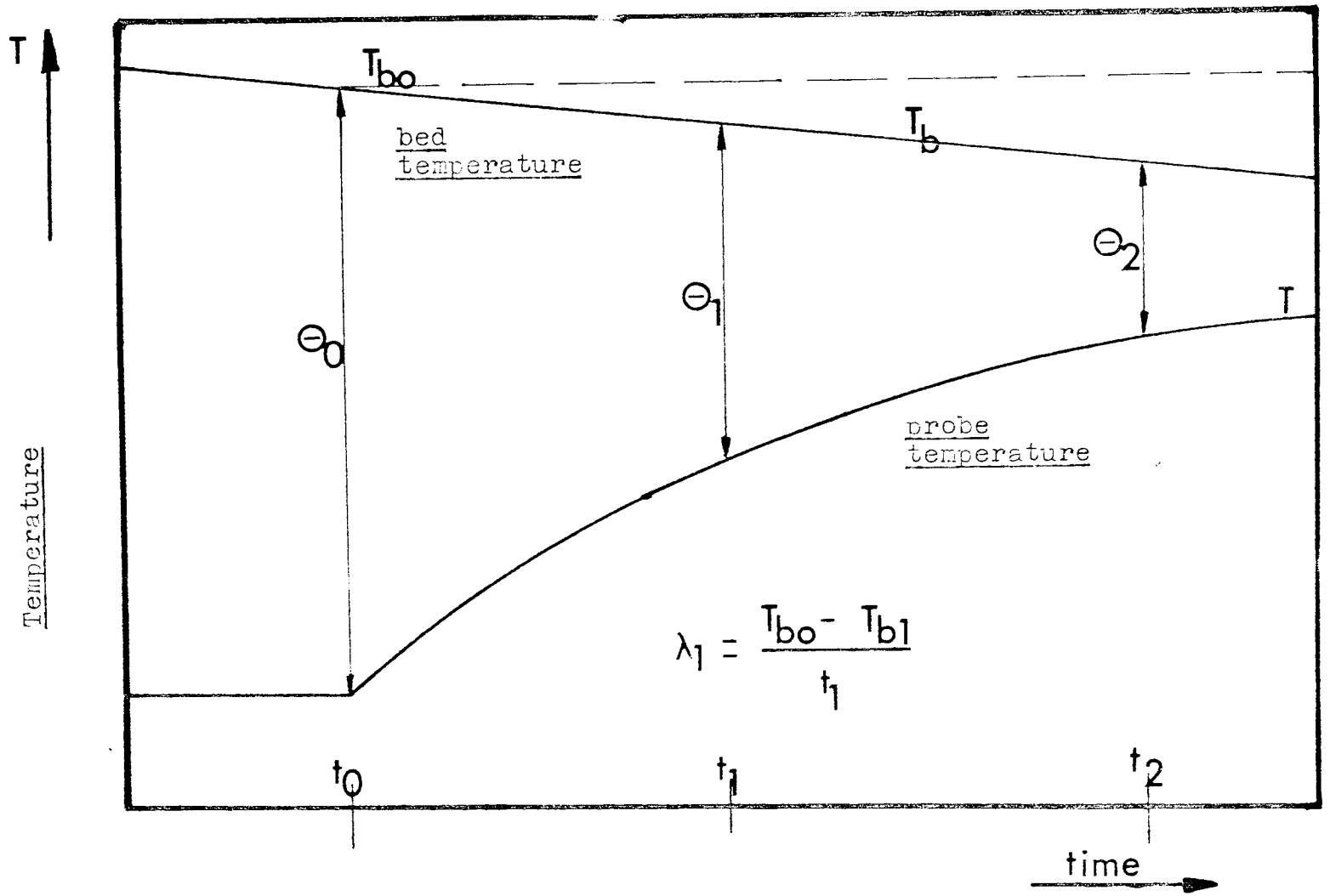


Fig.4.6 A typical experimental trace

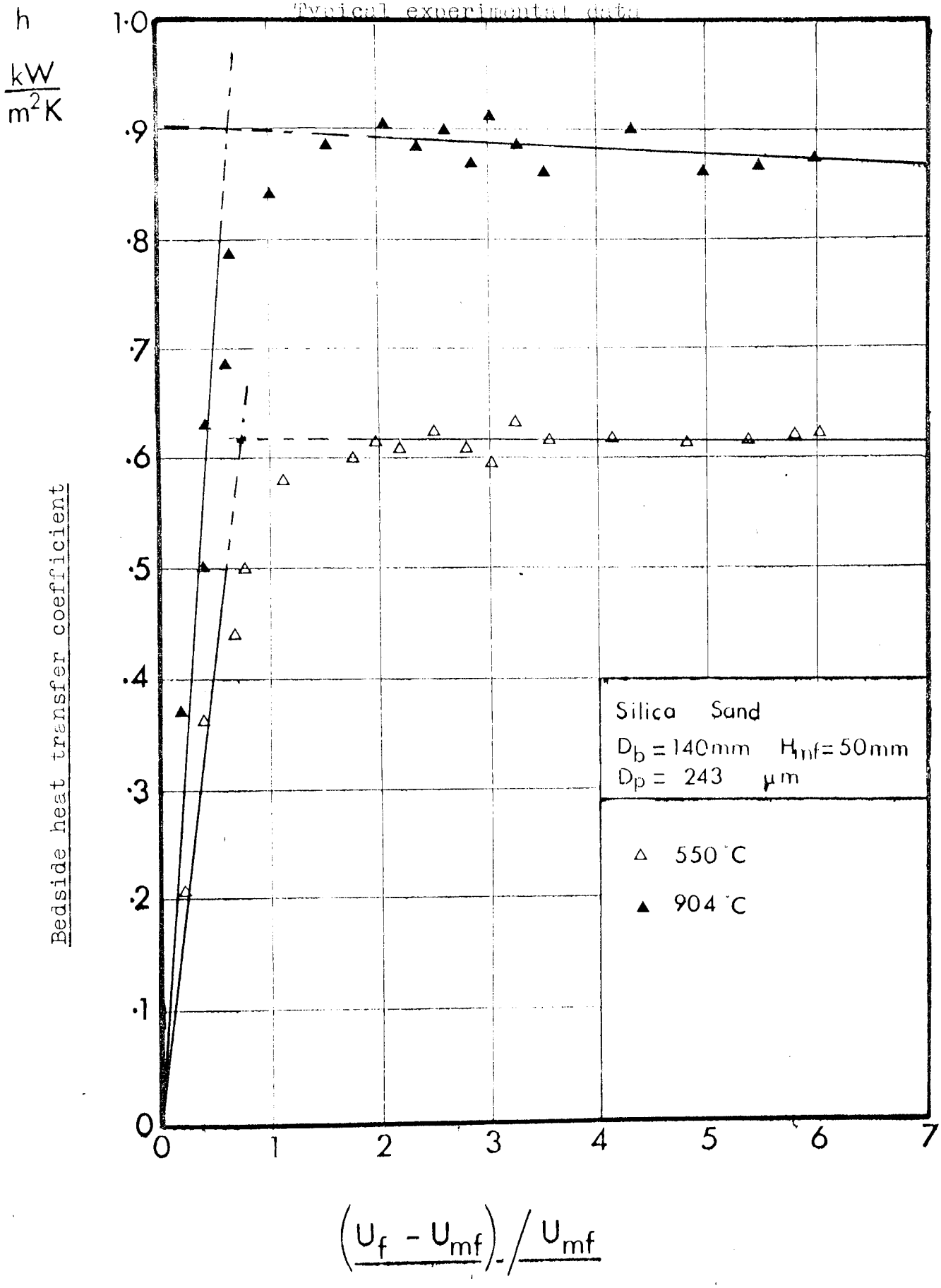


Fig. 4.7 Heat transfer data

Typical experimental data

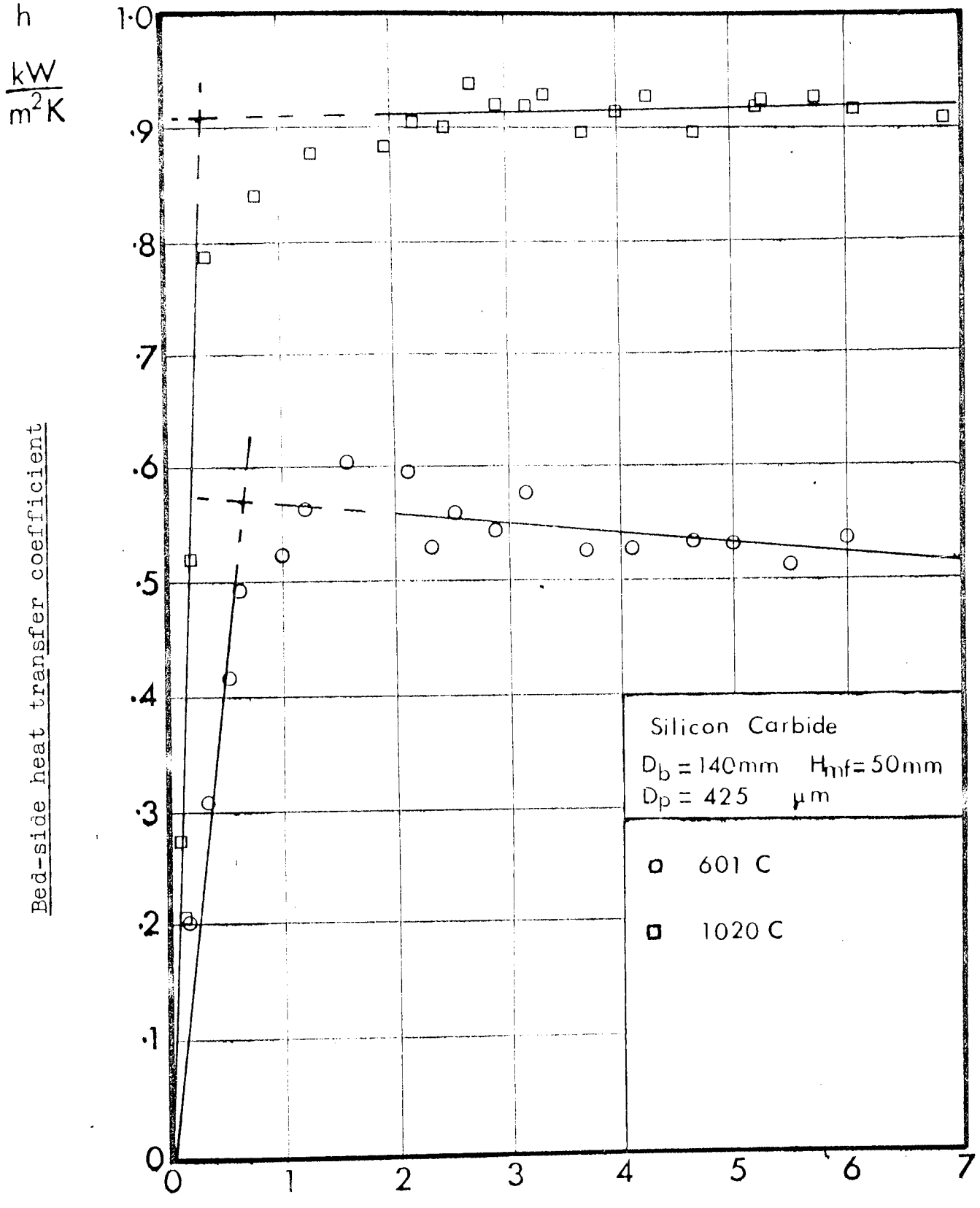


Fig. 4.8 Heat transfer data

Typical experimental data

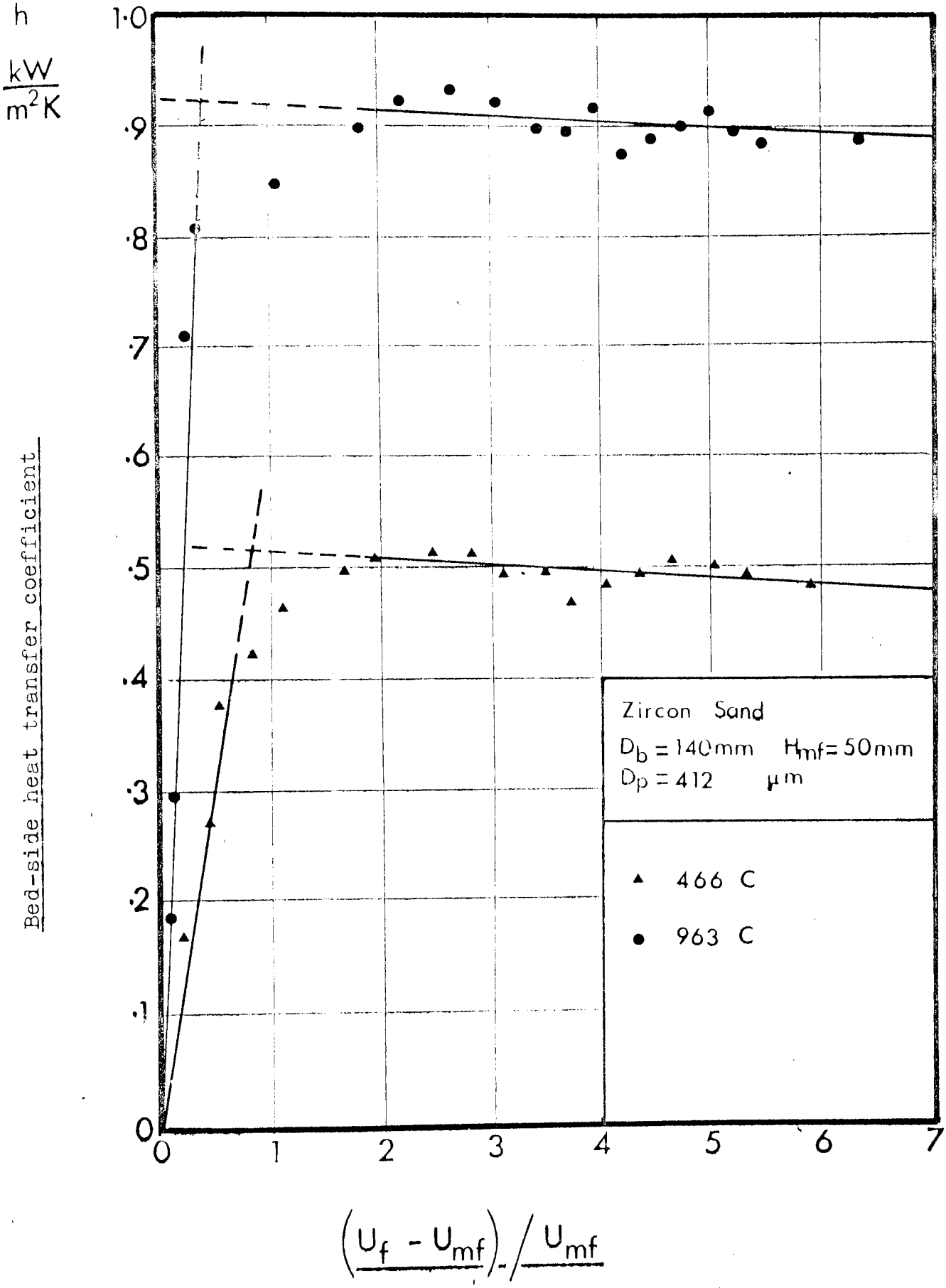


Fig. 4.9 Heat transfer data

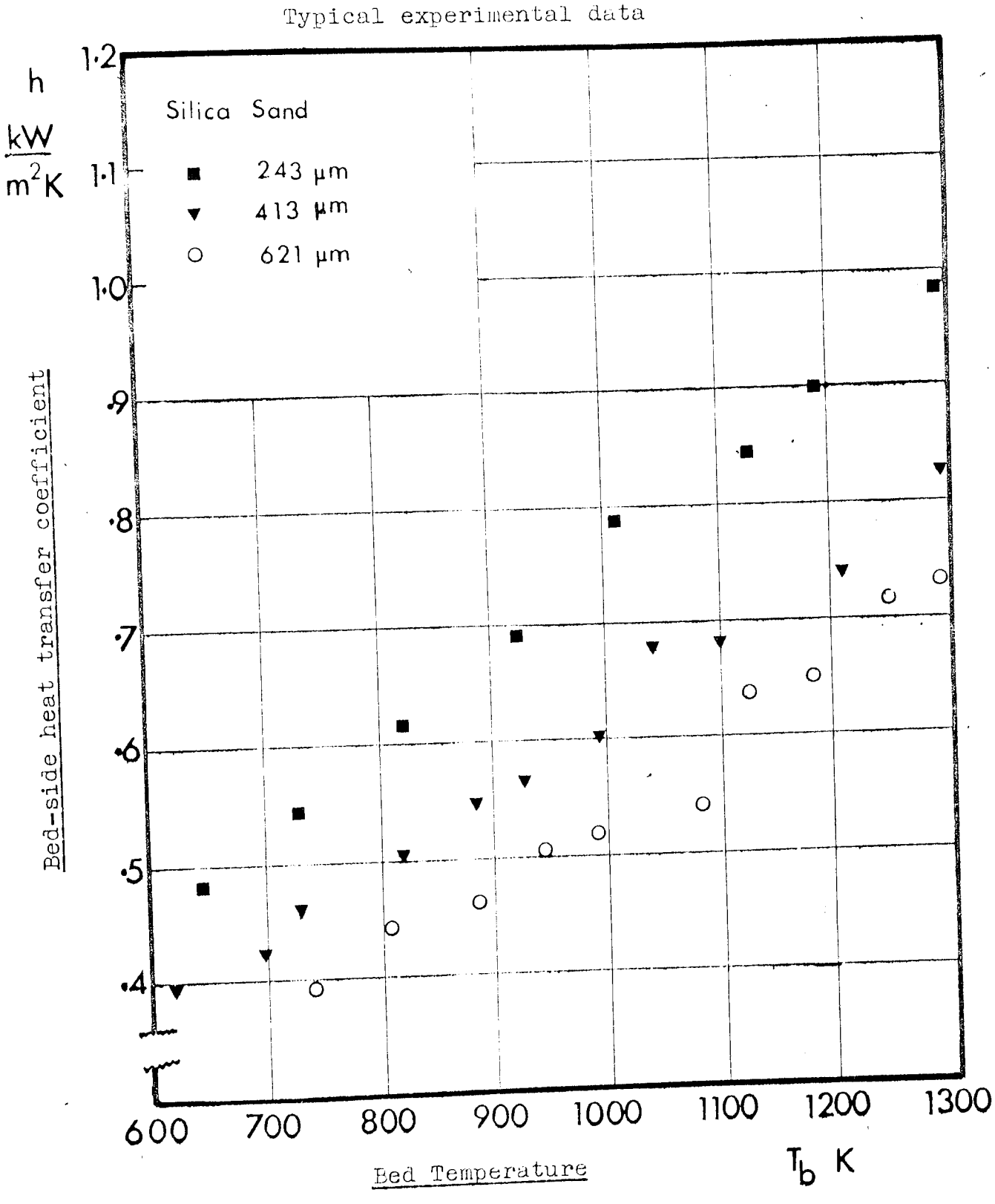


Fig 4.10 Temperature dependance of heat transfer coefficients.

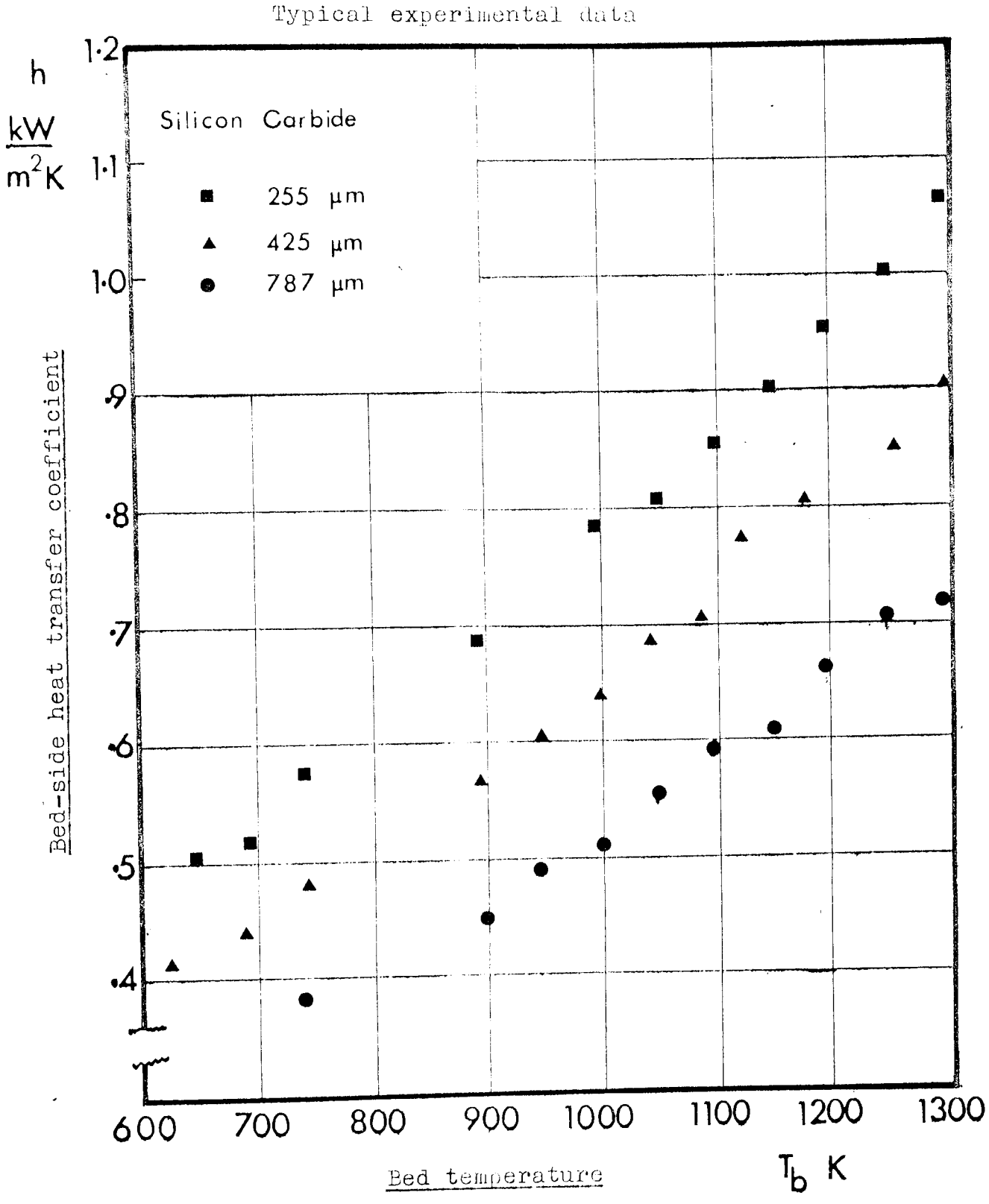


Fig. 4.11 Temperature dependance of heat transfer coefficients

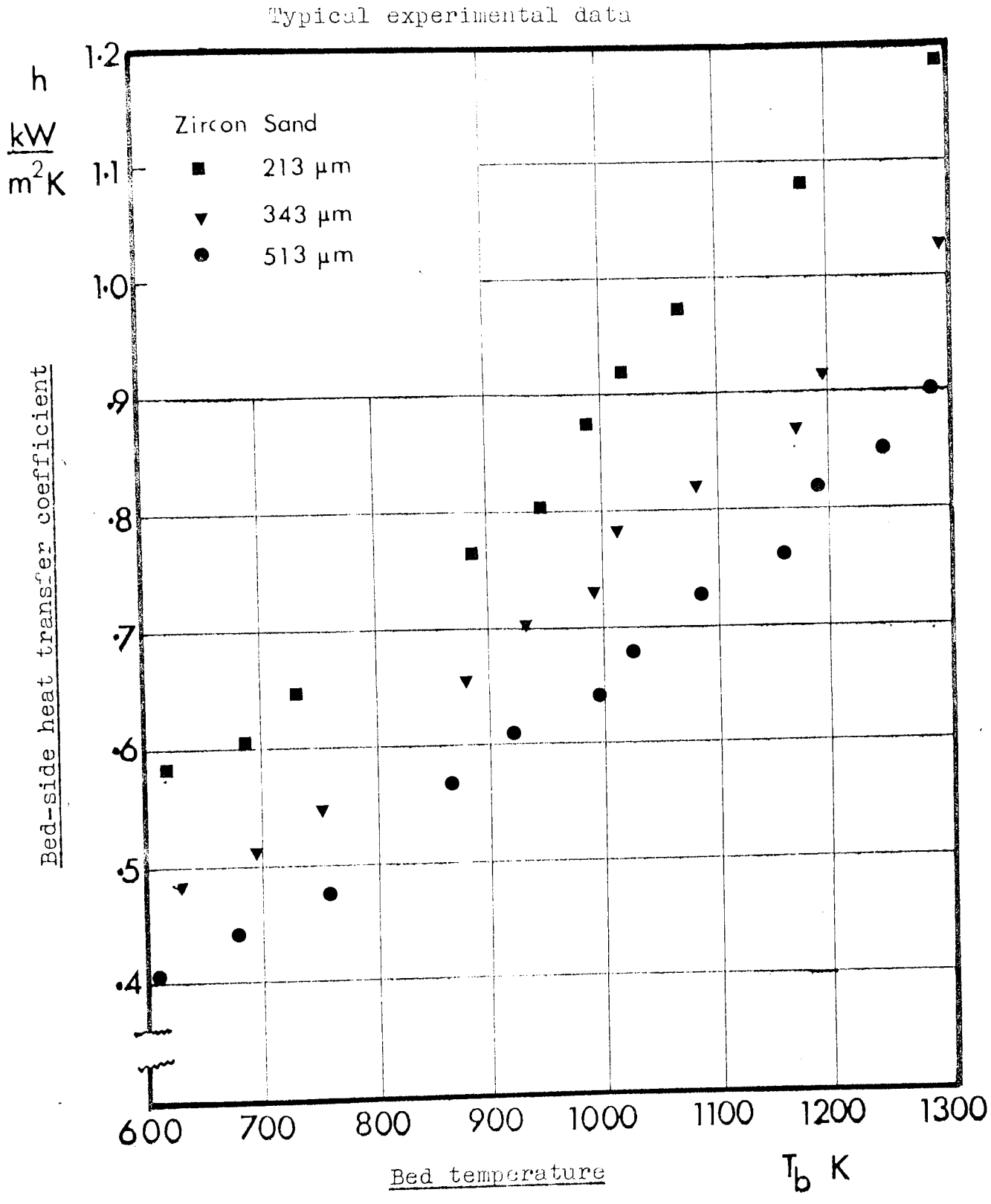


Fig.4.12 Temperature dependance of heat transfer coefficients.

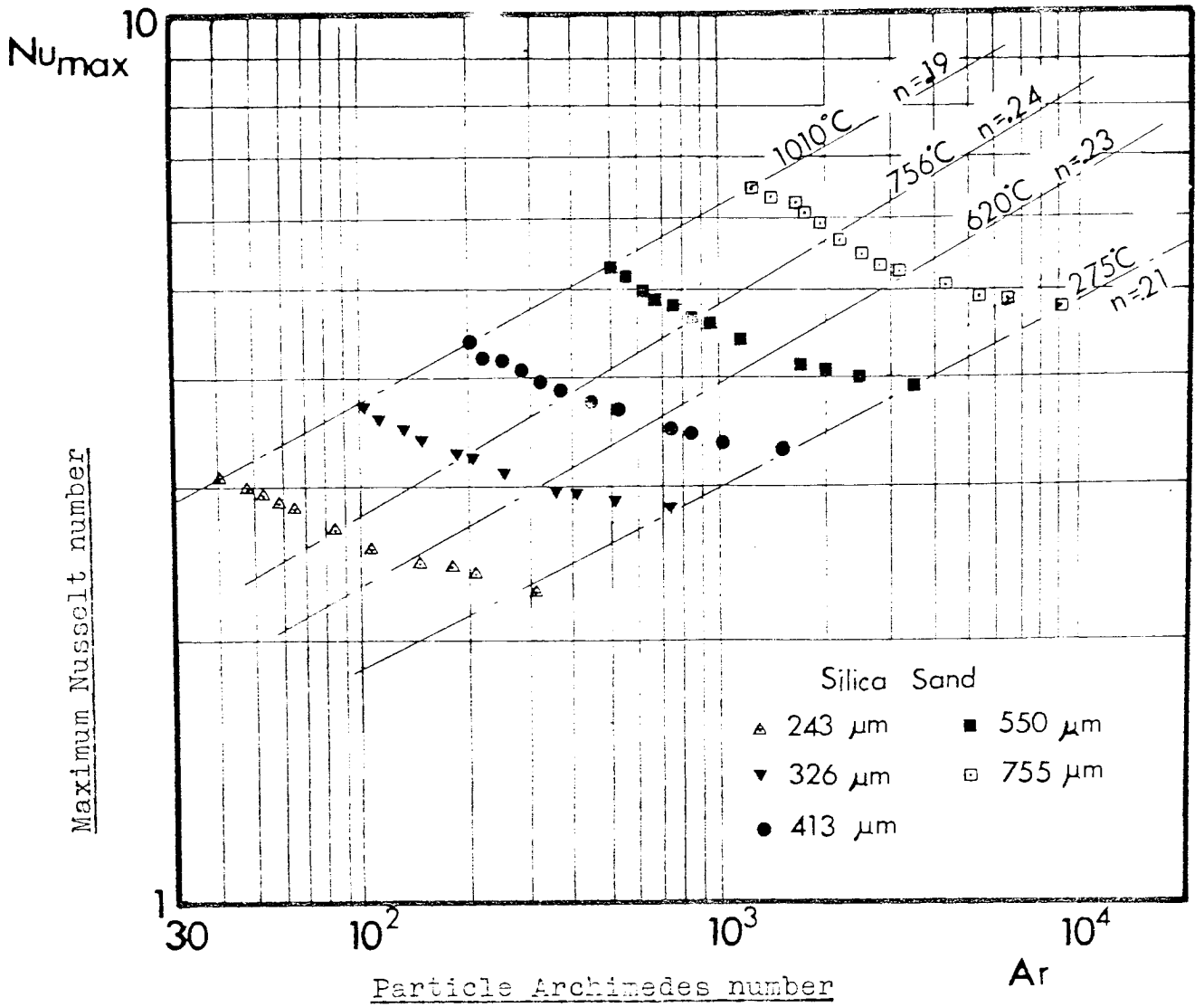


Fig. 4.13 Derived data

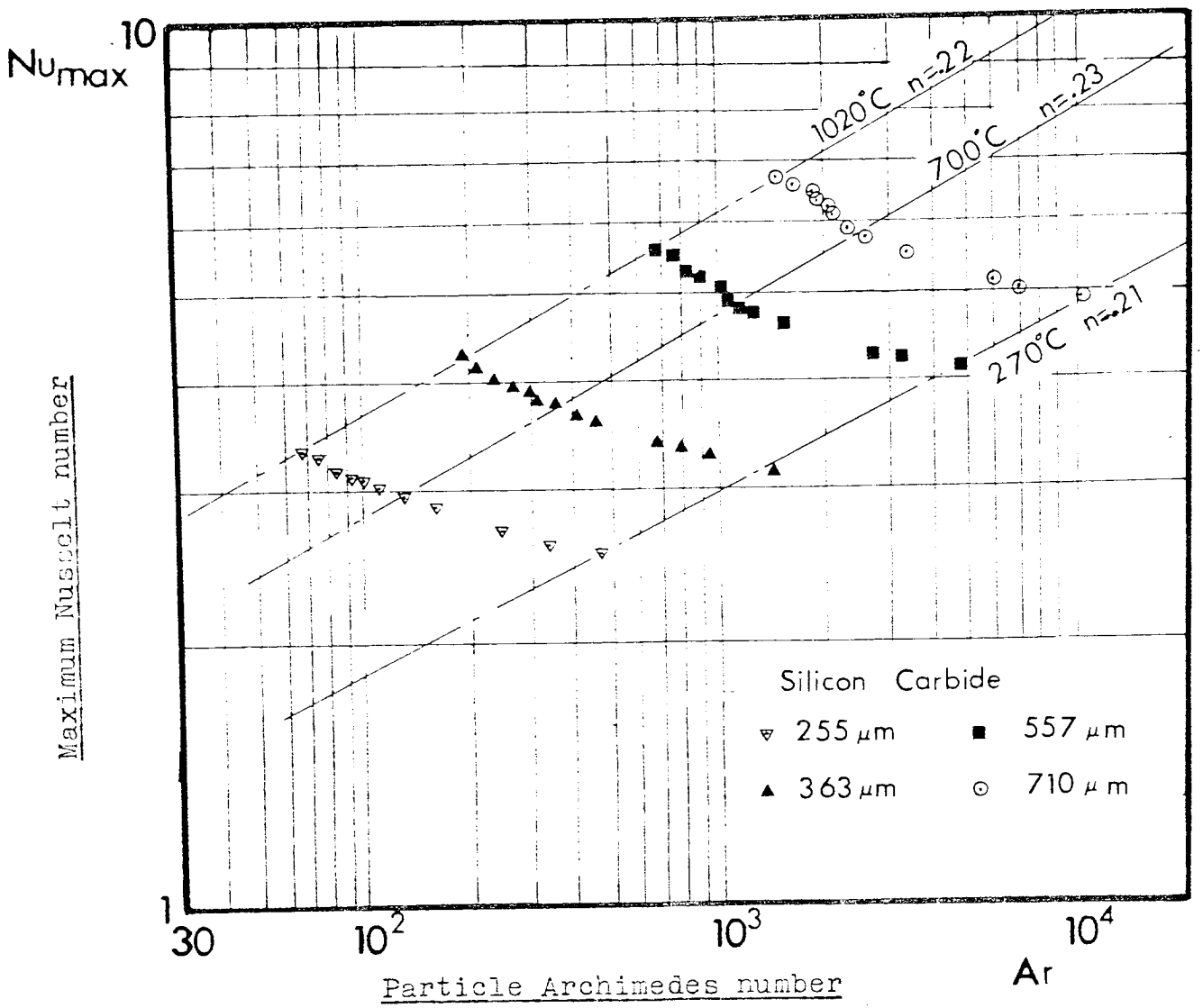


Fig. 4.14 Derived data

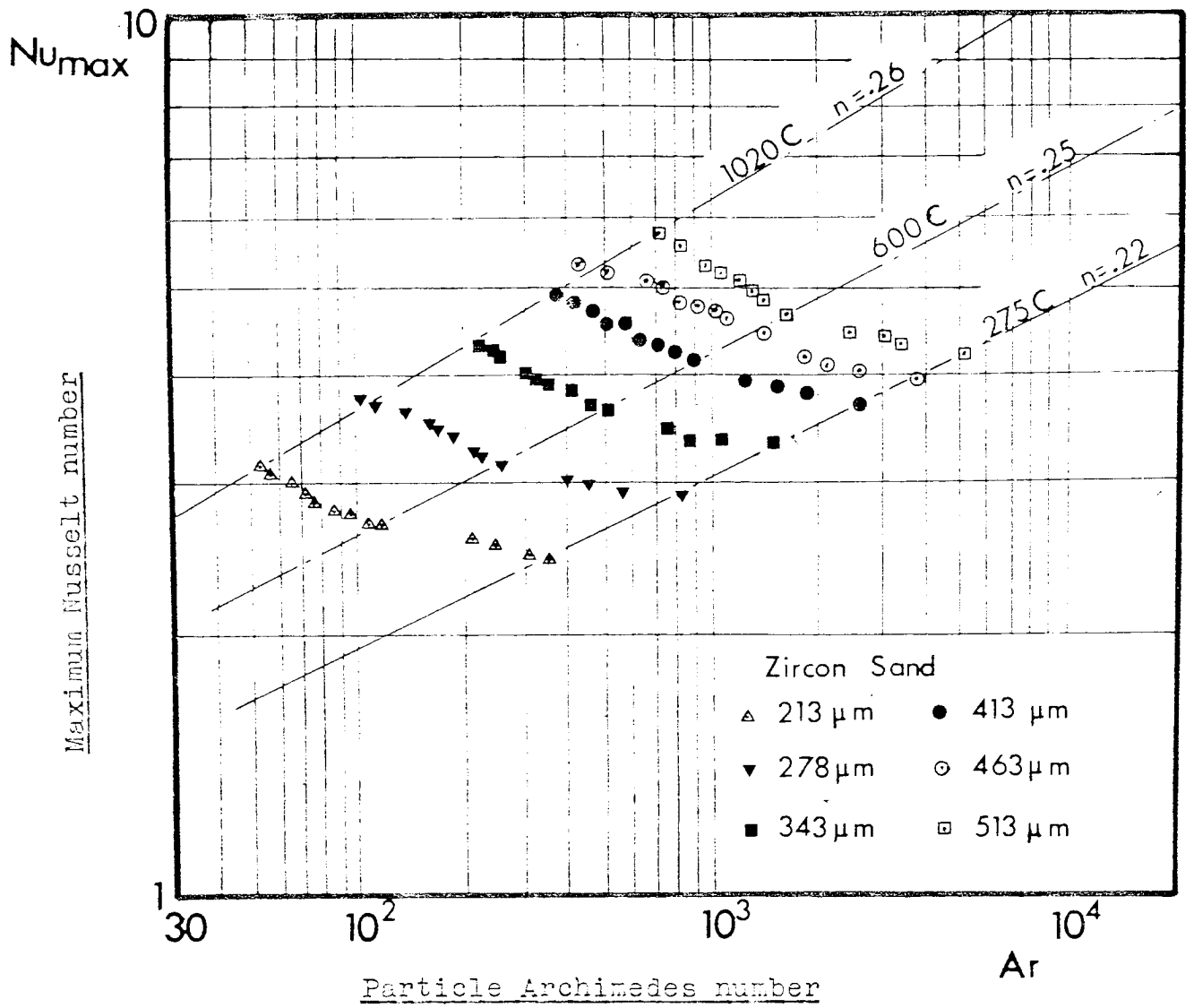


Fig. 4.15 Derived data

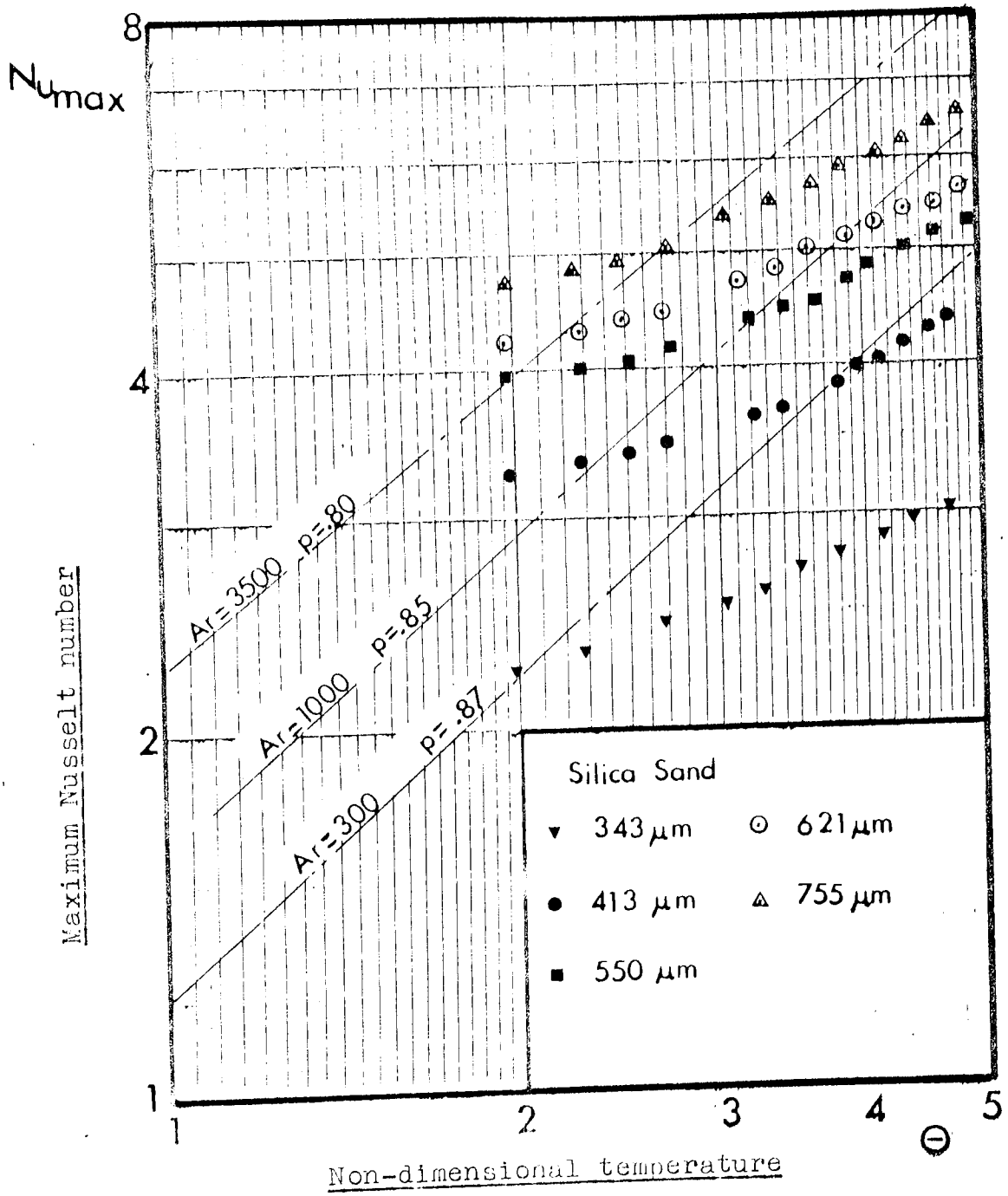


Fig. 4.16 Temperature regression

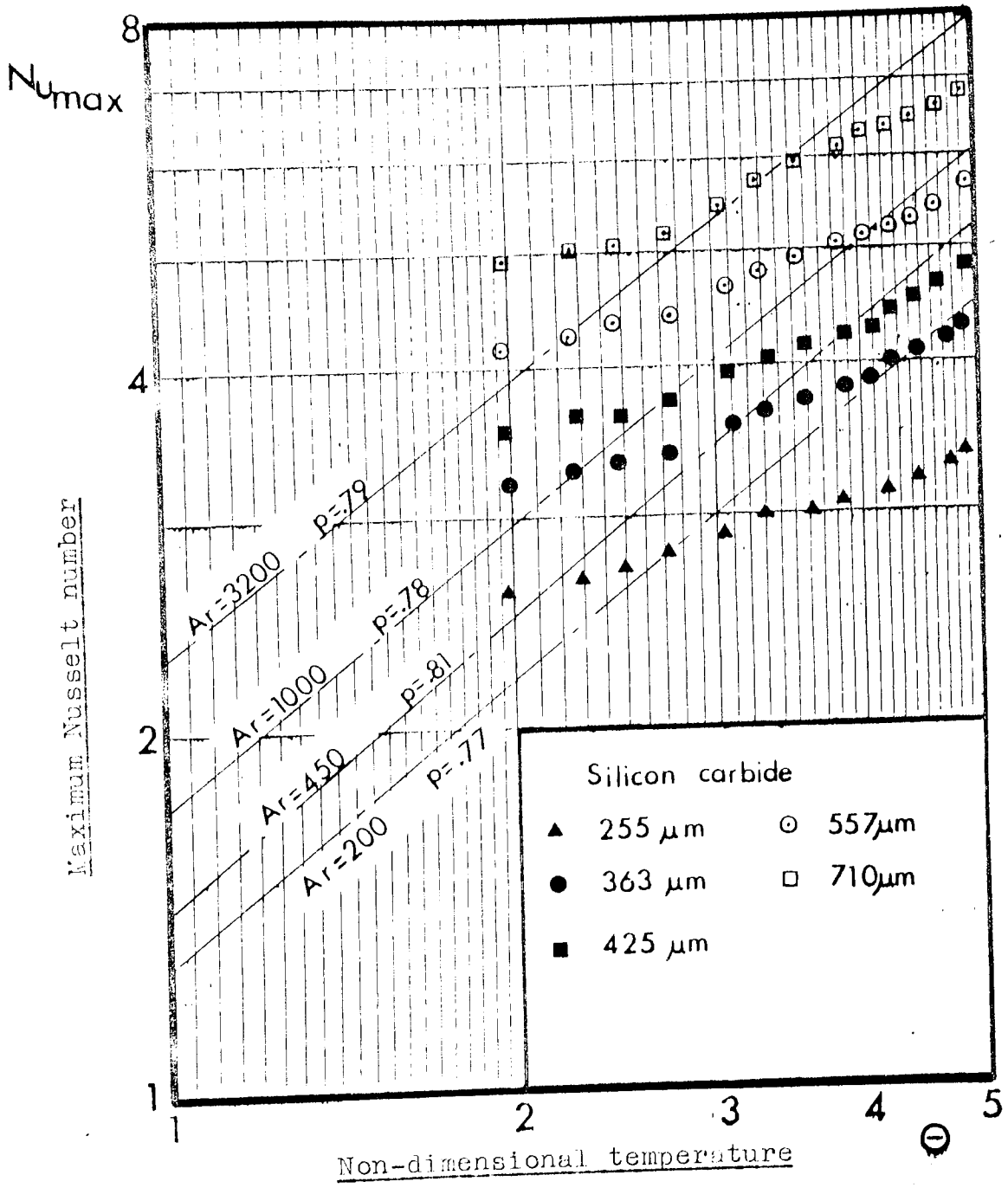


Fig. 4.17 Temperature regression

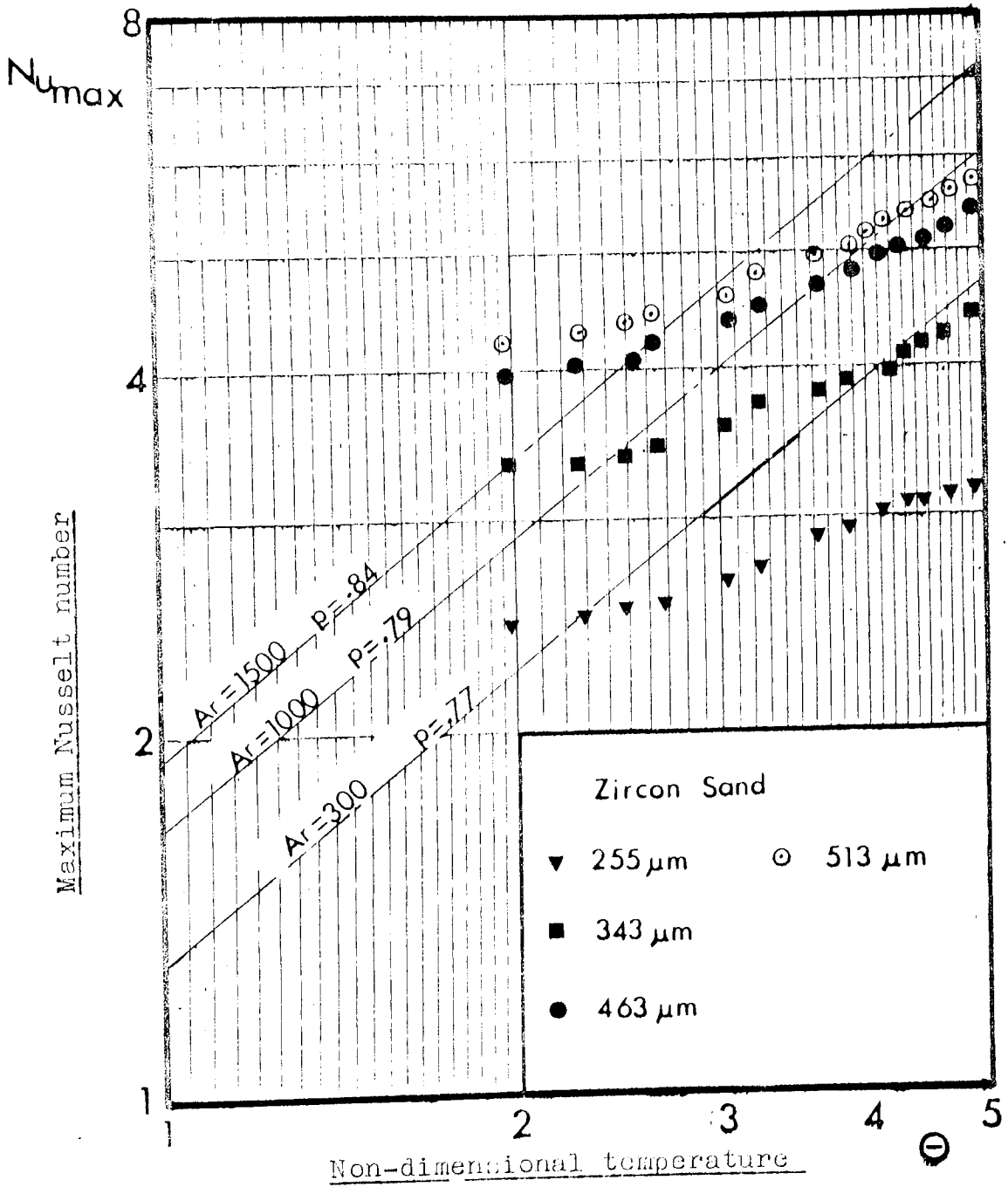


Fig. 4.18 Temperature regression

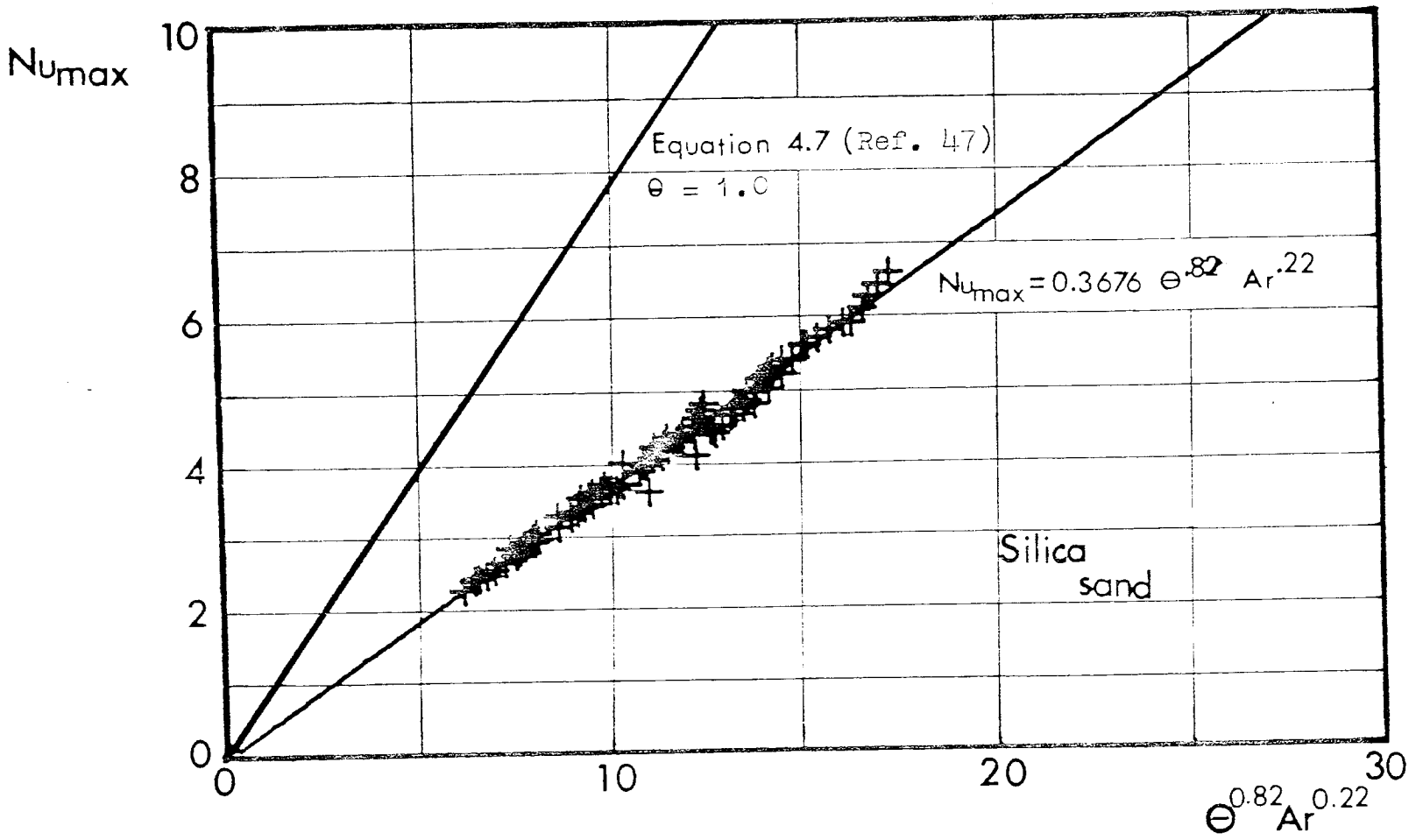


Fig. 4.19 Heat transfer correlation

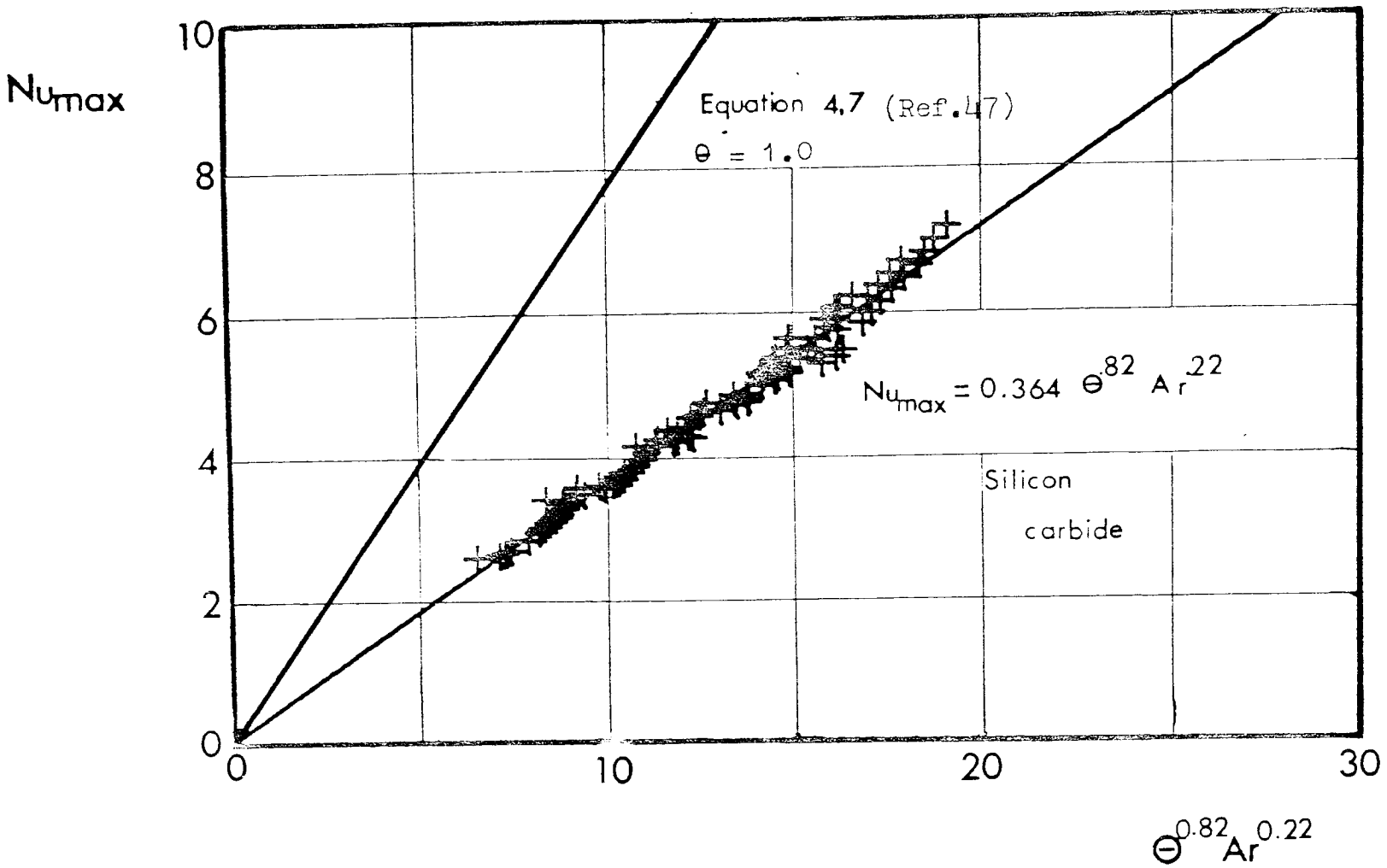


Fig. 4.20 Heat transfer correlation

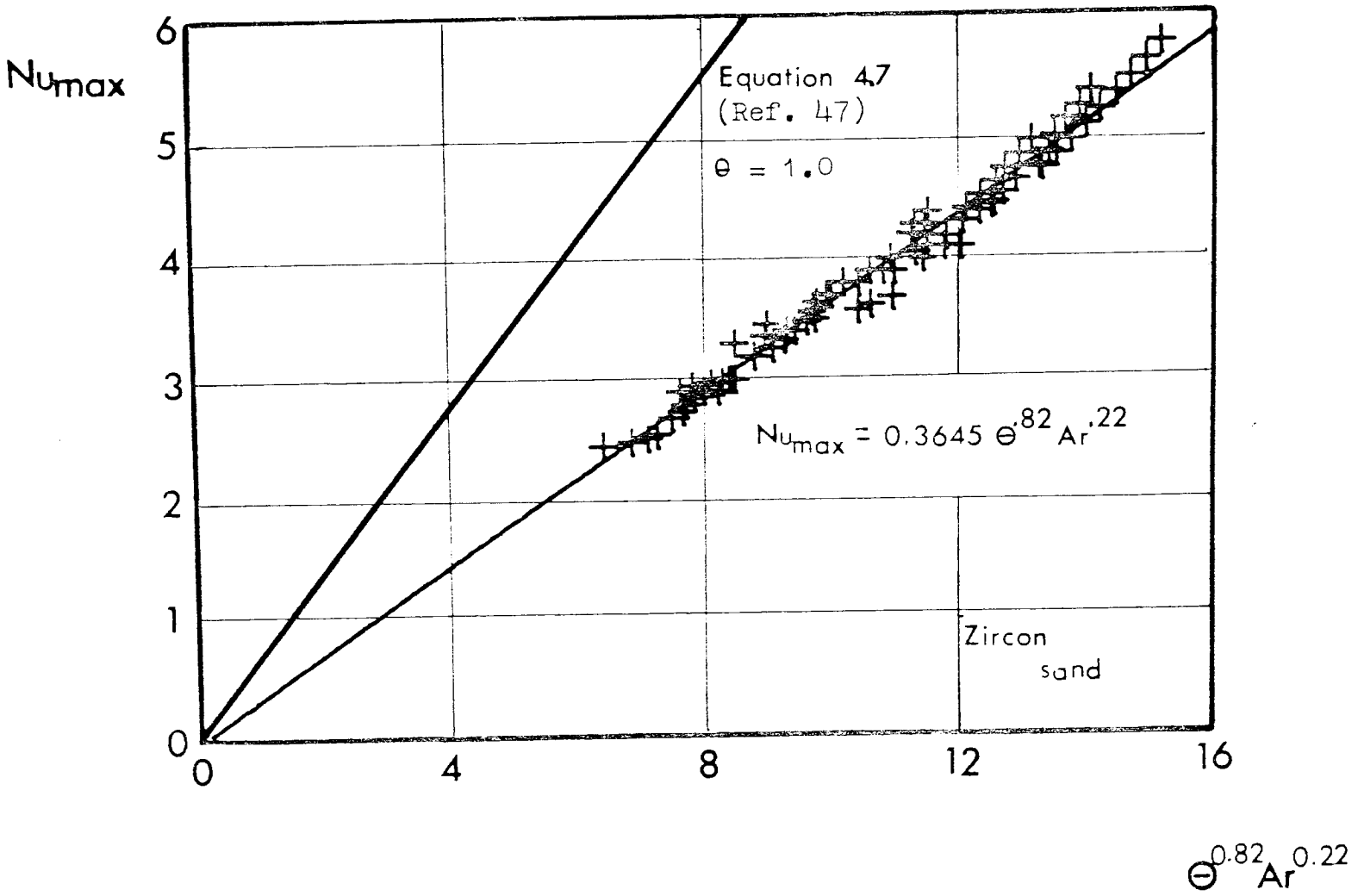


Fig. 4.21 Heat transfer correlation

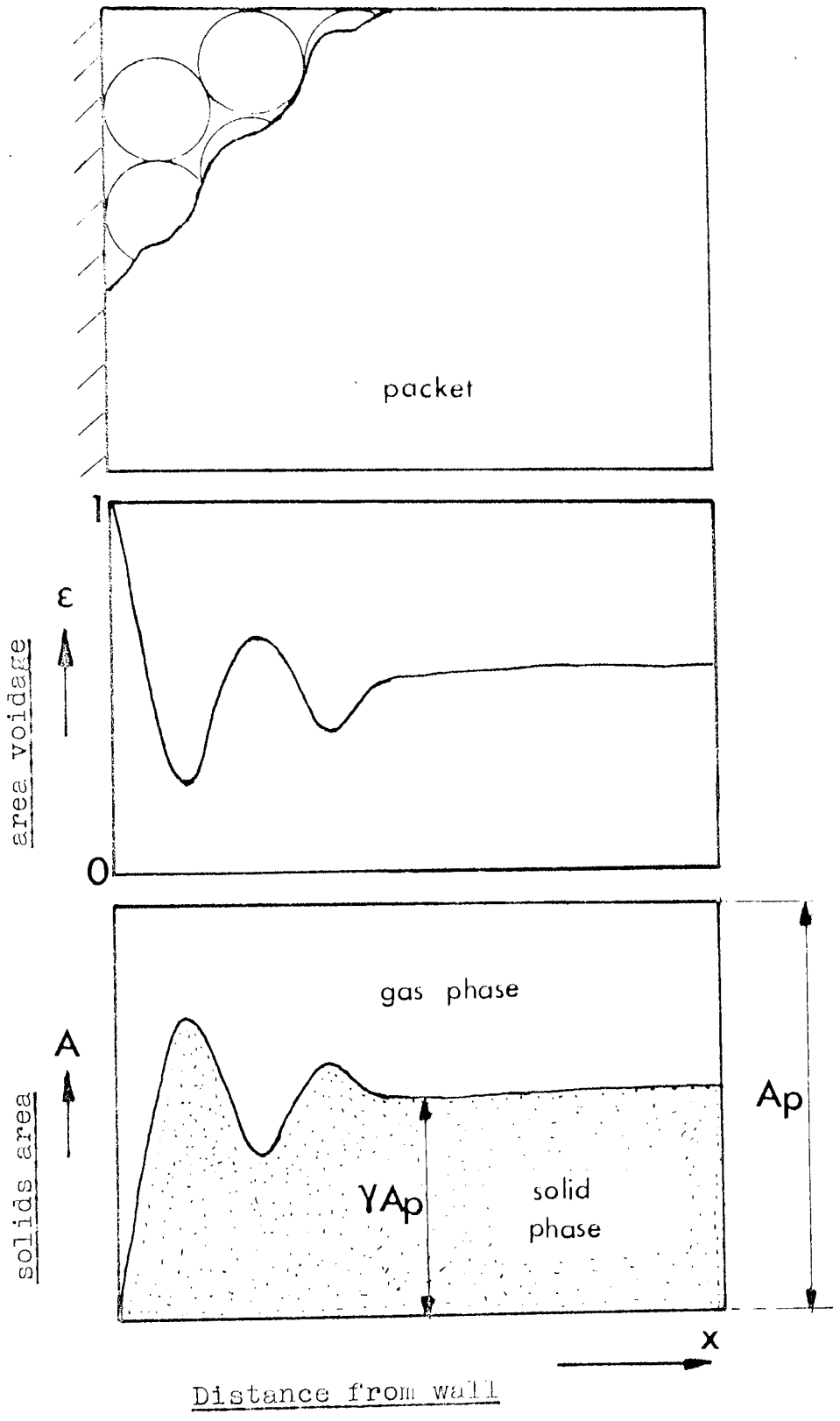


Fig. 4.22 The packet concept

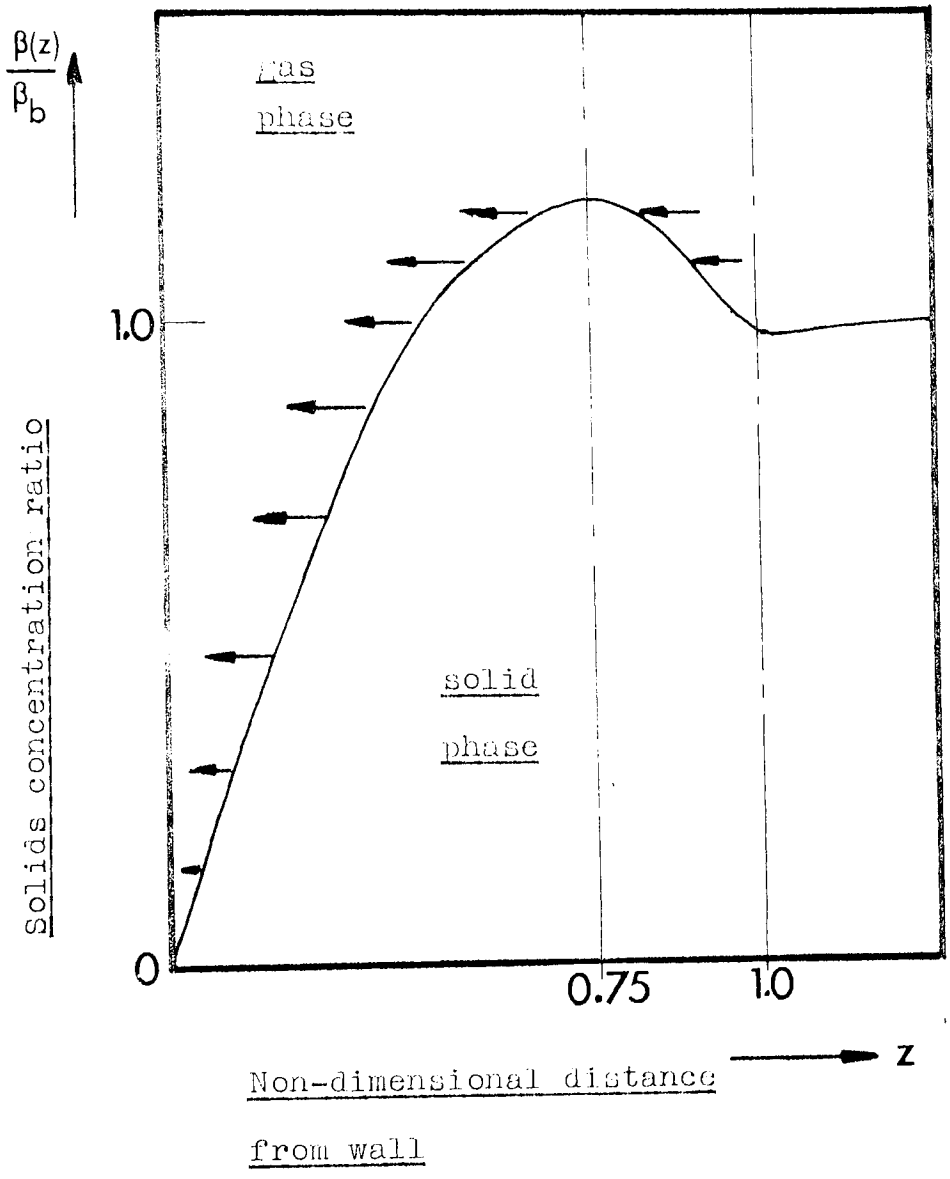


Fig. 4. 23 Radiative regions

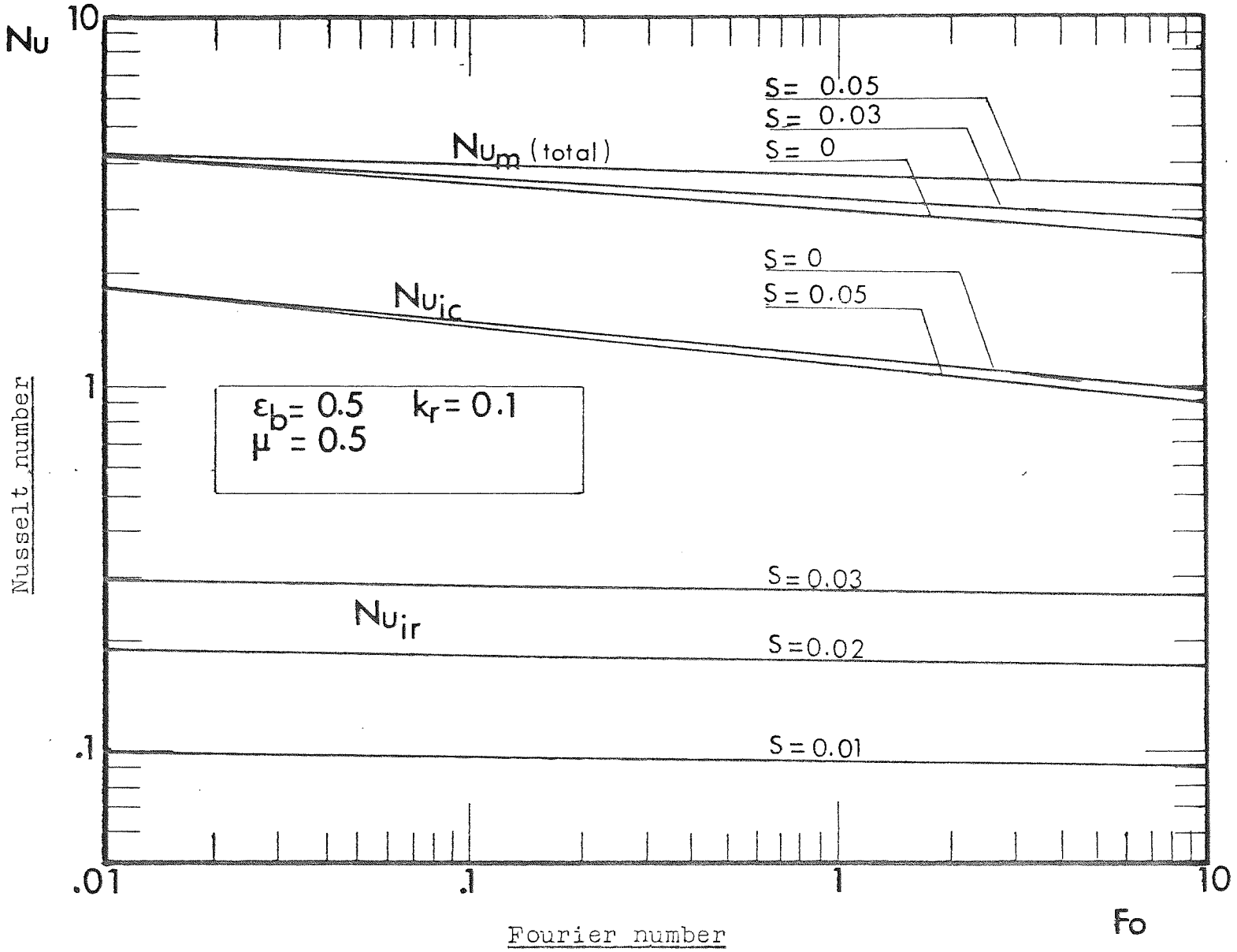


Fig. 4.24 Typical model solutions

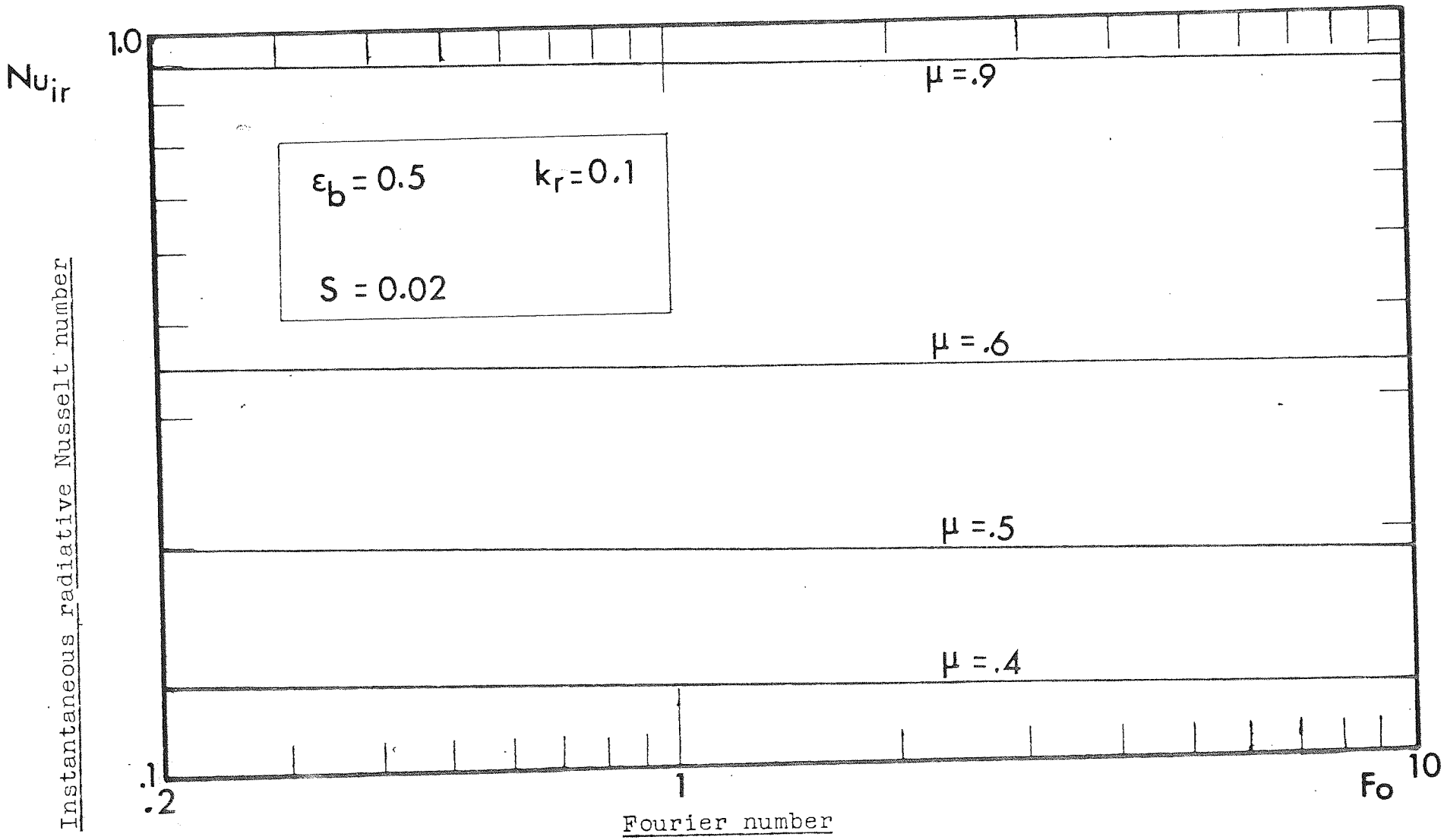


Fig. 4.25 Effect of wall temperature on radiative flux

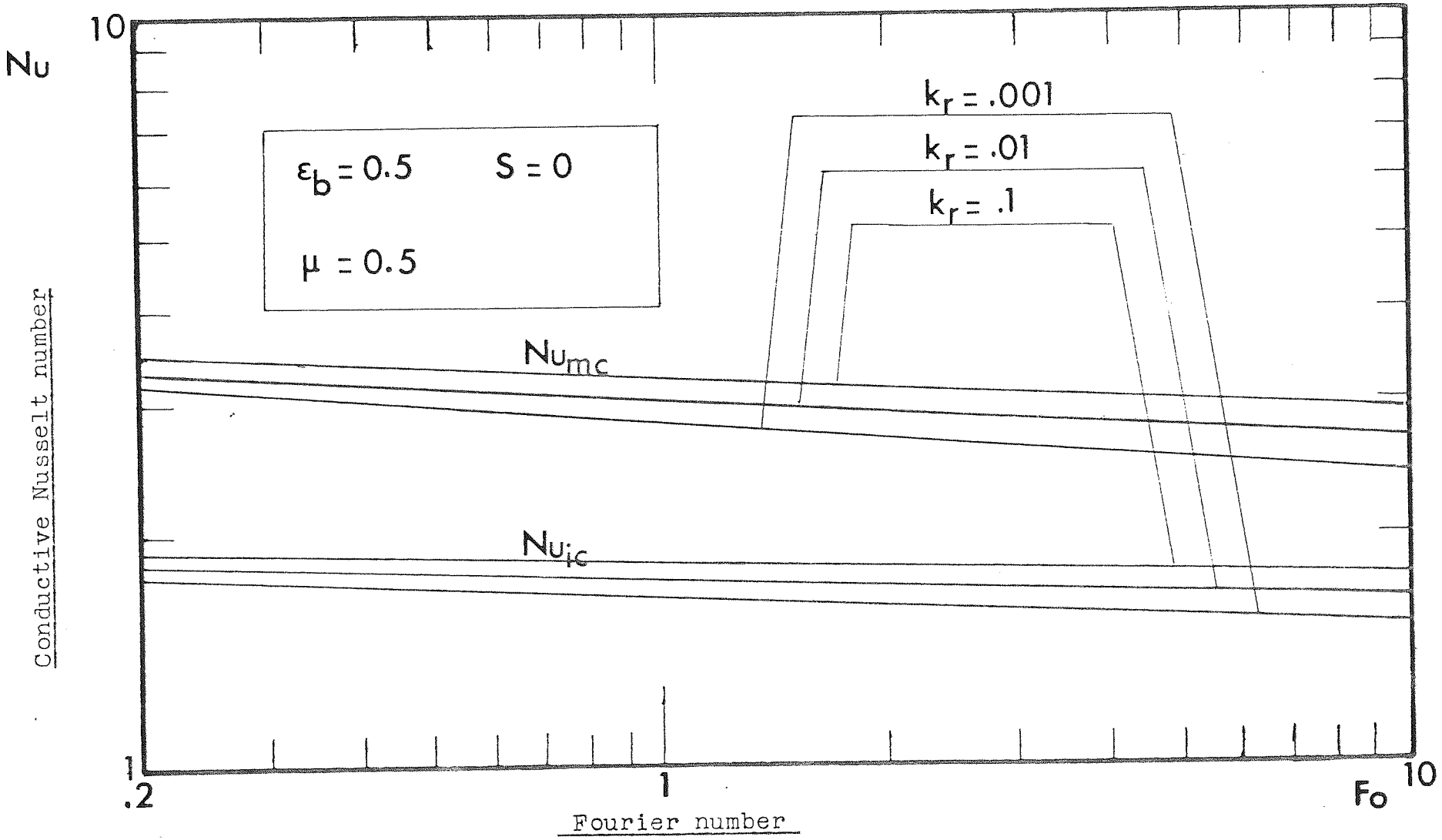


Fig 4.26 Effect of conductivity ratios

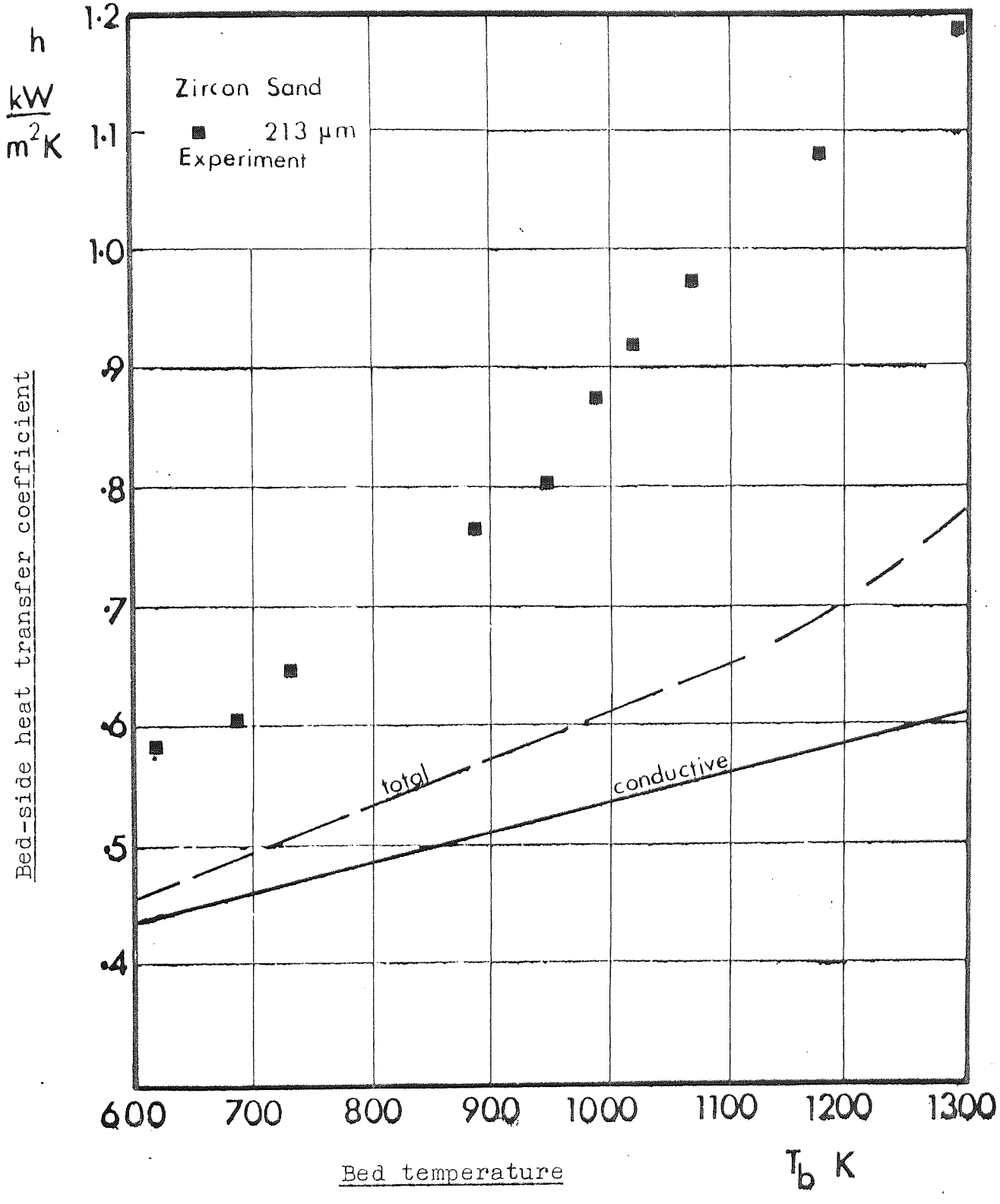


Fig. 427 Comparison of model with experiment

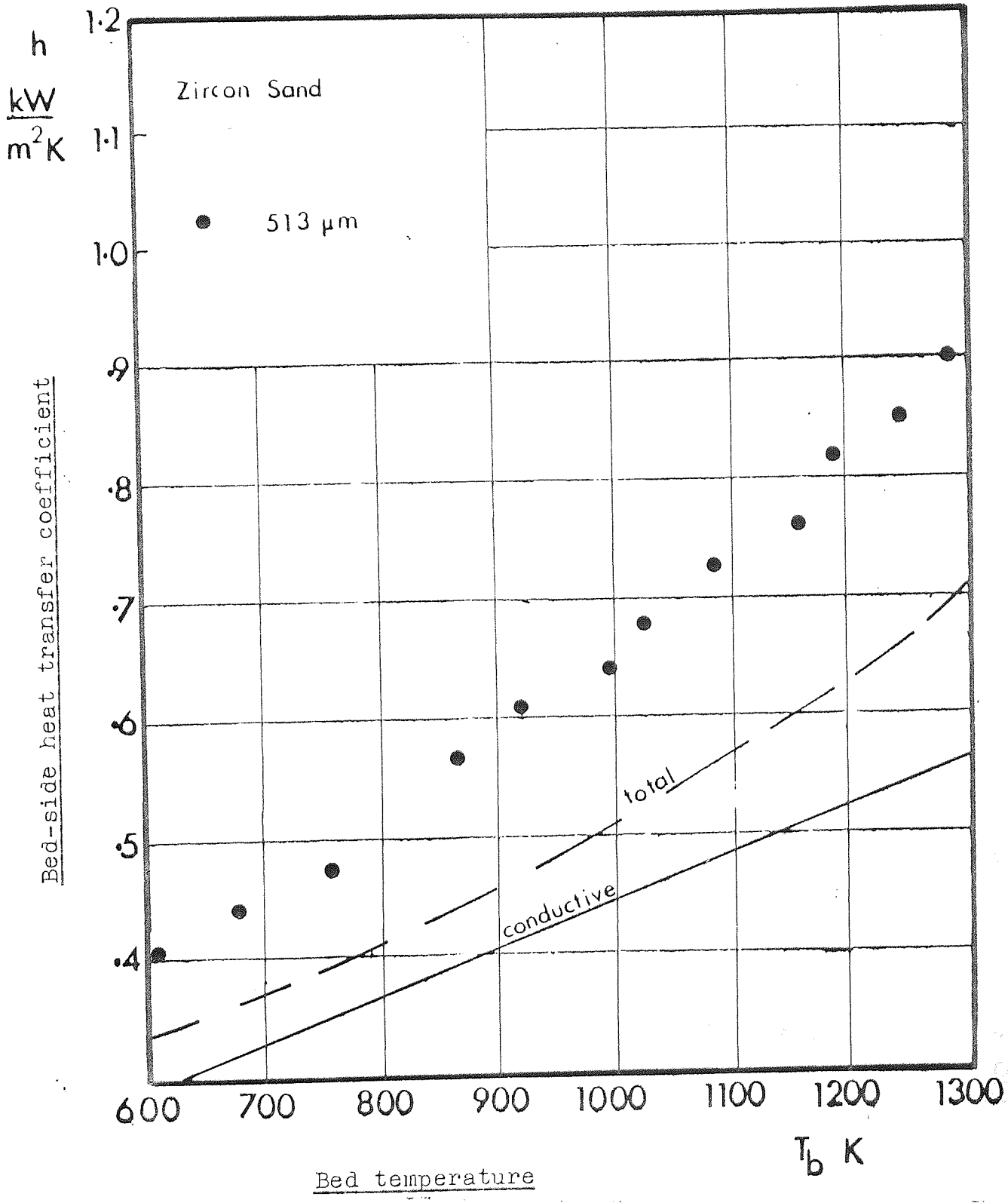


Fig. 428 Comparison of model with experiment

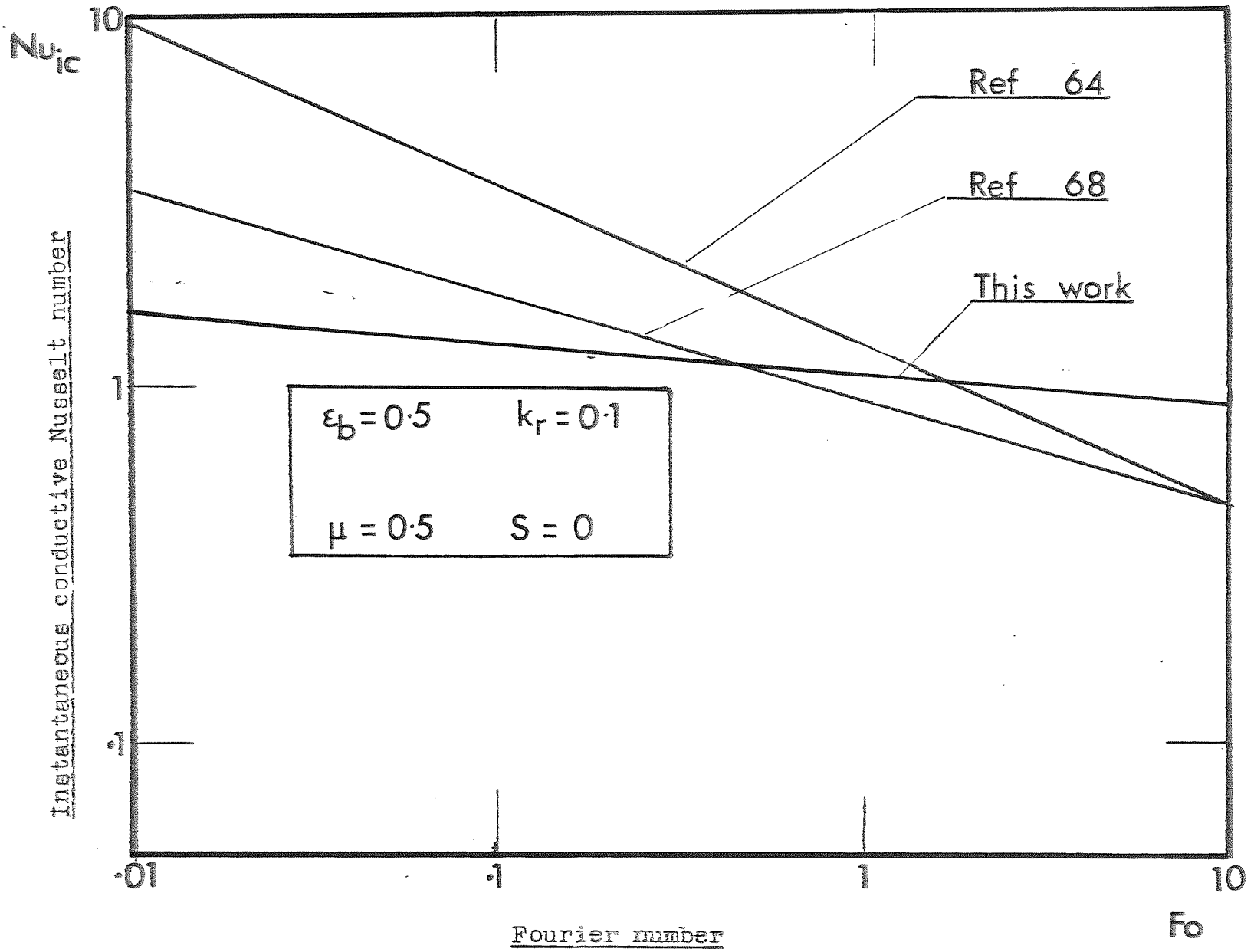


Fig 4.29 Comparison of models

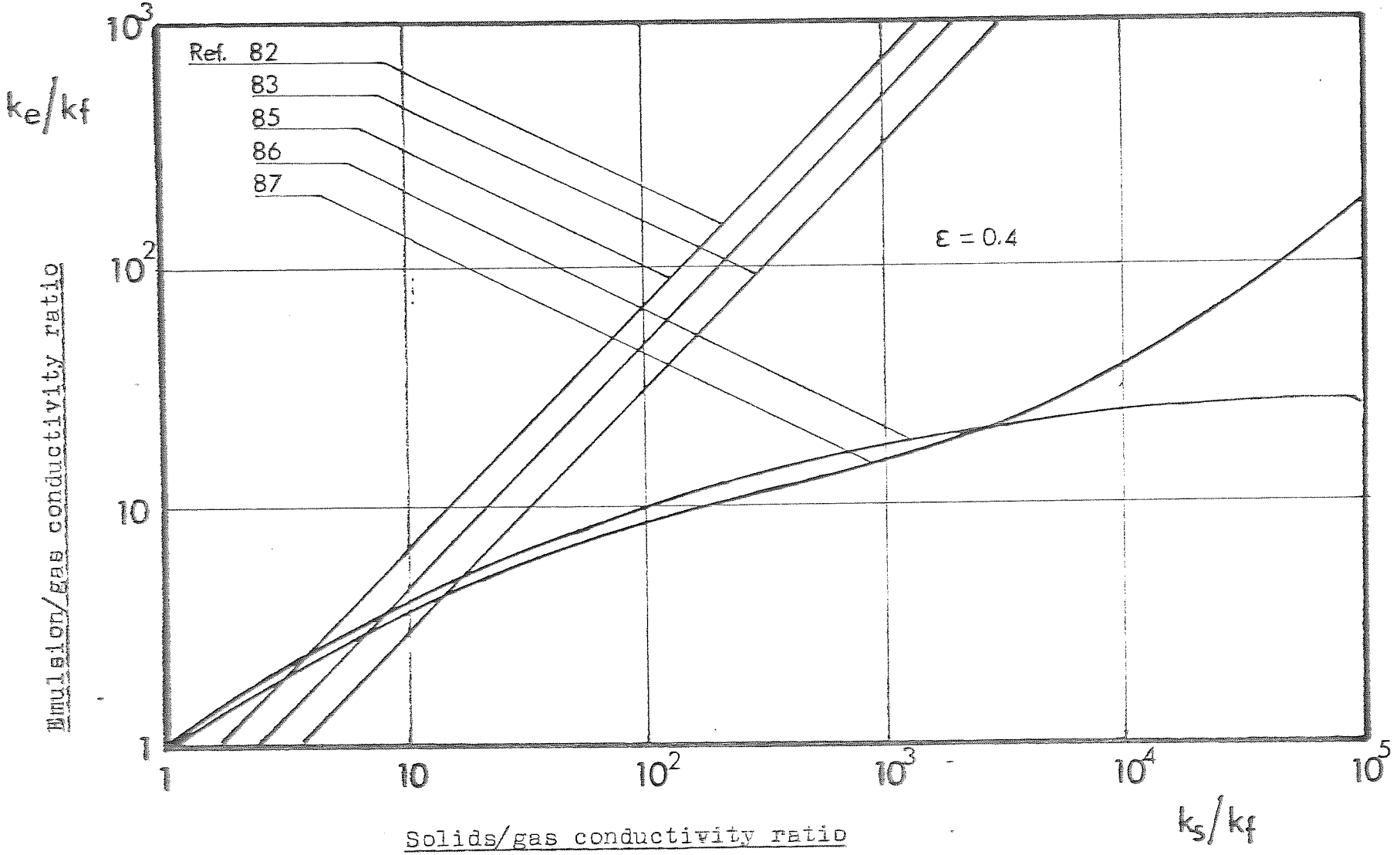


Fig.5.1 Conductivity of porous systems

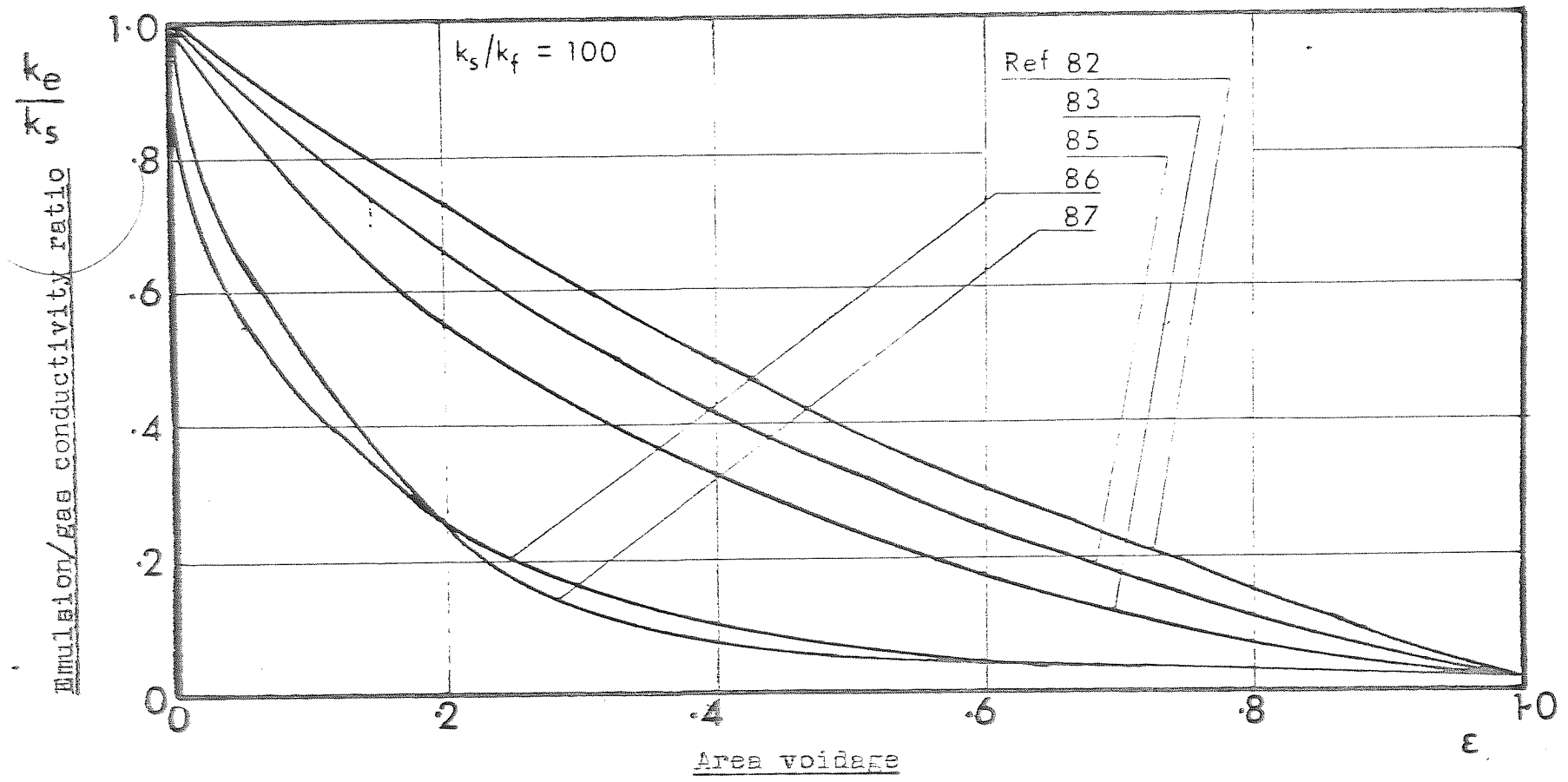


Fig.5.2 Conductivity of porous systems

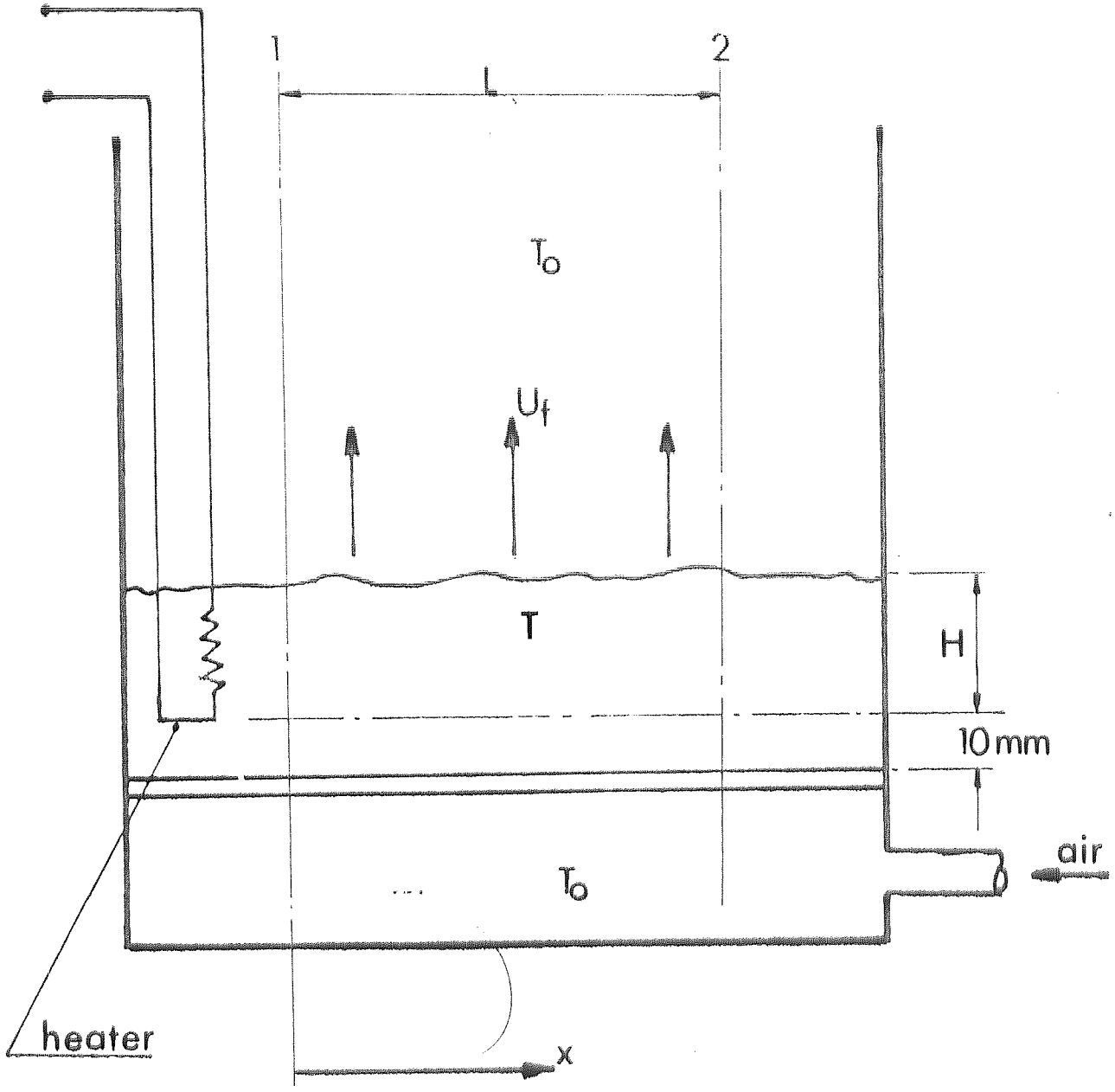


Fig. 5.3 Experimental layout

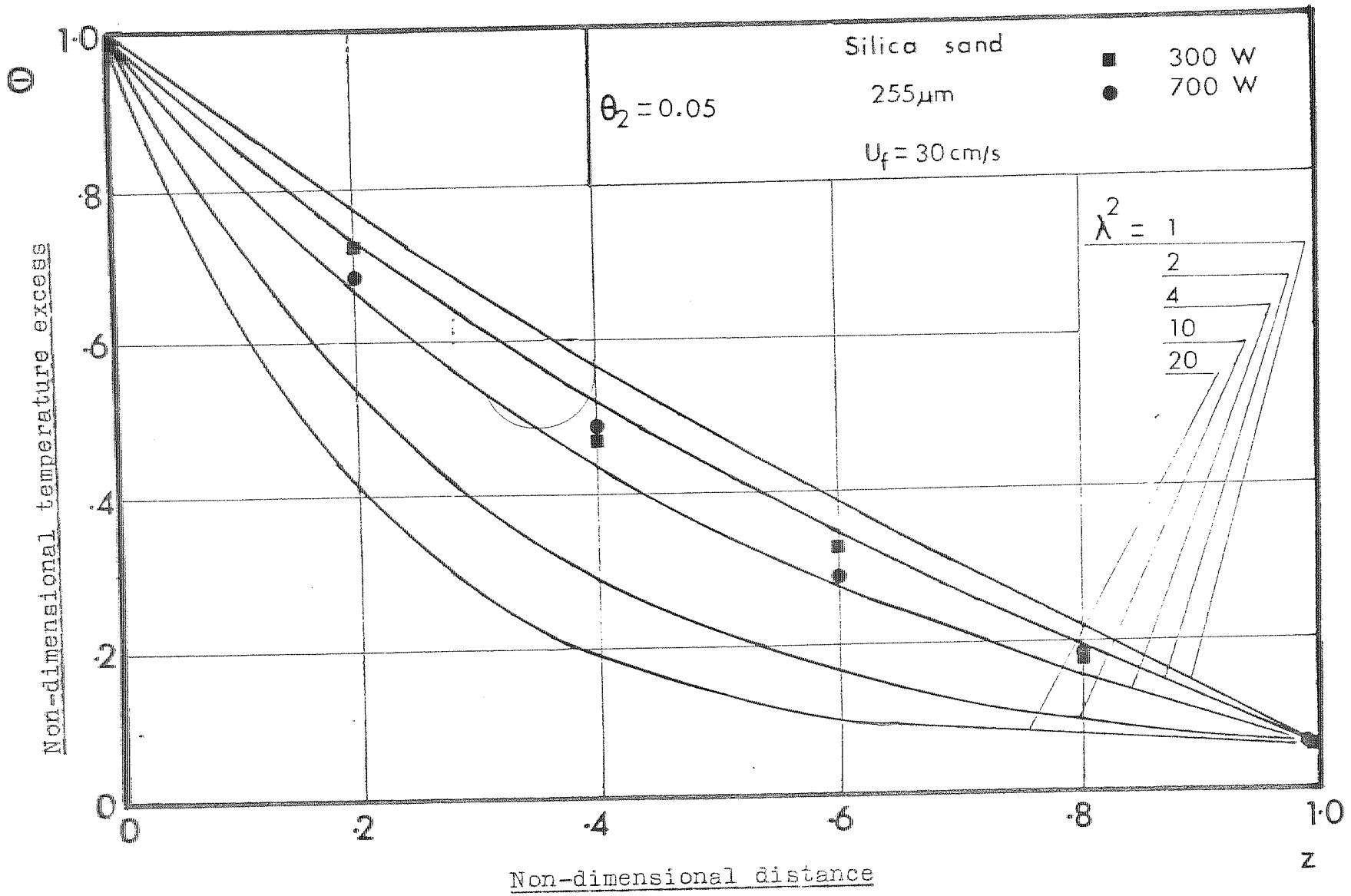


Fig. 5.4 Typical experimental data

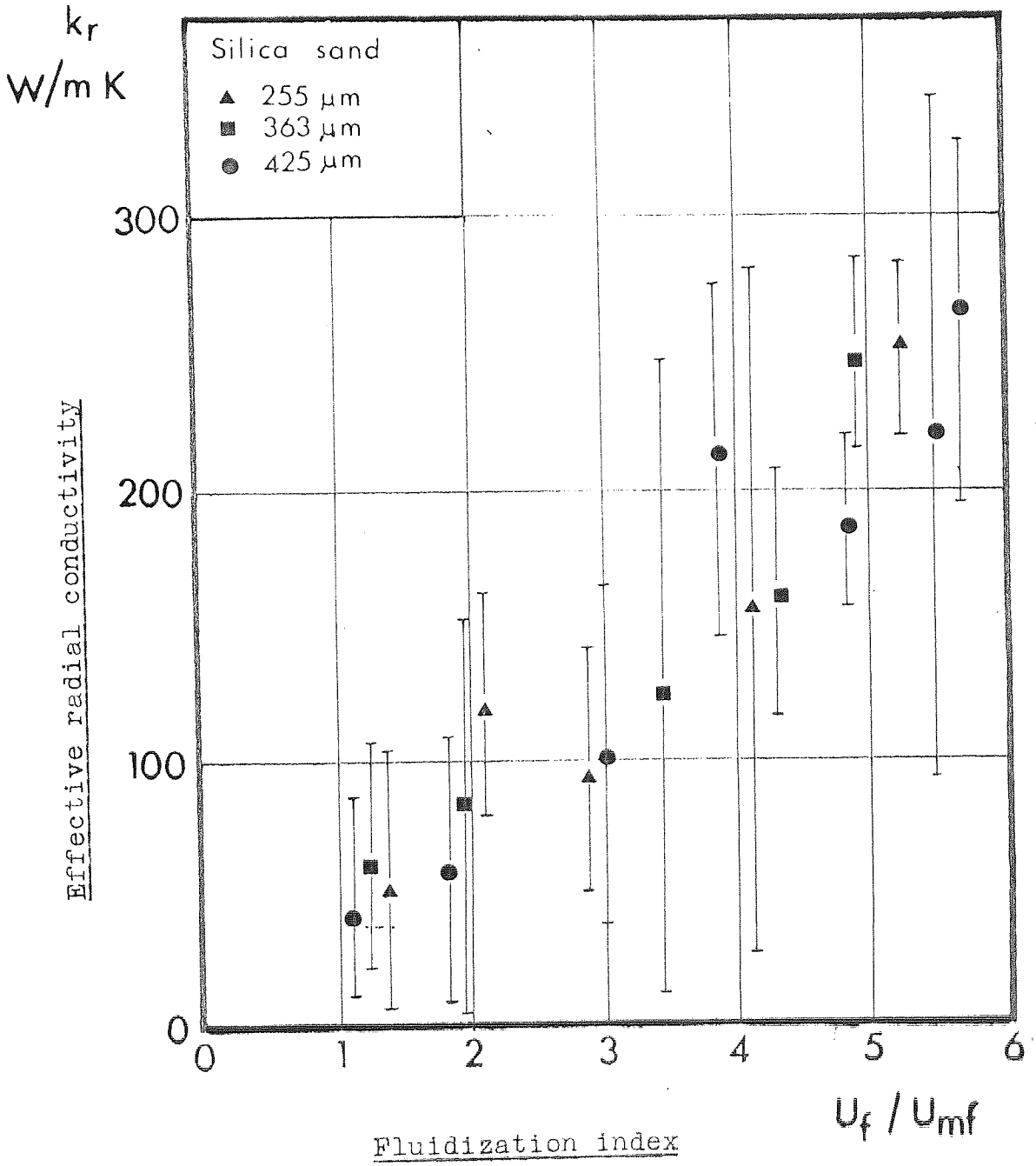


Fig. 5.5 Radial conductivity data

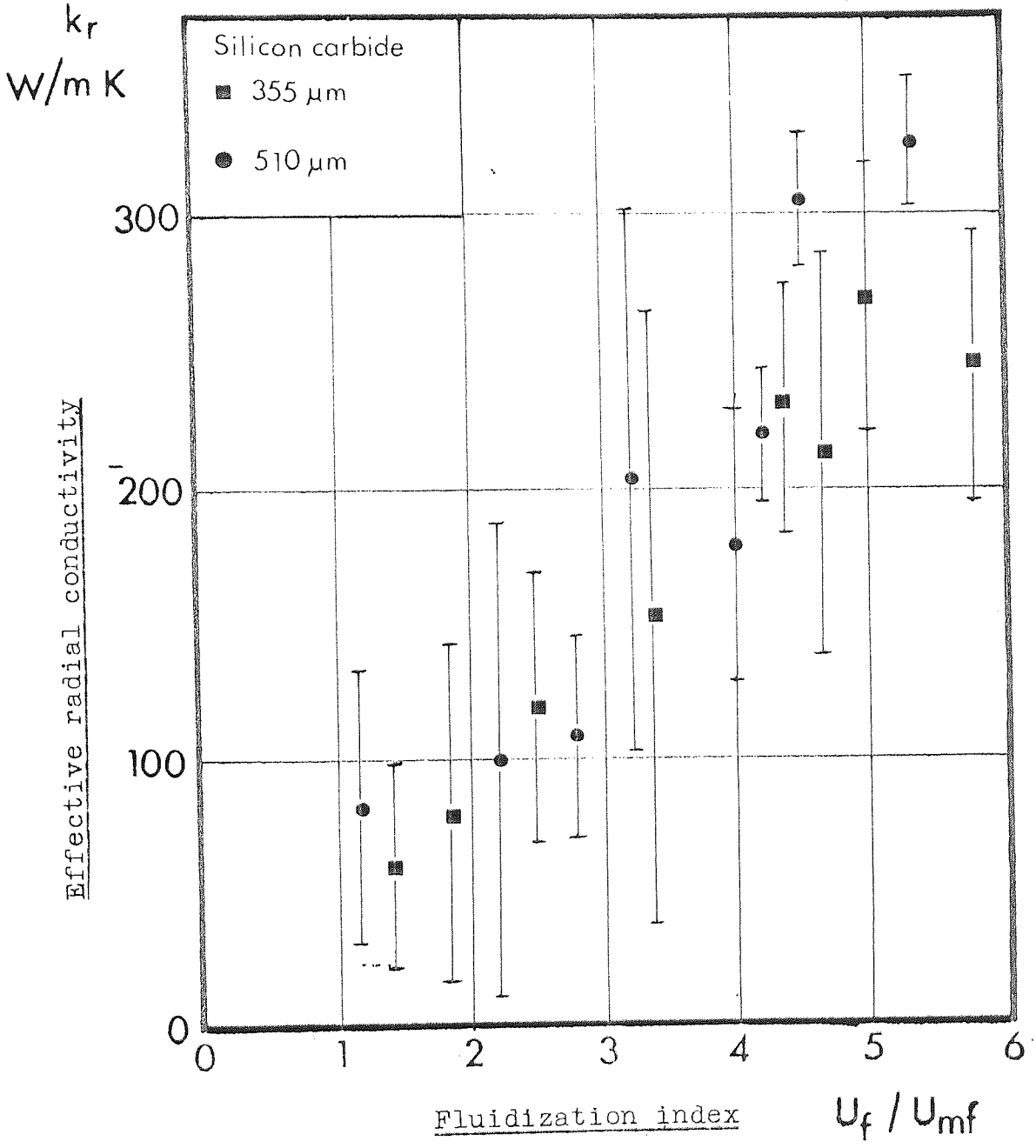


Fig. 5.6 Radial conductivity data

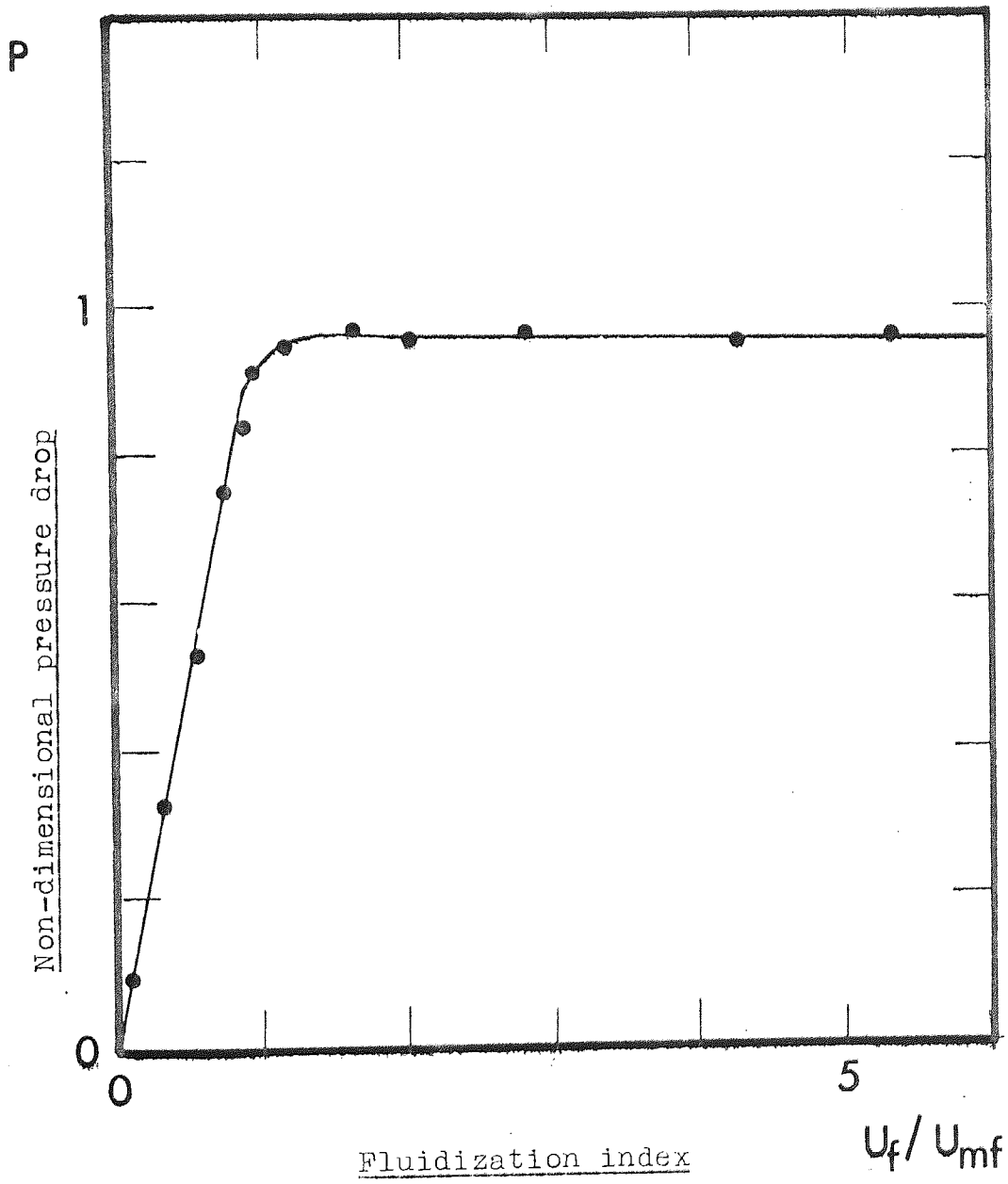


Fig. 6.1 A typical pressure drop curve

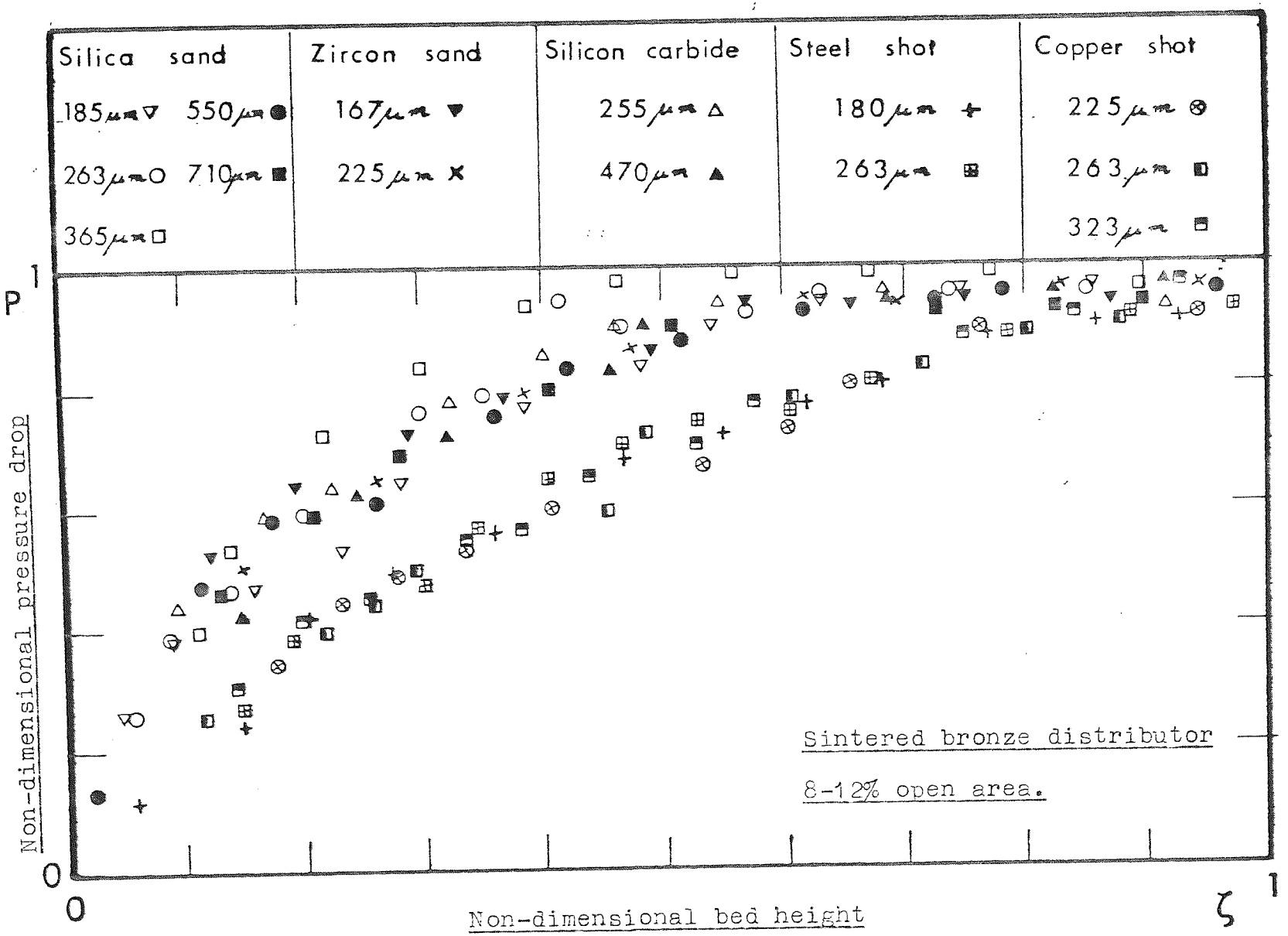


Fig.6.2 Pressure drop data

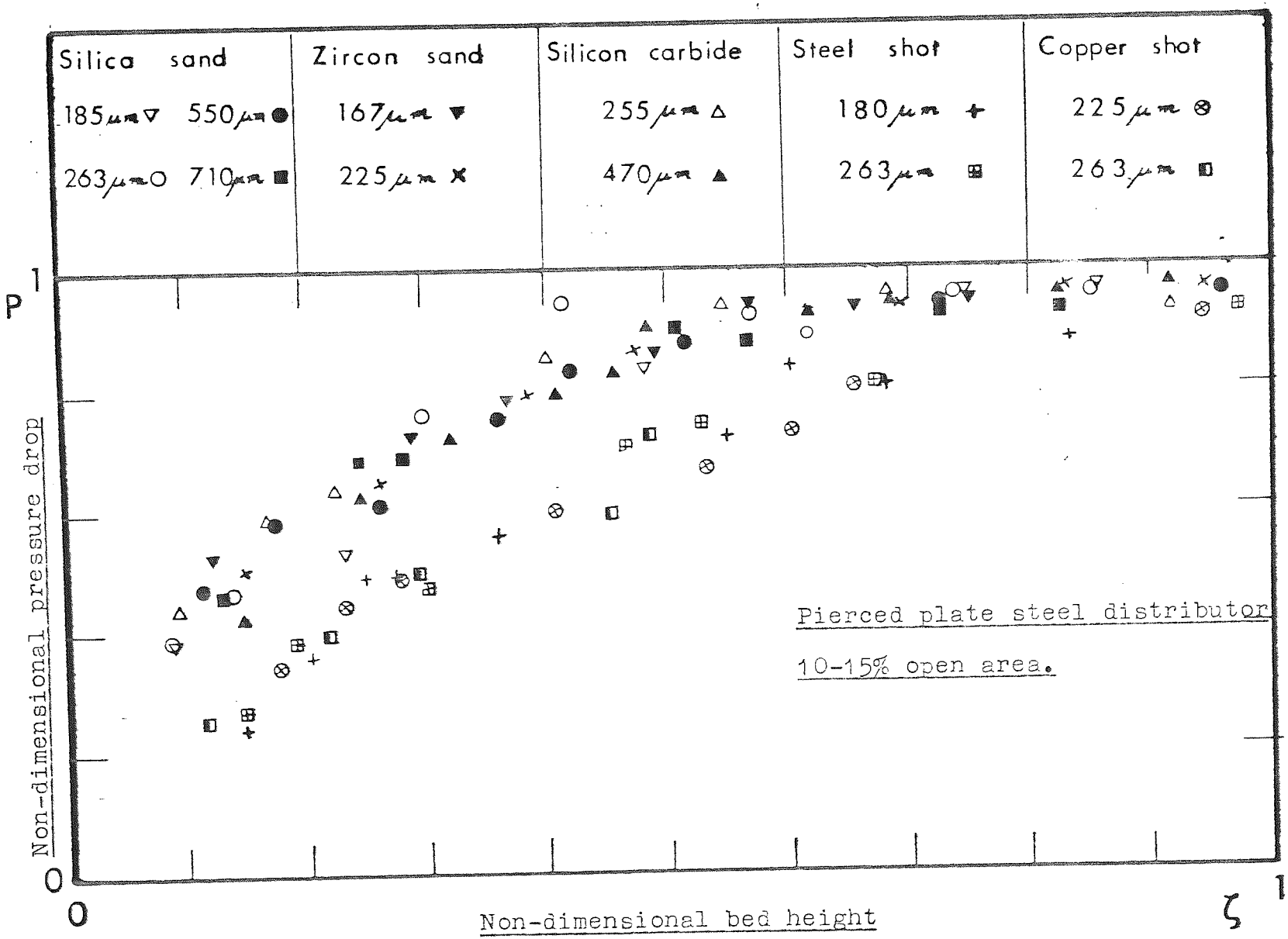


Fig 6 & Pressure drop data

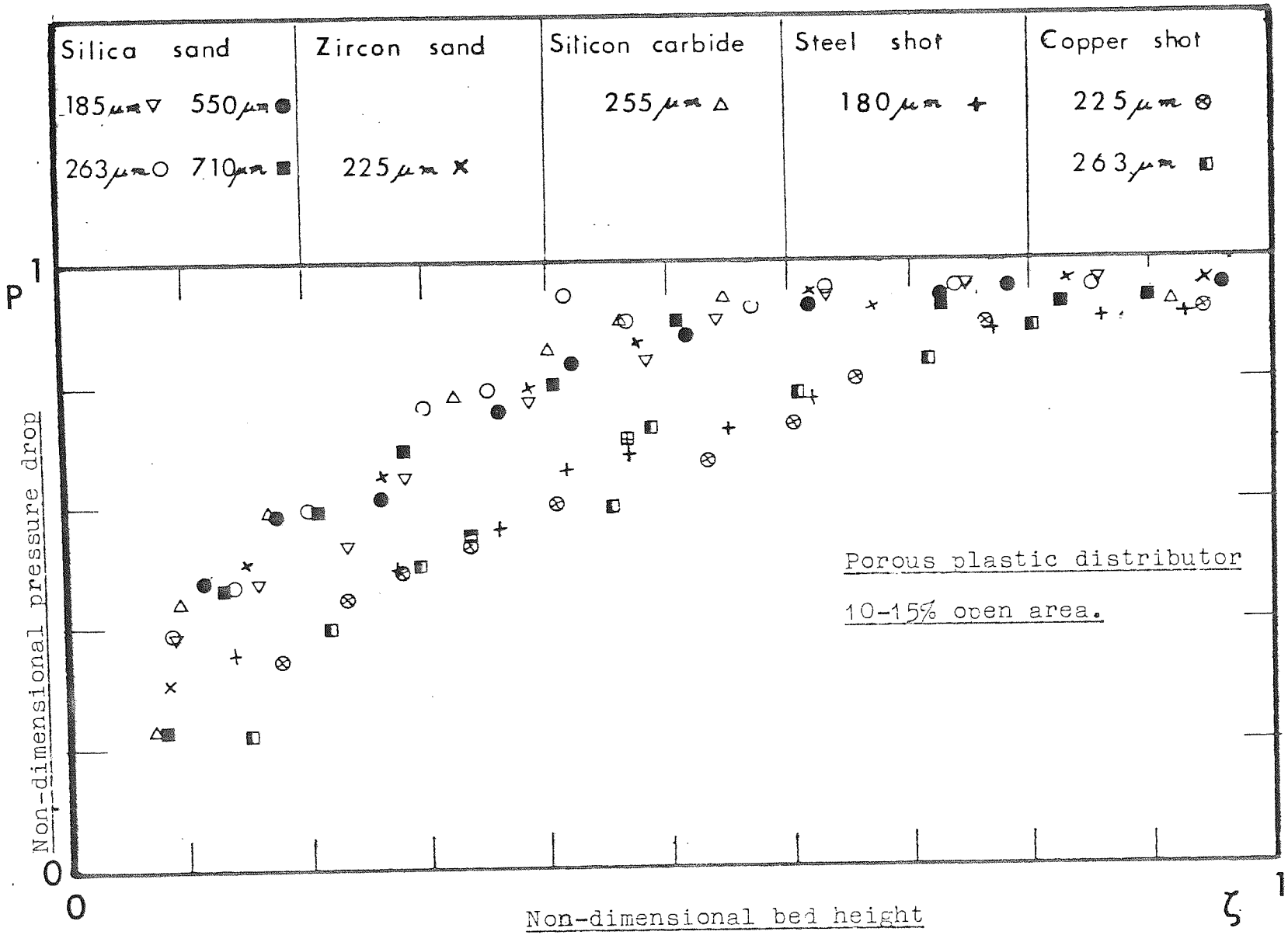


Fig.6.4 Pressure drop data

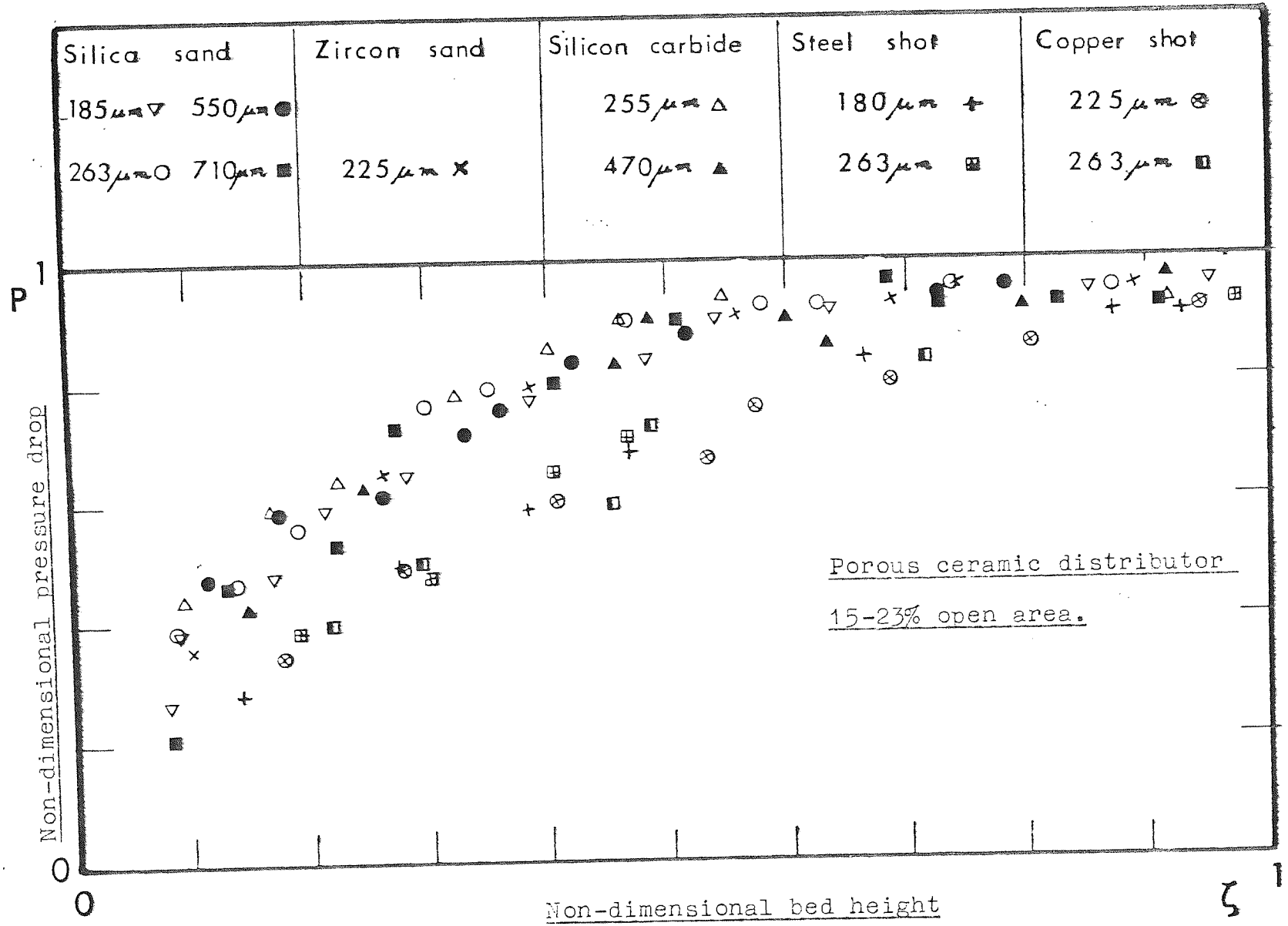


Fig.6.5 Pressure drop data

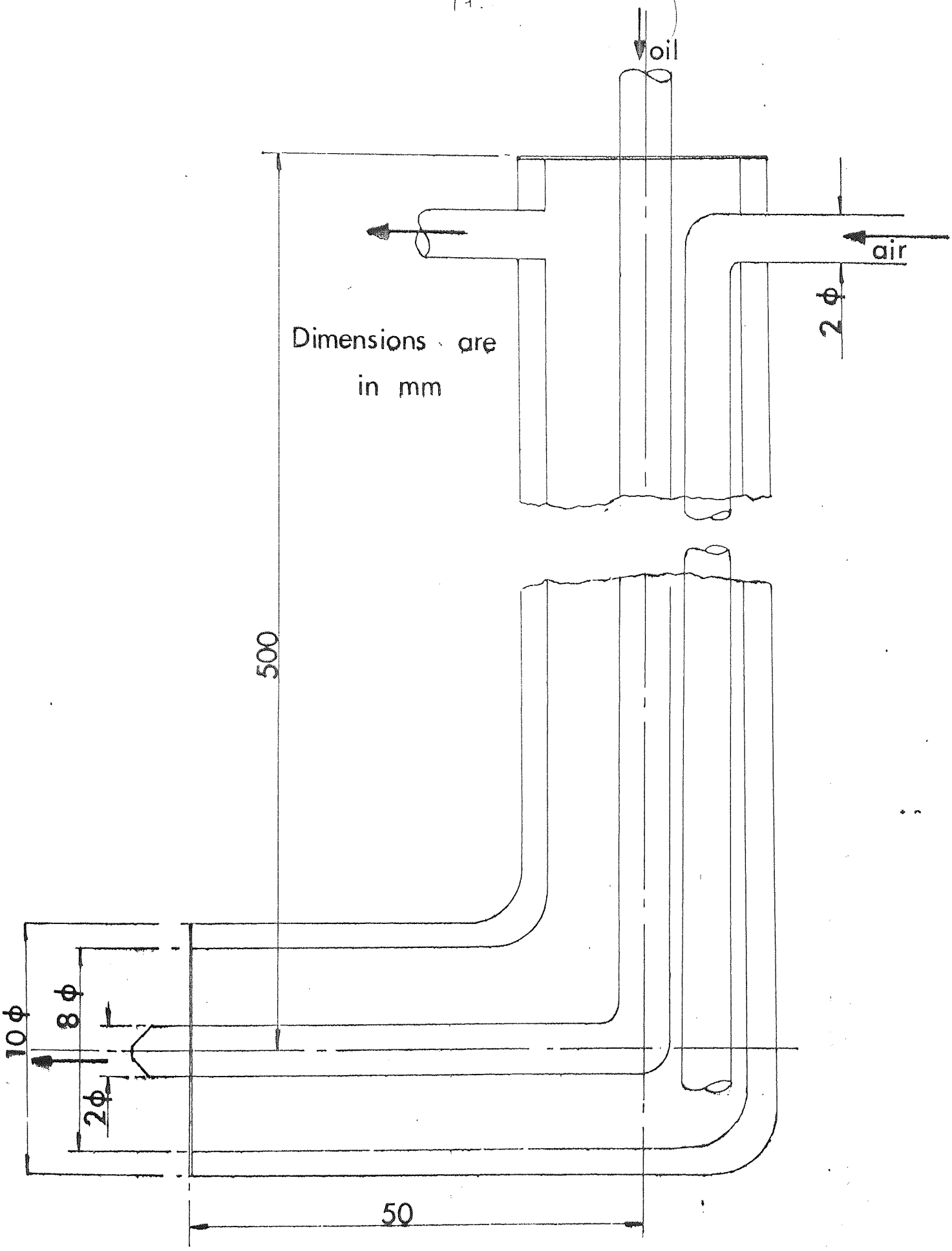


Fig. 7.1 Air-cooled, stainless steel, oil injector

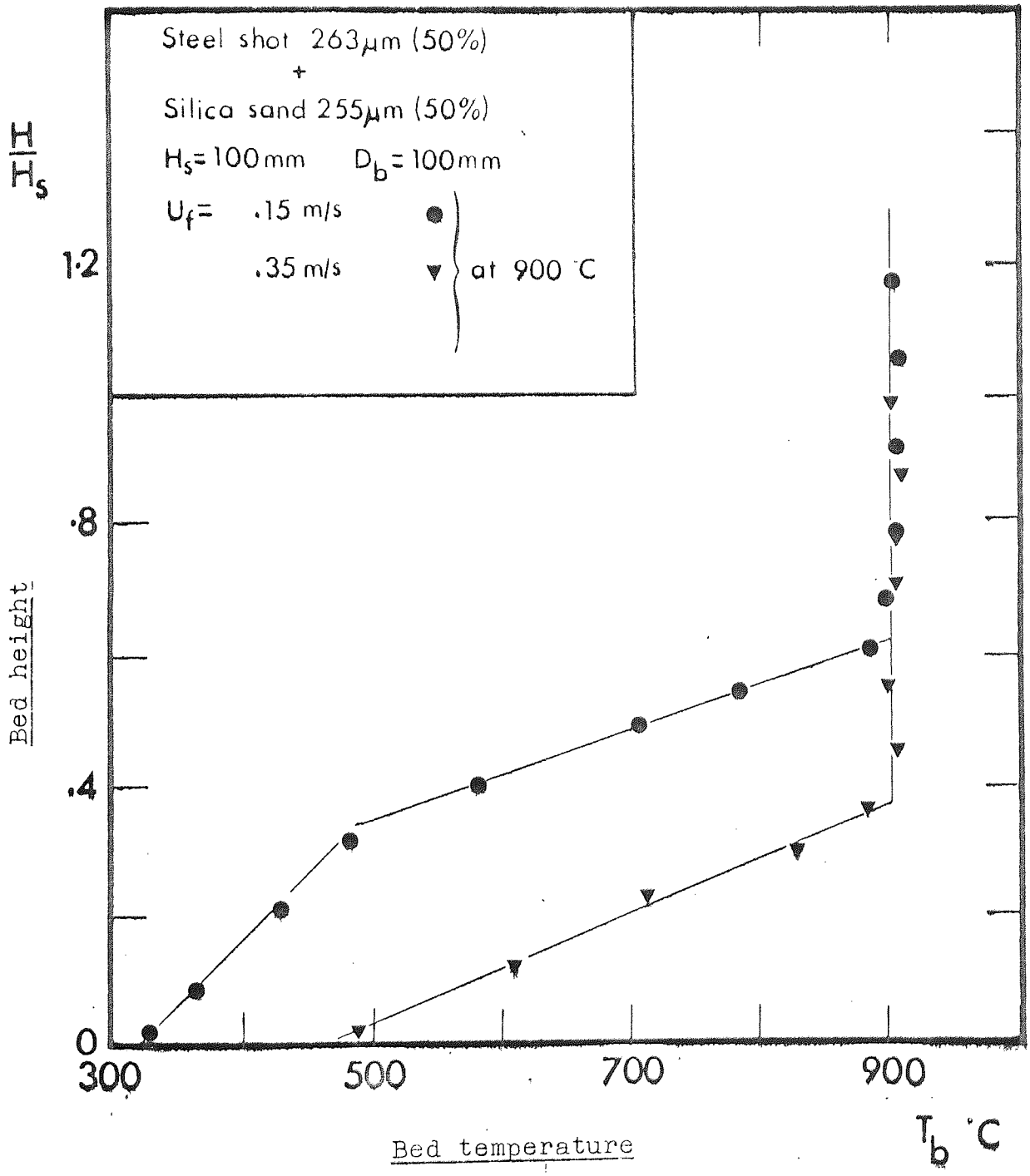


Fig.7.2 Temperature profiles in binary beds

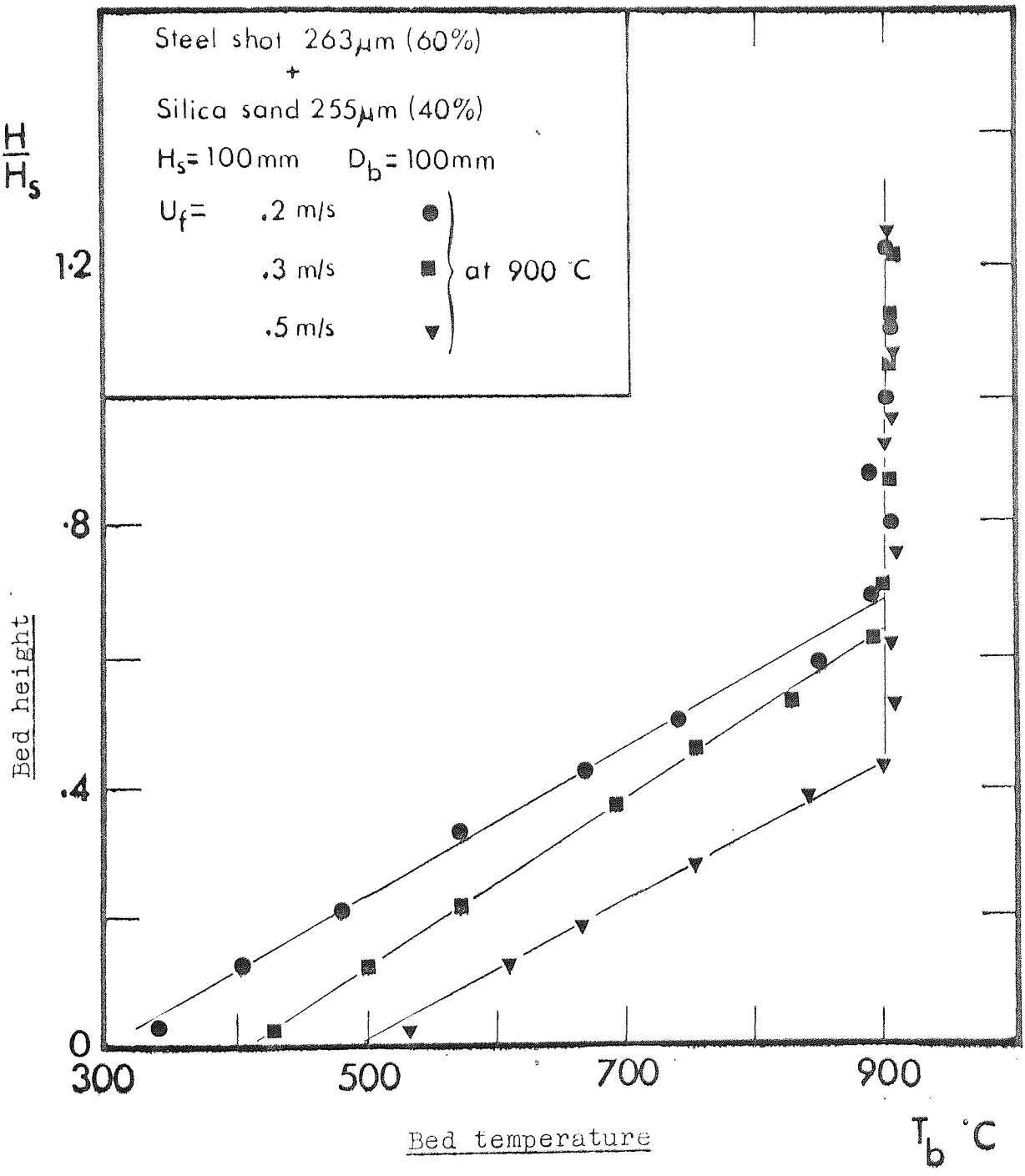


Fig.7.3 Temperature profiles in binary beds

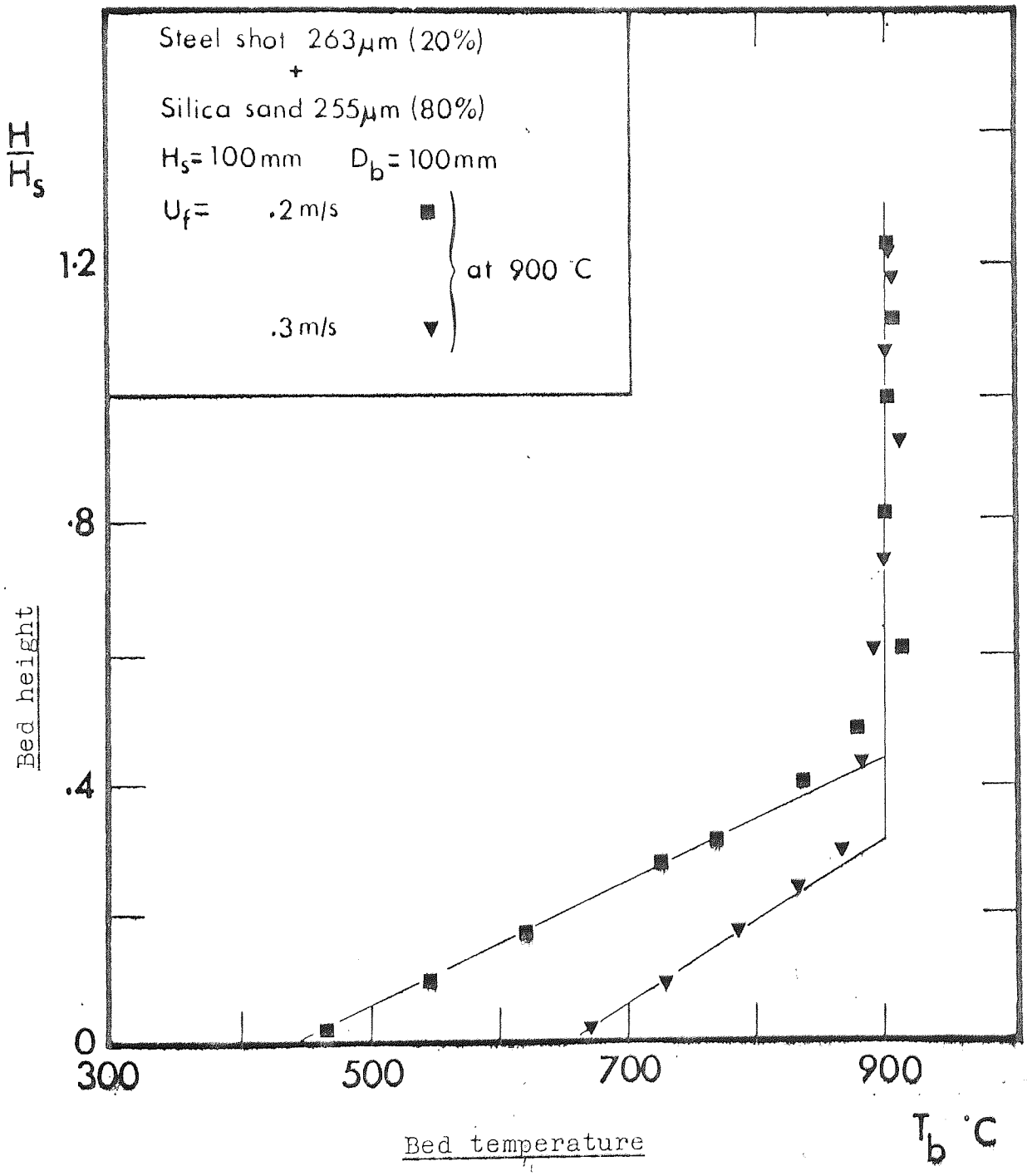


Fig.7.4 Temperature profiles in binary beds

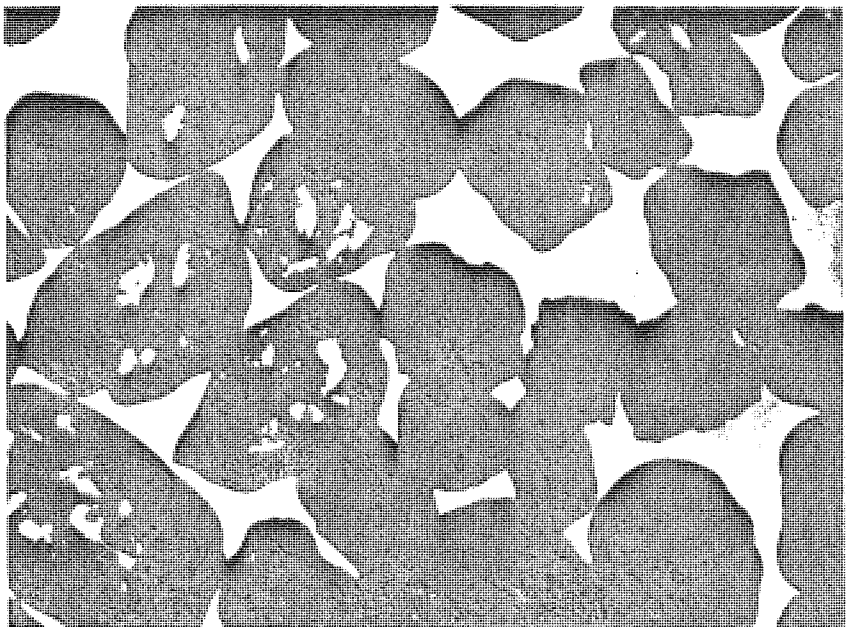

Silica Sand
463 μm

Fig. C.1 Projection micrographs

Zircon Sand
355 μm

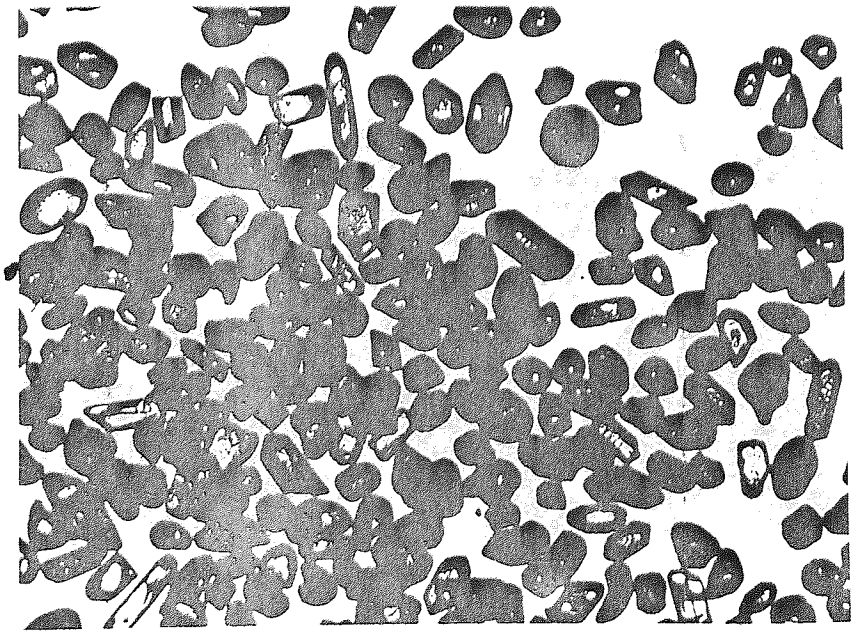

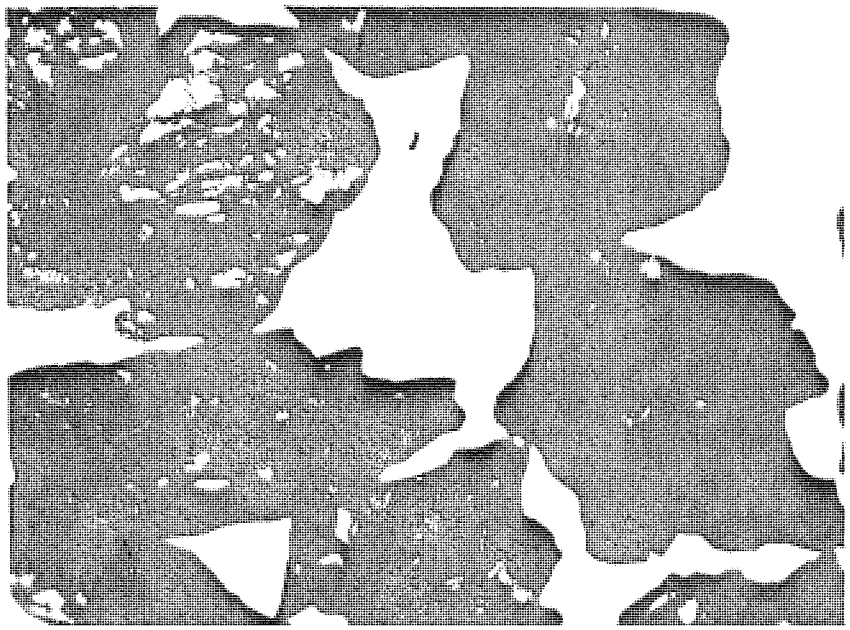

710 μm

Fig. C.2 Silicon Carbide

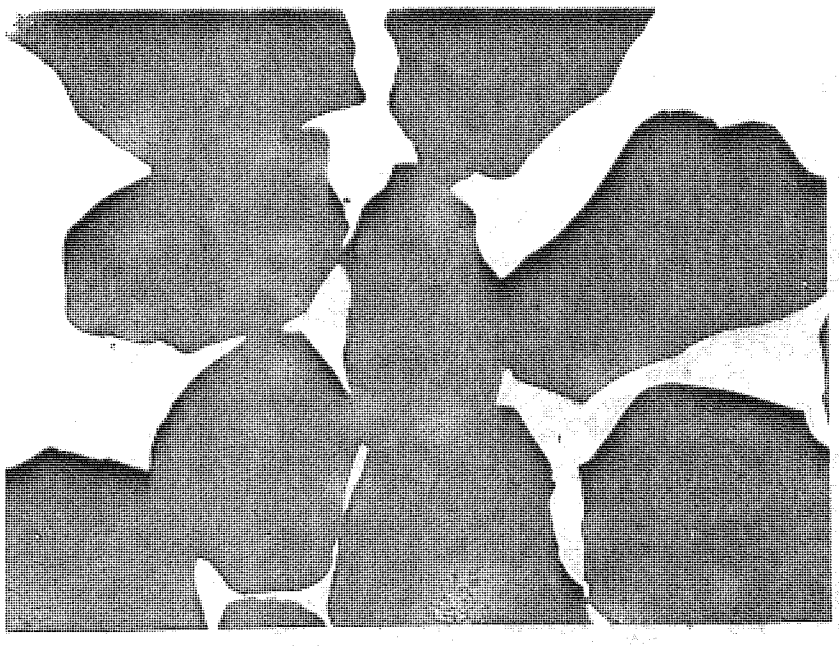

355 μm

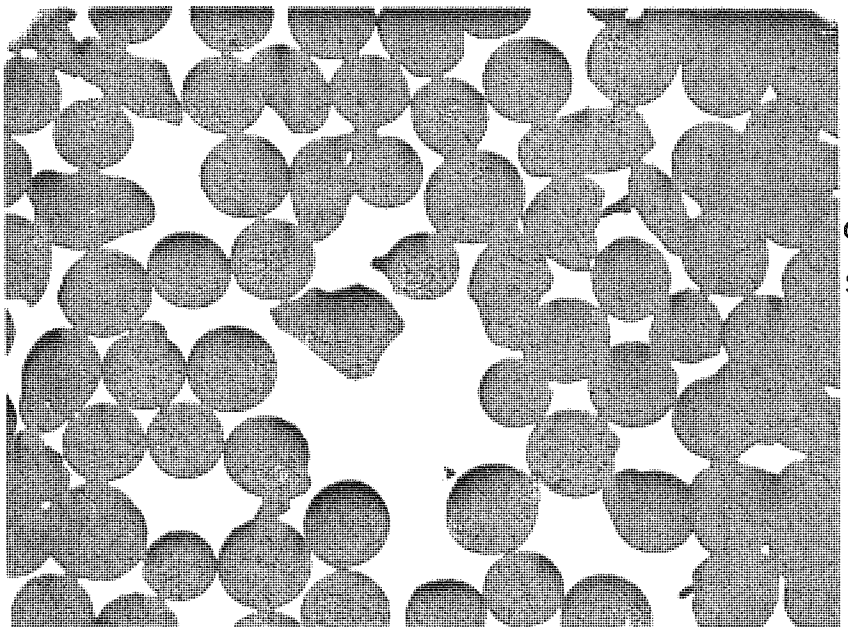

copper
shot

263 µm

Figure C.3

steel
shot
187µm

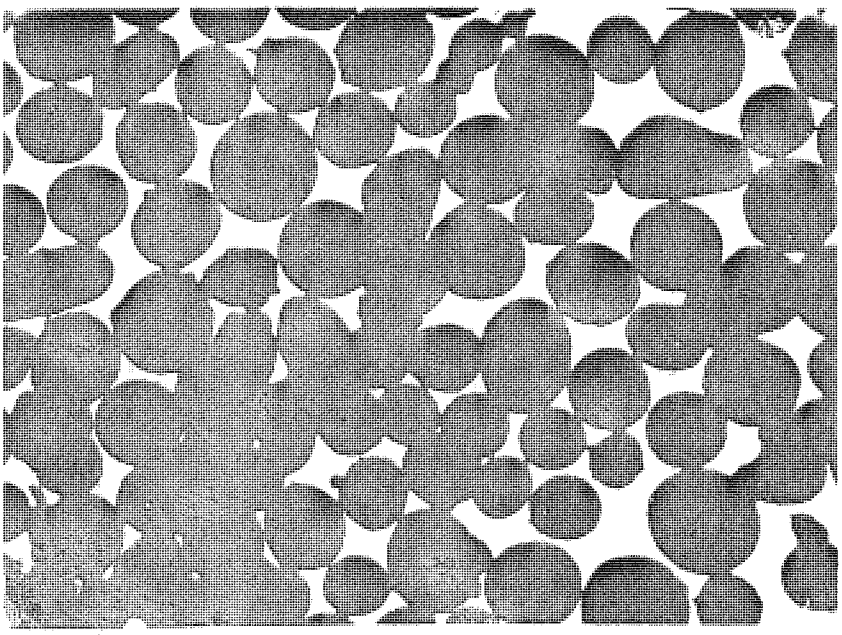

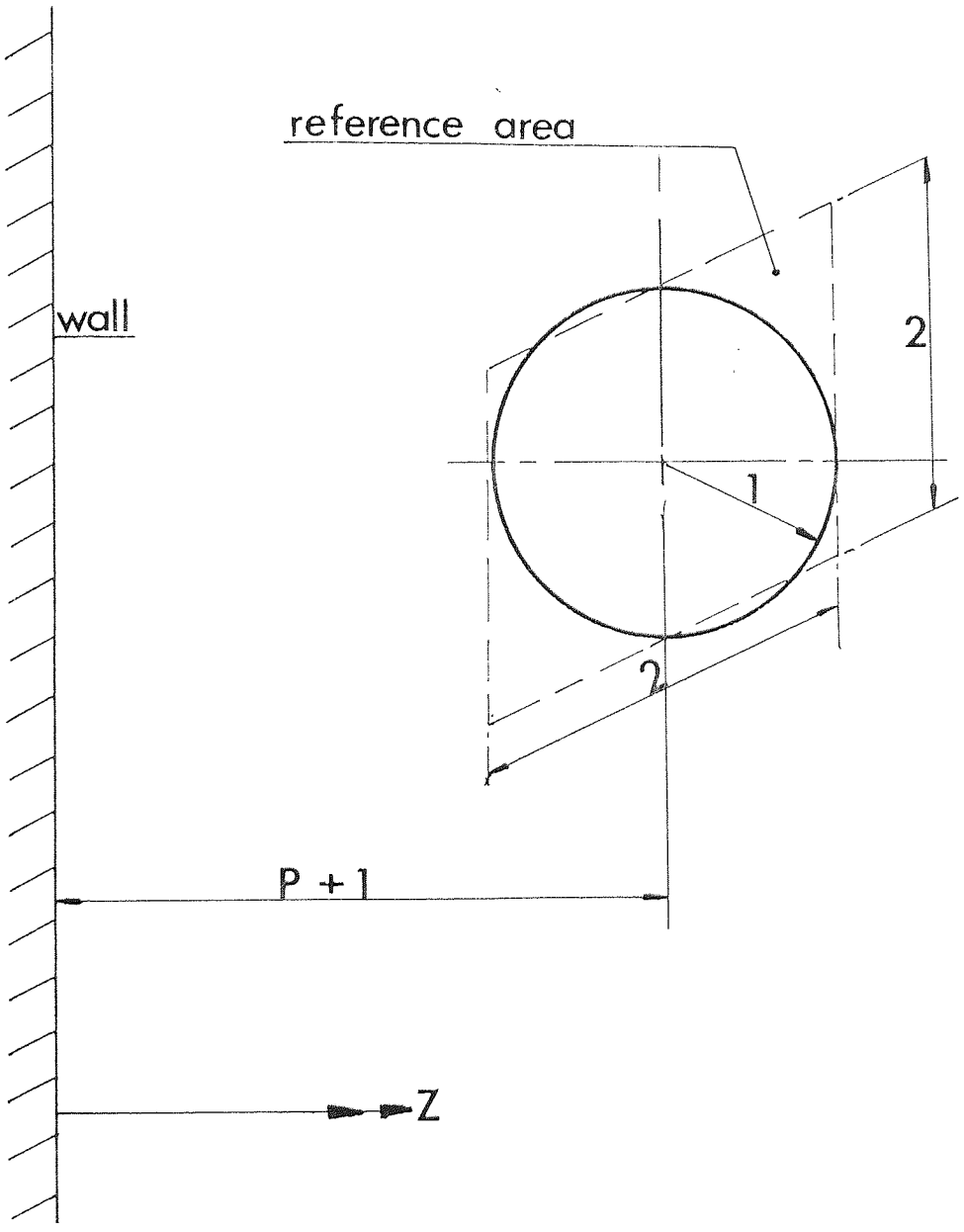


Fig.C4 Voidage Variation due to a Single Sphere

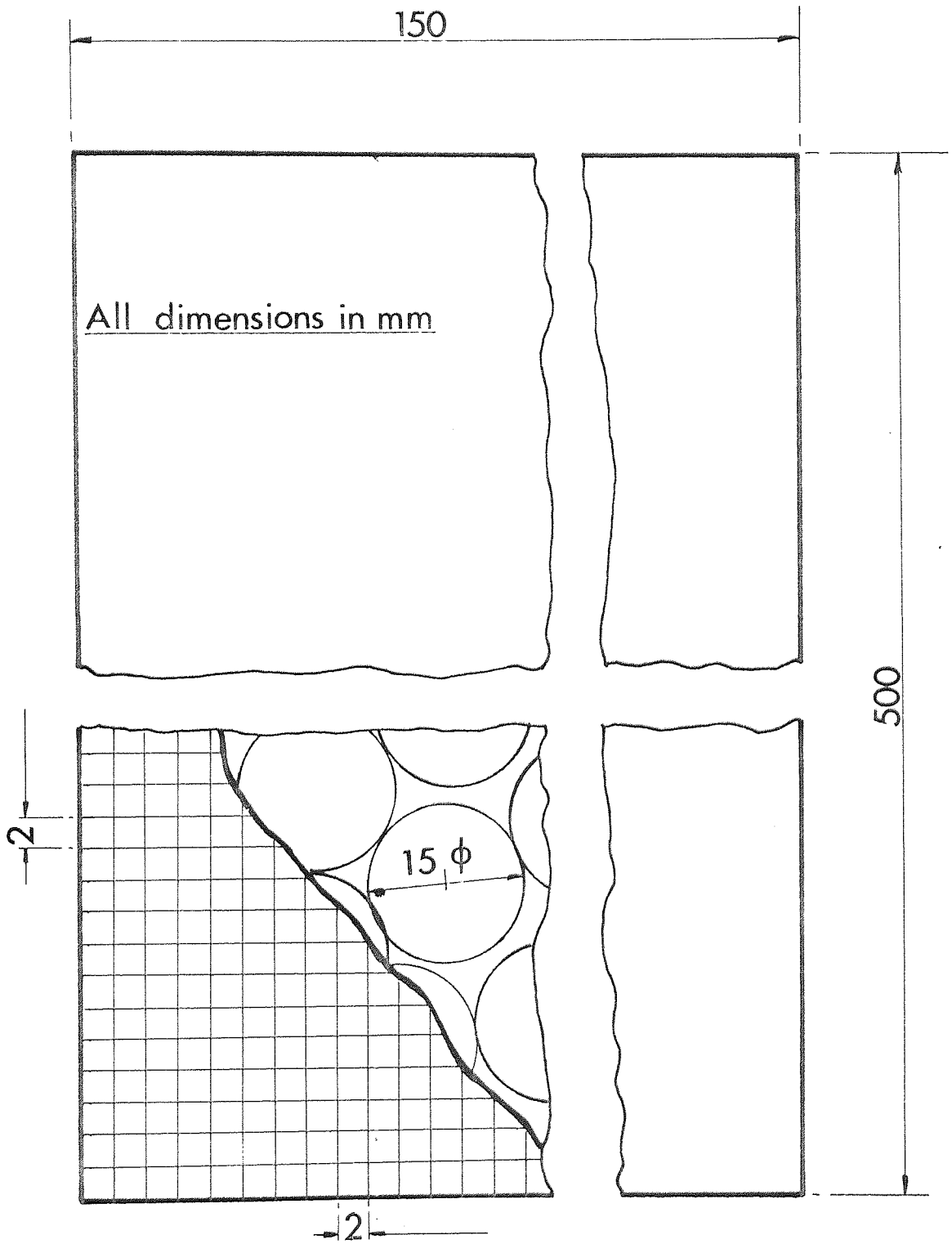


Fig. C5 Measuring Grid on the 2-D Bed

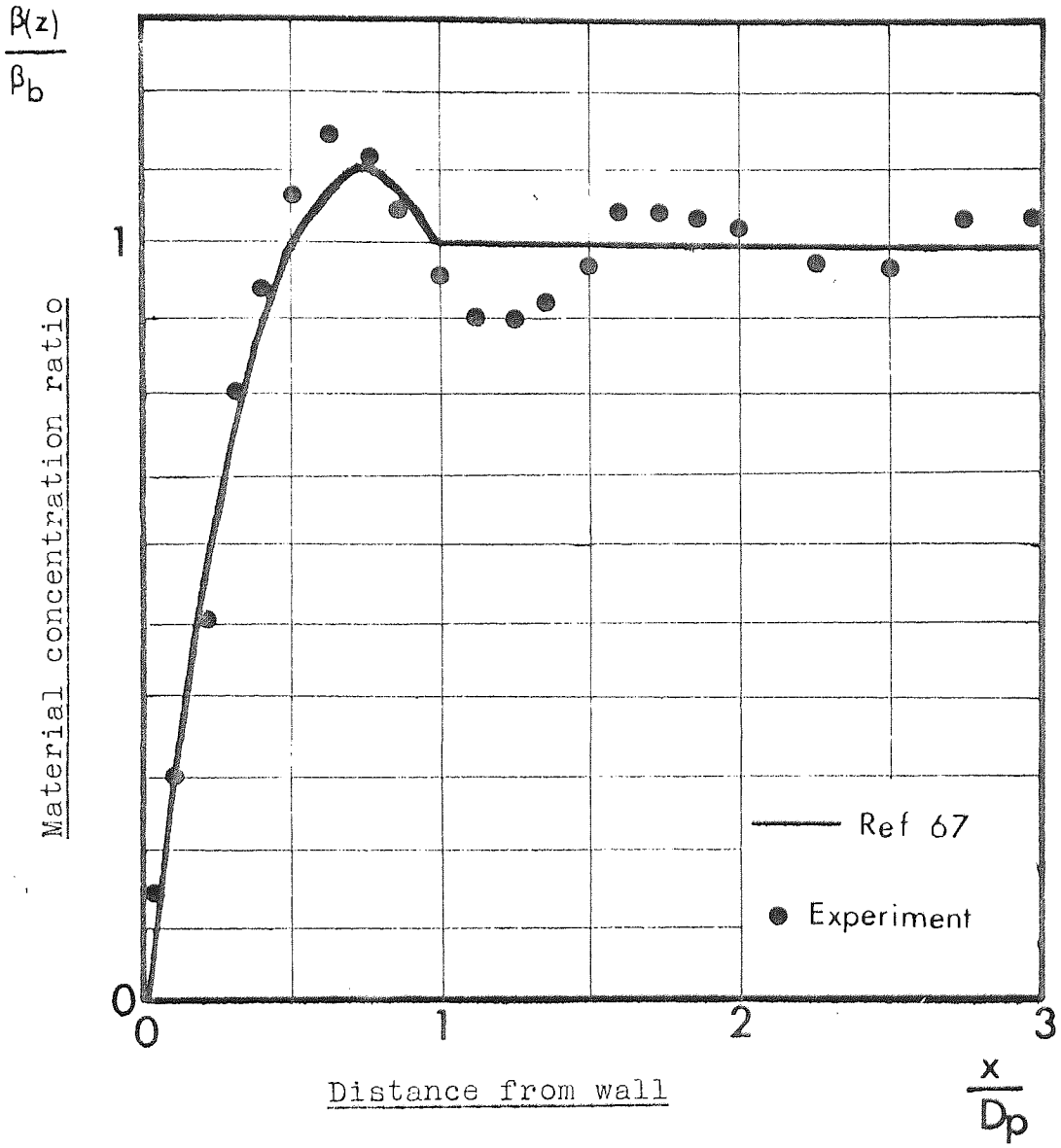


Fig. C.6 Material concentration at a surface

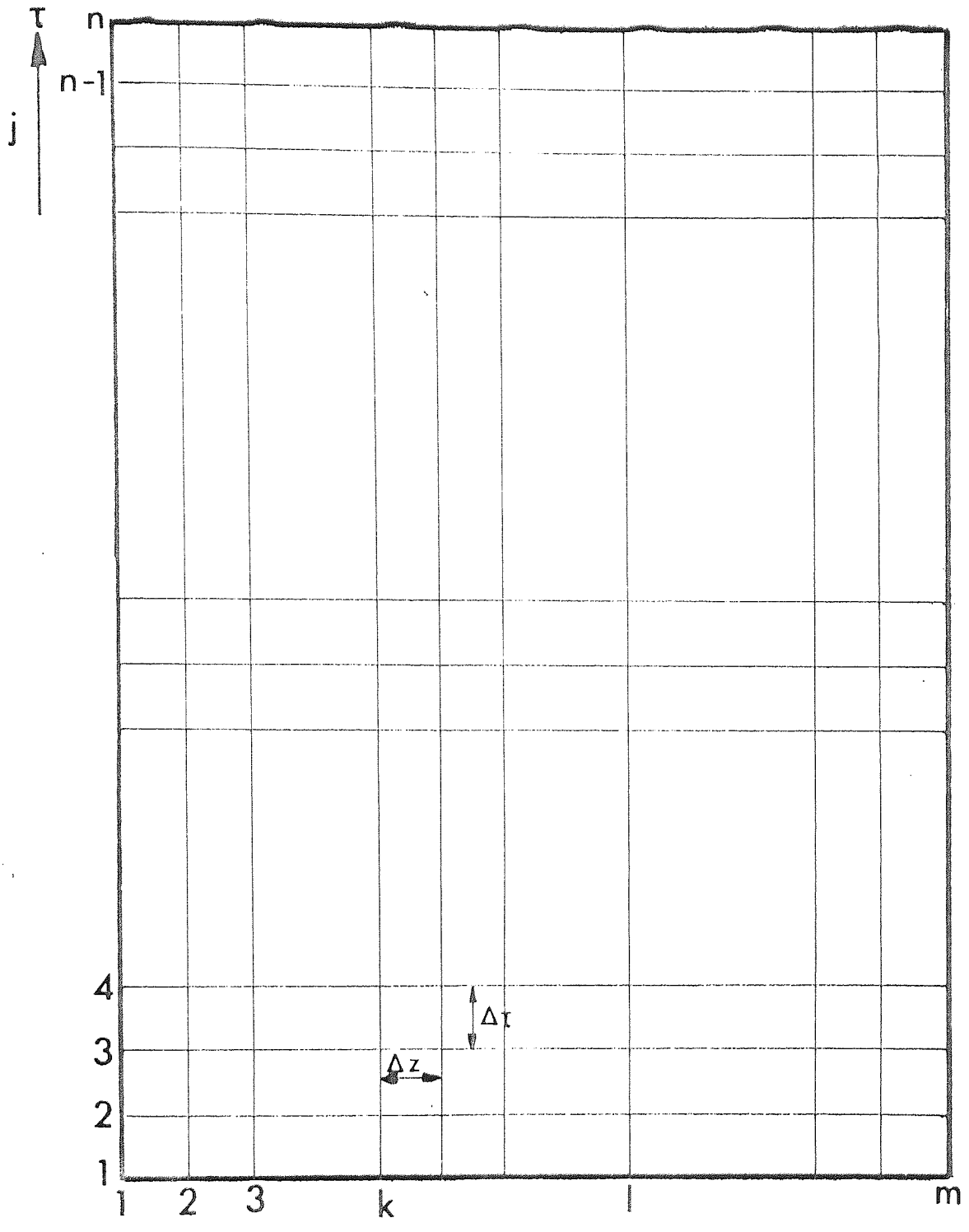


(k-1) $\Delta z = 0.75$

(l-1) $\Delta z = 1.0$

(m-1) $\Delta z = 10$

Fig. C.7 Grid for numerical solution

BED MATERIAL: SILICA SAND

MEAN PARTICLE DIAMETER: 243 microns.

BED DEPTH: 50 mm.

PROBE POSITION: 25 mm above distributor.

| TEST NO. | $T_b$ C | H kW/m$^2$K | $N_{opt}$ | $Nu_{max}$ | Ar |
|---|---|---|---|---|---|
| 270 | 275 | 0.402 | 1.87 | 2.257 | 302 |
| 271 | 367 | 0.482 | 1.67 | 2.393 | 207 |
| 272 | 410 | 0.514 | 1.48 | 2.422 | 176 |
| 273 | 465 | 0.547 | 1.59 | 2.452 | 151 |
| 274 | 550 | 0.617 | 1.84 | 2.531 | 115 |
| 275 | 648 | 0.691 | 1.61 | 2.627 | 91 |
| 276 | 751 | 0.771 | 1.77 | 2.735 | 73 |
| 277 | 797 | 0.814 | 1.63 | 2.792 | 65 |
| 278 | 848 | 0.858 | 1.45 | 2.851 | 59 |
| 279 | 904 | 0.900 | 1.64 | 2.916 | 53 |
| 280 | 955 | 0.953 | 1.83 | 2.970 | 48 |
| 281 | 1010 | 0.998 | 1.71 | 3.032 | 43 |

TABLE 4.1 DERIVED EXPERIMENTAL DATA.

BED MATERIAL: SILICA SAND.

MEAN PARTICLE DIAMETER: 326 microns.

BED DEPTH: 50 mm.

PROBE POSITION: 25 mm above distributor.

| TEST NO. | $T_b$ C | H kW/m$^2$K | $N_{opt}$ | $Nu_{max}$ | Ar |
|---|---|---|---|---|---|
| 290 | 265 | 0.375 | 1.34 | 2.835 | 730 |
| 291 | 360 | 0.432 | 1.59 | 2.878 | 501 |
| 292 | 415 | 0.461 | 1.72 | 2.913 | 425 |
| 293 | 455 | 0.492 | 1.44 | 2.956 | 366 |
| 294 | 600 | 0.589 | 1.52 | 3.119 | 246 |
| 295 | 698 | 0.660 | 1.85 | 3.250 | 196 |
| 296 | 751 | 0.698 | 1.82 | 3.321 | 175 |
| 297 | 801 | 0.738 | 1.49 | 3.395 | 158 |
| 298 | 850 | 0.779 | 1.445 | 3.548 | 142 |
| 299 | 897 | 0.822 | 1.67 | 3.600 | 128 |
| 300 | 960 | 0.867 | 1.51 | 3.627 | 116 |
| 301 | 1015 | 0.914 | 1.76 | 3.706 | 104 |

TABLE 4.2 DERIVED EXPERIMENTAL DATA.

BED MATERIAL: SILICA SAND

MEAN PARTICLE DIAMETER: 412.5 microns.

BED DEPTH: 50 mm.

PROBE POSITION: 25 mm above distributor.

| TEST NO. | $T_b$ C | H kW/m$^2$K | $N_{opt}$ | $Nu_{max}$ | Ar |
|---|---|---|---|---|---|
| 310 | 265 | 0.343 | 1.49 | 3.280 | 1478 |
| 311 | 350 | 0.396 | 1.72 | 3.337 | 1014 |
| 312 | 409 | 0.423 | 1.54 | 3.381 | 861 |
| 313 | 458 | 0.451 | 1.66 | 3.433 | 741 |
| 314 | 605 | 0.542 | 1.79 | 3.633 | 499 |
| 315 | 652 | 0.575 | 1.47 | 3.711 | 444 |
| 316 | 756 | 0.645 | 1.33 | 3.881 | 355 |
| 317 | 803 | 0.683 | 1.37 | 3.971 | 319 |
| 318 | 857 | 0.721 | 1.61 | 4.064 | 288 |
| 319 | 907 | 0.762 | 1.54 | 4.159 | 259 |
| 320 | 963 | 0.804 | 1.77 | 4.255 | 234 |
| 321 | 1009 | 0.839 | 1.53 | 4.350 | 211 |

TABLE 4.3 DERIVED EXPERIMENTAL DATA.

BED MATERIAL: SILICA SAND.

MEAN PARTICLE DIAMETER: 463 microns.

BED DEPTH: 50 mm.

PROBE POSITION: 25 mm above distributor.

| TEST NO. | $T_b$ C | H kW/m$^2$K | $N_{opt}$ | $Nu_{max}$ | Ar |
|---|---|---|---|---|---|
| 330 | 259 | 0.328 | 1.63 | 3.523 | 2090 |
| 331 | 357 | 0.353 | 1.42 | 3.587 | 1434 |
| 332 | 402 | 0.406 | 1.53 | 3.637 | 1218 |
| 333 | 460 | 0.433 | 1.59 | 3.695 | 1047 |
| 334 | 601 | 0.521 | 1.46 | 4.002 | 706 |
| 335 | 699 | 0.585 | 1.79 | 4.097 | 560 |
| 336 | 745 | 0.620 | 1.64 | 4.189 | 502 |
| 337 | 800 | 0.656 | 1.43 | 4.288 | 452 |
| 338 | 847 | 0.694 | 1.68 | 4.391 | 407 |
| 339 | 910 | 0.733 | 1.73 | 4.496 | 367 |
| 340 | 958 | 0.775 | 1.32 | 4.603 | 331 |
| 341 | 1006 | 0.818 | 1.48 | 4.716 | 298 |

TABLE 4.4 DERIVED EXPERIMENTAL DATA.

BED MATERIAL: SILICA SAND.

MEAN PARTICLE DIAMETER: 550 microns.

BED DEPTH: 50 mm.

PROBE POSITION: 25 mm above distributor.

| TEST NO. | $T_b$ C | H kW/m$^2$K | $N_{opt}$ | $Nu_{max}$ | Ar |
|---|---|---|---|---|---|
| 345 | 258 | 0.308 | 1.45 | 3.920 | 3504 |
| 346 | 360 | 0.356 | 1.83 | 3.997 | 2404 |
| 347 | 411 | 0.381 | 1.65 | 4.055 | 2041 |
| 348 | 473 | 0.407 | 1.79 | 4.123 | 1756 |
| 349 | 598 | 0.491 | 1.66 | 4.379 | 1183 |
| 350 | 702 | 0.552 | 1.51 | 4.584 | 939 |
| 351 | 747 | 0.585 | 1.43 | 4.694 | 842 |
| 352 | 797 | 0.619 | 1.73 | 4.809 | 757 |
| 353 | 861 | 0.655 | 1.64 | 4.928 | 682 |
| 354 | 923 | 0.693 | 1.49 | 4.997 | 615 |
| 355 | 997 | 0.733 | 1.53 | 5.173 | 555 |
| 356 | 1072 | 0.775 | 1.31 | 5.299 | 501 |

TABLE 4.5 DERIVED EXPERIMENTAL DATA.

BED MATERIAL: SILICA SAND

MEAN PARTICLE DIAMETER: 621 microns.

BED DEPTH: 50 mm.

PROBE POSITION: 25 mm above distributor.

| TEST NO. | $T_b$ C | H kW/m$^2$K | $N_{opt}$ | $Nu_{max}$ | Ar |
|---|---|---|---|---|---|
| 360 | 255 | 0.294 | 1.52 | 4.222 | 5020 |
| 361 | 358 | 0.340 | 1.91 | 4.309 | 3444 |
| 362 | 407 | 0.364 | 1.44 | 4.374 | 2924 |
| 363 | 465 | 0.389 | 1.69 | 4.449 | 2515 |
| 364 | 600 | 0.470 | 1.67 | 4.733 | 1695 |
| 365 | 652 | 0.499 | 1.36 | 4.843 | 1507 |
| 366 | 701 | 0.530 | 1.59 | 4.959 | 1346 |
| 367 | 755 | 0.562 | 1.47 | 5.081 | 1207 |
| 368 | 799 | 0.595 | 1.71 | 5.209 | 1085 |
| 369 | 852 | 0.630 | 1.52 | 5.340 | 977 |
| 370 | 908 | 0.667 | 1.33 | 5.475 | 881 |
| 371 | 970 | 0.705 | 1.39 | 5.612 | 795 |
| 372 | 1009 | 0.746 | 1.54 | 5.751 | 717 |

TABLE 4.6 DERIVED EXPERIMENTAL DATA.

BED MATERIAL: SILICA SAND.

MEAN PARTICLE DIAMETER: 755 microns.

BED DEPTH: 50 mm.

PROBE POSITION: 25 mm above distributor.

| TEST NO. | $T_b$ C | H kW/m$^2$K | $N_{opt}$ | $Nu_{max}$ | Ar |
|---|---|---|---|---|---|
| 375 | 243 | 0.273 | 1.66 | 4.771 | 9064 |
| 376 | 359 | 0.316 | 1.48 | 4.877 | 6219 |
| 377 | 415 | 0.339 | 1.52 | 4.954 | 5281 |
| 378 | 455 | 0.362 | 1.56 | 5.043 | 4542 |
| 379 | 600 | 0.439 | 1.63 | 5.378 | 3060 |
| 380 | 648 | 0.466 | 1.36 | 5.507 | 2721 |
| 381 | 698 | 0.495 | 1.72 | 5.645 | 2430 |
| 382 | 756 | 0.525 | 1.58 | 5.789 | 2179 |
| 383 | 802 | 0.557 | 1.23 | 5.939 | 1959 |
| 384 | 858 | 0.590 | 1.72 | 6.094 | 1764 |
| 385 | 902 | 0.625 | 1.48 | 6.253 | 1591 |
| 386 | 957 | 0.662 | 1.45 | 6.415 | 1435 |
| 387 | 1018 | 0.701 | 1.53 | 6.579 | 1294 |

TABLE 4.7 DERIVED EXPERIMENTAL DATA.

BED MATERIAL: SILICON CARBIDE.

MEAN PARTICLE DIAMETER: 255 microns.

BED DEPTH: 50 mm.

PROBE POSITION: 25 mm above distributor.

| TEST NO. | $T_b$ C | H kW/m$^2$K | $N_{opt}$ | $Nu_{max}$ | Ar |
|---|---|---|---|---|---|
| 25 | 247 | 0.439 | 1.47 | 2.595 | 476 |
| 26 | 366 | 0.505 | 1.38 | 2.632 | 326 |
| 27 | 413 | 0.529 | 1.56 | 2.662 | 277 |
| 28 | 460 | 0.574 | 1.64 | 2.700 | 238 |
| 29 | 601 | 0.687 | 1.65 | 2.843 | 161 |
| 30 | 697 | 0.769 | 1.58 | 2.960 | 128 |
| 31 | 747 | 0.812 | 1.36 | 3.022 | 114 |
| 32 | 797 | 0.858 | 1.79 | 3.088 | 103 |
| 33 | 850 | 0.905 | 1.66 | 3.155 | 93 |
| 34 | 904 | 0.955 | 1.57 | 3.223 | 84 |
| 35 | 964 | 1.006 | 1.43 | 3.292 | 75 |
| 36 | 1022 | 1.060 | 1.57 | 3.362 | 68 |

TABLE 4.8 DERIVED EXPERIMENTAL DATA.

BED MATERIAL: SILICON CARBIDE.

MEAN PARTICLE DIAMETER: 362.5 microns.

BED DEPTH: 50 mm.

PROBE POSITION: 25 mm above distributor.

| TEST NO. | $T_b$ C | H kW/m$^2$K | $N_{opt}$ | $Nu_{max}$ | Ar |
|---|---|---|---|---|---|
| 38 | 256 | 0.384 | 1.44 | 3.227 | 1367 |
| 39 | 349 | 0.443 | 1.63 | 3.282 | 938 |
| 40 | 410 | 0.474 | 1.39 | 3.325 | 796 |
| 41 | 459 | 0.505 | 1.67 | 3.377 | 685 |
| 42 | 598 | 0.607 | 1.83 | 3.572 | 461 |
| 43 | 650 | 0.643 | 1.47 | 3.649 | 410 |
| 44 | 708 | 0.681 | 1.65 | 3.729 | 366 |
| 45 | 759 | 0.721 | 1.73 | 3.814 | 329 |
| 46 | 808 | 0.763 | 1.61 | 3.982 | 295 |
| 47 | 862 | 0.806 | 1.53 | 3.993 | 266 |
| 48 | 907 | 0.851 | 1.68 | 4.086 | 240 |
| 49 | 972 | 0.899 | 1.55 | 4.181 | 216 |
| 50 | 1016 | 0.949 | 1.72 | 4.276 | 195 |

TABLE 4.9 DERIVED EXPERIMENTAL DATA.

BED MATERIAL: SILICON CARBIDE.

MEAN PARTICLE DIAMETER: .425 microns.

BED DEPTH: 50 mm.

PROBE POSITION: 25 mm above distributor.

| TEST NO. | $T_b$ C | H kW/m$^2$K | $N_{opt}$ | $Nu_{max}$ | Ar |
|---|---|---|---|---|---|
| 52 | 249 | 0.362 | 1.58 | 3.561 | 2203 |
| 53 | 349 | 0.418 | 1.25 | 3.627 | 1511 |
| 54 | 418 | 0.447 | 1.51 | 3.677 | 1283 |
| 55 | 460 | 0.477 | 1.42 | 3.736 | 1104 |
| 56 | 601 | 0.574 | 1.66 | 3.960 | 744 |
| 57 | 647 | 0.609 | 1.33 | 4.048 | 661 |
| 58 | 712 | 0.645 | 1.47 | 4.140 | 591 |
| 59 | 757 | 0.683 | 1.87 | 4.238 | 529 |
| 60 | 808 | 0.723 | 1.34 | 4.338 | 476 |
| 61 | 853 | 0.765 | 1.52 | 4.443 | 429 |
| 62 | 907 | 0.808 | 1.53 | 4.549 | 387 |
| 63 | 975 | 0.854 | 1.45 | 4.657 | 349 |
| 64 | 1020 | 0.902 | 1.33 | 4.767 | 315 |

TABLE 4.10 DERIVED EXPERIMENTAL DATA.

BED MATERIAL: SILICON CARBIDE.

MEAN PARTICLE DIAMETER: 557 microns.

BED DEPTH: 50 mm.

PROBE POSITION: 25 mm above distributor.

| TEST NO. | $T_b$ C | H kW/m$^2$K | $N_{opt}$ | $Nu_{max}$ | Ar |
|---|---|---|---|---|---|
| 67 | 240 | 0.328 | 1.39 | 4.179 | 4774 |
| 68 | 366 | 0.379 | 1.67 | 4.264 | 3275 |
| 69 | 413 | 0.406 | 1.48 | 4.328 | 2781 |
| 70 | 463 | 0.434 | 1.71 | 4.402 | 2392 |
| 71 | 599 | 0.524 | 1.69 | 4.681 | 1612 |
| 72 | 649 | 0.557 | 1.57 | 4.790 | 1433 |
| 73 | 703 | 0.591 | 1.74 | 4.905 | 1280 |
| 74 | 771 | 0.626 | 1.38 | 5.026 | 1148 |
| 75 | 803 | 0.663 | 1. 43 | 5.151 | 1032 |
| 76 | 857 | 0.702 | 1.56 | 5.280 | 929 |
| 77 | 900 | 0.743 | 1.44 | 5.413 | 838 |
| 78 | 959 | 0.786 | 1.37 | 5.548 | 756 |
| 79 | 1001 | 0.831 | 1.73 | 5.685 | 682 |

TABLE 4.11 DERIVED EXPERIMENTAL DATA.

BED MATERIAL: SILICON CARBIDE.

MEAN PARTICLE DIAMETER: 637 microns.

BED DEPTH: 50 mm.

PROBE POSITION: 25 mm above distributor.

| TEST NO. | $T_b$ C | H kW/m$^2$K | $N_{opt}$ | $Nu_{max}$ | Ar |
|---|---|---|---|---|---|
| 80 | 259 | 0.310 | 1.64 | 4.577 | 7417 |
| 81 | 362 | 0.359 | 1.27 | 4.676 | 5089 |
| 82 | 417 | 0.385 | 1.63 | 4.749 | 4321 |
| 83 | 467 | 0.412 | 1.52 | 4.833 | 3716 |
| 84 | 605 | 0.498 | 1.43 | 5.149 | 2504 |
| 85 | 653 | 0.529 | 1.47 | 5.272 | 2226 |
| 86 | 708 | 0.562 | 1.39 | 5.402 | 1988 |
| 87 | 754 | 0.596 | 1.54 | 5.538 | 1783 |
| 88 | 800 | 0.632 | 1.69 | 5.680 | 1603 |
| 89 | 861 | 0.669 | 1.58 | 5.827 | 1444 |
| 90 | 911 | 0.709 | 1.43 | 5.977 | 1302 |
| 91 | 952 | 0.750 | 1.38 | 6.130 | 1174 |
| 92 | 1019 | 0.794 | 1.49 | 6.285 | 1059 |

TABLE 4.12 DERIVED EXPERIMENTAL DATA.

BED MATERIAL: SILICON CARBIDE.

MEAN PARTICLE DIAMETER: 710 microns.

BED DEPTH: 50 mm.

PROBE POSITION: 25 mm above distributor.

| TEST NO. | $T_b$ C | H kW/m$^2$K | $N_{opt}$ | $Nu_{max}$ | Ar |
|---|---|---|---|---|---|
| 100 | 270 | 0.298 | 1.46 | 4.895 | 1.0270 |
| 101 | 366 | 0.345 | 1.56 | 5.006 | 7046 |
| 102 | 417 | 0.370 | 1.37 | 5.086 | 5983 |
| 103 | 469 | 0.396 | 1.75 | 5.179 | 5146 |
| 104 | 600 | 0.479 | 1.64 | 5.525 | 3467 |
| 105 | 697 | 0.541 | 1.52 | 5.801 | 2753 |
| 106 | 748 | 0.574 | 1.32 | 5.950 | 2469 |
| 107 | 882 | 0.609 | 1.53 | 6.106 | 2219 |
| 108 | 850 | 0.646 | 1.68 | 6.266 | 1999 |
| 109 | 904 | 0.684 | 1.63 | 6.431 | 1803 |
| 110 | 964 | 0.724 | 1.59 | 6.599 | 1626 |
| 111 | 1025 | 0.767 | 1.24 | 6.769 | 1466 |

TABLE 4.13 DERIVED EXPERIMENTAL DATA.

BED MATERIAL: SILICON CARBIDE.

MEAN PARTICLE DIAMETER: 787 microns.

BED DEPTH: 50 mm.

PROBE POSITION: 25 mm above distributor.

| TEST NO. | $T_b$ C | H kW/m$^2$K | $N_{opt}$ | $Nu_{max}$ | Ar |
|---|---|---|---|---|---|
| 112 | 268 | 0.286 | 1.45 | 5.218 | 13987 |
| 113 | 367 | 0.332 | 1.86 | 5.340 | 11478 |
| 114 | 419 | 0.356 | 1.49 | 5.428 | 9596 |
| 115 | 460 | 0.381 | 1.37 | 5.529 | 8148 |
| 116 | 609 | 0.462 | 1.42 | 5.906 | 4722 |
| 117 | 653 | 0.492 | 1.63 | 6.053 | 4198 |
| 118 | 697 | 0.522 | 1.61 | 6.207 | 3750 |
| 119 | 748 | 0.555 | 1.54 | 6.370 | 3362 |
| 120 | 801 | 0.589 | 1.49 | 6.539 | 3023 |
| 121 | 862 | 0.624 | 1.74 | 6.714 | 2723 |
| 122 | 904 | 0.661 | 1.63 | 6.893 | 2455 |
| 123 | 959 | 0.701 | 1.42 | 7.076 | 2215 |
| 124 | 1022 | 0.742 | 1.40 | 7.263 | 1997 |

TABLE 4.14 DERIVED EXPERIMENTAL DATA.

BED MATERIAL;ZIRCON SAND.

MEAN PARTICLE DIAMETER;212.5 microns.

BED DEPTH: 50 mm.

PROBE POSITION; 25 mm above distributor.

| TEST NO. | $T_b$ C | H kW/m$^2$K | $N_{opt}$ | $Nu_{max}$ | Ar |
|---|---|---|---|---|---|
| 400 | 271 | 0.498 | 1.27 | 2.453 | 363 |
| 401 | 350 | 0.572 | 1.38 | 2.486 | 298 |
| 402 | 411 | 0.611 | 1.31 | 2.514 | 249 |
| 403 | 460 | 0.650 | 1.50 | 2.548 | 211 |
| 404 | 610 | 0.777 | 1.87 | 2.681 | 122 |
| 405 | 661 | 0.822 | 1.59 | 2.733 | 109 |
| 406 | 700 | 0.869 | 1.36 | 2.789 | 97 |
| 407 | 749 | 0.918 | 1.47 | 2.847 | 87 |
| 408 | 804 | 0.969 | 1.55 | 2.907 | 78 |
| 409 | 850 | 1.022 | 1.42 | 2.969 | 71 |
| 410 | 900 | 1.078 | 1.58 | 3.032 | 64 |
| 411 | 967 | 1.135 | 1.47 | 3.096 | 57 |
| 412 | 1024 | 1.196 | 1.59 | 3.160 | 51 |

TABLE 4.5 DERIVED EXPERIMENTAL DATA.

BED MATERIAL: ZIRCON SAND.

MEAN PARTICLE DIAMETER: 278 microns.

BED DEPTH: 50 mm.

PROBE POSITION: 25 mm above distributor.

| TEST NO. | $T_b$ C | H kW/m$^2$K | $N_{opt}$ | $Nu_{max}$ | Ar |
|---|---|---|---|---|---|
| 414 | 269 | 0.450 | 1.70 | 2.898 | .812 |
| 415 | 345 | 0.518 | 1.63 | 2.943 | 557 |
| 416 | 420 | 0.553 | 1.53 | 2.979 | 473 |
| 417 | 465 | 0.590 | 1.67 | 3.023 | 407 |
| 418 | 589 | 0.707 | 1.36 | 3.192 | 274 |
| 419 | 653 | 0.749 | 1.41 | 3.257 | 244 |
| 420 | 704 | 0.793 | 1.39 | 3.327 | 218 |
| 421 | 756 | 0.838 | 1.64 | 3.400 | 195 |
| 422 | 812 | 0.886 | 1.67 | 3.476 | 175 |
| 423 | 854 | 0.935 | 1.43 | 3.555 | 158 |
| 424 | 899 | 0.987 | 1.69 | 3.635 | 142 |
| 425 | 951 | 1.042 | 1.37 | 3.716 | 129 |
| 426 | 1000 | 1.098 | 1.16 | 3.797 | 116 |

TABLE 4.16 DERIVED EXPERIMENTAL DATA.

BED MATERIAL: ZIRCON SAND.

MEAN PARTICLE DIAMETER;343 microns.

BED DEPTH: 50 mm.

PROBE POSITION; 25 mm above distributor.

| TEST NO. | $T_b$ C | H kW/m$^2$K | $N_{opt}$ | $Nu_{max}$ | Ar |
|---|---|---|---|---|---|
| 428 | 248 | 0.415 | 1.98 | 3.301 | 1525 |
| 429 | 343 | 0.479 | 1.26 | 3.358 | 1046 |
| 430 | 402 | 0.512 | 1.36 | 3.403 | 888 |
| 431 | 460 | 0.546 | 1.47 | 3.456 | 764 |
| 432 | 601 | 0.657 | 1.45 | 3.658 | 515 |
| 433 | 654 | 0.696 | 1.72 | 3.736 | 458 |
| 434 | 702 | 0.738 | 1.40 | 3.820 | 409 |
| 435 | 756 | 0.781 | 1.58 | 3.907 | 366 |
| 436 | 800 | 0.826 | 1.64 | 3.998 | 329 |
| 437 | 869 | 0.873 | 1.32 | 4.092 | 297 |
| 438 | 909 | 0.922 | 1.47 | 4.188 | 268 |
| 439 | 963 | 0.974 | 1.51 | 4.285 | 241 |
| 440 | 1004 | 1.028 | 1.66 | 4.384 | 218 |

TABLE 4.17 DERIVED EXPERIMENTAL DATA.

BED MATERIAL: ZIRCON SAND.

MEAN PARTICLE DIAMETER: 412.5 microns.

BED DEPTH: 50 mm.

PROBE POSITION: 25 mm above distributor.

| TEST NO. | $T_b$ C | H kW/m$^2$K | $N_{opt}$ | $Nu_{max}$ | Ar |
|---|---|---|---|---|---|
| 441 | 259 | 0.387 | 1.34 | 3.701 | 2652 |
| 442 | 366 | 0.447 | 1.25 | 3.771 | 1820 |
| 443 | 410 | 0.479 | 1.47 | 3.823 | 1545 |
| 444 | 466 | 0.511 | 1.86 | 3.886 | 1329 |
| 445 | 600 | 0.615 | 1.62 | 4.123 | 895 |
| 446 | 653 | 0.654 | 1.65 | 4.215 | 796 |
| 447 | 711 | 0.692 | 1.46 | 4.312 | 711 |
| 448 | 746 | 0.733 | 1.43 | 4.415 | 637 |
| 449 | 799 | 0.776 | 1.37 | 4.521 | 573 |
| 450 | 857 | 0.821 | 1.69 | 4.631 | 516 |
| 451 | 904 | 0.868 | 1.22 | 4.743 | 465 |
| 452 | 963 | 0.918 | 1.43 | 4.857 | 420 |
| 453 | 1021 | 0.969 | 1.78 | 4.973 | 379 |

TABLE 4.18 DERIVED EXPERIMENTAL DATA.

BED MATERIAL: ZIRCON SAND.

MEAN PARTICLE DIAMETER: 463 microns.

BED DEPTH: 50 mm.

PROBE POSITION: 25 mm above distributor.

| TEST NO. | $T_b$ C | H kW/m$^2$K | $N_{opt}$ | $Nu_{max}$ | Ar |
|---|---|---|---|---|---|
| 454 | 239 | 0.361 | 1.14 | 3.965 | 3750 |
| 455 | 348 | 0.428 | 1.33 | 4.054 | 2573 |
| 456 | 401 | 0.459 | 1.36 | 4.113 | 2185 |
| 457 | 465 | 0.490 | 1.51 | 4.182 | 1879 |
| 458 | 608 | 0.591 | 1.45 | 4.443 | 1266 |
| 459 | 653 | 0.627 | 1.32 | 4.545 | 1126 |
| 460 | 700 | 0.665 | 1.57 | 4.652 | 1005 |
| 461 | 763 | 0.708 | 1.63 | 4.765 | 901 |
| 462 | 809 | 0.747 | 1.59 | 4.882 | 810 |
| 463 | 849 | 0.791 | 1.31 | 5.003 | 730 |
| 464 | 899 | 0.836 | 1.47 | 5.127 | 658 |
| 465 | 956 | 0.884 | 1.75 | 5.253 | 594 |
| 466 | 1010 | 0.935 | 1.41 | 5.381 | 535 |

TABLE 4.19 DERIVED EXPERIMENTAL DATA.

BED MATERIAL: ZIRCON SAND.

MEAN PARTICLE DIAMETER: 513 microns.

BED DEPTH: 50 mm.

PROBE POSITION: 25 mm above distributor.

| TEST NO. | $T_b$ C | H kW/m$^2$K | $N_{opt}$ | $Nu_{max}$ | Ar |
|---|---|---|---|---|---|
| 468 | 270 | 0.356 | 1.25 | 4.236 | 5101 |
| 469 | 366 | 0.412 | 1.34 | 4.324 | 3500 |
| 470 | 415 | 0.442 | 1.47 | 4.388 | 2972 |
| 471 | 460 | 0.472 | 1.21 | 4.464 | 2556 |
| 472 | 601 | 0.570 | 1.39 | 4.749 | 1722 |
| 473 | 649 | 0.605 | 1.58 | 4.860 | 1531 |
| 474 | 697 | 0.642 | 1.43 | 4.977 | 1368 |
| 475 | 747 | 0.681 | 1.64 | 5.100 | 1226 |
| 476 | 797 | 0.722 | 1.81 | 5.227 | 1102 |
| 477 | 850 | 0.764 | 1.33 | 5.359 | 993 |
| 478 | 904 | 0.809 | 1.45 | 5.494 | 895 |
| 479 | 962 | 0.856 | 1.63 | 5.632 | 808 |
| 480 | 1022 | 0.905 | 1.44 | 5.772 | 728 |

TABLE 4.20 DERIVED EXPERIMENTAL DATA.

## REFERENCES

[1] DAVIDSON, J F and HARRISON, D (1971). *Fluidization*, Academic Press, London

[2] KUNII, D and LEVENSPIEL, O (1969). *Fluidization Engineering*, J Wiley & Sons, New York

[3] DAVIDSON, J F and HARRISON, D (1963). *Fluidized Particles*, Cambridge University Press

[4] ZABRODSKY, S S (1966). *Hydrodynamics and Heat Transfer in Fluidized Beds*, M I T Press

[5] BROUGHTON, J (1972). *Combustion in Fluidized Beds*, PhD Thesis, University of Newcastle-upon-Tyne

[6] ERGUN, S (1952). Chem.Eng.Prog. 48, 89

[7] TOOMEY, R D and JOHNSTONE, H F (1952). Chem.Eng.Prog. 48, 220

[8] ROWE, P N and PARTRIDGE, B A (1962). Trans.I.Chem.E. 43, 157

[9] ROWE, P N and PARTRIDGE, B A (1962). Proc.Symp.Interactions between Fluids and Particles, I.Chem.E., 135, June

[10] PERRY, R H and CHILTON, C H (1973). *Chemical Engineering Handbook*, 5th Ed., McGraw Hill, New York

[11] KUNII, D and LEVENSPIEL, O (1968). I & E C Fund., 7, 446

[12] ROWE, P N, PARTRIDGE, B A, CHENEY, A G, HENWOOD, G A and LYALL, E (1965). Trans.I.Chem.E., 43, T271

[13] ROWE, P N (1973). Chem.Eng.Sci., 28, 980

[14] MOSS, G, CRAIG, J W T and TINSDALL, D (1972). AIChE Symp.Ser. 68, (126), 277

[15] ROWE, P N, PARTRIDGE, B A and LYALL, E (1964). Chem.Eng.Sci.

19, 973

[16] REKTORYS, K (1969). *Survey of Applicable Mathematics*, Iliffe Books, London

[17] HIBY, J W (1967). Proc.Int.Symp.on Fluidization, Netherlands University Press, 99

[18] VERLOOP, J and HEERTJES, P M (1974). Chem.Eng.Sci. 29, 1035

[19] SAGE, C S (1928). Trans.ASHVE, 34, 243

[20] FOXALL, D and HOCKLY, D K A (1966). CPE Heat Transfer Survey

[21] BARTEL, W J, GENETTI, W E and GRIMMETT, E S (1971). AIChE Symp.Ser. 67, (116), 85

[22] PETRIE, J C, FREEBY, W A and BUCKHAM, J A (1968). Chem.Eng. Prog. 64, (7), 45

[23] GENETTI, W E, SCHMALL, R A and GRIMMETT, E S (1971). AIChE Symp.Ser. 67, (116), 98

[24] ELLIOTT, D E, HEALEY, E M and ROBERTS, D G (1971). in Conf. by Inst.Fuel and L'Institut Francais des Combustibles et de l'Energie, Paris, France

[25] van HEERDEN, C, NOBEL, P and van KREVELEN, D W (1960). IMechE/ASME, Gen.Disc.on Heat Transfer, 358

[26] VREEDENBURG, H A (1960). IMechE/ASME, Gen.Disc.on Heat Transfer, 373

[27] VREEDENBURG, H A (1958). Chem.Eng.Sci. 9, 52

[28] VREEDENBURG, H A (1960). Chem.Eng.Sci. 11, 274

[29] BARTHOLOMEW, R N and KATZ, D L (1952). AIChE Symp.Ser. 48, (4), 3

[30] EINSTEIN, V G and KARTOYANSKAYA, L A (1969). Int.Chem.Eng.

9, (1), 137

[31] PILLAI, K K and ELLIOTT, D E (1974). Proc.Multi-Phase Flow Systems, IMechE/IChemE, Paper B 4, Glasgow, April

[32] McGUIGAN, S J (1972). *Preliminary REport on the Performance of Extended Surface Heat Exchangers in a Fluidized Bed.* Internal Report, Aston University

[33] CARRIER, W H and ANDERSON, S W (1944). Heating Piping and Air-Conditioning, 10, 304

[34] GARDNER, K A (1945). Trans ASME, 621

[35] McADAMS, W H (1954). *Heat Transmission*, McGraw-Hill, New York

[36] HARPER, D R and BROWN, W B (1922). US National Advisory Committee on Aeronautics, Report No.158

[37] SCHMIDT, T E (1949). Jnl ASRE, 351

[38] RICH, D G (1966). Proc.Third Int.Heat Trans.Conf. 3, 281

[39] ZABRONSKY, H (1955). Trans ASME, 22E, 119

[40] VITKOVITCH, D (1966). *Field Analysis*, D Van Nostrand, London

[41] ROSS, D S and QURESHI, I H (1963). J.Scient.Instrum, 40, 513

[42] PILLAI, K K (1975). Int.J.Heat & Mass Transfer, 18, 341

[43] BAERG, A, KLASSEN, J and GISHLER, P E (1950). Can.J.Research 28F, 287

[44] van HEERDEN, C, NOBEL, A P and van KREVELEN, D (1951). Chem.Eng.Sci. 1, 51

[45] KHARCHENKO, N V and MAKHORIN, K E (1964). Int.Chem.Eng. 4, (4), 650

[46] MASKAEV, V K and BASKAKOV, A P (1974). Int.Chem.Eng. 14, (1), 80

[47] GELPERIN, N I, EINSTEIN, V G and KARTOYANSKAYA, L (1969).

Int.Chem.Eng. 9, (1), 137

[48] KIM, J K, KIM, D C, CHUN, K S and CHOO, S S (1967). Int.Chem.Eng. 7, (1), 79

[49] JOLLEY, L J (1949). Fuel, 28, 114

[50] CARSLAW, H S and JAEGER, J C (1947). *Conduction of Heat in Solids*, Clarendon Press, Oxford

[51] ILCHENKO, A I and MAKHORIN, K E (1967). Khim.Prom. 43, (6), 443

[52] BOTTERILL, J S M and SEALEY, C J (1970). Brit.Chem.Eng. 15, 1167

[53] ILCHENKO, A I, MAKHORIN, K E and PIKASHOV, V S (1968). Inz.Fiz.Zh. 14, (4), 602

[54] BASKAKOV, A P and GOLDOBIN, Y M (1970). Heat Transfer Soviet Research, 2, (6), 172

[55] BASKAKOV, A P (1968). Izd.Metallurgia, Moscow

[56] YOSHIDA, K, UENO, T and KUNII, D (1974). Chem.Eng.Sci. 29, 77

[57] BOTTERILL, J S M and WILLIAMS, J R (1963). Trans.I.Chem.E. 41, (5), 217

[58] GABOR, J D (1970). AIChE Symp.Ser. 66, (105), 76

[59] BOTTERILL, J S M and BUTT M H D (1968). Brit.Chem.Eng. 13, 1000

[60] BOTTERILL, J S M, BUTT, M H D, CAIN, G L and REDISH, K A (1967). Proc.Int.Symp.on Fluidization, Netherlands University Press, Amsterdam

[61] BOTTERILL, J S M, BUTT, M H D, CAIN G L, CHANDRASEKHAR, R and WILLIAMS, J R (1967). Proc.Int.Symp.on Fluidization, Netherlands University Press, Amsterdam

[62] ZIEGLER, E N, KOPPEL, L B and BRAZLETON, W T (1964). I & E C Fund. 3, (94), 324

[63] FAIRBANKS, D F (1953). *Heat Transfer to Fluidized Beds*, Sc.D. Thesis, M I T

[64] MICHLEY, H S and FAIRBANKS, D F (1955). AIChE Jnl. 1, 374

[65] BASKAKOV, A P (1964). Int.Chem.Eng. 4, (2), 320

[66] BASKAKOV, A P and BERG, B V (1967). Khim.Prom. 43, (6), 439

[67] KUBIE, J (1974). *Bubble Induced Heat Transfer in Two-Phase Systems*, PhD Thesis, Aston University

[68] KUBIE, J and BROUGHTON, J (1975). Int.J.Heat & Mass Transfer, 18, 289

[69] ELECTRICAL RESEARCH ASSOCIATION (1967). *1967 Steam Tables*, Arnold, London

[70] ROGERS, G F C and MAYHEW, Y R (1967). *Thermodynamic and Transport Properties of Fluids*, Blackwell, London

[71] RITTENHAUS, G (1955). Jnl.Sedimentary Petrology, 13, (2), 79

[72] VEDAMURTHY, V N and SASTRI, V M K (1974). Int.J.Heat & Mass Transfer, 17, 419

[73] LEWIN, D A (1975). PhD Thesis, to be submitted, Aston University

[74] KOROLEV, V N, SYROMYATNIKOV, N I and TOLMACHEV, E M (1971). J.Engrg.Phys. 21, (6), 973

[75] KOROLEV, V N and KYROMYATNIKOV, N I (1971). Heat Transfer Soviet Research, 3, (4), 112

[76] ROBLEE, L H S, BAIRD, R M and TIERNEY, J W (1958). AIChE Jnl. 4, (4), 460

[77] RIDGWAY, K and TARBUCK, K J (1967). Brit.Chem.Eng. 12, (3), 384

[78] SHRIKHANDE, K Y (1955). J.Sci.Ind.Res., 14B, 457

[79] LEWIS, W K, GILILAND, E R and GIROUARD, A (1962). AIChE Symp.Ser. 58, (38), 87

[80] CHENG, S C and VACHON, R I (1969). Int.J.Heat & Mass Transfer, 12, 1201

[81] YAGI, S and KUNII, D (1957). AIChE Jnl. 3, (3), 373

[82] SAEGUSA, T, KAMATA, K, IIDA, Y and WAKAO, N (1974). Int.Chem.Eng. 14, (1), 169

[83] KUIKOV, A V, SHASKOV, A G, VASILIEV, L I and FRAIMAN, Y E (1968). J.Heat & Mass Transfer, 11, 117

[84] MASAMUNE, S and SMITH, J M (1963). I & EC Fund, 2, (2), 136

[85] KUNII, D and SMITH, J M (1960). AIChE Jnl. 6, (1), 71

[86] KRUPICZKA, R (1967). Int.Chem.Eng. 7, (1), 122

[87] GELPERIN, N I and EINSTEIN, V G. In Reference Number 1

[88] PETERS, K, ORLICHEK, A and SCHMIDT, A (1953). Chem.Ing.Techn. 25, (6), 316

[89] GIBILARO, L G and ROWE, P N (1974). Chem.Eng.Sci. 29, 1403

[90] CHEUNG, L, NIENOW, A W and ROWE, P N (1974). Chem.Eng.Sci. 29, 1301

[91] ROWE, P N, NIENOW, A W and AGBIM, A J (1972). Trans.I.Chem.E. 50, 310

[92] ROWE, P N, NIENOW, A W and AGBIM, A J (1972). Trans.I.Chem.E. 50, 324

[93] ROWE, P N (1973). Chem.Eng.Sci. 28, 979

[94] BROUGHTON, J (1974). Trans.I.Chem.E. 52, 105

# APPENDICES

# APPENDIX A

## A.1 THE EFFICIENCY OF PRE-MIXED, STOICHIOMETRIC GAS COMBUSTION

Consider the bubble-cloud system as shown in Figure 2.2, subject to the assumptions as in Section 2.2.2.2. If the total volumetric gas exchange rate between bubble and cloud is Q, then considering a time interval $\delta t$, at any time t,

$$c_{t+\delta t} = \left[\frac{V_b - Q\,\delta t}{V_b}\right] c_t \qquad (A.1)$$

where $c_t$ = concentration at time t.

The concentration, c, is here defined as the ratio of the volume concentration of unburnt gas in the bubble at time t to the volume concentration of unburnt gas in the original fluidizing mixture. Thus

$$\frac{dc_t}{dt} = -\left[\frac{q_b}{V_b} + \frac{q_d}{V_b}\right] c_t \qquad (A.2)$$

Hence

$$\frac{dc_t}{dt} + a\,c_t^2 + b\,c_t = 0 \qquad (A.3)$$

where $a = q_d/V_b\ \Delta c$

$b = q_b/V_b$

$\Delta c$ = concentration difference across the bubble boundary

$= c_t - 0 = c_t$

The solution of (A.3) is[16]

$$\frac{1}{c_t} = e^{\int b\,dt} \int \frac{a}{e^{\int b\,dt}}\,dt \qquad (A.4)$$

This is subject to the initial condition

$$c_t = c_o \quad \text{at} \quad t = 0$$

The general solution is therefore

$$c_t = \left[\frac{b\,c_o}{(b + a\,c_o)e^{b\,t} - a\,c_o}\right] \qquad (A.5)$$

To obtain the parameters a and b, the following relationships are used:

The bubble eruption size is taken as (from [1])

$$D_s = 1.4\,D_p\,\rho_s\,H_{mf}\,(U_f/U_{mf}) \qquad (A.6)$$

and the effective bubble size as the average bubble size

$$D_e = 0.5\,D_s \qquad (A.7)$$

The diffusion coefficient, $D_g$, is taken as that applying between two multi-component systems; one system containing the combustible mixture, and the other the products of combustion. A value for $D_g$ is obtained using the predictative correlations available in Perry[10].

The bubble residence time, $t_b$, within a given height of bed, H, can be taken as

$$t_b = H_{mf}/U_b \tag{A.8}$$

Hence the concentration of unburnt gas within the bubble at the bed surface is given by

$$c_{t_b} = \frac{b\, c_o}{(b + a\, c_o)e^{b\, t_b} - a\, c_o} \tag{A.9}$$

Consequently, the fraction of gas passing through the bed unburnt is

$$f_u = \frac{U_f - U_{mf}}{U_f}\left[\frac{b\, c_o}{(a\, c_o + b)e^{b\, t_b} - a\, c_o}\right] \tag{A.10}$$

To take account of the effect of increasing bubble diameter, and hence of varying gas exchange rates, (A.10) may be put in the form

$$f_u = \left[\frac{U_f - U_{mf}}{U_f}\right]\frac{1}{t_b}\int_o^{t_b} c_{t_b}\, d_t \tag{A.11}$$

Equation (A.11) has to be integrated numerically, and this is best done by considering height intervals rather than time intervals.

$$f_u = \left[\frac{U_f - U_{mf}}{U_f}\right]\frac{1}{H_{mf}}\int_o^{H_{mf}} c_{t_b}\, dH \tag{A.12}$$

Figure 2.3 represents the numerical evaluation of equation (A.12) with every value of bed height being used divided into either 100 equal increments, or intervals of 0.1 mm, whichever provides the

greater number of intervals. The diffusion coefficient used was estimated as 0.0571 $cm^2/s$ and $c_o$ was taken to be 1.

## A.2 HEAT TRANSFER TO EXTENDED SURFACE TUBING

Given that the fluid temperature, $t_f$, and the effective metal temperature, $t_m$, are linear functions of tube length, l, and that the bed is isothermal at $T_b$, the heat transferred to the fluid is

$$Q = \frac{A_{ti}}{l} \int_o^{\ell} h_f(t_m - t_f)dx \qquad (A.13)$$

If the fluid-side heat transfer coefficient is considered to be a linear function of the temperature, $t_f$,

$$h_f = a + b(t_f - c) \qquad (A.14)$$

where a, b and c are constants, (A.13) now becomes

$$Q = \frac{A_{ti}}{l} \int_o^{\ell} (k_1 + k_2x)\left[\frac{(k_1 + k_2x)(k_3 + k_4x) + k_5}{k_2x + k_6 + k_1} - k_7x - k_8\right]dx \qquad (A.15)$$

where $k_1$ - $k_8$ are all constants.

The integral in equation (A.15) can be split into partial fractions and then integrated by parts. This evaluation leads to equation (2.19).

# APPENDIX B

## B.1 TWO-DIMENSIONAL ELECTRICAL CONDUCTING FIELDS

Consider a sheet of electrical conducting paper carrying a steady current flow. The electro-static field strength, $\underline{E}$, will be given by

$$\underline{E} = -\text{grad } V(x,y) \tag{B.1}$$

where the negative sign, by convention, indicates that a positive voltage gradient is opposite in sign to the direction of electron flow. By Ohm's Law, the current density, $\underline{S}(x,y)$, will be

$$\underline{S} = \gamma \underline{E} \tag{B.2}$$

where $\gamma$ is the electrical conductivity of the paper. Thus

$$\underline{S} = -\gamma \text{ grad } V \tag{B.3}$$

For steady current flow over a closed region, by the divergence theorem

$$\text{div } \underline{S} = 0 \tag{B.4}$$

$$\text{div}(-\gamma \text{ grad } V) = 0 \tag{B.5}$$

$$\frac{\partial}{\partial x}\left(\gamma_x \frac{\partial V}{\partial x}\right) + \frac{\partial}{\partial y}\left(\gamma_y \frac{\partial V}{\partial y}\right) = 0 \tag{B.6}$$

(B.6) implies that the voltage gradient in the z-direction is zero, and that the field is purely two-dimensional. If the paper is homogenous and isotropic

$$\text{div grad } V = \nabla^2 V = 0 \qquad \text{(B.7)}$$

Now if a current density $i_z(x,y)$ is externally induced over the paper normal to the xOy plane, the flow of current is still steady

$$\text{div } \underline{S} + i_z(x,y)/t(x,y) = 0 \qquad \text{(B.8)}$$

where $t(x,y)$ is the local paper thickness. Thus

$$\gamma \text{ div grad } V - i_z/t = 0 \qquad \text{(B.9)}$$

If $i_z \propto V$ and t is constant

$$\nabla^2 V - \mu^2 V = 0 \qquad \text{(B.10)}$$

where $\mu$ is a constant.

## B.2 DERIVED $\lambda$ FOR CONDUCTING PAPER LAMINATIONS

All laminations were made by pasting 1 m square sheets of Teledeltos paper together. Ordinary paper glue ("cow gum") was used as the adhesive, and the laminations were dried in a press subject to gentle heating.

| SAMPLE NUMBER | NUMBER OF PAPER THICKNESSES | DERIVED $\lambda$ $m^{-1}$ |
|---|---|---|
| 1 | 3 | 49.606 |
| 2 | 3 | 48.819 |
| 3 | 3 | 49.600 |
| 4 | 4 | 42.323 |
| 5 | 4 | 42.520 |
| 6 | 4 | 43.307 |
| 7 | 4 | 42.520 |
| 8 | 4 | 42.913 |
| 9 | 5 | 34.646 |
| 10 | 5 | 33.858 |
| 11 | 5 | 34.515 |
| 12 | 5 | 34.136 |
| 13 | 6 | 27.978 |
| 14 | 6 | 28.643 |
| 15 | 6 | 28.832 |
| 16 | 6 | 28.850 |
| 17 | 8 | 21.650 |
| 18 | 8 | 21.124 |
| 19 | 8 | 20.871 |
| 20 | 8 | 20.980 |

# APPENDIX C

## C.1 PROPERTIES OF EXPERIMENTAL MATERIALS

### C.1.1 Density

The densities of all particulate materials used were measured using a specific gravity bottle with a liquid of low surface tension (n-Heptane). Density values for all other materials have been obtained from references [10], [69] and [70].

| MATERIAL | DENSITY $kg/m^3$ |
|---|---|
| Silica sand | 2630 |
| Zircon sand | 4615 |
| Silicon carbide | 3583 |
| Steel shot | 7418 |
| Copper shot | 8230 |
| Water | 1000 |
| Air at 20°C | 1.190 |

### C.1.2 Particle Size

The mean particle size, $\bar{D}_p$, is here defined by

$$\bar{D}_p = 1/\Sigma(w/d_p) \qquad (C.1.1)$$

where w is the fraction by weight of particles of size $d_p$.

For all experimental work, narrow size cuts of about

100 microns in range were sieved and a sample of the resultant mixture was further sieved so that a mean size could be calculated. The size of a particle, $d_p$, was taken to be the arithmetic mean of the two closest constraining sieve sizes.

### C.1.3 Particle Sphericity

The particle sphericity is taken to be the ratio of the surface area of a sphere of equivalent volume to the surface area of the particle.

A visual method for estimating $\Phi_s$ has been used. Projection micro-graphs of all the materials used were made, and by comparison with the data of Rittenhaus[71], values for the sphericity were obtained (Figures C.1, C.2 and C.3).

| MATERIAL | SPHERICITY |
|---|---|
| Silica sand | 0.81 |
| Zircon sand | 0.79 |
| Silicon carbide | 0.73 |
| Copper shot | 0.96 |
| Steel shot | 0.92 |

### C.1.4 Voidage

The values for $\varepsilon_{mf}$ were obtained experimentally. The expanded height of a bed of known particles weight was measured in a 50 mm square bed. The point of minimum fluidization was taken to be the point at which bubbling commenced, and was estimated visually.

C.1.5 Thermal Properties

Thermodynamic and transport properties have been estimated from Perry and Chilton[10], all at 20°C.

| MATERIAL | THERMAL CONDUCTIVITY w/mK | SPECIFIC HEAT J/kgK |
|---|---|---|
| Silica sand | 1.87 | 845 |
| Zircon sand | 1.95 | 900 |
| Silicon carbide | 16.2 | 550 |
| Copper | 387 | 385 |
| Mild steel | 55 | 472 |
| Brass | 110 | 380 |
| Air | 0.024 | 1008 |

## C.2 TRANSIENT HEATING OF A SPHERE

Consider a sphere of radius R being heated in a medium at a temperature $T_b$ by a uniform and constant heat transfer coefficient, h. The temperature within the sphere, T, at any radius, r, and time, t, must satisfy the differential equation

$$\frac{\partial^2 T}{\partial r^2} + \frac{2}{r}\frac{\partial T}{\partial r} = \frac{1}{\alpha}\frac{\partial T}{\partial t} \qquad \text{(C.2.1)}$$

where $\alpha$ = thermal diffusivity of sphere material

r = radius

In terms of the temperature excess, $\theta = T_b - T$, this becomes

$$\frac{\partial^2\theta}{\partial r^2} + \frac{2}{r}\frac{\partial\theta}{\partial r} = \frac{1}{\alpha}\frac{\partial\theta}{\partial t} \qquad (C.2.2)$$

subject to the initial condition

$$\theta = \theta_o \qquad \text{at } t = 0 \text{ for all } r \qquad (C.2.3)$$

and to the boundary condition

$$k\frac{\partial\theta}{\partial r} + h\theta = 0 \qquad \text{at } r = R \text{ for all } t \qquad (C.2.4)$$

where k is the thermal conductivity of the sphere material.

The solution of (C.2.2) is given by Carslaw and Jaeger[50] as

$$\frac{\theta(z)}{\theta_o} = \sum_{n=1}^{\infty} A_n[e^{-X_n Fo}](\sin X_n z)/z \qquad (C.2.5)$$

where $X_n$ is given by the roots of

$$X \cot X + Bi - 1 = 0 \qquad (C.2.6)$$

and Bi = Biot number of the sphere

z = non-dimensional radius = r/R

Fo = Fourier Number = $\alpha t/R^2$

$$A_n = \frac{\sin X_n - X_n \cos X_n}{X_n [2 X_n - \sin 2 X_n]} \qquad (C.2.7)$$

Using (C.2.5) the ratio of the centre temperature to the surface temperature at any time, t, is a function only of the Biot number.

These ratios, for different Bi, are tabulated below:

| BIOT NUMBER | CENTRAL TEMPERATURE/SURFACE TEMPERATURE |
|---|---|
| 0.001 | 0.9995 |
| 0.002 | 0,9990 |
| 0.005 | 0.9975 |
| 0.010 | 0.9950 |
| 0.020 | 0.9901 |
| 0.050 | 0.9754 |
| 0.100 | 0.9517 |
| 0.200 | 0.9066 |
| 0.300 | 0.8646 |
| 0.400 | 0.8252 |

Thus, it is apparent that with Biot numbers less than 0.02, the temperature variation through the sphere is less than 1%.

## C.3 CALCULATION OF HEAT TRANSFER COEFFICIENTS USING A SPHERE OF LOW BIOT NUMBER

Consider a sphere being heated within a uniform medium by means of a uniform and constant heat transfer coefficient, h. Consider further that the medium temperature, $T_b$, is uniform but linearly dependant with time. Thus,

$$T_b = T_{bo} + \lambda t \qquad (C.3.1)$$

where $\lambda$ is a constant coefficient.

If the Biot number of the sphere is low enough for it to be considered isothermal

$$hA(T_b - T) = m c_p \frac{dT}{dt} \qquad (C.3.2)$$

where A = surface area of sphere

m = mass of sphere

T = sphere temperature

$c_p$ = specific heat.

Putting $p = h A/mc_p$ and $\theta = T_b - T$, (C.3.2) transforms to

$$\frac{d\theta}{dt} + p\,\theta - \lambda = 0 \qquad (C.3.3)$$

The general solution from [16] is

$$\theta(t) = e^{-a}[\int \lambda\, e^{a}\, dt + k] \qquad (C.3.4)$$

where $a = \int p\, dt = p\, t$

and k = constant.

Hence

$$\theta(t) = k\, e^{-pt} + \lambda/p \qquad (C.3.5)$$

(C.3.3) is subject to the initial condition

$$\theta = \theta_o \quad \text{at } t = 0$$

and consequently

$$k = (p\,\theta_o - \lambda)/p \tag{C.3.6}$$

Thus

$$\frac{\theta}{\theta_o} = e^{-3\,Bi\,Fo}\left[1 - \frac{\lambda}{p\theta_o}\right] + \frac{\lambda}{p\theta_o} \tag{C.3.7}$$

Equation (C.3.7) can be put into the form

$$p = \frac{1}{t}\,\ell n\,\frac{p\,\theta/\theta_o - \lambda/\theta_o}{p - \lambda/\theta_o} \tag{C.3.8}$$

This is a convergent equation which, given t, $\lambda$, and $\theta/\theta_o$, can be solved iteratively for p. The heat transfer coefficient can then be calculated from

$$h = p\,m\,c_p/A \tag{C.3.9}$$

The special case of constant medium temperature, $T_b$, gives the well known solution

$$p = \frac{1}{t}\,\ell n\,\frac{\theta}{\theta_o} \tag{C.3.10}$$

Consequently, the solution of (C.3.10) can be used as a starting solution for the iterative equation (C.3.8).

## C.4 VOIDAGE VARIATION AT A CONSTRAINING SURFACE WITHIN A FLUIDIZED BED

Various workers have investigated the variation of voidage at a surface, both within packed beds[76,77], and within fluidized beds[74,75]. It is generally observed that voidage variations follow an oscillatory form which is heavily damped. Kubie[67] has proposed a simple geometrical function for a distance of up to one particle diameter from the surface. An experimental investigation has been carried out in packed, two-dimensional beds to test the validity of Kubie's function.

Consider a single spherical particle of radius r, positioned with its centre some distance p + 1 from a vertical surface. (All distances are non-dimensionalised by dividing by the particle radius) (see Figure C.4).

The area voidage along any square plane, distance z from the surface, of height 2, parallel to the surface and symmetrical about the particle will be for $0 < z < p$

$$\varepsilon = 1 \qquad \text{(C.4.1)}$$

for $p < z < p + 2$

$$\varepsilon = 1 - \frac{\pi}{4}\{2(z - p) - (z - p)^2\} \qquad \text{(C.4.2)}$$

For the general case, where more than one particle is present

$$\varepsilon = 1 - \beta(z) \qquad \text{(C.4.3)}$$

where $\beta(z)$ is the solids concentration at the plane z. The solids concentration due to a single particle, $\beta_s$, can be expressed as

$$\beta_s = \frac{\pi}{4}\left[2(z - p) - (z - p)^2\right]\left[H\{z - p\} - H\{z - p - 2\}\right] \quad (C.4.4)$$

where $H\{a\}$ represents the Heaviside Unit Step function, discontinuous at a.

If now, in a bed of particles, the function $\Phi(p)$ is defined as one which specifies the fraction of particles having their centres along the plane P + 1, then along any plane, z,

$$\beta(z) = \beta_b \int_0^z \beta_s \, \Phi(p) \, dp \quad (C.4.5)$$

where $\beta_b$ is the particle concentration in the bulk of the bed.

The experimental study utilised a two-dimensional perspex bed into which discs, 15 mm in diameter, were introduced. A measuring grid, 2 mm square, was scribed on to the walls of the bed (Figure C.5). After shaking, the distribution of particles at a wall was quantified by counting the number of particles having their centre between any two consecutive grid lines. The counting was carried out up to a distance of 3 particle diameters from the wall, and a total of 625 counts were made. Instead of attempting to fit a continuous function to the distribution, the discrete values obtained were used directly in a numerical form of (C.4.5) and values for the voidage variation were calculated for various values of z. The results are shown in Figure C.6 where they are compared with Kubie's geometrical function.

The damped nature of the oscillation is clearly evident. The geometrical function is shown to be a very good approximation for up to 1 particle diameter from the wall. However, the error in

assuming a constant bed voidage beyond this region is less than 10%, and in situations where the thermal penetration depth is less than one particle diameter, should not be significant.

## C.5 NUMERICAL SOLUTION OF THE SYSTEM OF EQUATIONS (4.32 - 4.37)

A finite difference, marching solution has been used. The grid is as shown in Figure C.7. The finite difference equations are as follows:

(a) Initial condition:

$$\theta_{i,j} = 1 \qquad \text{for all } i,j \tag{C.5.1}$$

(b) For $2 \leq i \leq k$

$$\theta_{i,j+1} = \frac{\Delta\tau}{\Delta z}\left[1 + Kr\,\frac{(1-\beta(i))}{\beta(\ell)}\right]\left[\frac{\theta_{i+1,j}+\theta_{i-1,j+1}-2\theta_{i,j}}{\Delta z}\right] + \frac{(1-k_r)}{\beta(i)}\,P\left[\frac{\theta_{i+1,j}-\theta_{i-1,j+1}}{2}\right] - S\,P\,\Delta z\left[\theta_{i,j}^4-\mu^4\right] \tag{C.5.2}$$

(c) For $k < i \leq 1$

As for (C.5.2) with $\mu = 1$, and $S = -S$ (C.5.3)

where

$$P = \frac{1}{\beta}\frac{d\beta}{dz} = \left[\frac{3-4(i-1)\Delta z}{3-2(i-1)\Delta z}\right]\left[\frac{1}{(i-1)\Delta z}\right] \tag{C.5.4}$$

(d) For $1 < i < m$

$$\theta_{i,j+1} = \theta_{i,j} + \frac{\Delta\tau}{\Delta z^2}\left[1 + Kr\,\frac{(1-\beta(i))}{\beta(i)}\right]$$

$$[\theta_{i+1,j}+\theta_{i-1,j+1}-2\theta_{i,j}] \qquad \text{(C.5.5)}$$

(e) For $i = m$

$$\theta_{i,j} = 1 \qquad \text{for all } j \qquad \text{(C.5.6)}$$

(f) Surface boundary condition: $i = 1$

$$\theta_{i,j+1} = \theta_{i,j} + \frac{\Delta\tau}{\Delta z^2}\,\frac{1}{\beta(\Delta z/2)}\,[\beta(\Delta z) + k_r(1-\beta(\Delta z))][\theta_{3,j}-\theta_{2,j}]$$

$$- 2\,\frac{\Delta\tau}{\Delta z^2}\left[1 + k_r\left[\frac{1}{\beta(\Delta z/2)} - 1\right]\right][\theta_{i,j}-\mu] \qquad \text{(C.5.7)}$$

$$- S\,\beta(\Delta z/2)\,[\theta_{i,j}-\mu^4]$$

The above set of equations has been solved on an ICL 1905 digital computer. To satisfy stability criteria, very small time steps have been necessary. The step sizes used in the solution were:

$$\Delta z = 0.015$$

$$\Delta\tau = 0.00001.$$